Springer Proceedings in Mathematics & Statistics

Shaibal Mukherjee
Abhirup Datta
Santanu Manna
Swadesh Kumar Sahoo *Editors*

Computational Mathematics, Nanoelectronics, and Astrophysics

CMNA 2018, Indore, India, November 1–3

Springer

Springer Proceedings in Mathematics & Statistics

Volume 342

Springer Proceedings in Mathematics & Statistics

This book series features volumes composed of selected contributions from workshops and conferences in all areas of current research in mathematics and statistics, including operation research and optimization. In addition to an overall evaluation of the interest, scientific quality, and timeliness of each proposal at the hands of the publisher, individual contributions are all refereed to the high quality standards of leading journals in the field. Thus, this series provides the research community with well-edited, authoritative reports on developments in the most exciting areas of mathematical and statistical research today.

More information about this series at http://www.springer.com/series/10533

Shaibal Mukherjee · Abhirup Datta ·
Santanu Manna · Swadesh Kumar Sahoo
Editors

Computational Mathematics, Nanoelectronics, and Astrophysics

CMNA 2018, Indore, India, November 1–3

Springer

Editors
Shaibal Mukherjee
Department of Electrical Engineering
Indian Institute of Technology Indore
Indore, Madhya Pradesh, India

Santanu Manna
Department of Mathematics
Indian Institute of Technology Indore
Indore, Madhya Pradesh, India

Abhirup Datta
Department of Astronomy, Astrophysics and Space Engineering
Indian Institute of Technology Indore
Indore, Madhya Pradesh, India

Swadesh Kumar Sahoo
Department of Mathematics
Indian Institute of Technology Indore
Indore, Madhya Pradesh, India

ISSN 2194-1009 ISSN 2194-1017 (electronic)
Springer Proceedings in Mathematics & Statistics
ISBN 978-981-15-9707-7 ISBN 978-981-15-9708-4 (eBook)
https://doi.org/10.1007/978-981-15-9708-4

Mathematics Subject Classification: 65Dxx, 85-XX, 65L60, 90-XX

This Springer imprint is published by the registered company Springer Nature Singapore Pte Ltd.
The registered company address is: 152 Beach Road, #21-01/04 Gateway East, Singapore 189721, Singapore

Preface

This book is a collection of selected papers presented at the International Conference on Computational Mathematics in Nanoelectronics and Astrophysics (CMNA 2018), held at the Indian Institute of Technology Indore, India, during November 1–3, 2018. With over 70 participants from around the world, the conference aimed at fostering international cooperation in areas of computational mathematics, nanoelectronics, and astrophysics. It promoted further interaction between Indian experts of the symposium's theme and researchers of applied mathematics, electrical engineering, and astrophysics from around the globe.

Areas of computational mathematics, nanoelectronics, and astrophysics have their roots in applied science and engineering and hence are closely connected. Conference sessions were designed to provide participants with an in-depth understanding of computational mathematics and its usage in nanoelectronics and astrophysics, hence, meeting an important goal of discussing recent developments and allowing them to benefit from the lessons learnt during the implementation of its agenda. Different sessions provided the framework for wider discussions on how research on the symposium topic has been fostered to date and what can be done in the future. Indeed, three days were buzzing with lively discussions, not only during the interactive sessions, but also during coffee time, symposium lunch, and dinner! Three parallel sessions on the first two days and two parallel sessions on the last day, consisting of 49 contributed talks by young researchers, 9 invited talks by researchers from India and abroad, 3 plenary talks, and 3 keynote talks were delivered by eminent speakers from India and abroad.

Key speakers at the conference were Prof. Navakanta Bhat (India), Prof. Anil Bhardwaj (India), Dr. Badam Singh Kushvah (India), Dr. M. Tanveer (India), Prof. Dr. Clemens Heske (Germany), Prof. Damayanti Gharpure (India), Dr. Myo Than Htay (Japan), Dr. Dipu Pramanik (USA), Prof. Amita Das (India), Prof. Karuna Kar Nanda (India), Dr. Aveek Sarkar (India), Dr. Pravata K. Mohanty (India), Dr. Sanjeev Singh (India), Dr. Antony Vijesh (India), and Prof. Durga Charan Dalal (India). We thank them all for their kind effort and contributions. It is our hope and intent that their lecture material will inspire people working in the mentioned areas.

Organizers are grateful for the support of Prof. Pradeep Mathur, Director, IIT Indore, in making it possible to organize the first joint event of three disciplines at IIT Indore. The organizing committee is also thankful to the following funding and sponsoring agencies for their financial support in organizing CMNA 2018 successfully: Science and Engineering Research Board (SERB), New Delhi; Council of Scientific and Industrial Research (CSIR), New Delhi; and other industry sponsors. The organizers also acknowledge the financial support provided by IIT Indore. We also express our special gratitude to the advisory committee members of CMNA 2018 for their suggestions on the academic contents and the organizing committee for their cooperation and timely execution of all tasks related to the conference. Finally, special thanks to Springer Nature for accepting to publish the book.

Indore, India

Dr. Shaibal Mukherjee
Dr. Abhirup Datta
Dr. Santanu Manna
Dr. Swadesh Kumar Sahoo

Contents

Computational Mathematics

Radial Basis Function Based Probabilistic Buckling Behavior of Sandwich Plates

R. R. Kumar, K. M. Pandey, and S. Dey

Abstract This paper presents the effect of thickness on probabilistic buckling load of sandwich plate using radial basis function (RBF) approach. Due to inevitable material anisotropy and manufacturing inaccuracy such type of structure are always subjected to spatial variability. So, it is required to consider the stochastic effect which makes computational approach more challenging. Using C^0 stochastic finite element method (FEM) model and higher order zigzag theory, the mathematical formulation has been developed. Cost-effective and computationally efficient RBF-based surrogate is used to get the result without compromising with accuracy in comparison with direct Monte Carlo simulation technique. Skyline technique is used to store global stiffness matrix in a single array and it is solved by subspace iteration.

Keywords Sandwich plate · Probabilistic buckling load · Radial basis function · Higher order zigzag theory · Monte Carlo simulation

1 Introduction

Sandwich composites are extensively used in aerospace, boats, high performance automobiles, wind turbines, civil construction, marine, and sports equipment. Normally, a sandwich plate comprises a low stiffness, low density inner soft core placed between two highly stiff outer face-sheets generally made from carbon fiber or aerospace grade aluminum. The whole structure is compacted by some structural adhesive. The basic principle of design of sandwich composite is adopted from an I-beam, where the face-sheet represents the flanges and the core represents the web. The only difference between these two is that in case of sandwich the core is made of different material from the face-sheet. The function of core is to resist shear stresses and stabilizes the face-sheets against buckling or wrinkling whereas two face-sheets act together as an efficient stress couple, counteracting the external bending moment. There must be a strong bond between the face-sheets and the core so that the final

R. R. Kumar (✉) · K. M. Pandey · S. Dey
Department of Mechanical Engineering, National Institute of Technology, Silchar, India
e-mail: ravinits2014@gmail.com

S. Mukherjee et al. (eds.), *Computational Mathematics, Nanoelectronics, and Astrophysics*,
Springer Proceedings in Mathematics & Statistics 342,
https://doi.org/10.1007/978-981-15-9708-4_1

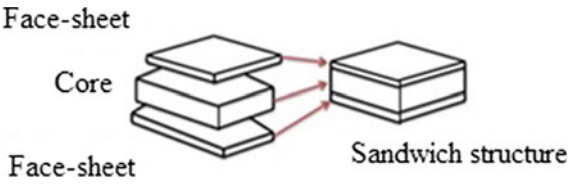

Fig. 1 A simple rectangular sandwich plate

structure can resist the tensile and shear stresses occurring in between them. High bending strength-to-weight and high stiffness-to-weight ratio makes sandwich plate of great importance. Sandwich plate eliminates the use of additional thermal insulator due to low thermal conductivity cellular cores inherent in plate ensures light structural weight. Sandwich plate is having layered construction which causes variation in properties throughout the thickness. Because of this typical construction it possesses very high variation in the material and geometric properties which results in uncertain behavior of structure. These inevitable uncertainties should be carefully considered in the analysis for realistic and safe design. So, it is necessary to predict the probabilistic behavior of overall response. Figure 1 depicts typical construction of sandwich structure.

Many researchers [1–4] worked on deterministic analysis of sandwich plate. Some authors [5–11] experimentally performed bending, buckling, and free vibration analysis of sandwich plates. According to Brush and Almroth [12] transverse shearing force is also responsible for the rotation and curvature of sandwich. They also explained that critical load does not represent its ultimate strength. Hoff and Mautner [13] worked on rectangular sandwich plate and found that buckling consists of a ripple of short wavelength across the plate. For CFRP panels, Pearce and Webber [14] found that experimental failure load was higher than the experimental buckling load. Ko [15] worked on honeycomb sandwich panel and found the combined buckling equations by using Raleigh-Ritz method. Various other authors [16] worked on the delamination growth and stability analysis and found that with the increase in delamination size, buckling load decreases. Hahn et al. and others [17] worked on simply supported rectangular panel and evaluated pre- and post-buckling response and found that failure occur at larger load than those required to initiate localized and elastic overall buckling. The parametric control and instability in buckling of FRP sandwich was determined by Hansen [18]. A design analysis of CSB specimen was presented by Carlsson [19]. Some research [20–28] has been reported in the field of uncertainty quantification of composites by using surrogate approach.

The above discussions show that many studies have been done related to buckling behavior of sandwich plate. However, the effect of stochasticity in input parameter has been avoided. Moreover, these literatures do not reveal any work related to plate thickness effect on probabilistic buckling response. So in this paper, we have taken a systematic approach in studying the effect of plate thickness on probabilistic buckling load.

2 Theoretical Formulation

The generalized displacement vector $\{S(\varpi)\}$ at any point can be expressed as

$$\{S(\varpi)\} = \sum_{k=1}^{n} N_i(\varpi) S_i(\varpi) \tag{1}$$

where $\{S\} = \{u_o\ v_o\ w_o\ \theta_x\ \theta_y\ u_u\ v_u\ w_u\ u_l\ v_l\ w_l\}^T$ by imposing the condition of transverse shear stress continuity at the interface between layers and utilizing zero transverse shear stress condition at bottom and top surface along with $u = u_l$, $v = v_l$, at the bottom and $u = u_u$, $v = v_u$ at the top of plate. Displacement vector corresponding to node i is denoted by S_i, shape function associated with node i by N_i and number of nodes per element by n. By using Eq. (1), strain vector can be expressed as

$$\{\varepsilon(\varpi)\} = [A(\varpi)]\{S(\varpi)\} \tag{2}$$

where $[A]$ is Cartesian strain–displacement matrix.

The Eigen value solution for buckling analysis can be represented as

$$[K_e(\varpi)]\ \{S\} = \lambda(\varpi)[K_G(\varpi)]\ \{S\} \tag{3}$$

where $\lambda(\varpi)$ is stochastic buckling load factor. Global stiffness matrix is stored in a single array by using skyline technique and stochastic buckling equation is solved by simultaneous iteration technique.

3 Radial Basis Function

The Euclidean distances of linear combination presented in surrogate-based model is represented as

$$\hat{Y}(x) = \sum_{k=1}^{n} w_k \varphi_k(X,\ x_k) \tag{4}$$

where

w_k = weight determined by the least-squares method.

n = number of sampling points, and

$\varphi_k(X,\ x_k)$ = kth basis function determined at the sampling point x_k.

In the basis function, various symmetric radial functions are used. RBF model is represented by using radial function, which is expressed as

$$F(x) = \frac{1}{\sqrt{1 + \frac{(x-c)^T (x-c)}{r^2}}} \quad \text{(For inverse multi-quadratic)} \tag{5}$$

$$F(x) = \exp\left(-\frac{(x-c)^T (x-c)}{r^2}\right) \quad \text{(For Gaussian)} \tag{6}$$

$$F(x) = \frac{1}{1 + \frac{(x-c)^T (x-c)}{r^2}} \quad \text{(For Cauchy)} \tag{7}$$

$$F(x) = \sqrt{1 + \frac{(x-c)^T (x-c)}{r^2}} \quad \text{(For multi-quadratic)} \tag{8}$$

Here $r^2 = 1$ is taken as fixed parameter to apply Gaussian basis function. It exactly passes through all the sampling point which implies that function value from approximate function equals to that of true function. It is computational which is of keen interest to researcher due to versatile problem-solving ability like optimization, pattern recognition, prediction, associative memory, and control tool which is modeled as per our biological brain. It acts in a similar way to that of brain.

4 Result and Discussions

In present study, a sandwich plate of length (l) 10 cm, breadth (b) 10 cm, and varying thickness (t) of 0.5, 1, and 1.5 cm is considered with 10% stochasticity in thickness to get the probabilistic buckling load for CCCC, CFCF, SCSC, and SSSS boundary condition (C-Clamped, F-Free, S-Simply Supported). Considered sandwich plate core (0°) thickness is taken as 80% of total thickness and face-sheet thickness is equally divided into 12 number of laminate (upper and lower both) having ply-orientation angle (90°/0°/90°/0°/90°/0°/90°/0°90°/0°/90°/0°). The convergence study on non-dimensional deterministic buckling load is presented in Table 1 along with the previous result of Reddy [29], Kant and Manjunath [30]. It is remarked from

Table 1 Convergence study on non-dimensional deterministic buckling load for simply supported laminated composite [0°/90°/0°] plate ($E_{11}/E_{22} = 40$)

Span thickness ratio	Present FEM			Reddy [25]	Kant and Manjunath [26]
	4 × 4	8 × 8	12 × 12		
10	21.906	21.899	21.898	22.120	22.067
50	35.259	35.208	35.206	35.229	35.224
100	36.036	35.918	35.916	35.921	35.921

the table that the present result is in good agreement with previous works. Finite element formulation is made using nine nodded isoparametric bending element and surrogate-based finite element iterations are made using layer-wise random variable approach. RBF-based surrogate model is applied to get probabilistic buckling analysis of soft core sandwich plate corresponding to number of random input parameters. Figure 2 represents the layout of stochastic buckling analysis of sandwich plate using RBF model.

Result obtained from Direct Monte Carlo simulation (MCS) and RBF approach are plotted using probability density function (PDF) plot and scatter plot in Fig. 3. Negligible deviation of RBF model from finite element based direct MCS model (Fig. 3) represents the validity and high level accuracy of surrogate-based RBF approach. In scatter plot, low deviation of points from diagonal line shows high prediction capability, pattern recognition, and applicability of RBF model instead of computationally expensive finite element model. Here although the same numbers of samples as in direct MCS (10,000 samples) are used to characterize the probability, it requires only 512 number of sample run through direct MCS approach.

Therefore, this method provides an economical way to calculate probabilistic buckling load accurately in very less time and effort. Material properties are considered based on ref [31] for the present analysis. Buckling load follows the sequence of

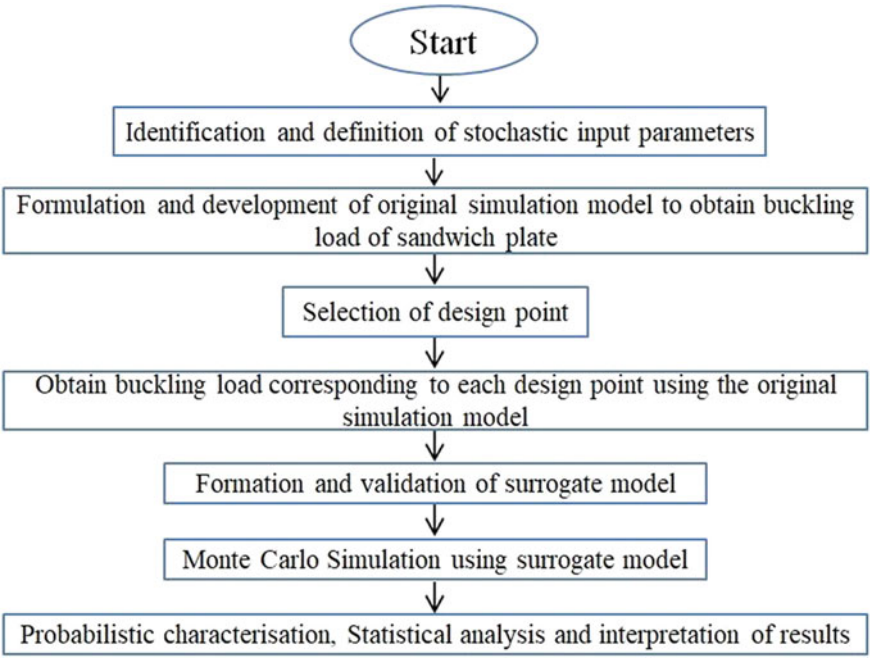

Fig. 2 Flow diagram of stochastic buckling analysis using surrogate (RBF) model

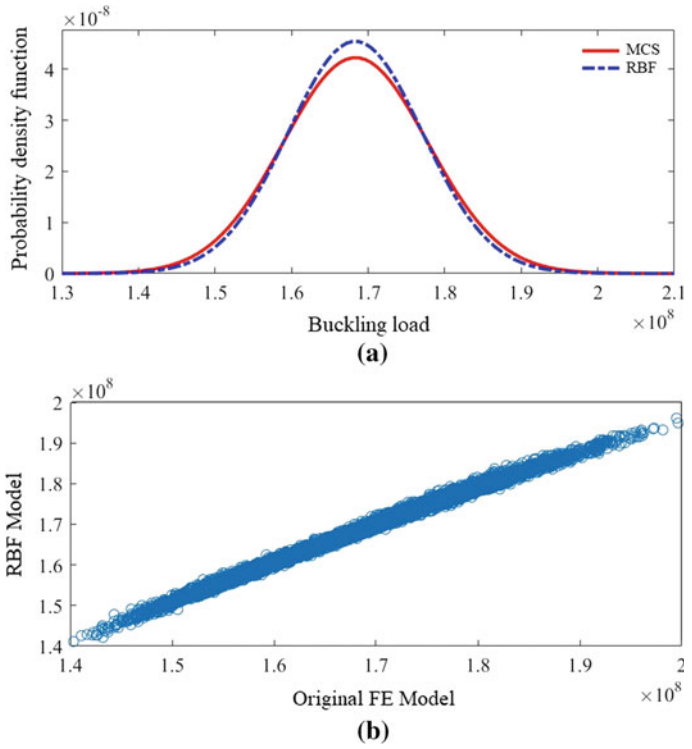

Fig. 3 **a** Probability density function for MCS and RBF model **b** Scatter plot of original FE Model with RBF model, considering variation in all parameter of 8 layer sandwich plate

CFCF, SSSS, CCCC, and SCSC in their increasing order as illustrated in Fig. 4. Buckling load increases with increase in plate thickness for a particular boundary condition. Response bound is observed to be increasing with increase in plate thickness whereas decreasing density function is observed with increase in thickness.

5 Conclusions

In this paper, radial basis function based bottom up stochasticity propagation approach is applied to get effect of plate thickness on probabilistic buckling behavior. RBF is observed as highly efficient computational tool in comparison with direct Monte Carlo simulation with negligible inaccuracy. The study of probabilistic behavior for buckling load with highly time saving RBF computational tool in accordance with finite element modeling is the key novelty in present study. Variation (10%) in plate thickness (core and face-sheet) is considered to study their individual effect. Probabilistic buckling analysis illustrates remarkable deviation of result from their deterministic value due to unavoidable uncertainty source present in real-life

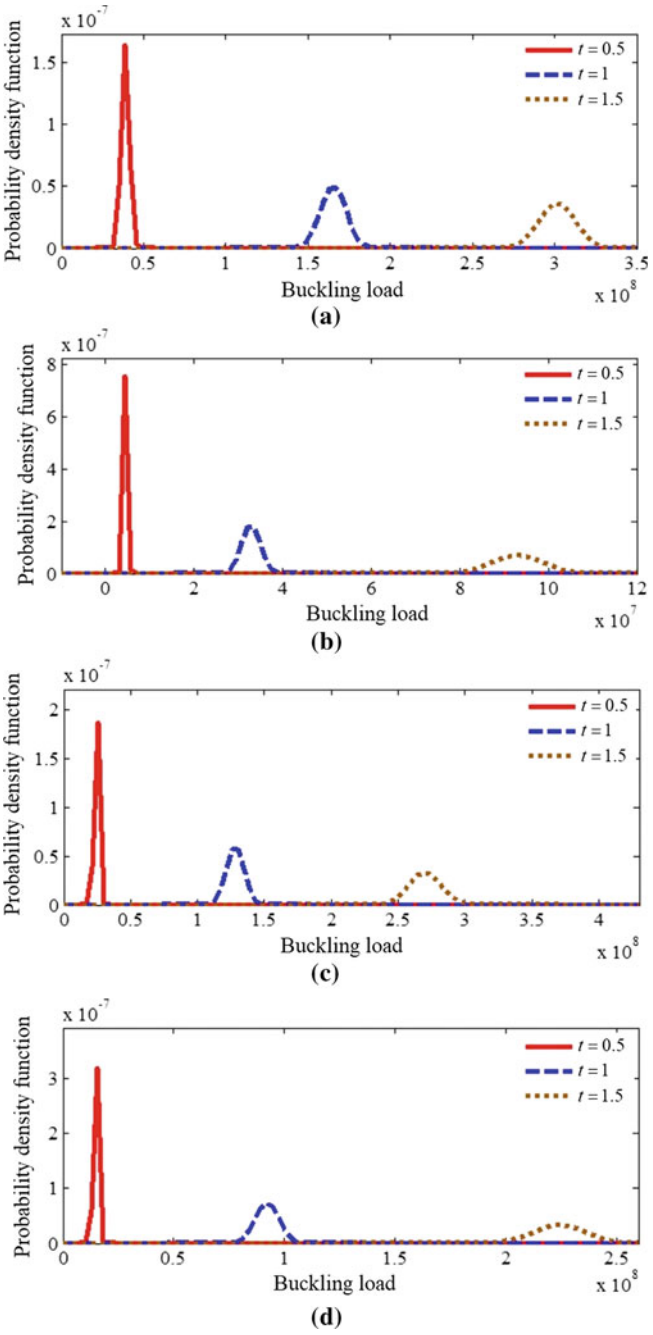

Fig. 4 Stochastic buckling load (N) of sandwich plates having different plate thickness considering stochasticity in thickness only, for **a** CCCC **b** CFCF **c** SCSC **d** SSSS boundary condition

problem. Hence, for better reliable and sustainable design it is requisite to consider the probabilistic effect in design parameter. Proposed approach can be further extended for static, dynamic, and control analysis of complex structure.

References

1. Noor, A.K., Burton, W.S., Bert, C.W.: Computational models for sandwich panels and Shells. Appl. Mech. Rev. **49**, 155–199 (1996)
2. Bert, C.W.: Literature review: research on dynamic behavior of composite and sandwich plates–V: Part II. Shock Vib. Digest **23**, 9–21 (1991)
3. Mallikarjuna, K.T.: A critical review and some results of recently developed refined theories of fiber-reinforced laminated composites and sandwiches. Compos. Struct. **23**, 293–312 (1993)
4. Altenbach, H.: Theories for laminated and sandwich plates. Mech. Compos. Mate. **34**, 243–252 (1998)
5. Alibeigloo, A., Alizadeh, M.: Static and free vibration analyses of functionally graded sandwich plates using state space differential quadrature method. Eur. J. Mech. A/Solid **54**, 252–266 (2015)
6. Carrera, E., Brischetto, S.: A survey with numerical assessment of classical and refined theories for the analysis of sandwich plates. Appl. Mech. Rev. **62**, 1–17 (2009)
7. Mukhopadhyay, T., Dey, T.K., Chowdhury, R., Chakrabarti, A., Adhikari, S.: Optimum design of FRP bridge deck: an efficient RS-HDMR based approach. Struct. Multidiscipl. Optimiz. **52**, 459–477 (2015)
8. Dey, T.K., Mukhopadhyay, T., Chakrabarti, A., Sharma, U.K.: Efficient lightweight design of FRP bridge deck. Proc. Inst. Civil. Eng. Struct. Build **168**, 697–707 (2015)
9. Singh, A., Panda, S., Chakraborty, D.: A design of laminated composite plates using graded orthotropic fiber-reinforced composite plies. Compos. Part B Eng. **79**, 476–493 (2015)
10. Mukhopadhyay T., Dey T.K., Dey S., Chakrabarti, A.: Optimization of fiber reinforced polymer web core bridge deck–A hybrid approach. Struct. Eng. Int. **25**, 173–183 (2015)
11. Mukhopadhyay, T.: A multivariate adaptive regression splines based damage identification methodology for web core composite bridges including the effect of noise. J. Sandwich Struct. Mater. 1099636216682533 (2017)
12. Brush, D.O., Almroth, B.O., Hutchinson, J.W.: Buckling of bars, plates and shells. J. Appl. Mech. **42**, 911 (1975)
13. Hoff, N.J.: The buckling of sandwich-type panels. J. Aeronaut. Sci. **12**(3), 285–297 (1945)
14. Pearce, T.R.A., Webber, J.P.H.: Experimental buckling loads of sandwich panels with Carbon Fiber faceplates. Aeronaut. Q. **24**(4), 295–312 (1973)
15. Ko, W.L.: Mechanical and thermal buckling analysis of rectangular sandwich panels under different edge conditions. NASA **4585**, 1994 (1994)
16. Davison, B.D.: Delamination buckling: Theory and Experiment. J. Comput. Mater. **25**(10), 1351–1378 (1991)
17. Hahn, E.K., Carlsson, L.A., Westerlind, B.S.: Edge-compression fixture for buckling studies of corrugated board panels. Exp. Mech. **32**(3), 252–258 (1992)
18. Hansen, U.: Compressive behavior of FRP sandwich specimen with interface debonds. J. Comput. Mater. **32**(4), 335–360 (1998)
19. Carlsson, L.A.: On the design of cracked sandwich beam specimen. J. Reinf. Plast. Compos. **10**(4), 434–444 (1991)
20. Kumar, R.R., Mukhopadhyay, T., Pandey, K.M., Dey, S.: Stochastic buckling analysis of sandwich plates: The importance of higher order modes. Int. J. Mech. Sci. **152**, 630–643 (2019)
21. Karsh, P.K., Kumar, R.R., Dey, S.: Radial basis function-based stochastic natural frequencies analysis of functionally graded plates. Int. J. Comput. Methods 1950061 (2019)

22. Kumar, R.R., Pandey, K.M., Dey, S.: Probabilistic assessment on buckling behavior of sandwich panel:-A radial basis function approach. Struct. Eng. Mech. **7**(12), 197–210 (2019)
23. Kumar, R.R., Karsh, P.K., Pandey, K.M., Dey, S.: Stochastic natural frequency analysis of skewed sandwich plates. Eng. Comput. (2019)
24. Kumar, R.R., Mukhopadhyay, T., Naskar, S., Pandey, K.M., Dey, S.: Stochastic low-velocity impact analysis of sandwich plates including the effects of obliqueness and twist. Thin-Walled Struct. **145**, 106411 (2019)
25. Karsh, P.K., Kumar, R.R., Dey, S.: Stochastic impact responses analysis of functionally graded plates. J. Br. Soc. Mech. Sci. Eng. **41**(11), 501 (2019)
26. Kumar, R.R., Mukhopadhya, T., Pandey, K.M., Dey, S.: Prediction capability of polynomial neural network for uncertain buckling behavior of sandwich plates. In: Handbook of Probabilistic Models, pp. 131–140. Elsevier (2020)
27. Kumar, R.R., Pandey, K.M., Dey, S.: Stochastic free vibration analysis of sandwich plates: a radial basis function approach. In: Reliability, Safety and Hazard Assessment for Risk-Based Technologies, pp. 449–458. Springer, Berlin (2020)
28. Kumar, R.R., Pandey, K.M., Dey, S.: Effect of skewness on random frequency responses of sandwich plates. In: Recent Advances in Theoretical, Applied, Computational and Experimental Mechanics, pp. 13–20. Springer, Singapore (2020)
29. Reddy, J.N.: A simple higher-order shear deformation theory for laminated composite plates. J. Appl. Mech. **51**(4), 745–752 (1984)
30. Kant, T., Manjunath, B.S.: An unsymmetric FRC laminated finite element model with 12 degree of freedom per node. Eng. Comput. **5**(4), 300–308 (1998)
31. Kollar, L.P., Springer, G.S.: Mechanics of Composite Structures. Cambridge (2003)

Stochastic Natural Frequencies of Functionally Graded Plates Based on Power Law Index

P. K. Karsh and S. Dey

Abstract The present paper deals with the stochastic natural frequency analysis of functionally graded material (FGM) plates by employing the multivariate adaptive regression splines surrogate (MARS) model. The gradation of material properties of constitute materials is carried out by power law distribution. The variation in material properties for different value of power law index or exponent is considered as input variables, while the first three natural frequencies are considered as output responses. The MARS model is coupled with the finite element model to reduce computational time. The results of the MARS model are validated with the results obtained from the traditional Monte Carlo simulation (MCS). The statistical analysis is portrayed to describe the probability density function of natural frequencies corresponding to power law index.

Keywords Stochastic natural frequency · Functionally graded materials · Monte Carlo simulation · Multivariate adaptive regression splines · Uncertainty quantification

1 Introduction

Functionally graded materials are different from the conventional homogeneous material in which two materials are heterogeneously mixed to obtain the predefined functionally requirements. Due to its spectacular functionalities, it has wide applications in engineering science such as automobiles, marine, sports, aerospace and civil structures. Commonly, ceramic and metals are constitutes of FGM, and their volume fraction is smoothly and continuously distributed from one surface to another. Due

P. K. Karsh (✉)
Mechanical Engineering Department, Parul Institute of Engineering & Technology, Parul University, Vadodara, India
e-mail: pradeepkumar.karsh270071@paruluniversity.ac.in; pradeepkarsh@gmail.com

P. K. Karsh · S. Dey
Mechanical Engineering Department, National Institute of Technology, Silchar, India

S. Mukherjee et al. (eds.), *Computational Mathematics, Nanoelectronics, and Astrophysics*, Springer Proceedings in Mathematics & Statistics 342,
https://doi.org/10.1007/978-981-15-9708-4_2

to the continuous mixture of materials, the interface joint is absent inside the FGM structure. So that FGM can perform service in a high-temperature environment. The main lacuna of the composite structure is the delamination of laminates at the higher temperature due to the poor bonding between the interfaces of two laminates. This problem of the composite structure can be sort out by employing the functionally graded materials to maintain structural integrity. As the application and development of functionally graded materials rise dramatically, accurately modelling their mechanical properties is greatly needed.

Many researchers carried out work on the material modelling and dynamic analysis of functionally graded materials. Xu and Meng [1] determined material properties of FGM beams by using the three different distribution laws, namely, power law, sigmoid law and exponential law, and performed the dynamic analysis of FGM beams by employing the analytical method. Naebe and Shirvanimoghaddam [2] presented the review paper on the material selection, fabrication and material modelling of functionally graded materials. Moita et al. [3] carried out structural and sensitivity analysis along with the material modelling and sizing optimization of FGM structures by employing the high-order shear deformation theory. The power law index and thickness are considered as design parameters, while mass, displacement, natural frequency and critical loads are taken as response parameters. Burlayenko et al. [4] applied finite element (FE) method for thermal analysis of FGM plates as well as material modelling is also carried out by using power law distribution. Kumar et al. [5] applied dynamic stiffness method for dynamic analysis of FGM rectangular plates with different boundary conditions. Classical plate theory is employed for the formulation of dynamic stiffness method. Attia and Rahman [6] carried out free vibration analysis of FGM nano-beams with considering the influence of microstructure rotation and surface energy by using the Bernoulli–Euler beam theory and found the effects of the power law index, material damping, surface elasticity, thickness and Poisson's effects. Zur [7] employed quasi-Green's function method for the free axisymmetric and non-axisymmetric vibration of FGM plates and determined the effects of boundary conditions, gradient index and core radius. Salinic et al. [8] performed free vibration analysis of FGM structure with different geometry by using the symbolic–numeric method of initial parameters approach. Further, some researches carried out work in the past on the dynamic analysis of FGM and composite structures [9–19]. In the present paper, the effects power law exponent on the stochastic free vibration of FGM cantilever plate are determined. The variability in the material properties is considered as the input variables with $\pm 10\%$ degree of stochasticity. The direct Monte Carlo simulation required large number of simulation which leads to high cost and time. To mitigate this lacuna of Monte Carlo simulation, a surrogate-based MARS model is coupled with the finite element formulation. Figure 1 illustrates the geometric view of cantilever FGM plate.

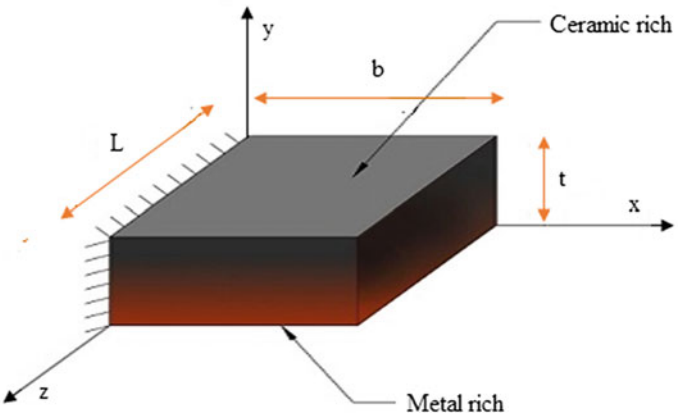

Fig. 1 Geometric view of functionally graded material cantilever plate

2 Mathematical Formulation

The dynamic equation of motion of the system can be expressed as [20]

$$\left[\tilde{M}(\Theta)\right]\{\ddot{\delta}\} + \left[\tilde{C}(\Theta)\right]\{\dot{\delta}\} + \left[\tilde{K}(\Theta)\right]\{\delta\} = \left[\overline{F}\right], \tag{1}$$

where $\left[\tilde{M}(\Theta)\right]$, $\left[\tilde{C}(\Theta)\right]$, $\left[\tilde{K}(\Theta)\right]$ are the randomised mass matrix, damping matrix and stiffness matrix, respectively, while $\left[\overline{F}\right]$ is the external applied force. (Θ) represents the degree of stochasticity. For the free vibration analysis without damping, Eq. (1) becomes

$$\left[\tilde{M}(\Theta)\right]\{\ddot{\delta}\} + \left[\tilde{K}(\Theta)\right]\{\delta\} = 0. \tag{2}$$

For free vibration displacement vector can be written as

$$\{\delta\} = [\psi]\sin\phi t, \tag{3}$$

$$\{\delta\}'' = -\phi^2[\psi]\sin\phi t, \tag{4}$$

where $[\psi]$ represents the Eigen vector, ϕ is the Eigen value or natural frequency. So the Eq. (2) becomes

$$-\phi^2\left[\tilde{M}(\Theta)\right]\{\psi\}\sin\phi t + \left[\tilde{K}(\Theta)\right]\{\psi\}\sin\phi t = 0, \tag{5}$$

$$\left(\left[\tilde{K}(\Theta)\right] - \phi^2\left[\tilde{M}(\Theta)\right]\right)\{\psi\} = 0. \tag{6}$$

The material properties of constitute materials of functionally graded materials are varying continuously and smoothly throughout the depth of the plate. The local volume fraction ($f(z)$) of FGM plate which follows the power law can be expressed as [21]

$$f(z) = \left(\frac{h + \frac{t}{2}}{t}\right)^p, \tag{7}$$

where p is the power law exponent, t is the thickness of FGM plate, $h = -t/2$ for top surface and $h = t/2$ for bottom surface. After calculation of local volume fraction, the material properties of FGM can be determined by using the rule of mixture as

$$R(z) = f(z)R_c + [1 - f(z)]R_m, \tag{8}$$

where R is the material properties.

3 Multivariate Adaptive Regression Splines (MARS)

Friedman pioneered to propose MARS for establishing the relationship between the set of input variables and target [22]. Similar to a machine learning model, MARS also uses iterative approach. There is no assumption considered for the functional relationship between response variable and predictor variable. MARS is the nonparametric regression statistical approach in which multiple linear regression model are created cross the range of predictor variables. In the first step of MARS model, training data sets are divided into splines (linear segments) with different slops called basic functions. Each set of training data have a separate regression model. The regression lines are connected together by using the knots. The MARS model searches the best location for the knots having the pair of basic functions [23]. The relationship between the environmental variable and responses are described by the basic functions. Each pair of basic function at the knot gives the maximum reduction in the sum-of-squares residual error. The basic functions are increased continuously until the number of basic function reached maximum level. This process causes the complicated and over fitted model. In the second step of MARS algorithm, the insignificant redundant basic function is removed [24]. The MARS model works well also for large number of input variables. Another advantage of this model is that it automatically finds the interaction between input and response variables. The MARS model $f(x)$ with basic function and interaction can be written as [25]

$$f(x) = \gamma_0 + \sum_{n=1}^{M} \gamma_n \beta_n^f(z_i), \tag{9}$$

where β_n is the basic function and γ is the constant coefficient, which is calculated by least-square method. The basic function can be written as

$$\beta_n^f(z_i) = \prod_{i=1}^{i_n} \left[Y_{i,n}\left(z_{j(i,n)} - q_{i,n}\right) \right]_T^g,$$

where i_n denotes the interaction order, $Y_{i,n} = \pm 1$, $z_{j(i,n)}$ represents the jth variable, $1 \le j(i,n) \le m$, and $q_{i,n}$ is the knot position of corresponding variables. 'T' denotes truncated power function. The basic function may be in following shapes.

$$\begin{aligned} \left[Y_{i,n}\left(z_{j(i,n)} - q_{i,n}\right) \right]_T^g &= \left[Y_{i,n}\left(z_{j(i,n)} - q_{i,n}\right) \right]^g \text{ for } \left[Y_{i,n}\left(z_{j(i,n)} - q_{i,n}\right) \right] < 0 \\ \left[Y_{i,n}\left(z_{j(i,n)} - q_{i,n}\right) \right] &= 0, \text{ otherwise} \end{aligned} \tag{10}$$

Thus, all basic function can be written as

$$A = \left\{ \left[Y_{i,n}\left(z_{j(i,n)} - q_{i,n}\right) \right]_T^g \right\}, \quad q \in \left\{ z_{1j},\ z_{2j},\ \ldots\ldots z_{Mj} \right\}. \tag{11}$$

In the present study, combined variation in material properties is considered as input variables, while first three natural frequencies are taken as responses. Different values of power law exponent such as $p = 1, 5, 10$ are considered. For each value of power law exponent, deterministic material properties of FGM plate are calculated. The degree of stochasticity in material properties is taken as $\pm 10\%$. The stochastic input variables can be represented as

$$\Psi(p) = \Phi[p,\ \{E(z)\}(\Theta),\ \{G(z)\}(\Theta),\ \{\rho(z)\}(\Theta),\ \{\mu(z)\}(\Theta)],$$

where Φ is the Monte Carlo operator. Figure 2 represents the flowchart of stochastic free vibration analysis by using the MARS model.

4 Results and Discussion

The material properties of the constitutes are considered as $E_m = 70$ Gpa, $E_c = 151$ Gpa, $\upsilon_m = 0.25$, $\upsilon_c = 0.30$, $\rho_m = 2707$ Kg/m^3, $\rho_c = 3000$ Kg/m^3 where E, υ, ρ are the elastic modulus, Poisson's ratio and mass density, respectively. Subscript 'c' and 'm' represent the ceramic and metal. The validation of the results is carried out in two ways, namely, scatter and probability density function (PDF) plots. Figure 3 illustrates the scatter plots between the original finite element model and MARS

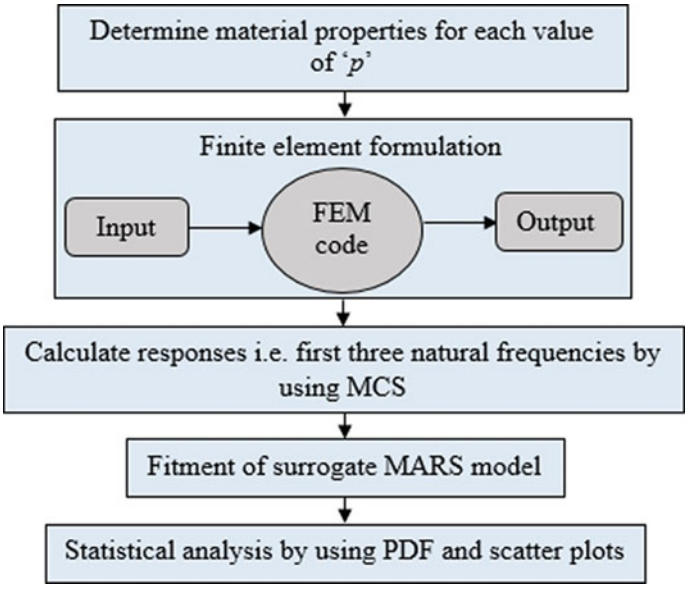

Fig. 2 Flowchart of free vibration analysis by using the MARS model

model for first three natural frequencies with considering different sample size (n). The scatter plots reveal that sample size 2048 is well fitted with the original FE model. The accuracy of the results increased with an increase in the number of sample size. Figure 4 represents the PDF plots for first three natural frequencies of Monte Carlo simulation and the MARS model, and found that both have almost same results. The sample size 2018 is sufficient to predict the response by using MARS model. The effect of power law index on the natural frequencies are determined by using the MARS model and shown in Fig. 5. The Fig. 5 illustrates that with the increase in the power law exponent (p) all natural frequencies decreased. Because with increase in the power law exponent ($p > 1$), all material properties of functionally graded material suddenly decreased at the top surface (at the ceramic rich surface), ultimately reduction in the stiffness of the plate as shown in Fig. 6. The number of sample size taken for model formation is 2048 so that computational time is reduced significantly, while for the same results, the Monte Carlo simulation required 10,000 number of simulation.

5 Conclusions

The novelty of the present paper includes the stochastic natural frequency analysis of FGM plates by using the MARS model. The material modelling of the FGM plate is carried out by using the power law distribution. Different values of power law

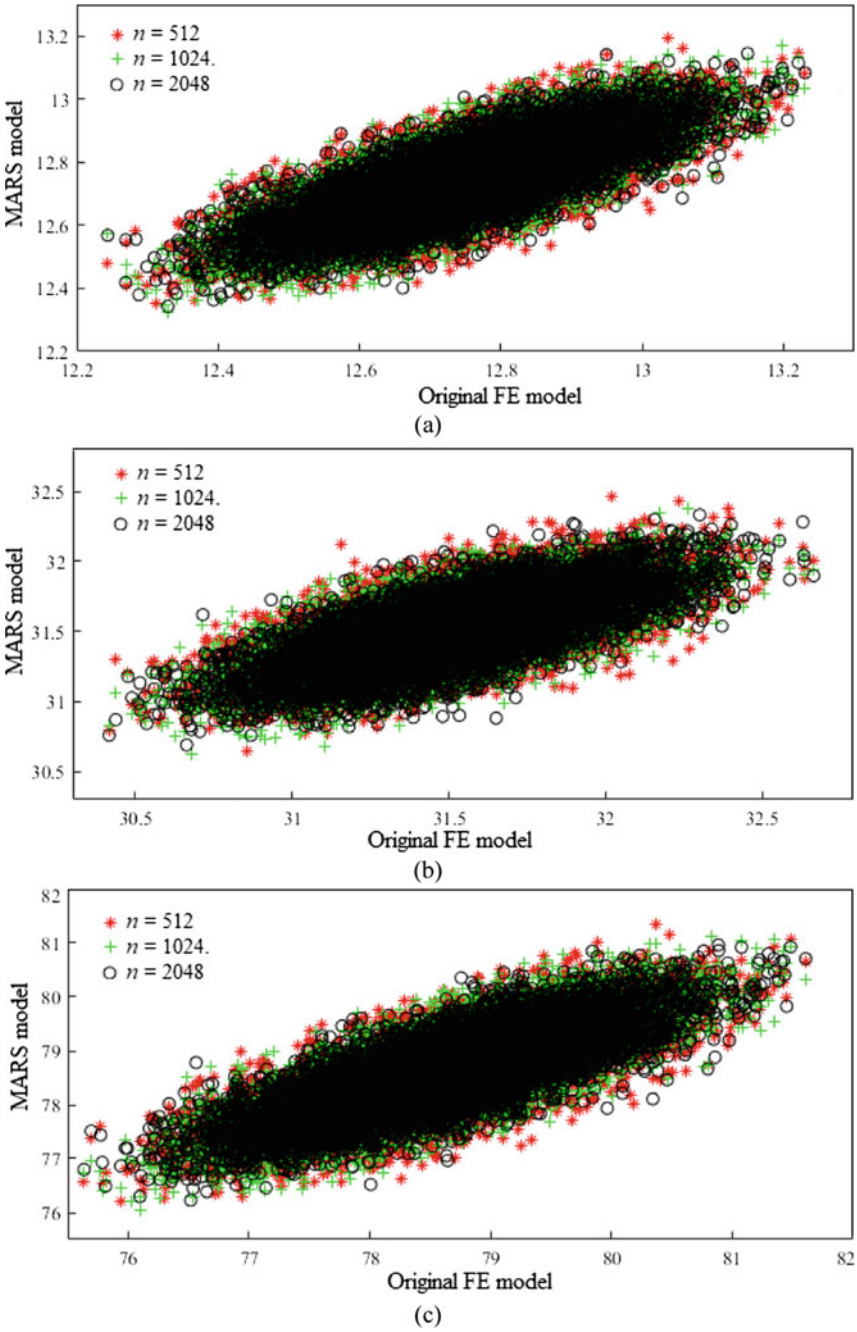

Fig. 3 Scatter plots of first three natural frequencies between original FE model and MARS model

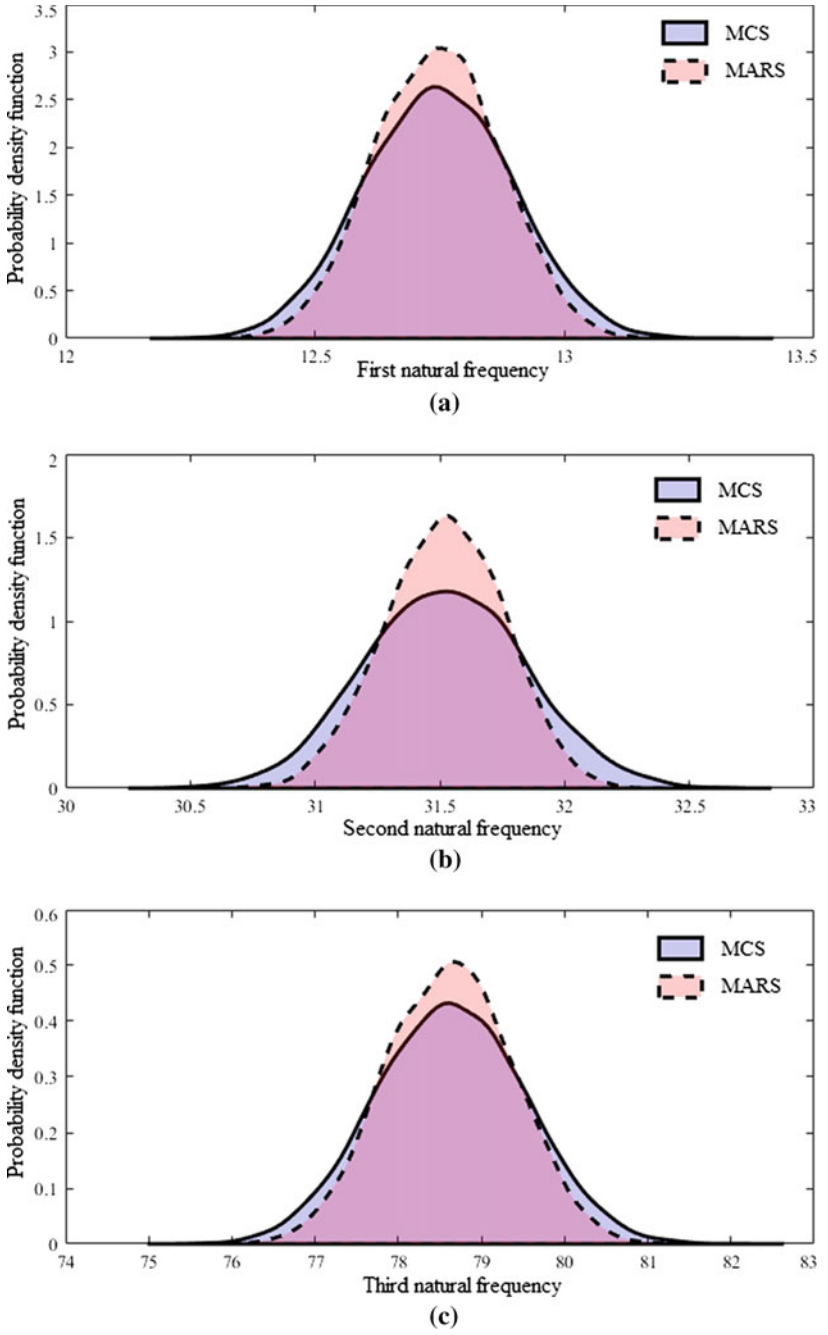

Fig. 4 PDF plots of first three natural frequencies for MCS and MARS with $n = 2048$

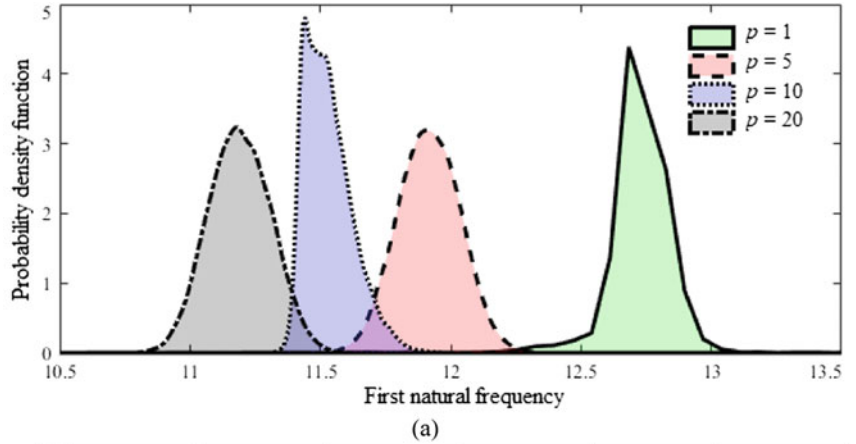

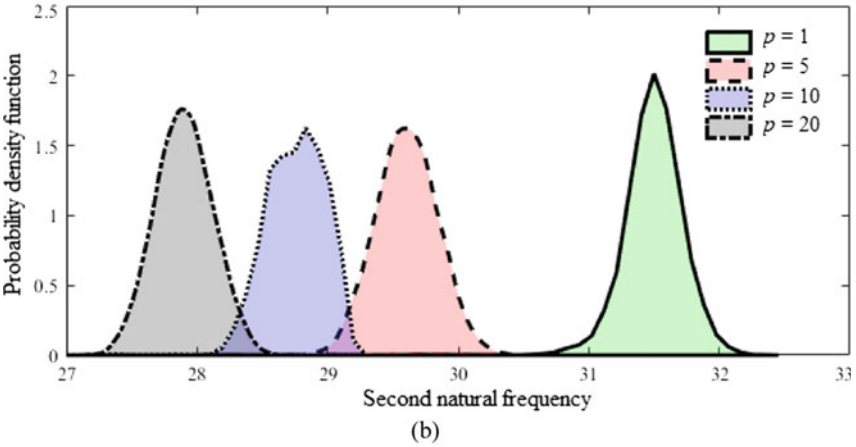

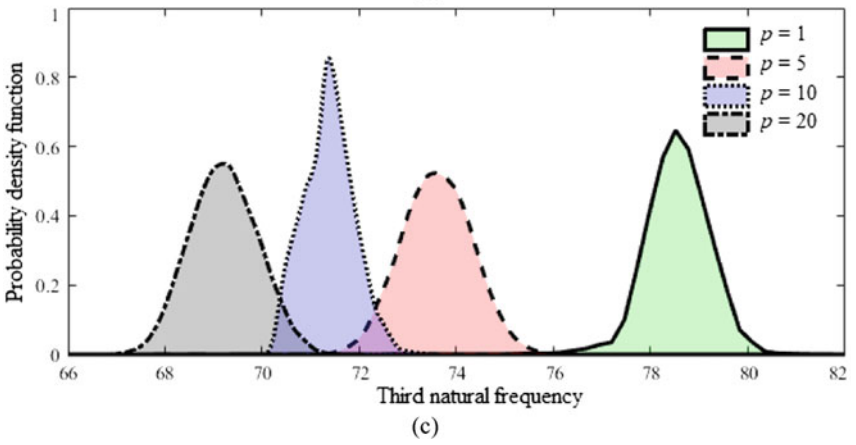

Fig. 5 Effect of power law index (p) on the first three natural frequencies by using MARS model

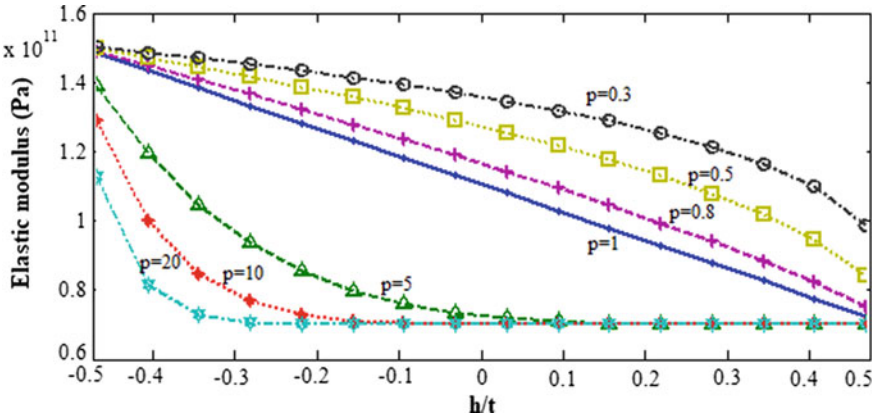

Fig. 6 Variation in elastic modulus across the depth of plate due to change in power law index (p)

exponents are considered as input variables. For ±10% degree of stochasticity in the material properties, it is observed that the power law exponent influences the material properties which causes to vary the natural frequencies of FGM plates. The validation of the MARS model is carried out by using the scatter plot and probability density function plot, respectively. The power law exponent and natural frequencies are found to be inversely related with each other. In future, the present model can be applied for both static and dynamic analysis of complex structures. In the present study, FGM plate is considered, but in future, this work can be extended for other structures such as sandwich structure, honeycomb structures along with the different surrogate models such as artificial neural network, polynomial neural network and radial basis function. Other boundary condition may be considered for different structures.

Acknowledgements P.K. Karsh received financial support from the TEQIP-III, NIT Silchar and MHRD Government of India, during research work.

References

1. Xu, X.J., Meng, J.M.: A model for functionally graded materials. Compos. B Eng. **145**, 70–80 (2018)
2. Naebe, M., Shirvanimoghaddam, K.: Functionally graded materials: a review of fabrication and properties. Appl. Mater. Today **5**, 223–245 (2016)
3. Moita, J.S., Araujo, A.L., Correia, V.F., Soares, C.M.M., Herskovits, J.: Material distribution and sizing optimization of functionally graded plate-shell structures. Compos. B Eng. **142**, 263–272 (2018)
4. Burlayenko, V.N., Altenbach, H., Sadowski, T., Dimitrova, S.D., Bhaskar, A.: Modelling functionally graded materials in heat transfer and thermal stress analysis by means of graded finite elements. Appl. Math. Mod. **45**, 422–438 (2017)

5. Kumar, S., Ranjan, V., Jana, P.: Free vibration analysis of thin functionally graded rectangular plates using the dynamic stiffness method. Comput. Strut. **197**, 39–53 (2018)
6. Attia, M.A., Rahman, A.A.A.: On vibrations of functionally graded viscoelastic nanobeams with surface effects. Int. J. Eng. Sci. **127**, 1–32 (2018)
7. Żur, K.K.: Free vibration analysis of elastically supported functionally graded annular plates via quasi-Green's function method. Compos. B Eng. **144**, 37–55 (2018)
8. Salinic, S., Obradovic, A., Tomovic, A.: Free vibration analysis of axially functionally graded tapered, stepped, and continuously segmented rods and beams. Compos. Part B Eng. (2018)
9. Arefi, M., Bidgoli, E.M.R., Dimitri, R., Tornabene, F.: Free vibrations of functionally graded polymer composite nanoplates reinforced with graphene nanoplatelets. Aerosp. Sci. Technol. **81**, 108–117 (2018)
10. Karsh, P.K., Mukhopadhyay, T., Chakraborty, S., Naskar, S., Dey, S.: A hybrid stochastic sensitivity analysis for low-frequency vibration and low-velocity impact of functionally graded plates. Compos. B Eng. **176**, 107221 (2019)
11. Dey, S., Mukhopadhyay, T., Adhikari, S.: Stochastic free vibration analysis of angle-ply composite plates–A RS-HDMR approach. Compos. Struct. **122**, 526–536 (2015)
12. Karsh, P.K., Mukhopadhyay, T., Dey, S.: Stochastic investigation of natural frequency for functionally graded plates. In: IOP Conference Series: Materials Science and Engineering, vol. 326, No. 1, p. 012003. IOP Publishing (2018)
13. Dey, S., Mukhopadhyay, T., Sahu, S.K., Adhikari, S.: Effect of cutout on stochastic natural frequency of composite curved panels. Compos. B Eng. **105**, 188–202 (2016)
14. Karsh, P.K., Kumar, R.R., Dey, S.: Radial basis function-based stochastic natural frequencies analysis of functionally graded plates. Int. J. Comput. Methods 1950061 (2019)
15. Kumar, R.R., Karsh, P.K., Pandey, K.M., Dey, S.: Stochastic natural frequency analysis of skewed sandwich plates. Eng. Comput. (2019). https://doi.org/10.1108/EC-01-2019-0034https://doi.org/10.1108/EC-01-2019-0034
16. Dey, S., Mukhopadhyay, T., Spickenheuer, A., Adhikari, S., Heinrich, G.: Bottom up surrogate based approach for stochastic frequency response analysis of laminated composite plates. Compos. Struct. **140**, 712–727 (2016)
17. Wang, Y., Wu, D.: Free vibration of functionally graded porous cylindrical shell using a sinusoidal shear deformation theory. Aerosp. Sci. Technol. **66**, 83–91 (2017)
18. Nguyen, H.X., Hien, T.D., Lee, J., Nguyen-Xuan, H.: Stochastic buckling behaviour of laminated composite structures with uncertain material properties. Aerosp. Sci. Technol. **66**, 274–283 (2017)
19. Dey, S., Mukhopadhyay, T., Adhikari, S.: Metamodel based high-fidelity stochastic analysis of composite laminates: A concise review with critical comparative assessment. Compos. Struct. **171**, 227–250 (2017)
20. Karsh, P.K., Mukhopadhyay, T., Dey, S.: Stochastic dynamic analysis of twisted functionally graded plates. Compos. B Eng. **147**, 259–278 (2018)
21. Chi, S.H., Chung, Y.L.: Mechanical behavior of functionally graded material plates under transverse load—Part I: Analysis. Int. J. Solids Struct. **43**(13), 3657–3674 (2006)
22. Friedman, J.H.: Multivariate adaptive regression splines. Ann. Stat. 1–67 (1991)
23. Zhang, W., Goh, A.T.: Multivariate adaptive regression splines and neural network models for prediction of pile drivability. Geosci. Front. **7**(1), 45–52 (2016)
24. Dey, S., Mukhopadhyay, T., Naskar, S., Dey, T.K., Chalak, H.D., Adhikari, S.: Probabilistic characterisation for dynamics and stability of laminated soft core sandwich plates. J. Sandwich Struct. Mater. 1099636217694229 (2016)
25. Mukhopadhyay, T.: A multivariate adaptive regression splines based damage identification methodology for web core composite bridges including the effect of noise. J. Sandwich Struct. Mater. 1099636216682533 (2017)

Homotopy Analysis Method For Oscillatory Systems With Cubic and Trigonometric Non-Linearity

Sumit J. Patil, Anisha R.V. Kashyap, and Kiran M. Kolwankar

Abstract Analytical solutions to nonlinear oscillating systems cannot be represented without the help of special functions or they can be studied only using numerical techniques. We have studied an oscillating system which has a linear term, as well as a cubic and a trigonometric nonlinearity all at once. Approximate solutions to such nonlinear problems can be given using perturbation and decomposition techniques provided that the nonlinearity is small or perturbation is small enough. We have applied a promising technique of Homotopy Analysis which works even in the case of large nonlinearity in the system. Using this method, we have successfully obtained the approximate analytical solution to this system (with cubic and trigonometric nonlinearity) which fits numerical solution for several cycles of oscillations unlike perturbation and Adomian decomposition method which provide solutions that barely fit for more than a half cycle. Some of the implicit difficulties in handling two different kinds of nonlinearities in a single system were overcome by using a simple technique of representing nonlinear terms using their Maclaurin expansion truncated to the required order of precision so that all the terms now are polynomial in nature. In this way, it has been shown that the nonlinearity thus represented can be effectively and far more easily handled using Homotopy Analysis Method. The approximate analytical results of three different techniques and their comparison for this nonlinear oscillating system has been made thoroughly with respect to computations and accuracy.

S. J. Patil (✉)
Department of Mechanial Engineering, Veermata Jijabai Technological Institute, Matunga (E), Mumbai 400 019, India
e-mail: sjpatil_b15@me.vjti.ac.in

A. R.V. Kashyap · K. M. Kolwankar
Department of Physics, Ramniranjan Jhunjhunwala College, University of Mumbai, Ghatkopar (W), Mumbai 400 086, India
e-mail: anisha.kashyap27@gmail.com

K. M. Kolwankar
e-mail: Kiran.Kolwankar@gmail.com

S. Mukherjee et al. (eds.), *Computational Mathematics, Nanoelectronics, and Astrophysics*, Springer Proceedings in Mathematics & Statistics 342,
https://doi.org/10.1007/978-981-15-9708-4_3

Keywords Homotopy analysis method · HAM · Non-linear oscillations · Semi analytical methods

1 Introduction

The nonlinearities in nature are far more natural to neglect them very often in engineering problems. The most convincing example is the problem of *Simple Pendulum*. This problem appears in numerous mechanical applications and is always linearized with small angle approximation. The linearization of the simple pendulum equation leads to convincing results; but only up to 10–15° of amplitudes. The deviations in the solution henceforth are significant and need attention in design and modeling.

Likewise, many other oscillating phenomena are linearized by convenient and domain-specific assumptions. Even the very common Hooke's law holds good only for small displacements in springs and shows cubic dependency for larger deflections from the mean. Here we have mainly tried to study the *nonlinear oscillations* without recourse to linearization but by using mathematical tools like special functions, decomposition methods, and series approximations (Fourier approach).

From a physical point of view, the system under study is an oscillating single vertical segment fixed at the bottom. The restoring force in this oscillatory system is nonlinear and proportional to deflection from the mean position. There is a usual linear dependency governed by Hooke's law and also a cubic dependency on deflection. Also, when there is a deflection, the displaced center of gravity is acted upon by gravitational force in the opposite direction of equilibrium point. Hence, a destabilizing gravitational component $g\sin(x)$ is also there. In literature, this model is known as 'Chimney Model' [1]. Hence, the system under study is governed by the following equation:

$$\ddot{x} - g\sin x + k\alpha x^3 + kx = 0 \tag{1}$$

where k is the stiffness and g is the acceleration due to gravity and α can be given the desired value based on the weight of cubical dependency. Our focus in this study is more on finding the approximate solutions of this system rather than studying the physical properties of the system resulting from the nonlinearities. Owing to a unique combination of the nonlinearities (one cubic and one trigonometric), the methods studied and developed in this paper to tackle such systems with such two different kinds of nonlinearities are, in our opinion, of importance.

Duffing [2] has done prototypical work in nonlinear oscillations with his Duffing Oscillator equation which encompasses the cubical restoring term in the equation of motion of second order forced damped oscillator. It is given by

$$\ddot{x} + r\dot{x} + \omega_0^2 x + \beta x^3 = f\cos\omega t \tag{2}$$

and is used in various fields ranging from mechanical, electrical, and civil engineering to model physical processes such as stiffening springs, buckling of beams, electronic circuits [3]. Our system has, in addition, the gravitational nonlinear destabilizing force (without small angle approximation). This makes the system particularly challenging with both nonlinearities in one system. For the sake of exploring various methods to approach the problem, we have assumed that there is neither forcing nor damping in the system as in Eq. (2).

There is no exact solution for Duffing oscillator. Although simplified cases of nonlinear oscillators can be solved. For example, the simple pendulum has exact solution in terms of elliptic sine function [4]

$$\theta(t) = 2\sin^{-1}\left(\sin\frac{\theta}{2}sn\left(\frac{\omega_0}{\omega}(\pi/2-\omega t)\middle|\sin\frac{\theta_0}{2}\right)\right) \tag{3}$$

But for the case under study which involves two nonlinear terms- one trigonometric (g*sin x) and one cubic (kax^3), the integral involved in its solution, unlike simple pendulum case, cannot be reduced to some standard elliptical integral of first or second kind. Hence, to get some insight into the problem, we hereby try to solve the equation at various orders of approximation following the Fourier Series Approach, Adomian Decomposition, and finally using Homotopy Analysis Method.

The Homotopy Analysis Method (HAM) was first proposed by Shijun Liao [5], in 1992. Homotopy is a concept from topology and works on the deformation of known solution of ODE into solution of Non-linear Differential Equation (NLDE). It turns out that the Homotopy Analysis Method (HAM) works far better than the Series approximation or Decomposition method for the type of system under study in this work where trigonometric, as well as polynomial nonlinearity is involved. This method is more convincing than other methods for the simple reason that it guarantees the convergence of series solution with the right choice of basis function, operator, and convergence parameter [6]. It is also independent of the small or large deviation from the linear case, as is the case with Perturbation techniques. There has been an extensive work on this method within the first two decades of its introduction. In 1990's, Liao published multiple works laying out the new method he had invented [7], its application in solving simple nonlinear differential equations [8] and refining it through improvements [9]. In early 2000, a slightly modified method called Homotopy Perturbation Method (HPM) was introduced by Ji-Huan He [10, 11], which is more or less the same as HAM. Different nonlinear problems have been solved for approximate analytical results during the past two decades since Liao's new technique became known in the field. Several recent works attempt to apply HAM to obtain approximate analytical solutions to highly nonlinear systems, for example, Abbasbandy et al. [12] using it on Sturm-Liouville problems, Motsa et al.'s [12] Improved Spectral Homotopy Analysis Method (ISHAMS) (see also [14–17]), Ghiasi and Saleh's application of HAM to solve nonlinear Harry-Dym equation [18]. A lot of detailed treatment of HAM can be found in books written by Liao [6, 19] exclusively on this topic. The future direction of this field and advancements in this method can be found in his recent book [20].

Moving onto applications of this method, Liao himself has worked on the application of HAM to nonlinear oscillations [21] during his early work in 90's. Recently, in 2014, Y. Liu has published a HAM-based package for periodic oscillations of nonlinear dynamic systems [22]. But there are limitations to what kind of nonlinearity it can handle. The cubic-algebraic, as well as trigonometric nonlinearity, cannot be handled directly in one system using HAM. Liao in one of his papers on large deformations of a beam [23] came across a trigonometric nonlinearity along with others. There, he has made the small angle approximation (replacing $\sin\theta$ with θ) to proceed with the solution. We, in our study, have tried to tackle such kind of nonlinearity with HAM to get approximate analytical solutions to this system (Eq. (2)), and our plan is to further use these solutions to extract more information like transitions into chaos by Melnikov Analysis. So the main contribution of authors has been following -

- Successfully handling a system with two different types of nonlinearities (cubic-algebraic as well as trigonometric) to get fairly accurate approximate analytical solutions.
- Proposing the use of a simple technique of Maclaurin series expansion to represent trigonometric terms in the system equation to make all terms of polynomial nature.
- The technique used in this work can be used in applying HAM more effectively to any other problem which has more than one nonlinear terms of different kinds. For example, if one term is trigonometric and the other is exponential, or if one term is cubic and the other is exponential. It will work even in the case of a system with three nonlinear terms—trigonometric, exponential, and a polynomial.

We have presented our work in this paper in order of the least convincing methods (Series Approximation) to the most convincing HAM. The next section on the series approximation method demonstrates one of the approaches to get approximate analytical solutions to NLDEs. The steps used in this method, as well as its results are presented along with difficulties in using this method to get more convincing results. Subsequent section is on another method called "Adomian Decomposition" which is usually used to get approximate analytical solutions of NLDEs and is known to work better than series approximation methods. The results and reasons for the failure of the above two methods in giving approximate analytical solutions to desired level of accuracies are discussed in the fourth section before moving onto the most important section on the Homotopy analysis method. The section on HAM depicts why and how it has been applied to the problem under study. Results of the same are presented in the second last section, whereas the article ends with the conclusion and future scope of this work. An appendix is given at the very end for readers who want more details on Adomian decomposition and the steps involved in it.

2 Series Approximation Method

Landau [24] has approached to solve Duffing oscillator by assuming the solutions to be a series whose terms are the functions of frequency of the oscillator and for more

and more accurate solution, more terms need to be included, thus increasing computational requirements. Then, Fulcher and Davis [25], originally used the Fourier series based approach to solve the pendulum equation by an iterative method. Their method iteratively determined the coefficients of terms of truncated series which is assumed as an approximate solution. Borghi [26] showed that results that can be improved if the Fourier expanding coefficients are not expressed via polynomial approximants, but rather obtained through suitable orthogonal expansions, in terms of suitable linear combinations of Bessel functions [27]. It should make more sense to take trigonometric functions in a series rather than polynomial series considering the oscillatory nature of our system.

Hence, we use this approach by making the lowest order approximation and determine the solution for Eq. 2. For the motion of oscillator is periodic and x is an even function of time, we can assume solution of this differential equation to be a Fourier series -

$$x(t) = \sum_{n=0}^{\infty} c_{2n+1} \cos(2n+1)\omega t \tag{4}$$

where c_{2n+1} are the constants that weigh different frequency terms in the solution, ω is the angular frequency of oscillation at the time t. We have taken only odd multiples of ω for the parity of all the restoring force terms is odd. Let the initial conditions for oscillator be at $t = 0$

$$x(0) = x_0 \text{and} \, \dot{x}(0) = 0$$

Hence, it gives

$$c_1 + c_3 + c_5 + \cdots = x_0.$$

Now that we have assumed the Fourier series to be the solution of the differential equation, it must satisfy the differential equation, so

$$-\omega^2(c_1 \cos \omega t + 9c_3 \cos 3\omega t + \cdots) = g \sin(c_1 \cos \omega t + c_3 \cos 3\omega t + \cdots) - k(c_1 \cos \omega t + \cdots) - k\alpha(c_1 \cos \omega t + ...)^3 \tag{5}$$

Now working on the lowest order approximation of this solution, we would take only first term of the proposed solution—Fourier series—we neglect all the terms except first one , so $c_3 = c_5 = c_7 = \cdots = 0$ and from the initial condition, $c_1 = x_0$. Hence, we can write the differential equation

$$-\omega^2[x_0 \cos \omega t] = g \sin(x_0 \cos \omega t) - kx_0 \cos \omega t - k\alpha x_0^3 \cos^3 \omega t \tag{6}$$

Now for the simplification of the above equation, we use Fourier expansion of the first term on right hand side, $\sin[x_0 \cos \omega t]$. From the table of special functions [26]

$$\sin[x_0 \cos \omega t] = 2J_1(x_0) \cos \omega t - 2J_3(x_0) \cos 3\omega t + 2J_5(x_0) \cos 5\omega t - \cdots \tag{7}$$

where, the J_n denotes nth order Bessel function of first kind. Again following the lowest order approximation, we take only the first term of the expansion because the series is converging and higher order terms have lesser value. Hence, we can take-sin$[x_0 \cos \omega t] = 2J_1(x_0) \cos \omega t$ With this approximation, we get

$$\omega^2 = k + k\alpha x_0^2 \cos^2 \omega t - \frac{2gJ_1(x_0)}{x_0} \tag{8}$$

But the frequency ω in the approximate solution of our differential equation, has to be represented implicitly in terms of Bessel function, amplitude, other constants, and time (in this case, as it will turn out, angular frequency is time dependent). Our approach would be to approximate the cosine term in polynomial expansion up to 2 terms, so as to get ω out of cosine. This finally gives us the approximate solution of considered Nonlinear oscillatory system as

$$x(t) = x_0 \cos \omega t$$

where, ω is given by following relation:

$$\omega^2 = \frac{k(1 + x_0^2\alpha) - \frac{2gJ_1(x_0)}{x_0}}{1 + 2t^2} \tag{9}$$

The result of this approximation compared with the numerical solution (with initial condition $x_0 = 1$ and unit parameters k and α) of this differential equation is given in Fig. 1.

As we can see, the results are not so impressive. We may consider more and more terms in Bessel function expansion for the term $\sin(x_0 \cos \omega t)$ hoping for better

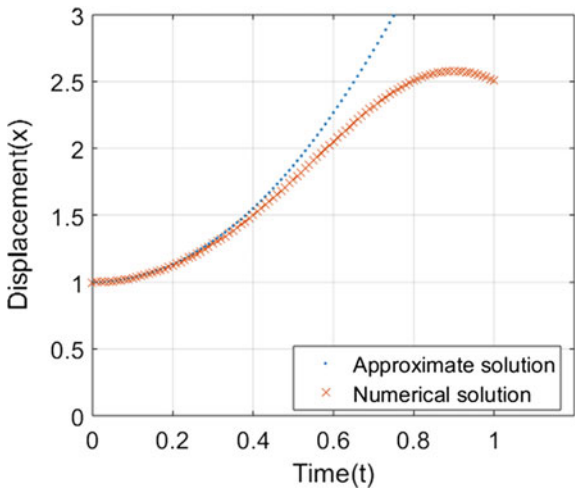

Fig. 1 Comparison of the lowest order approximation and the numerical solution. ($k = 1, \alpha = 1$)

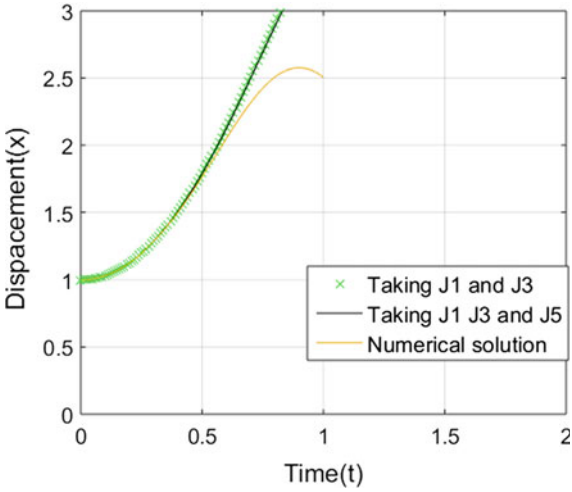

Fig. 2 Effect of considering further Bessel function terms in series approximation method. ($k = 1, \alpha = 1$)

results. Figure 2 shows the comparison of results when J_1 and J_3 terms are taken into consideration and when J_1, J_3, and J_5 are taken into consideration from Eqs. 8 into 9. But as we see, including further Bessel function terms is not giving any improvement in the results.

3 Adomian Decomposition

In this approach, we have used the decomposition method to solve the differential equation. Adomian [28] has originally reviewed these methods extensively which are iterative in nature and give a series solution to the nonlinear differential equations. It is particularly useful for nonlinear problems because a smart choice of operators while decomposing the equation can give you improved convergence of the series solution. Also, this method does not change the problem into a convenient one for use of linear theory. It, therefore, provides more realistic solutions [28].

3.1 Decomposition of Second Order Derivative as Linear Operator (L)

In Adomian Decomposition Method, the nonlinear differential equation is decomposed into linear (L), nonlinear(N) and a remaining term (R) and the choice of decomposition is in the hands of the solver. Based on one's discretion and the nature of the problem, one can try different decompositions to see which one gives greatest convergence. Hence, Eq. 2 has been decomposed into various operators in first

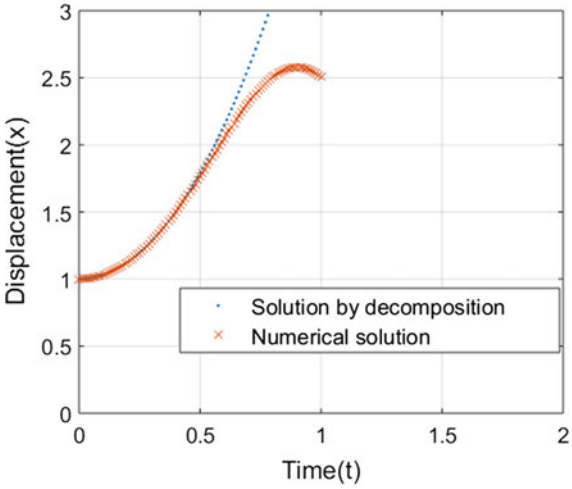

Fig. 3 Comparison of solution (4-terms) by Decomposition with Numerical solution. ($k = 1, \alpha = 1$)

attempt as

$$Lx + Rx + Nx = 0 \tag{10}$$

where linear part of NLDE is decomposed into $L + R$ such that L is easily invertible. N is the nonlinear part of the equation. The advantage of taking the highest order derivative as L is that the further integrations are simplified for determining the solution. Hence,

$$L = \frac{\mathrm{d}^2}{\mathrm{d}t^2}; R = k; N = -\frac{g}{\sin x} + k\alpha x^3.$$

We have solved for x using Adomian's method on above operators up to four iterations and the results as shown in Fig. 3 are close to what we achieved on lowest order approximation using Fourier based approach. This shows that the convergence of this solution is not desirable. Hence, we should try to change L operator, thus sacrificing the ease in computation to gain improved convergence.

3.2 Decomposition by Taking $L = \frac{\mathrm{d}^2}{\mathrm{d}t^2} + k$

As pointed out by Adomian [28] in his paper, choosing L as any operator other than the highest derivative leads to complicated integrals for evaluation, though it can lead to an increase in convergence. Hence, we checked the feasibility of changing the L operator in this problem by decomposing in a slightly different way. The only other way in which L can be chosen such that it is linear and it is invertible is, if we take the only other linear term in the system equation—'kx' along with differential operator. Using this decomposition and solving, unfortunately, one term in the solution at first

iteration involves integral of the form

$$I = \int \sin(C * \cos(\sqrt{k}t)) * \cos(\sqrt{k}t)\mathrm{d}t \tag{11}$$

where C is a constant term which pops up in subsequent solution steps. Whereas k and t are the same terms in the original NLDE that represents the system under study. This integral is not solvable to get an analytical expression. Hence, Adomian decomposition won't work for this problem. The main reason why such an integral appears is the combination of cubic and trigonometric nonlinearity in the system. Convoluted terms such as $\sin(C * \cos(\sqrt{k}t))$ appear due to exactly the same reason. Hence, even-though promising on the convergence aspect, the Adomian method is not convenient on the computation aspect if two different kinds of nonlinear functions are involved in the system equation. For details of Adomian Decomposition calculations steps, look in the Appendix.

4 Discussion on Series Approximation and Decomposition Method

In the problem under consideration, we followed two approaches to get approximate analytical solutions to the nonlinear oscillator with gravitational instability and cubic plus linear restoring forces for studying the dynamics of the system. With series approximation approach, the lowest order approximation matches with numerical solution up to $\frac{x}{xo} = 2$ at the best. Whereas, the Adomian decomposition too did almost as good as the series approach, but not better.

The errors in the above two approaches will be as represented in Fig. 4. The errors remain below 10% only up to 0.75 seconds. The time period of this system is about 1.79 seconds (from numerical evaluation for parameters $\mathrm{k} = 1$, $\alpha = 1$, and $\mathrm{g} = 9.81$). It means, the solution fits good only for 42% of one cycle. This is not so satisfactory result. We aim at gaining an approximate solution that fits at least several cycles within 1% error limit. Hence, we will move onto HAM in the next section.

5 Homotopy Analysis Method

Liao [6, 19, 20] have lucidly explained the way to do HAM on a given system; providing guidelines on how to chose convergence parameter, auxiliary operator, and the basis functions. Here, we will right away start with the derivation of the solution for our system, pointing to the references for details of proofs and first principles.

The original system we are tackling is

$$\ddot{x} - g \sin x + k\alpha x^3 + kx = 0 \tag{12}$$

The pain this system is giving in revealing its analytical approximations is mainly due to the two different natures of nonlinearities involved in this system's dynamics. One is a polynomial, cubic nonlinearity ($k * \alpha * x^3$), whereas the other in conjunction with it is trigonometric ($g * \sin(x)$). As pointed out by Liao [19], it is one of the limitations of HAM that despite giving too much freedom on the choice of basis functions and auxiliary operator, it provides no set rules and rigorous theories to direct us in these choices. Hence, it can be a problem of ensuring the convergence in the case of altogether different kinds of problems with strange nonlinearities as in our system. From the practical point of view, Liao and subsequent researchers in this field have come up with some fundamental guidelines such as the rule of solution expression, the rule of coefficient ergodicity, and the rule of solution's existence to ensure convergence and solution ergodicity. Following these rules and attempting to solve the system still leads to failure. The reason being again the nature of sin term which upon incorporating basis function into it and giving rise to terms like $\sin(\cos(x))$ or $\sin(x^n)$, does not produce expressions that can be solved in subsequent iterations and orders of solutions. This is the biggest hindrance to solution existence. Hence, we need to somehow make all nonlinear terms in the equation of the same nature (all trigonometric or all polynomial). One way to do it is to approximate $\sin(x)$ using its Maclaurin series which expands sin into polynomial terms which are of the same nature as that of other restoring nonlinear terms. In this way; we can ensure the solution existence. But to ensure that the desired accuracy is achieved within computational limits; we need to check how many terms from the Maclaurin series need to be replaced for $\sin(x)$. This simple technique was not used in any similar problems in literature. Either the systems under study did not involve such starkly different kinds of nonlinear terms or they used slightly complicated methods

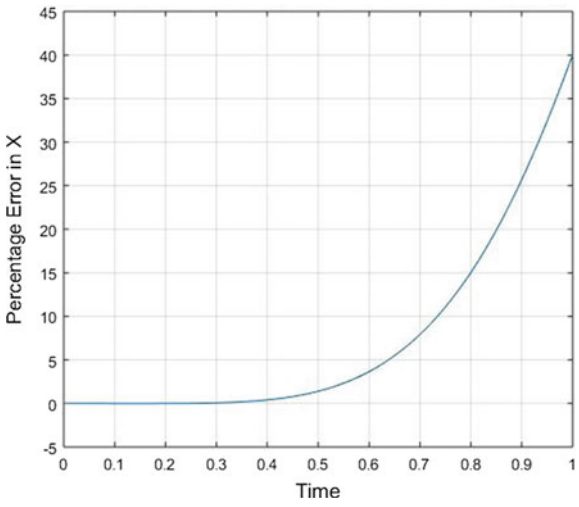

Fig. 4 Percentage error in displacement (x) calculated using series approximation method

to go around the problems to get solutions using HAM. Whereas, if we simply use Maclaurin expansions of the dissimilar nonlinear terms and truncate the infinite series to the desired accuracy, the resulting polynomial terms in the NLDE can be handled easily whatsoever may be the number of them as long as they are all polynomials.

The Maclaurin series of $\sin(x)$ is

$$\sin(x) = x - \frac{x^3}{6} + \frac{x^5}{125} - \frac{x^7}{5040} + \cdots \tag{13}$$

Hence, we will check by taking first only up to x^3, then terms up to x^5 and finally taking terms up to x^7. Hence, our system equations will become

$$\ddot{x} + (k-g)x + \left(k\alpha + \frac{g}{6}\right)x^3 = 0 \tag{14}$$

$$\ddot{x} + (k-g)x + \left(k\alpha + \frac{g}{6}\right)x^3 - \left(\frac{g}{125}\right)x^5 = 0 \tag{15}$$

$$\ddot{x} + (k-g)x + \left(k\alpha + \frac{g}{6}\right)x^3 - \left(\frac{g}{125}\right)x^5 + \left(\frac{g}{5040}\right)x^7 = 0 \tag{16}$$

The system in Eq. 14 is exactly the Duffing Oscillator with no damping and no forcing. Homotopy analysis has been successfully applied to this system by Liao [6]. In this work, Mathematica code is also available to solve the m^{th} order deformation equations and determining the optimum convergence parameter [29]. Even exact analytical solutions to this system exist in terms of Jacobi Cos Elliptical function [30] like the simple pendulum case pointed out in Eq. 3. Hence, these solutions of system 14 can be checked for how much they are conserving the original dynamics of system 12 in question for which system 14 is just an approximation. This comparison is demonstrated in Fig. 5. It shows that though the approximate system 14 has preserved the nature of oscillations and the period is also close to the original period; it is not able to keep up with the system 12 for more than half a cycle. The error goes on increasing in subsequent cycles as evident in Fig. 5.

Hence, we must go on for incorporating further terms from approximation series to get solutions closer to the original system 12. Hence, we proceed for applying HAM to system 15 and system 16.

5.1 Steps In HAM

For details of derivation and steps, one can refer Liao's books on homotopy [6, 19].

The first step in HAM is to choose a proper set of basis functions for the given system. Considering the oscillatory and periodic nature of the system; the wisest of all choices for basis functions would be the multiples of trigonometric *cos* functions. So that the solution expression can be represented in the form

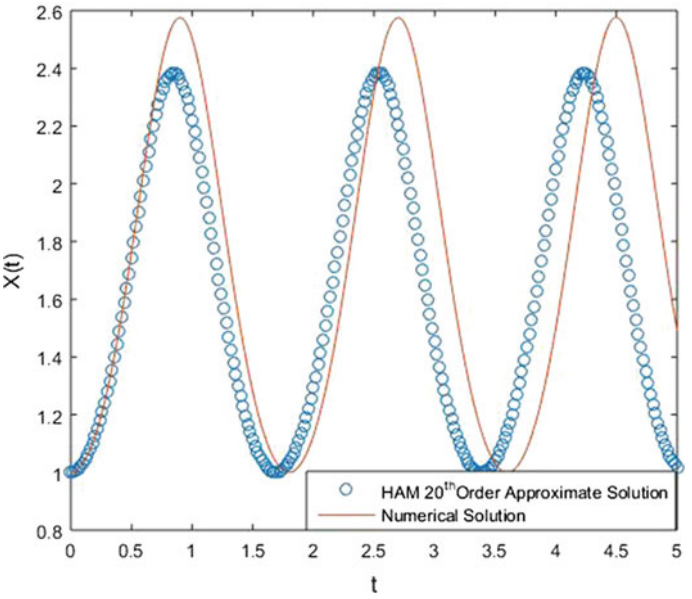

Fig. 5 Comparison of system 14 (solved using HAM) and system 12 (solved numerically) ($k = 1, \alpha = 1$)

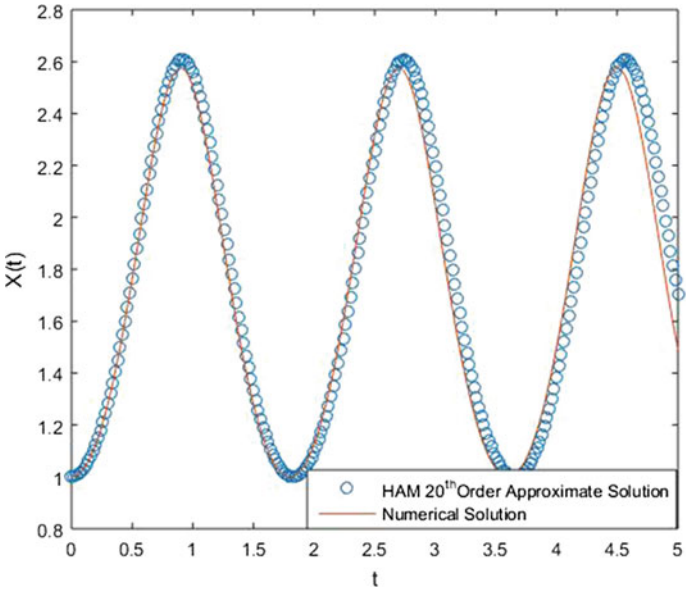

Fig. 6 HAM results for Eq. 15 ($k = 1, \alpha = 1$)

$$x = a_0 + \sum_{k=1}^{\infty} a_n \cos(k\tau) \ldots \tau = \omega t \tag{17}$$

The transformation $\tau = \omega t$ is a dimensionless time with ω representing the frequency and $T = 2\pi/\omega$ as the time period. This transformation leads to a slight change in Eqs. 15 and 16. Where $\gamma = \omega^2$

$$\gamma\ddot{x} + (k-g)x + \left(k\alpha + \frac{g}{6}\right)x^3 - \left(\frac{g}{125}\right)x^5 = 0 \tag{18}$$

$$\gamma\ddot{x} + (k-g)x + \left(k\alpha + \frac{g}{6}\right)x^3 - \left(\frac{g}{125}\right)x^5 + \left(\frac{g}{5040}\right)x^7 = 0 \tag{19}$$

Now we need to choose the initial approximation x_0 which must satisfy the initial conditions for the problem which we set as $x(0) = x_*$ and $\dot{x}(0) = 0$. So a good initial approximation would be

$$x_0 = \beta + (x_* - \beta)\cos(\omega t) \tag{20}$$

where β is the nearest equilibrium point in the system. As we are solving for the oscillatory system; our choice of parameters will always be such that the restoring terms in Eqs. 15 and 16 will be positive so that the net force acts towards the equilibrium and not away from it. Hence, we will calculate where such attractors in the system lie and use them as β. Now we have to take two operators, one linear auxiliary operator (L) which should fulfill the condition that $L(0) = 0$ and a nonlinear operator (N). The nonlinear operator is the original equation whose solutions we need, hence

$$N(x) = \gamma\ddot{x} + (k-g)x + \left(k\alpha + \frac{g}{6}\right)x^3 - \left(\frac{g}{125}\right)x^5 \tag{21}$$

$$N(x) = \gamma\ddot{x} + (k-g)x + \left(k\alpha + \frac{g}{6}\right)x^3 - \left(\frac{g}{125}\right)x^5 + \left(\frac{g}{5040}\right)x^7 \tag{22}$$

There are two more introduced parameters, one called convergence parameter c_0 which is in conjunction with $N(x)$ and ensures the rapid convergence of solution series if chosen properly. The other parameter is homotopy parameter $q = [0 \to 1]$ which is used to construct the homotopy between $L[x(\tau) - x_0(\tau)]$ and $c_0 N[x(\tau)]$.

The homotopy is constructed as

$$H(x, q) = (1-q)L[x(\tau) - x_0(\tau)] - qc_0 N[x(\tau)] \tag{23}$$

The essence homotopy is that when $q = 0$; the homotopy $H = L[x(\tau) - x_0(\tau)]$ which is a linear ODE. And when $q = 1$; the homotopy $H = -c_0 N[x(\tau)]$ is the solution we are seeking. Hence, as the homotopy parameter varies from 0 to 1, the function $H(x, 0)$ deforms into function $H(x, 1)$ whose solutions are sought after. Then enforcing $H(x, q) = 0$; we have a two parameter family of differential equations-

$$(1-q)L[x(\tau,q)-x_0(\tau,q)] = qc_0N[x(\tau,q)] \tag{24}$$

subject to initial conditions $x(0,q) = x_*$ and $\dot{x}(0,q) = 0$.

Obviously, when $q = 0$, because of the property $L(0) = 0$ of any linear operator L, Eq. 22 has the solution $x(\tau;0) = x_0(\tau)$. When $q = 1$, as c_0 is a non zero parameter; subject to initial conditions, Eq. 22 is equivalent to the system we want solve (Eqs. 15 and 16). Hence, $x(\tau;1) = x(\tau)$. Once again it is evident that as q varies from 0 to 1; the solution deforms from initial guess function $x_0(\tau)$ to required function $x(\tau)$. Note that $\gamma = \omega^2$ is an unknown constant and still we can regard γ as a function of q, denoted by $\gamma(q)$, which varies continuously from $\gamma(0) = \omega_0^2$ to unknown frequency $\gamma(1) = \omega^2$ more like a homotopy itself- from initial guess to unknown. Liao [31] argues that such homotopy of γ is essential in nonlinear systems with polynomial functions to avoid the kind of terms we have discussed previously which lead to non-convergence of solution.

The Eq. 24 is called as *zeroth order deformation equation* in the jargon of topology. Since $x(\tau,q)$ and $\gamma(q)$ depend on the embedding parameter$q \to [0,1]$, they can be expanded in a power series of q as follows:

$$x(\tau,q) \sim x_0(\tau) + \sum_{n=1}^{\infty} x_n(\tau)q^n \tag{25}$$

$$\gamma(q) \sim \gamma_0 + \sum_{n=1}^{\infty} \gamma_n q^n \tag{26}$$

where

$$x_n = \frac{1}{n!}\left|\frac{\partial^n x(\tau,q)}{\partial q^n}\right|_{q=0} = D_n[x(\tau,q)],\ \gamma_n = \frac{1}{n!}\left|\frac{d^n\gamma(q)}{dq^n}\right|_{q=0} = D_n[\gamma(q)] \tag{27}$$

The series 25 and 26 are called Homotopy-Maclaurin Series. At $q = 1$, the series becomes solution of the NLDE we are solving. For that purpose; it is essential that we ensure the convergence of this Homotopy-Maclaurin series. The m^{th} order homotopy-approximation unlike infinite terms taken in Eqs. 25 and 26, would be

$$x(\tau,q) \approx x_0(\tau) + \sum_{n=1}^{m} x_n(\tau) \tag{28}$$

$$\gamma(q) \approx \gamma_0 + \sum_{n=1}^{m} \gamma_n \tag{29}$$

For this entire solution using HAM is to be solved in computer; we define sets like $X_m = [x_0, x_1, \ldots, x_m]$ and $\Gamma_m = [\gamma_0, \gamma_1, \ldots, \gamma_m]$ which can be used in successive iterations in the program.

Now to determine these terms; we need more equations like zeroth order deformation equation. They are called *higher order deformation equations* and are derived by differentiating the zeroth order deformation equation successively and setting $q = 0$ after dividing by $n!$. If we want n^{th} order deformation equation; following mentioned procedure, we get

$$L[x_n(\tau) - \chi_n x_{n-1}(\tau)] = c_0 \delta_{n-1}(X_{n-1}, \Gamma_{n-1}) \tag{30}$$

Subject to initial conditions, $x_n(0) = x_*$ and $\dot{x}_n(0) = 0$ where $\delta_k(X_k, \Gamma_k) = D_k[N(x(\tau, q))]$ and $\chi_n = [0, n <= 1|1, n > 1]$ For the derivation of n^{th} order deformation equation by two different procedures; look in Appendix of Liao [6].

The D_k is as defined in Eq. 27. For our problem; the D_k for each term is defined as

$$D_k[\gamma(q)\ddot{x}(\tau, q)] = \sum_{i=0}^{k} \gamma_i \ddot{x}_{k-i}(\tau) \tag{31}$$

$$D_k[x(\tau, q)] = x_k(\tau) \tag{32}$$

$$D_k[x^3(\tau, q)] = \sum_{i=0}^{k} x_{k-i}(\tau) \sum_{j=0}^{i} x_{i-j}(\tau) x_j(\tau) \tag{33}$$

For calculations of higher D's of higher power of x, a theorem by Turkyilmazoglu [32] is useful. It simply shows that the D's for higher powers can be built on D's of lower powers of x. Hence, general expression for D_k is

$$D_k[x^p(\tau, q)] = \sum_{i=0}^{k} D_{k-i}[x^{p-1}(\tau, q)] \tag{34}$$

Following which we can write $D_k[x^5]$ and $D_k[X^7]$ easily.

Now comes the most important part of choosing the auxiliary liner operator (L). There is a great freedom in this choice, but we need to ensure that the convergence is rapid and that the choice confers to the rule of solution expression. The rule of solution expression is a fundamental guide to choose the auxiliary linear operator and initial guess. It states that—"As long as a set of base functions is determined, the auxiliary function, the initial approximation, and the auxiliary linear operator must be chosen in such a way that all solutions of the corresponding high-order deformation equations exist and can be expressed by this set of base functions" [19]. Hence, from that aspect; as the original oscillatory system equation is governed by the second order differential equation, it would be a natural and wise choice to take L as a general second order differential operator

$$L[x_\tau] = \ddot{x}(\tau) + A(\tau)\dot{x}(\tau) + B(\tau)x(\tau) \tag{35}$$

where the constants A and B are decided from the conditions imposed on L such as $L(0) = o$ and also the important condition that when the basis functions ($\cos k\tau$) are put in the L; it must give out non-secular terms means which are of the same nature as the basis function. More details on this can be found in [6, 19]. Hence, doing this analysis; we came up with

$$L(x) = \ddot{x} + x \tag{36}$$

Now writing down different orders of deformation equations, we can solve them as they are linear differential equations, unlike the main NLDE. Hence, what HAM has essentially done is converting a NLDE into a number of linear ODEs. Solving them on computer programs is even easier. But now we have m different linear differential equations which can give us the whole set X_m as defined above. But the number of unknowns are $2m$. We need to determine the set of frequencies Γ_m too. For this; the trick is to incorporate the concept of those unwanted terms called secular terms ($\tau \cos \tau$) in the solution expression as discussed in (refer Chap. 2 [6]) the previous section. Hence, in order to avoid this, just equate coefficient of cos term in each x_n expression to zero. Doing so will give us an additional algebraic equation which can be solved for γ_n. In this way, the set Γ_m can be evaluated completely.

6 Results

Having all the theory and procedure at hand; we solved the higher order deformation equations. The procedure for the system similar to the one in Eq. 14 is made available by Liao et al. [29]. But our system has extra terms—higher order polynomial than solved in that code. So we referred to that work and got the results by modification as per the additional nonlinear terms.

The results of solving Eqs. 15 and 16 using HAM are shown in Figs. 6 and 7. Where it is evident that the convergence at the same order 20 is more if we approximate $\sin(x)$ with 3 terms and still more (almost exactly matching) if we approximate with 4 terms up to x^7.

7 Conclusions

In this work, HAM has been successfully used to get the approximate analytical solutions of order 20 to the highly nonlinear system under study. The accuracy of these solutions is given in Figs. 8 and 9. This shows that for the approximation of the order x^5, the error over 3 cycles approximately go up to a maximum of 15%. Whereas the error percentage for the first cycle is almost zero, it increases in further cycles. The approximation of the x^7 order has improved the accuracy by ten folds over 3 cycles. Thus, the maximum error over 5 seconds of system evolution is only

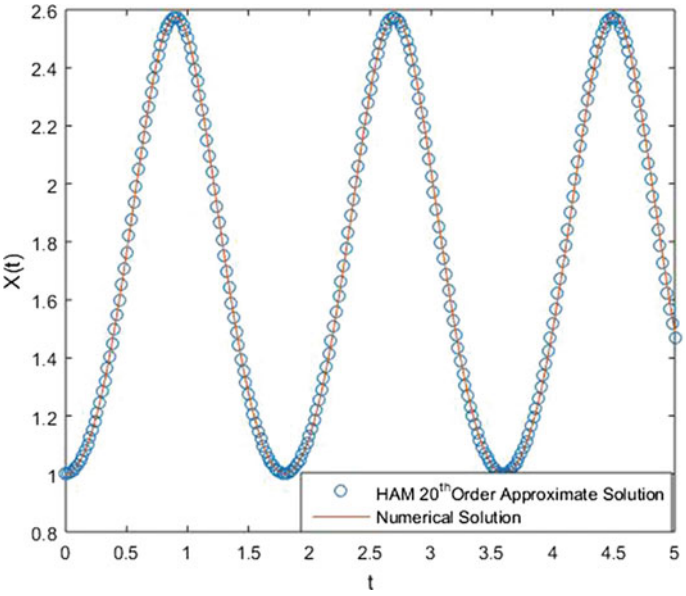

Fig. 7 HAM results for Eq. 16 ($k = 1, \alpha = 1$)

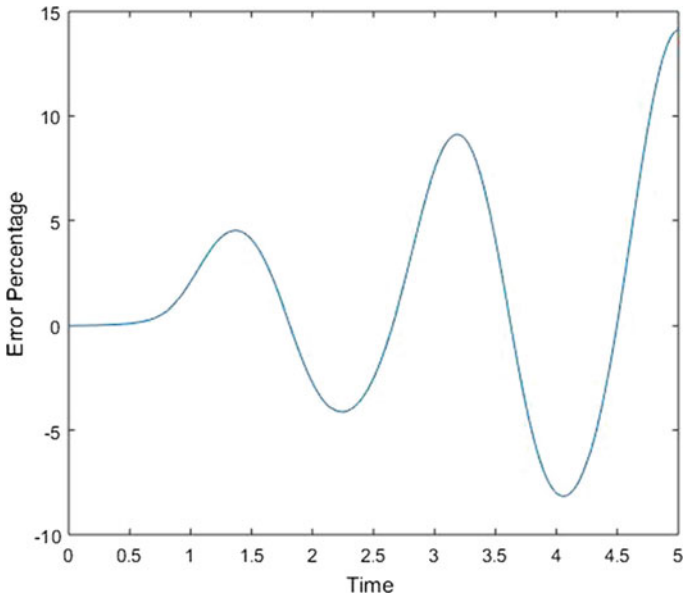

Fig. 8 %Error in HAM results for Eq. 15

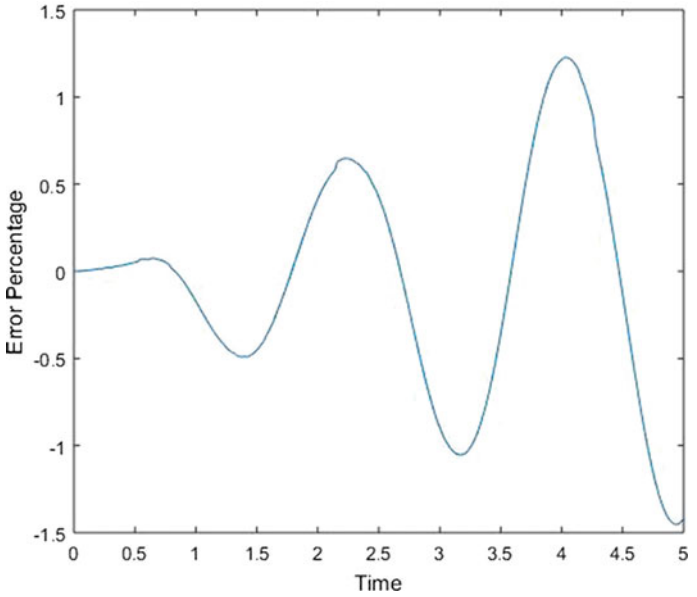

Fig. 9 %Error in HAM results for Eq. 16

1.5%. This result is very convincing compared to all the previous methods applied to solve the trigonometric and cubic nonlinearity together.

Future scope of this work is to do Melnikov Analysis for this system using approximate analytical solution expression generated through application of HAM to predict the emergence of chaos. Present analysis can give further and deeper understanding of this system which deals with a vertical segment with nonlinear restoring and destabilizing forces as well as other similar nonlinear systems' dynamics.

Still, we must bear in mind that the use of Maclaurin series to replace trigonometric nonlinear terms as implemented in this work may not be directly and straightforwardly implementable in some other system with different nonlinearities such as exponential terms combined with trigonometric or logarithmic terms. The choice of auxiliary linear operator & basis function, checking for convergence of solution and choosing suitable order of solution that is balanced in terms of accuracy and computational efforts still requires human judgment, as well as preliminary understanding of the system that the NLDE represents. Hence, a major improvement in this work will be a more efficient and user-friendly use of these approximate analytical techniques using modern computational softwares similar to that of numerical techniques.

Acknowledgements Authors would like to acknowledge the financial assistance from Science and Engineering Research Board, India (EMR/2014/000255) and Council for Scientific and Industrial Research, India (03(1357)/16/EMR-II).

Appendix

This section will provide only an introduction to Adomian's method of decomposition to solve nonlinear differential equations. This introduction to his method is taken from his own work "A review of the decomposition method and some recent results for nonlinear equations" [28].

Let the equation be

$$Lu + Ru + nu = g$$

where Nu represent nonlinear term. Solving for Lu,

$$Lu = g - Ru - Nu.$$

L is invertible, so we can write-

$$L^{-1}Lu = L^{-1}g + L^{-1}Ru - L^{-1}Nu$$

(Note- Refer [2] for further details.) If L is second order operator-

$$u = A + Bt + L^{-1}g - L^{-1}ru - L^{-1}Nu$$

The nonlinear term Nu will be equated to $\sum_{n=0}^{\infty} A_n$, where theA_n are special polynomials and u will decomposed into $\sum_{n=0}^{\infty} u_n$, with $u_0$identified as $A + Bt + L^{-1}g$.

$$\sum_{n=0}^{\infty} u_n = u_0 - L_{-1}R\sum_{n=0}^{\infty} u_n - L_{-1}\sum_{n=0}^{\infty} A_n$$

Now, the series of special polynomials for Nu is equal to a generalized Taylor series for $f(u_0)$, that $\sum_{n=0}^{\infty} u_n$ is a generalized Taylor series about the function u_0. Hence, the special polynomials A_n are given as

$$A_0 = f(u_0)$$

$$A_1 = u_1(d/du_0)f(u_0)$$

$$A_2 = u_2(d/du_0)f(u_0) + (u_1^2/2!)(d^2/du_0^2)f(u_0)$$

Hence, the series solution $u = u_1 + u_2 + u_3$, with the above special polynomials and proper initial conditions given, can be obtained by the decomposition method.

References

1. Kashyap, A.R.V., Kolwankar, K.M.: Chaotic properties of single element nonlinear chimney model: Effect of directionality. Int. J. Bifurcation Chaos **29**(04), 1950048 (2019)
2. Duffing, G.: Erzwungene Schwingungen bei veränderlicher Eigenfrequenz und ihre technische Bedeutung, pp. 41–42. F. Vieweg and sohn (1918)
3. Korsch, H., Jodl, H., Hartmann, T.: Chaos: A Program Collection for the PC. Springer Science and Business Media (2007)
4. Ochs, K.: A comprehensive analytical solution of the nonlinear pendulum. Eur. J. Phys. **32**(2), 479 (2011)
5. Liao, S.-J.: The proposed homotopy analysis technique for the solution of nonlinear problems. PhD thesis, Ph. D. Thesis, Shanghai Jiao Tong University Shanghai (1992)
6. Liao, S.: Homotopy Analysis Method in Nonlinear Differential Equations. Springer, Berlin (2012)
7. Liao, S.: Homotopy analysis method: a new analytical technique for nonlinear problems. Commun. Nonlinear Sci. Numer. Simul. **2**(2), 95–100 (1997)
8. Liao, S.-J.: An approximate solution technique not depending on small parameters: a special example. Int. J. Non-Linear Mech. **30**(3), 371–380 (1995)
9. Liao, S.J.: An approximate solution technique which does not depend upon small parameters (part 2): an application in fluid mechanics (1997)
10. He, J.-H.: Homotopy perturbation method: a new nonlinear analytical technique. Appl. Math. Comput. **135**(1), 73–79 (2003)
11. He, Ji-Huan: Comparison of homotopy perturbation method and homotopy analysis method. Appl. Math. Comput. **156**(2), 527–539 (2004)
12. Abbasbandy, S., Shirzadi, A.: Homotopy analysis method for multiple solutions of the fractional sturm-liouville problems. Numer. Algorithms **54**(4), 521–532 (2010)
13. Motsa, S.S., Marewo, G.T., Sibanda, P., Shateyi, S.: An improved spectral homotopy analysis method for solving boundary layer problems. Boundary Value Problems (1), 3 (2011)
14. Liu, T.: Reconstruction of a permeability field with the wavelet multiscale-homotopy method for a nonlinear convection-diffusion equation. Appl. Math. Comput. **275**, 432–437 (2016)
15. Mirzazadeh, M., Ayati, Z.: New homotopy perturbation method for system of burgers equations. Alexandria Eng. J. **55**(2), 1619–1624 (2016)
16. Vishal, K., Kumar, S., Das, S.: Application of homotopy analysis method for fractional swift hohenberg equation-revisited. Appl. Math. Model. **36**(8), 3630–3637 (2012)
17. Vosoughi, H., Shivanian, E., Abbasbandy, S.: Unique and multiple pham series solutions of a class of nonlinear reactive transport model. Numer. Algorithms **61**(3), 515–524 (2012)
18. Ghiasi, E.K., Saleh, R.: A mathematical approach based on the homotopy analysis method: Application to solve the nonlinear harry-dym (hd) equation. Appl. Math. **8**(11), 1546 (2017)
19. Liao, S.: Beyond Perturbation: Introduction to the Homotopy Analysis Method. CRC Press (2003)
20. Liao, S.: Advances in the Homotopy Analysis Method. World Scientific (2013)
21. Liao, S.J.: A second-order approximate analytical solution of a simple pendulum by the process analysis method. J. Appl. Mech. **59**(4), 970–975 (1992)
22. Liu, Y.: Ham-based package noph for periodic oscillations of nonlinear dynamic systems. In: Advances In The Homotopy Analysis Method, p. 309 (2013)
23. Liao, S.: Series solution of large deformation of a beam with arbitrary variable cross section under an axial load. ANZIAM J. **51**(1), 10–33 (2009)
24. Landau, L.D., Lifshitz, E.M., Donnelly, R.J.: Mechanics, vol. i of course on theoretical physics. Am. J. Phys. **40**(7), 1050–1051 (1972)
25. Fulcher, L.P., Davis, B.F.: Theoretical and experimental study of the motion of the simple pendulum. Am. J. Phys. **44**(1), 51–55 (1976)
26. Borghi, R.: Simple pendulum dynamics: revisiting the fourier-based approach to the solution. arXiv:1303.5023 (2013)

27. Release 1.0.5 of 2012 10-01. Nist digital library of mathematical functions (2012). http://dlmf.nist.gov/
28. Adomian, G.: A review of the decomposition method and some recent results for nonlinear equations. Comput. Math. Appl. **21**(5), 101–127 (1991)
29. Liao, S.: Homotopy analysis method in non linear differential equations. http://numericaltank.sjtu.edu.cn/HAM.htm
30. Salas, A.H.: Exact solution to duffing equation and the pendulum equation. Appl. Math. Sci. **8**(176), 8781–8783 (2014)
31. Liao, S.: Basic Ideas of the Homotopy Analysis Method, pp. 15–94. Springer, Berlin (2012)
32. Turkyilmazoglu, M.: A note on the homotopy analysis method. Appl. Math. Lett. **23**(10), 1226–1230 (2010)

Astrophysics

Design and Analysis of Circular Polarize Micro Strip Patch Antenna for X Band in Low Temperature Co-Fired Ceramic Technology (LTCC)

Pranoti S. Bansode and D. C. Gharpure

Abstract This paper presents the design of a compact circularly polarized patch antenna in LTCC technique for X band (10.87 GHz) frequency range. The proposed antenna consists of a corner truncated ceramic microstrip patch antenna with small circular shaped ground plane. The coaxial probe feed technique is used to excite the patch antenna. The probe feed position improves the impedance bandwidth. The antenna consists of Dupont 951 dielectric material having dielectric constant of 7.8 and thickness 1.6 mm. Various simulations were carried out to optimize the feed position and truncated corners as well as the ground plane size in high frequency simulation software (HFSS) for center frequency 10.87 GHz. The S_{11} parameter at this frequency is −17 dB and gain is 0.5 dB with axial ratio beam width of around 107° of the antenna.

Keywords Microstrip patch antenna · LTCC · Circular polarization · Finite ground plane

1 Introduction

In recent wireless communication world demand of microstrip patch antenna is growing very fast because of advantages like small size, low profile, and ease of fabrication. Microstrip patch antennas are designed to operate in single band, dual band and multi-band applications with either dual or circular polarization. These antennas are used in different handheld communicating devices [1, 2].

LTCC is low temperature cofired ceramic technology. LTCC is a multilayer platform technology that is used in fabrication of components, modules and packages in wireless, automotive, military, and medical and several other areas [3]. It is the ceramic substrate system which is applicable in electronic circuits as a cost effective and competitive substrate technology with nearly arbitrary number of layers [4]. The LTCC package is formed by layered dielectric glass/ceramic sheets or tapes over

P. S. Bansode (✉) · D. C. Gharpure
Department of Electronic Science, Savitribai Phule Pune University, Pune, India
e-mail: pranotisbansode@gmail.com

S. Mukherjee et al. (eds.), *Computational Mathematics, Nanoelectronics, and Astrophysics*,
Springer Proceedings in Mathematics & Statistics 342,
https://doi.org/10.1007/978-981-15-9708-4_4

which the metallization is manufactured using the screen-printing or photo-imaging technologies. The substrate consists of silver, gold and alloy with platinum conductors. LTCC has high dielectric constant which helps to reduce the antenna size. In LTCC, glass/ceramic substrates have sintering temperatures below 900 °C making it very rigid and applicable for use in space applications. LTCC has advantages in design a multilayer structure of antenna.

Applications of Circular polarized patch antennas are in mobile communication, wireless communication such as GPS and RFIDs etc. In microstrip patch antenna various methods are available to obtain the circular polarization [5, 6]. The truncated corners of the rectangular patch antenna give the circular polarization [7]. X band is primarily used by the military. Used in radar applications including continuous-wave, pulsed, single-polarization, dual- polarization, synthetic aperture radar and phased arrays. X-band radar frequency sub-bands are used in civil, military and government institutions for weather monitoring, air traffic control, maritime vessel traffic control, defense tracking and vehicle speed detection for law enforcement [8].

Bhattacharya [9] explains the analytical techniques to determine the effect of finite ground plane on antenna characteristics such as antenna radiation, input impedance, etc.

Noghanian [10] presents the effect on electrical parameters such as antenna radiation pattern, reflecting coefficient, input impedance, etc. of circular microstrip patch antenna by optimizing the various physical parameters such as ground plane size and shape. In the cavity model analysis, the ground plane size had been optimized for TM_{11} is approximately 0.6λ to maximize the antenna gain.

Chae [11] Perform the experiment of Ceramic circular shape microstrip patch antenna for 1.57–1.62 GHz frequency range. The antenna is placed in a radom fuze. In this antenna structure the two small rectangular slots are realized to improve the circular polarization bandwidth and additional truncation on patch used for enhancing the required impedance bandwidth. The fabricated results of this antenna shows the Axial ratio of 5.1−11.6 dB and gain is 2.5–4.2dBi.The axial ratio bandwidth of this antenna is less and above 3 dB.

Ranjan [12] in this paper circular microstrip patch antennas has been made with single cut. The centre frequency of antenna designed at 16 GHz. The antenna is made up of a 15 μm thick copper with width $W = 6.19392$ and length $L = 7.41159$ which is located height at 0.254 mm above the ground plane. The substrate for the patch is Rogers RT/duroid 5880(tm) with a dielectric constant $\varepsilon r = 2.2$ and loss tangent is $\tan\delta = 0.0013$. Feeding is done through edge feeding. Theoretical value of corner cutting edge is 2.58 mm for 16 GHz. Location of the feed point improving the impedance bandwidth. In this paper the optimized axial ratio value and gain values has been taken for different cutting length of the corner. At cutting length 2.5 mm the sufficient axial ratio and gain is achieved. But, the radiation pattern is getting tilt.

Tayade [13] in the proposed paper author has designed the circular disc slotted antenna with a concentric elliptical cut designed for 2.4 GHz frequency. The coaxial feed is used for the excitation of the patch antenna. After the fabrication the return loss of about −30 dB within an impedance bandwidth of 130 MHz, a measured gain of 0.4812 dB and a 5.27 dB axial ratio at 2.40 GHz with a corresponding modal phase

difference of 87°. The FR4 material having dielectric size In this paper the elliptical slot is present at the center of the circular shape patch. The field will be affected based on the even and odd mode of transmission. With the effect of slit degeneration and annular effect the central elliptical cut is introduce circular polarization.

Zhao [14] in the proposed paper the stacked patch antenna designed and analyze at 1.27 GHz frequency using LTCC technology. This was investigated for enhancing the impedance bandwidth. The antenna is composed of the two-layer stacked patch and LTCC substrate. The LTCC material No. 1 with the relative permittivity of 14 and loss tangent of 0.002 was used as the upper substrate. The LTCC material No. 2 with the relative permittivity of 6 and loss tangent 0.001 was used as the lower substrate. The lower patch with length L1 worked at a lower frequency, while the upper patch with length L2 worked at a higher frequency. The probe was directly connected to the upper patch via a hole in the lower patch. HFSS software was used to simulate and optimize the resonant properties of the proposed antenna. The return loss for the proposed antenna is −28.47 dB at 1.27 GHz. The antenna has an impedance bandwidth of 36 MHz. The proposed antenna shows good circular polarization as AR is below 3 dB in an angle of $-89° < \theta < 89°$.

The references show that a lot of work has been done on the Circular polarized patch antenna but very few papers related to Low temperature co-fired ceramic (LTCC) have been reported. In the present paper the conventional corner truncated microstrip patch antenna is designed for X band frequency range in LTCC. The patch antenna is designed and simulated for 10.87 GHz frequency. The truncated corners in the patch antenna improve the axial ratio beam width to around 107°. The S_{11} parameter of the antenna is −17 dB at 10.87 GHz.

2 Antenna Design

In the design the rectangular microstrip patch antenna consist of one dielectric substrate Dupont 951 having dielectric constant of 7.8 and thickness of the substrate is 1.6 mm. The metallic patch antenna is present on the top side of the substrate and ground plane is on the bottom side of the substrate as shown in Fig. 1. The dimensions of the patch antenna for 10.87 GHz frequency are calculated by using following formulas,

Width of the patch.

$$W = \frac{C_0}{2f_r}\sqrt{\frac{2}{\varepsilon_r + 1}} \tag{1}$$

W = width of the patch antenna.
f_r = Center frequency of the patch antenna.
h = Height of the substrate.
ε_r = dielectric constant of the substrate.

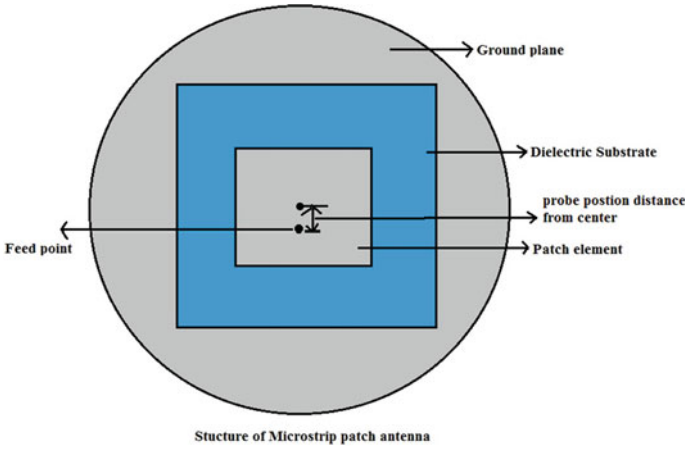

Fig. 1 Structure of microstrip patch antenna

Effective dielectric constant (ε_{eff}):

$$\varepsilon_{\text{reff}} = \frac{\varepsilon_r + 1}{2} + \frac{\varepsilon_r - 1}{2}\left[1 + 12\frac{h}{w}\right]^{-1/2} \tag{2}$$

Electrical length of the antenna:

$$\frac{\Delta L}{h} = 0.412\frac{(\varepsilon_{\text{reff}} f + 0.3)\left(\frac{w}{h} + 0.264\right)}{(\varepsilon_{\text{reff}} - 0.258)\left(\frac{w}{h} + 0.8\right)} \tag{3}$$

Length of the patch antenna:

$$L = \frac{C_0}{2f_r\sqrt{\varepsilon_{\text{reff}}}} - 2\Delta L \tag{4}$$

The simulation results show that the axial ratio beam width and S11 parameter is optimum at 10.87 GHz frequency. In rectangular patch antenna the electric field travels along the patch antenna so it has linear polarization. If the edges are cut then the electric field direction will change from the linear to vertical. Figure 2 shows the structure of truncated corners of patch antenna. The truncated corner helps to improve the axial ratio of patch antenna. Δx is the length of the truncated corner of the patch antenna.

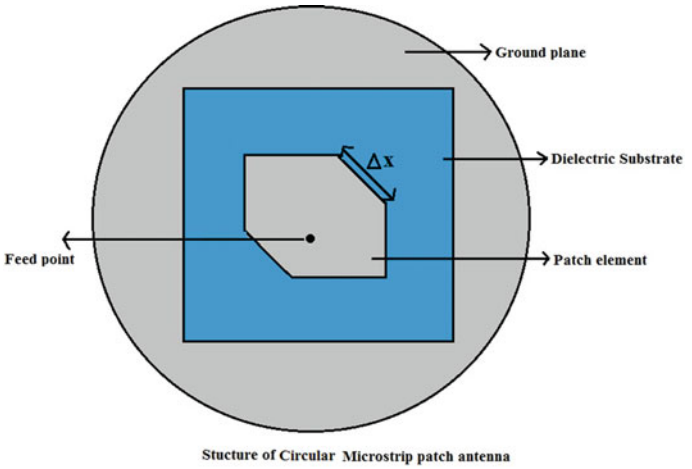

Fig. 2 Structure of microstrip patch antenna with. truncated corner

3 Design Optimization

The probe feed position from the centre point of the patch as shown in Fig. 1. were changed over 0.6 mm to 1.2 mm and the optimized S_{11} paramter is obtained using HFSS software. The variation in S_{11} parameters for various feed positions is shown in Fig. 3 and Table 1 shows the values of gain and reflection coeff for 10.87 GHz frequency at different feed positions.

From the above graph and the table it can be conclude that at probe position 0.8 mm from the center the patch antenna is giving sufficient reflection coefficient (S_{11}) i.e. −17 dB and gain value is also positive i.e. 0.35 dB.

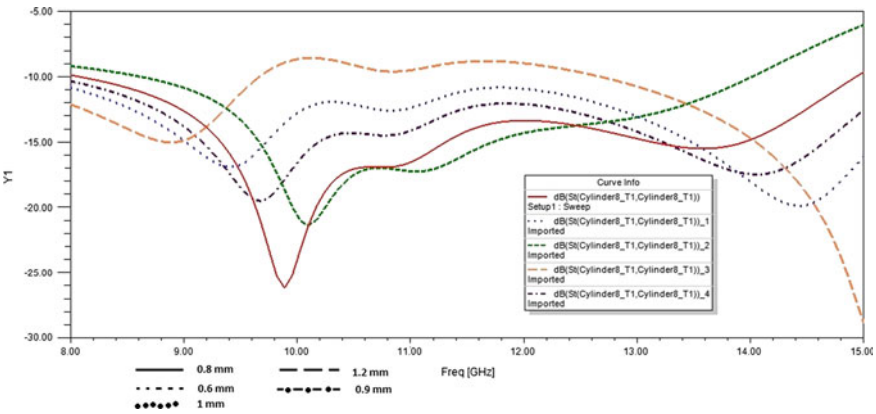

Fig. 3 S11 parameter with probe feed positions of rectangular microstrip patch antenna

Table 1 Probe feed positions of the patch antenna

Sr.No	Probe feed Positions (from center) in mm	Resonating Frequency (f_r) GHz	Reflection coefiecient (S11) in dB	Gain (dB)
1	0.6	10.87	−17.10	−0.69
2	0.8	10.87	−17	0.3534
3	1	10.87	−12.61	1.05
4	1.2	10.87	−9.63	1.24

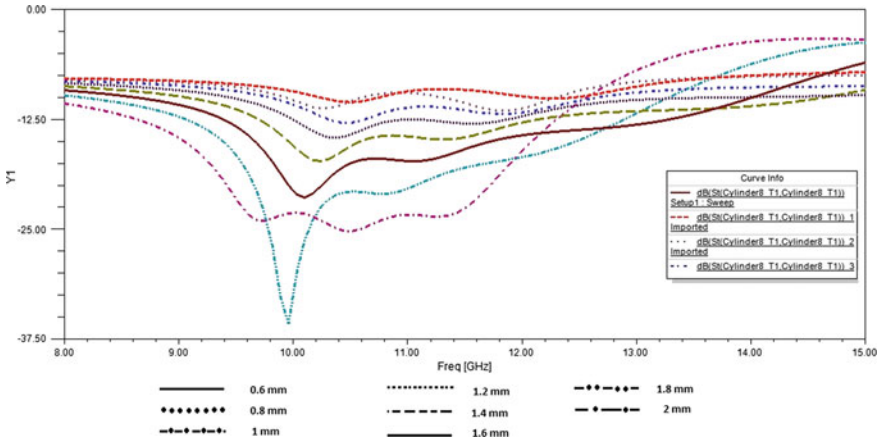

Fig. 4 Result of S_{11} parameter for different thickness of Microstrip patch antenna

Table 2 Values of S11 parameter and axial ratios for different thickness of the dielectric substrate

Height of the dielectric substrate (mm)	S_{11} parameter (dB)	Axial Ratio (dB)	Frequency (GHz)	Bandwidth (MHz)
0.6	−9.6611	4.6604	10.87	–
0.8	−9.4909	4.466	10.87	–
1	−11.49	4.2753	10.87	2.95
1.2	−12.67	2.9207	10.87	4.2
1.4	−14.34	1.8209	10.87	5.72
1.6	−17	2.012	10.87	4
1.8	−20.89	4.388	10.87	4.9
2	−23.85	7.3415	10.87	4.48

The bandwidth of the antenna is depends upon the thickness of the substrate material. Impedance Bandwidth of the microstrip patch antenna is an important characteristic which can be significantly improved by using multilayer dielectric configuration. The impedance bandwidth of microstrip antennas can be improved by

using the substrate of lower dielectric constant or by increasing the substrate thickness. The substrate thickness and lower permittivity increases surface wave resulting in low gain, low efficiency of the antenna and distorts the radiated field pattern. Thus, as the dielectric substrate height increases beyond 2% of the wavelength these effects become significant [12]. Following graph shows the optimized S parameter with different heights of dielectric substrates (Fig. 4 and Table 2).

From the above graph and table it shows that at 1.6 mm thickness the S11 parameter and the axial ratio is better. So, the height of the dielectric material is fixed at 1.6 mm thickness.

Axial ratio is the parameter which is majorly used to describe the polarization nature of circularly polarized antenna. The Axial Ratio (AR) is defined as the ratio between the minor and major axis of the polarization ellipse. If the ellipse has an equal minor and major axis it transforms into a circle, and therefore the antenna is circularly polarized. It also enhances the axial ratio beam width. The following Fig. 5 and Table 3 Shows the S11 variations for different values of the truncated corner lengths (Δx).

Based on the above results the probe feed position and the length of the truncated corners (Δx) has been decided. Figure 6 shows the final structure of the circular polarization patch antenna with proper dimensions.

Following table shows the Dimesions of the circular poarized patch antenna in LTCC technology.Here a high dielectric constant substrate Dupont 951 is used having dielectric constant is 7.8, loss tangent is 0.002 and thickness of the material is 1.6 mm. The center frequency of the patch antenna is 10.87 GHz (Table 4).

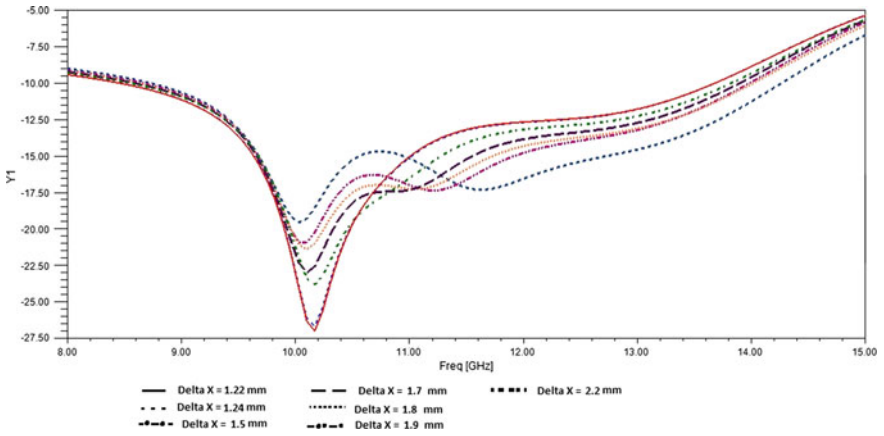

Fig. 5 Result of S_{11} parameter for different truncated corner lengths of Microstrip patch antenna

Table 3 Optimize values of the truncated values and axial beam width

Distance (Δx) in mm	Frequency (GHz)	S11 Parameter (dB)	Axial ratio (dB)
1.24	10.87	−15	@0º = 8.3922
1.5	10.87	−17.1	@0º = 8.3467
1.7	10.87	−17.23	@0º = 4.99
1.8	10.87	−17.5	@0º = 2.01 Beam width = 107°
1.9	10.87	−16.2	@0º = 0.91 Beam width = 100°
2.2	10.87	−14.8	@0º = 1.54 Beam width = 70°

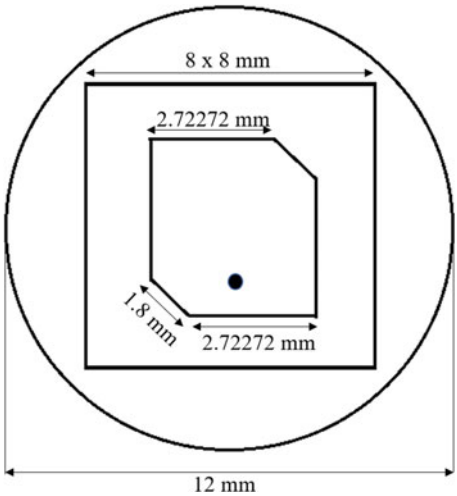

Fig. 6 Structure of circular polarized microstrip patch antenna

Table 4 Dimensions of the circular polarized microstrip patch antenna

S.No	Parameters of the antenna	Dimensions (mm)
1	Patch antenna	4 mm × 4 mm
2	Substrate	8 mm × 8 mm
3	Ground plane size (Diameter)	12 mm
4	Δx (truncated corner length)	1.8 mm
5	Probe feed position (from center of the patch)	0.8 mm from the center

4 Effect of Ground Plane on Axial Beam Width

In circular polarized antenna the axial beam width plays an important role to determine the circular polarization. In the present research optimization of the ground plane size (diameter) has been done with axial ratio beam width. As the ground plane size increases the axial ratio beam width will decreases. Following figs. shows the simulated analysis of ground plane size (Figs. 7, 8, 9, 10, 11 and 12).

The following table shows the optimization of Ground plane size (diameter) and the changes in axial ratio beam width (Table 5).

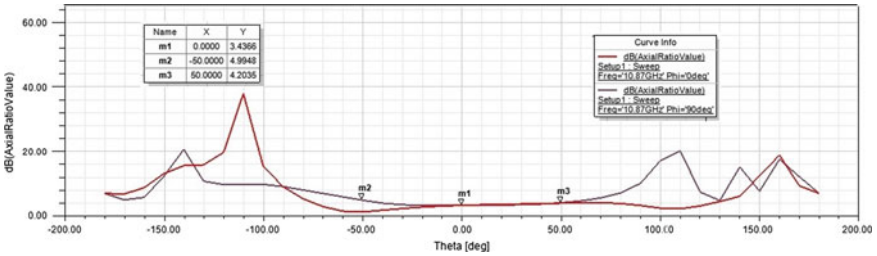

Fig. 7 Ground plane radius is 3 mm (0.1λ)

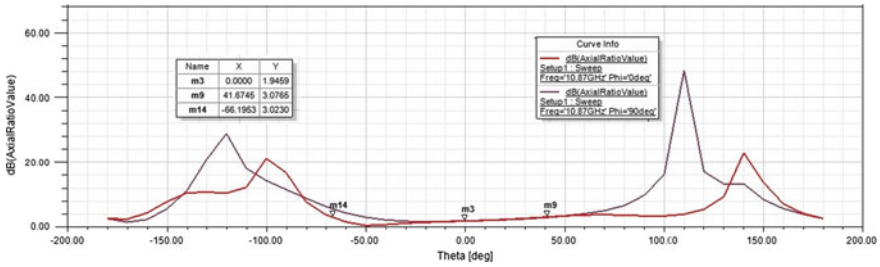

Fig. 8 Ground plane radius is 6 mm (0.2λ)

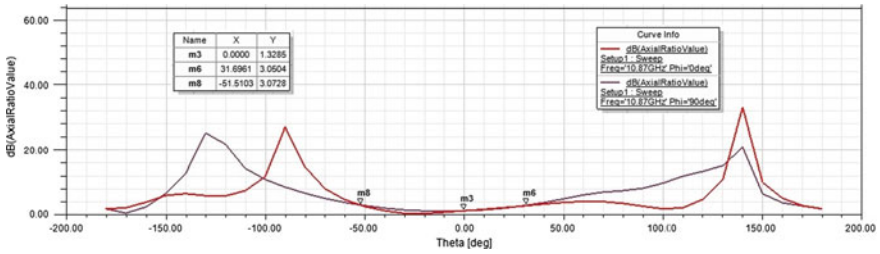

Fig. 9 Ground plane radius is 9 mm (0.3λ)

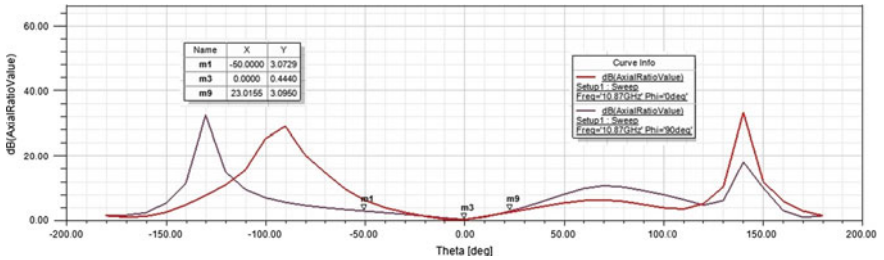

Fig. 10 Ground plane radius is 12 mm (0.4λ)

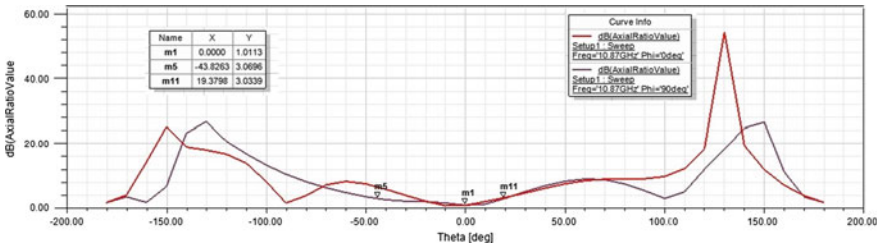

Fig. 11 Ground plane radius is 15 mm (0.5λ)

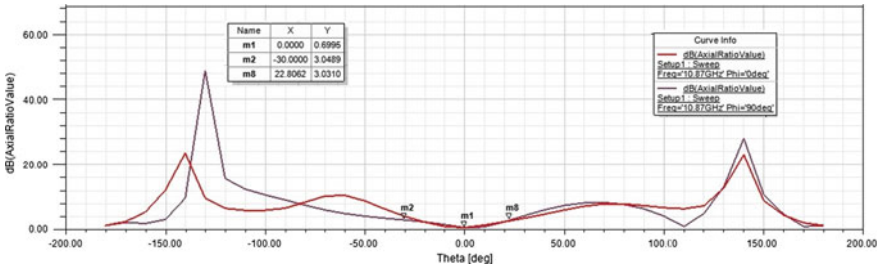

Fig. 12 Ground plane radius is 18 mm (0.6λ)

Table 5 Optimized values of the ground plane size (diameter) and the changes in axial ratio beam width

S.No	Ground plane size (λ)	Axial ration beam width (°)
1	0.1	20
2	0.2	107
3	0.3	82
4	0.4	73
5	0.5	62
6	0.6	53

5 Simulation Results

The simulated S_{11} Parameter of the antenna is as shown in the Fig. 13. From the results it can be concluded that at 10.87 GHz frequency the S parameter is −17 dB. The −10 dB bandwidth of the antenna is approximately 4 GHz. In LTCC technology the height of the single DuPont 951 substrate is 100 Micron. To achieve 1.6 mm thickness total 16 sheets of DuPont 951 substrate has been taken. To reduce the thickness the no. of DuPont sheets can reduce. Bandwidth can be reducing by reducing the height of the substrate.

The following Fig. 14 Shows the Simulated Voltage standing wave ratio (VSWR) of the patch antenna. VSWR describes the power reflected from the antenna which is 1.33 at 10.87 GHz.

The following Figs. 15 and 16 shows the simulated 2D and 3D radiation pattern of the microstrip patch antenna at frequency 10.87 GHz. The gain of the antenna is

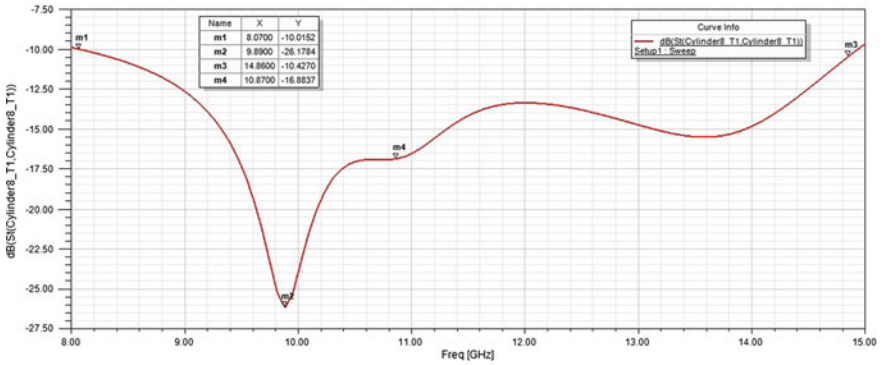

Fig. 13 S11 parameter of circular polarized microstrip patch antenna

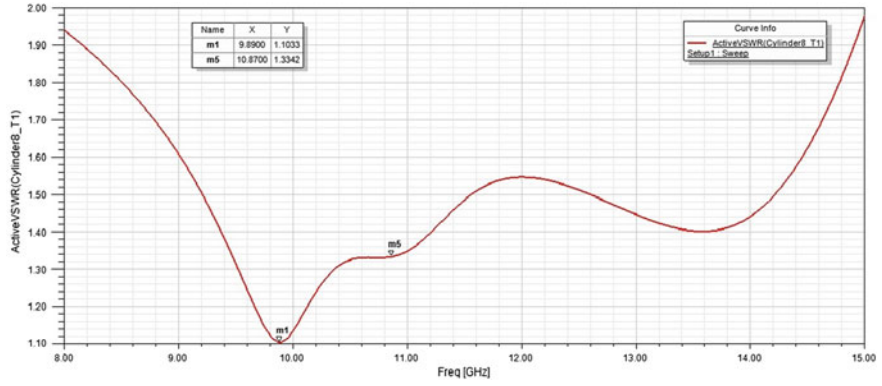

Fig. 14 Simulated VSWR of circular polarized microstrip patch antenna

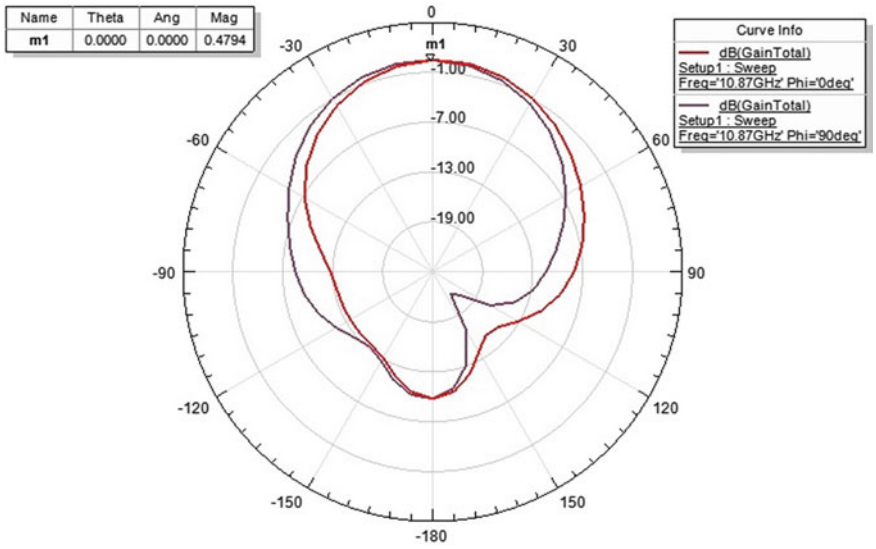

Fig. 15 Simulated 2 D radiation pattern

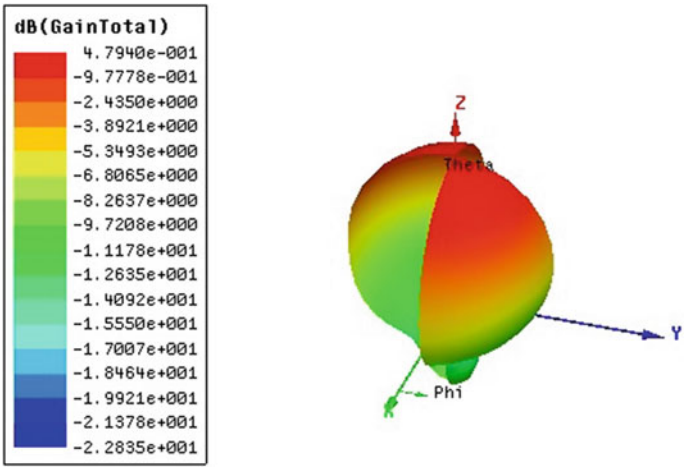

Fig. 16 Simulated 3D polar radiation pattern

0.5 dB. The gain of the antenna is proportional to the dimension of the antenna. Here as the high dielectric constant of the substrate provides the small size of the antenna therefore the gain will be less.

Figure 17 shows the axial ratio of simulated microstrip patch antenna. The Axial Ratio (AR) is defined as the ratio between the minor and major axis of the polarization ellipse.The circular polrization can achieved by corner truncation of the patch element. Here the axial ratio beamwidth is 107°.

The current distribution pattern of the simulated circular microstrip patch antenna is as shown in Fig. 18 which shows the behavior of current in the patch antenna after the excitation.

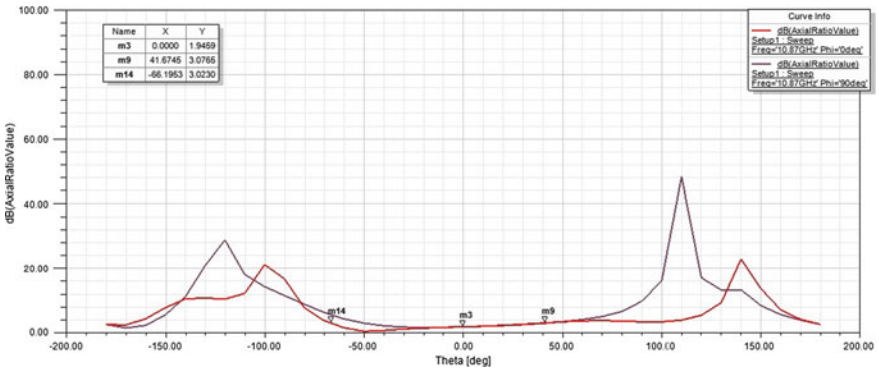

Fig. 17 Simulated axial ratio of circular polarized microstrip patch antenna

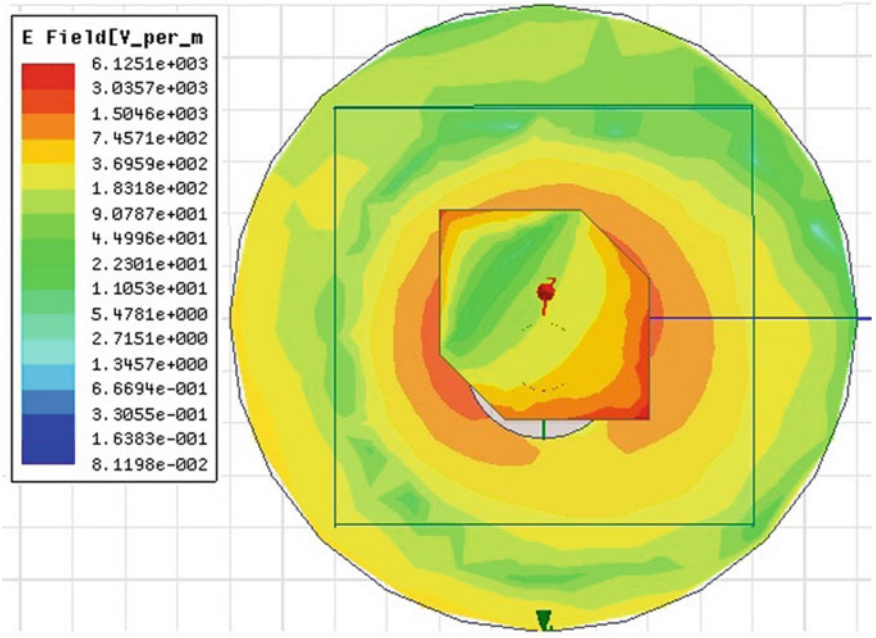

Fig. 18 Simulated current distribution pattern of circular polarized microstrip patch antenna

6 Conclusion

A circular microstrip patch antenna has been designed, analyzed and simulated. A microstrip patch antenna is designed in low temperature cofired ceramic technology where a high dielectric constant material dupont 951 having dielectric constant 7.8 is used.

In the present paper the circular patch antenna is designed with circular shaped ground plane to improve the axial ratio beamwidth of the antenna. In the referred papers few techniques are described to get circular polarization like slots were used to get the circular polarization plus truncation in the patch to improve the impedance bandwidth [15]. In [9] cutting corner length of antenna decides the axial ratio and probe position decides the impedance bandwidth but, the radiation pattern was tilted. Some papers describes stacked patch antenna structure also which is difficult to fabricate. As compared with the above referred techniques the presented technique is simple, to achieve circular polarization by cutting the corner edge of the patch element and improve the axial ratio by optimizing the ground plane size. Paper presents a better impedance bandwidth as compared to others. The S11 parameter and axial ratio beam width is optimized by varying thickness of the dielectric substrates, probe feed positions and different lengths of the truncated corners of patch antenna. The referred paper shows from simulation graph, the height of the substrate is optimized as 1.6 mm, the probe feed position as 0.8 mm from the center of the patch and truncated corner length as 1.8 mm. With these specifications the Simulated S11 parameter was found to be below −17 dB, the axial ratio beam width was 1070 and gain of the antenna is 0.5 dBi. The ground plane size is optimized to improve the axial ratio beam width. Microstrip patch antenna is in the fabrication process.

References

1. Bhalla, D.: Design of a rectangular microstrip patch antenna using inset feed technique. IOSR J. Electron. Commun. Eng. **7**(4) (2013). (IOSRJECE) e-ISSN: 2278–2834, p- ISSN: 2278–8735
2. Ali, S.A.: Multiband microstrip patch antenna for microwave applica tions. IOSR J. Electron. Commun. Eng. **3**(5), 43–48 (2012). (IOSR-JECE) ISSN: 2278–2834, ISBN: 2278–8735
3. Tentzeris, E: Design of compact stacked patch antennas on LTCC Technology for wireless communication applications. In: IEEE Antennas and Propagation Society International Symposium (2002)
4. Wolff, I.: Design and technology of microwave and millimeter wave LTCC circuits and systems. IEEE Trans. (2007)
5. Ferrero, F.: Dual-band circularly polarized microstrip antenna for satellite applications. IEEE Antennas Wirel. Propag. Lett. **4**, 13–15 (2005)
6. Chen, H.-M.: Microstrip-fed circularly polarized square-ring patch antenna for GPS applications. IEEE Trans. Antennas Propag. **57**(4), 1264–1267 (2009)
7. Heidari, A.A.: A Dual-band circularly polarized stub loaded microstrip patch antenna For GPS applications. Progress Electromag. Res. PIER **92**, 195–208 (2009)
8. Prakash, K.C.: Circularly polarized dodecagonal patch antenna with polygonal slot for RFID applications. Progress Electromag. Res. C **61**, 9–15 (2016)

9. Bhattacharya, A.K.: Effects of finite ground plane on the radiation characteristics of a circular patch antenna. IEEE Trans. Antennas propag. *18*(2) (1990)
10. Noghanian, S.: Control of microstrip antenna radiation characteristics by ground plane size and shape. IEEE Proc.-Microwave Antennas Propag. **145**(3) (1998)
11. Chae, Y.-K.: Design of a ceramic patch antenna for artillery projectile positioning applications. J. KIIT **15**, 81–85 (2017)
12. Ranjan, P.: Design of Circularly polarized rectangular patch antenna with single cut. In: Conference on Advances in Communication and Control Systems (2013)
13. Tayade, S.N.: Single-Feed circular polarization microstrip antenna. ITSI Trans. Electr. Electron. Eng. **1**(1) (2013). ISSN (PRINT): 2320–8945
14. Tayade, S.N.: Single-feed circular polarization microstrip antenna. ITSI Trans. Electr. Electron. Eng. **1**(1) (2013). ISSN (PRINT): 2320–8945
15. Amal, K.A.: Compact multiband microstrip patch antenna for wireless applicationsr. In: 2016 International Conference on Communication Systems and Networks (CommNet) (2016). ISBN (Online): 978–1–5090–3349–2
16. Karli, R.: A simple and original design of multi-band microstrip patch antenna for wireless communication. Int. J. Microwaves Appl. **2**(2) (2013)
17. Kumar, S.: Slotted circularly polarized microstrip antenna for RFID application. Radio Eng. **26**(4), 1025–1032 (2017)
18. Palson, C.L.: Circularly Polarized Square Patch Antenna with Improved Axial Ratio Bandwidth. IEEE Xplore (2016)
19. Zhao, Y.: Simulation and Design of Broadband Circular Polarization Stacked Patch Antenna in LTCC Technology. IEEE Xplore (2011)
20. Shodhganga: A reservoir of Indian thesis. Bandwidth enhancement of the antenna, Chap. 4

Design and Implementation of Data Acquisition and Analysis System for SEAPS

Rupali Borade, Damayanti Gharpure, and Subramaniam Anathakrishnan

Abstract One of the last unexplored frequency ranges in radio astronomy is the frequency band below 30 MHz. This is an important frequency regime as it can yield valuable information about the interaction between the solar wind and the Earth's magnetosphere, decametric radiation from other planets within the solar system or exoplanets, supernova remnants and continuum emission from pulsars and very high redshift (z∼500) cosmic radio sources. Therefore, several initiatives have been started recently to explore this unexplored frequency band. Space Electromagnetic and Plasma Sensor (SEAPS) is a system being designed for low frequency radio astronomical observations. This paper elaborates the design, implementation, and testing of a laboratory prototype of the FPGA based backend data acquisition and analysis system for SEAPS.

Keywords Data acquisition · Fourier transform · FPGA · Radio astronomy

1 Introduction

New interesting astronomical science drivers for very low frequency radio astronomy have emerged, ranging from studies of the astronomical dark ages, the epoch of reionization, exoplanets, to ultra-high energy cosmic rays. However, Earth-based radio astronomy below frequencies of 30 MHz is severely restricted due to man-made interference, ionospheric distortion, and almost complete non-transparency of the ionosphere below 10 MHz. Space-based observatory is the only solution to study the universe at these frequencies. If successfully implemented, they will trace a completely new area of radio astronomical research [1–5]. SEAPS is an instrument being designed, for the same purpose.

Space Electromagnetic and Plasma Sensor (SEAPS) is a proposed space payload with a front end consisting of electric field vector sensor (EFVS)—a tri-axial

R. Borade (✉) · D. Gharpure · S. Anathakrishnan
Department of Electronic Science, Savitribai Phule Pune University, Pune, India
e-mail: rup.1889@gmail.com

S. Mukherjee et al. (eds.), *Computational Mathematics, Nanoelectronics, and Astrophysics*,
Springer Proceedings in Mathematics & Statistics 342,
https://doi.org/10.1007/978-981-15-9708-4_5

arrangement of monopoles in a mutually orthogonal configuration and a magnetic field vector sensor—tri-axial arrangement of mutually perpendicular loop antennas (MFVS), both operating between 0.5 and 16 MHz. Its backend data acquisition and analysis system will receive data through six channels: three from the EFVS and MFVS each. SEAPS science objectives, design of front end laboratory prototype along with brief about backend system are explained in paper [6].

This paper presents detail about the design and development of the backend data acquisition and analysis system. This paper is organized as follows: Sect. 2, deals with the design considerations. Design implementation is described in Sect. 3. System integration results with integrated system test set up is shown in Sect. 4. Conclusions and future scope are presented in Sect. 5.

2 Design Consideration

Backend data acquisition and analysis system design comprises of ADC interface, memory interface for logging the acquired and processed data, hardware for obtaining the Fourier Transform, and communication interface for data transmission.

The signal from each arm of the electric antenna and magnetic loop antenna is fed via a low-noise amplifier to an analog to digital converter (ADC) as shown in Fig. 1. ADC samples the signal at 33 MHz to cover the entire radio frequency (RF) range of interest. For a short dipole, the dynamic range of the input signal is expected to be 60–70 dB [7, 8]. The ADC used is 14 bits providing a dynamic range of 76 dB. The digitized time series is Fourier transformed in real time with 2048 point FFT providing spectral width of 16 KHz.

The telemetry bandwidth to transmit the data to the Earth is an important design driver for space-based designs. All the earlier proposals chose to transmit the Nyquist

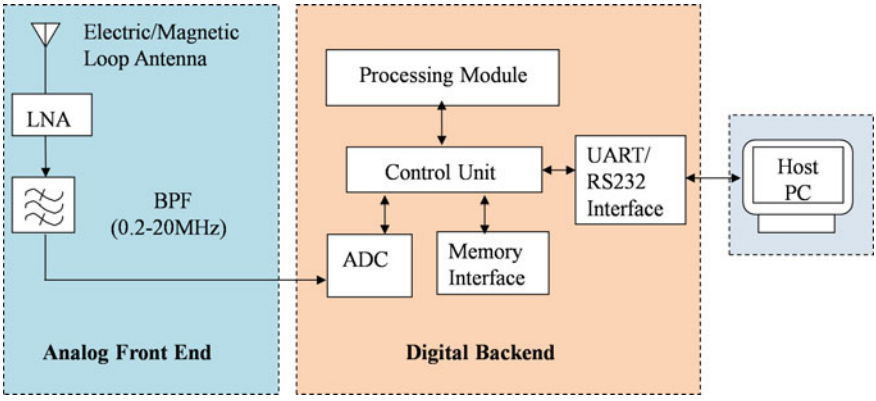

Fig. 1 Simplified block diagram of the SEAPS system

sampled time series from the receiver on each of the spacecraft to the Earth and data processing was carried out offline [9]. This classical approach provided a simpler spacecraft design with increased data volume. However, current development in technology has made it possible to increases the computational capabilities of space-qualified hardware which opens the option of on-board computation and subsequent time and frequency averaging to reduce the data volume [10]. The recent studies extensively discuss about designing an on-board digital signal processing and communication architecture with effort towards minimizing downlink data rate [2–10]. Taking these studies into consideration, SEAPS backend data acquisition and analysis system exploits the frequency binning concept to reduce the size of the data which eases any subsequent interface bandwidth requirements and processing loads.

From hardware implementation point of view, FPGAs present a powerful tool to implement systems, due to its design flexibility, reconfigurability, parallel processing, low power consumption, and high density [11, 12]. There has been significant progress over the last decade in the understanding and development of FPGA technology that is resistant to and tolerant of the effects of radiation. The success of these efforts has facilitated the use of FPGAs in many existing spacecraft systems [13, 14]. Considering the advantages of FPGA, a prototype model of single channel data acquisition and analysis system has been implemented on Virtex-5 FPGA, for realizing the SEAPs backend.

3 Design Implementation

Implementation of the design has been carried out using Xilinx Virtex5 based xc5vlx50 FPGA device. LTC2255 14 bit, 100 Msps ADC from Linear Technology, is used to sample and digitize the signal. Sampling rate is further reduced to 33 MHz by down sampling. Design modules are implemented in VHDL language using Xilinx ISE Design Suite. The Data acquisition and analysis system is made up of different processing stages such as; Data acquisition and windowing, FFT Computation, FFT Magnitude calculation, and Frequency Binning as shown in Fig. 2.

In the first stage, N consecutive input samples of signal x (n) are multiplied with the corresponding values of window coefficient [15]. In the second stage, frame consisting of the N windowed input samples is fed to the Fast Fourier Transform (FFT) block, which generates the same number of complex values X(k), where k = 0 N–1 is the discrete variable in the frequency domain. Further, Complex values are presented to the magnitude stage where magnitude is calculated by using the formula $sqrt(real^2 + imaginary^2)$. The final step of processing consists of the frequency binning; where multiple FFTs are summed together.

Intellectual Property (IP) cores offered by Xilinx are exploited to design the system. Xilinx FFT IP core implements the Cooley-Tukey FFT algorithm, a computationally efficient method for calculating the DFT [16]. Mathematical operations required for FFT Magnitude computation are performed using an in-built multiplier, adder, and square root IP core. Window coefficients generated using MATLAB are

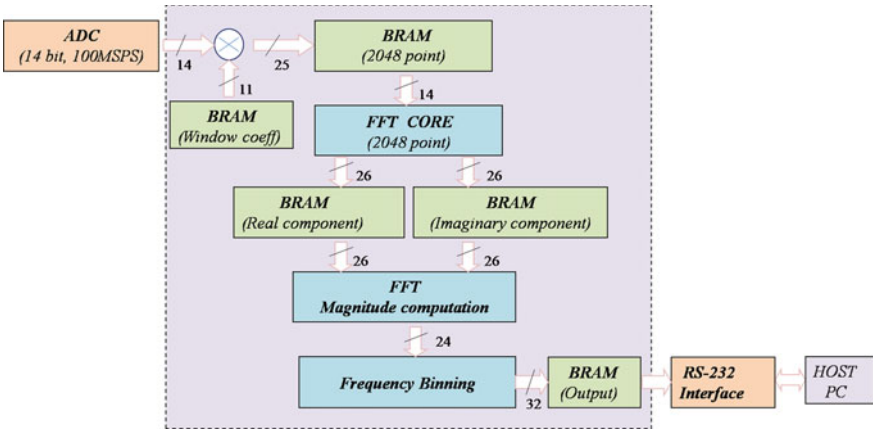

Fig. 2 Detailed block diagram for the implementation of single channel data acquisition and analysis system

stored in Xilinx BRAM instantiated as ROM; coefficients are scaled appropriately to fit into fixed size signed integer word type.

The data stored as 2048 point samples (N = 2048) have been input to the FFT block. Consequently, the selected window has the same length, and all data processing is made in groups of 2048 samples. With the 14-bit input samples x(n) and 11-bits window coefficients w(n),windowing result generates 25-bit output which is fed to FFT core with a truncated dimension of 14-bits. With an input of 14-bits, 2048-point transform has an unscaled output of 26-bits (for each of the real and imaginary parts). Real and imaginary parts are presented to the magnitude stage which produces 24-bits output. After computing the FFT magnitude, the resulting values are accumulated in 32-bit memory. Accumulated output stored into the output memory is transferred to the host computer through the RS 232 serial interface. Each processing stage output such as windowed input, FFT real and imaginary part and FFT magnitude are stored in the dual port block RAM which provides read and write access through two different ports.

3.1 On-Board Calibration

On-board calibration is an important aspect for designing the space-based system. On-board calibration is performed to calibrate the system before actual observation start. For this, various test signals such as sine of 1MHz frequency with different amplitudes, i.e., −10, −15, −20 dBm, and 1 MHz trapezoidal signal with −15 dbm amplitude are generated through digital to analog converter (DAC) and provided to the whole design chain.

Table 1 Command list

Command	Command description
RESET	Initialize the system
Sampling rate	Select the sampling rate
Non-averaged FFT	Compute one shot FFT
Averaged FFT	Perform frequency binning, i.e., averaging of multiple FFTs computed
Calibration	System operates in the calibration mode.Test signals generated through DAC are provided to the whole design chain
Observation	System operates in observation mode. Data acquisition and analysis of the signals picked up by the antenna is carried out in the observation mode

Table 2 Device utilization summary

Slice logic utilization	Used	Available	Utilization (%)
Number of slice registers	4712	28,800	16
Number of slice LUTs	6285	28,800	21
Number of occupied slices	2195	7200	30
Number of bonded IOBs	28	440	11
Number of block RAM	15	48	31
Number of DSP48Es	17	48	35

3.2 Command Prompt

System operation is defined in two modes; calibration mode and observation mode. In the design, the option for computation of one shot FFT or averaging of multiple FFTs is provided based on the phenomena to be observed. In addition, sampling rate can be selected depending on the frequency range of interest and desired spectral resolution. Signal sampling rate is reduced by the down sampling. Modes of operation, sampling rate selection, computation of one shot FFT or multiple FFTs, etc., are controlled through the different commands. Various commands defined for the system are listed in Table 1.

The single channel backend data acquisition and analysis system utilizes about 40% of Virtex 5 FPGA resources as detailed in Table 2.

4 System Integration

One arm of the EFVS was connected to FPGA backend though a matching amplifier with 20 dB gain and a fifth order Butterworth bandpass filter with a pass band of 0.2 20 MHz as shown in Fig. 3. To validate FPGA results, they are compared with Agilent

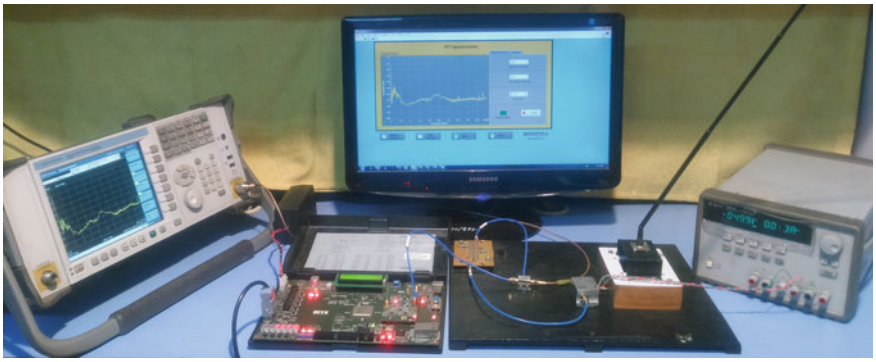

Fig. 3 Integrated system test setup

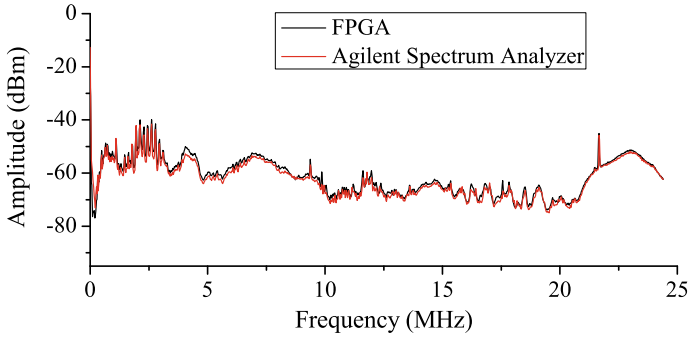

Fig. 4 Spectrum of local environmental noise picked up by the monopole antenna

N1996Aspectrum analyzer. Therefore, the output of the filter was split using a Mini Circuits ZX10R-14-S+ splitter, and one output is fed to an Agilent spectrum analyzer and the other to the FPGA backend system. For the purposes of these measurements, the resolution bandwidth of the Agilent spectrum analyzer was kept at 16 kHz; the frequency span at 16 MHz with 1024 sweep points to match the specification of the FPGA backend.

The experiments were repeated a number of times during day and night with the antenna placed on the roof of laboratory or in the laboratory directing outside through the window. It is observed that results from FPGA based system and Agilent spectrum analyzer show excellent agreement, with a correlation factor of 0.99. A typical output is shown in the Fig. 4. The results from both instruments are superimposed for comparison.

It must be noted that the signal components present here are man-made RFI and completely local—originating from, presumably, power lines, automobiles and other electrical equipment in the vicinity of the university.

5 Conclusion and Future Scope

In this paper, the design and development of the laboratory prototype model of single channel data acquisition and analysis system on FPGA platform has been discussed for a future space payload. As a proof of concept, a system was designed and realized using COTS (commercial off the shelf) components such as LTC 2255 ADC, DAC 2904, and Virtex-5 FPGA. It satisfies the requirement of SEAPS project for low frequency radio observation providing a bandwidth of 16 MHz with 16 KHz spectral resolution and 80 dB dynamic range.

To validate the system performance, local environmental noise is measured by integrating FPGA backend with the antenna and RF front end; these results are compared with Agilent spectrum analyzer. FPGA backend results are closely matching with Agilent spectrum analyzer showing 0.99 correlation coefficient.

In future, considering the tri-axial arrangement of electric and magnetic loop antenna at the front end, single channel acquisition system needs to extend for six channels. Further, will have to work on details about payload data rate, telemetry details, and data transfer to the ground. To make system space applicable, system design needs to be carried out considering space-qualified components. It is also necessary to consider key requirement like mass, power, size, and communication interface specification that drives the design of the payload.

Acknowledgements This work was supported by the Indian Space Research Organization (ISRO), India [Grant Number GOI-A-574].

References

1. Jester, S., Falcke, H.: Science with a lunar low-frequency array: from the dark ages of the universe to nearby exoplanets. New Astron. Rev. **53**(1), 1–26 (2009). https://doi.org/10.1016/j.newar.2009.02.001
2. Rajan, R.T., Boonstra, A.J., Bentum, M., et al.: Space-based aperture array for ultra-long wavelength radio astronomy. Exp. Astron. **41**(1), 271–306 (2016). https://doi.org/10.1007/s10686-015-9486-6
3. Bentum, M.J.,Verhoeven, C.J.M., Boonstra, A.J. van der Veen, A.J., Gill, E.K.A.: A novel astronomical application for formation flying small satellites. In: 60th International Astronautical Congress, pp. 12–16. Daejeon, Republic of Korea (2009)
4. Bentum, M. J., Boonstra, A.-J.: Low frequency astronomy the challenge in a crowded RFI environment in general assembly and scientific symposium. In: 2011XXXth URSI, pp. 1–4. Istanbul, Turkey (2011). https://doi.org/10.1109/URSIGASS.2011.6050736
5. Bentum, M. J., Boonstra, A. J., Baan, W.: Space-based ultra-long wavelength radio astronomy An overview of today's initiatives. In: 2011 XXXth URSI General Assembly and Scientific Symposium, pp. 1–4. Istanbul (2011). https://doi.org/10.1109/URSIGASS.2011.6051209
6. Makhija, K., Borade, R., Shaifullah, G., et al.: Space Electromagnetic and Plasma Sensor (SEAPS): a laboratory prototype for a space payload. MAPAN **31**(4), 283–289 (2016). https://doi.org/10.1007/s12647-016-0188-y
7. Bougeret, J.-L.: Very low frequency radio astronomy. Adv. Space Res. **18**, 35–41 (1996)

8. Basart, J.P., Burns, J.O., Dennison, B.K., Weiler, K.W., Kassim, N.E., Castillo, S.P., McCune, B.M.: Directions for space-based low frequency radio astronomy: 1. System considerations. Radio Sci. **32**(1), 251–263(1997). https://doi.org/10.1029/96RS02407
9. Jones, D., et al.: The astronomical low frequency array: a proposed explorer mission for radio astronomy. Radio Astron. Long Wavelengths, Geophys. Monograph Ser. **119**, 339–349 (2000). https://doi.org/10.1029/GM119p0339
10. Oberoi, D. and Pincon, J.-L.: A new design for a very low frequency space borne radio interferometer. Radio Sci. **40**(4) (2005). https://doi.org/10.1029/2004RS003211
11. Iglesias, V., Grajal, J., Sánchez, M. A., López-Vallejo, M.: Implementation of a real-time spectrum analyzer on FPGA platforms. IEEE Trans. Instrum. Meas. **64**(2), 338–355 (2015). https://doi.org/10.1109/TIM.2014.2344411
12. Qi, D., Guo, X., Du, W.: Design of digital signal spectrum analyzer based on FPGA. In: IEEE International Conference on Information and Automation, pp. 2725–2729. Lijiang, China (2015)
13. Pingree, P.J., Bekker, D.L., Werne, T.A., Wilson, T.O.: The prototype development phase of the CubeSat On-board processing validation experiment. In : 2011 IEEE Aerospace Conference, pp. 1–8. Big Sky, MT (2011). https://doi.org/10.1109/AERO.2011.5747230
14. Jones, D.L., Lazio, T.J.W., Burns, J.O.: Dark ages radio explorer mission: probing the cosmic dawn. In: IEEE Aerospace Conference, pp. 1–8. Big Sky, MT (2015). https://doi.org/10.1109/AERO.2015.7118941
15. Borade, R., Dimber, A., Gharpure, D., Ananthakrishnan, S.: Design and development of FPGA based spectrum analyzer. IETE J. Edu. **59**(1), 5–17 (2018). https://doi.org/10.1080/09747338.2018.1450648
16. Xilinx. http://www.xilinx.com/support/documentation/ip_doumentation/ds808_xfft.pdf

Higher Order Stability Analysis for Astrophysical Accretion Processes

Sayan Kundu and Kinsuk Giri

Abstract We have done n^{th} order perturbation analysis of the Navier-Stokes equation with the presence of turbulent viscosity in the context of thin accretion flow around a black hole. In order to find the stability criteria, we used Green's function to solve the n^{th} order velocity perturbation equation. Finally, we have proposed a velocity stability criterion which helps to find whether the base flow is stable for a higher order perturbation.

Keywords Stability analysis · Fluid dynamics · Turbulent viscosity · Accretion · Green's function

1 Introduction

Nowadays, the study of the stability of a standard thin accretion disk is coming out to be an important topic. Few important issues, viz., how the turbulent viscosity arises, and also the stability criterion due to small perturbation are still a mystery in the context of this topic.

Various studies on accretion flows around a black hole have been proposed since last three decades. The stability analysis have been performed for a significant part of this proposed accretion disk models. In case of stability analysis of thin accretion disk, it is concluded that the disk is thermally and viscously unstable in the inner region [12, 24], which excludes the thin disk from the accretion flows in real world.

S. Kundu (✉)
Discipline of Astronomy Astrophysics and Space Engineering, Indian Institute of Technology, Indore 453552, India
e-mail: sayan.astronomy@gmail.com

K. Giri
National Inst. of Technical Teachers' Training & Research, Block - FC Sector - III, SaltLake City, Kolkata 106, India
e-mail: kinsuk@nitttrkol.ac.in

S. Mukherjee et al. (eds.), *Computational Mathematics, Nanoelectronics, and Astrophysics*, Springer Proceedings in Mathematics & Statistics 342,
https://doi.org/10.1007/978-981-15-9708-4_6

In addition, the thin accretion flow which is dominated by radiation pressure is found to be secularly and thermally unstable. However, another model for an optically thin, two-temperature accretion flow was put forward by [25] to explain the hard X-rays from Cyg X-1, and it was found to be thermally unstable [22, 23], though this model is been widely studied for X-ray binaries and AGNs [9, 11, 13, 26, 27]. Piran [22] derived a general criteria for thermal and viscous modes for accretion processes. Both optically thin and thick disks with radial advection have been studied extensively [1, 3, 4, 9, 15, 18–21]. If viscous heating could not get balanced by the cooling process via radiation, then their has to be an inward energy advection toward the central region and the effect cannot be neglected. [1, 4, 21] suggested, by analyzing the slope of $\frac{\partial M(\Sigma)}{\partial t}$ curve, that both the optically thick and thin advection dominated disks are thermally and viscously stable. Though these stability analysis, as well as Piran's criteria are for long wavelength perturbations, a short wavelength perturbations was also been examined by [8, 10], and argued that for short wavelength perturbation the ADAF flow is thermally unstable for optically thick disks but thermally stable for the optically thin ones. This result was confirmed by [28]. Again, as suggested by [7], thin disks might get pulsationally unstable. This phenomenon was verified by [2]. Stability analysis for accretion flow around a black hole with the effects of Bremsstrahlung and Synchrotron cooling has been studied by [14]. The stability of accretion flows in the presence of nucleosynthesis has been performed by [17]. The stability performance for a rotating black hole accretion disk was also been done by [16].

Here we present a technique to study the higher order (higher than the linear) perturbation analysis with the help of Green's function approach. We have taken the viscosity prescription given by [24], which is true for turbulent accretion disk. For the initial results to present here, we have used the Cartesian coordinate system for our analysis and use some simple approximations to find the stability criteria.

2 Basic Equations

We have used the fluid equations in the Cartesian system and used the Einstein's summation index to simplify the writing. The first one is the continuity equation

$$\frac{\partial \rho}{\partial t} + \nabla.(\rho \mathbf{v}) = 0 \tag{1}$$

which we write using summation index as

$$\partial_t \rho + \partial_i (\rho v_i) = 0 \tag{2}$$

Here, we will consider only the incompressible fluids, so for our purpose the continuity equation becomes

$$\partial_i v_i = 0. \tag{3}$$

Next is the Navier-Stokes equation, using the summation index

$$\rho(\partial_t v_i + (v_j.\partial_j)v_i) = -\partial_i P + \rho f_i^{ext} + \mu \partial_k \partial^k v_i, \tag{4}$$

where v_i is the ith component of the velocity, ρ is the density, P is the pressure and μ is the coefficient of viscosity. The coefficient of viscosity is dependent on velocity, pressure, density, etc. Here, we are only going to discuss about the Shakura-Sunyeev α prescription [24], where the coefficient of viscosity is taken to be of the form [6]

$$\mu = \frac{2}{3}\frac{\alpha a^2 \rho r}{v_\phi}, \tag{5}$$

where α is a parameter whose value lies between 0 and 1, a is the adiabatic sound speed and v_ϕ is the rotational velocity.

Now, we apply the perturbation series on $\mathbf{v}$, ρ, P, μ as

$$A = \sum_{i=0}^{\infty} \lambda_i A^i, \tag{6}$$

where A is the variable on which the perturbation is applied. We did not perturb the gravitational potential due to the Cowling approximation [5].

3 Methodology

Applying Eq. (6) to Eqs. (5) and (4) and neglecting $\mathcal{O}(\frac{1}{v_\phi^2})$ and higher order terms, we get

$$\rho^0(\partial_t v_i^k + (v_j^k.\partial_j)v_i^0 + (v_j^0.\partial_j)v_i^k) - \mu^0 \partial_a \partial^a v_i^k = S_i, \tag{7}$$

where, S_i, is the source term and it does not include any term concerning the kth order perturbation of velocity, v_i^k. Also, μ^0 is given by

$$\mu^0 = \frac{2}{3}\frac{\alpha a^2 \rho^0 r}{v_\phi^0}$$

and applying Eq. (6) in Eq. (3) for kth order, we get

$$\partial_i v_i^k = 0. \tag{8}$$

We now solve the Eq. (7) with the help of Green's function method. Before that, we need to take into account the Eq. (8) because it gives a constraint on the fluid flow. We can deal with that condition by observing the term $(v_j^k.\partial_j)v_i^0$ as

$$(v_j^k.\partial_j)v_i^0 = \partial_j(v_j^k v_i^0) - v_i^0(\partial_j v_j^k) = \partial_j(v_j^k v_i^0), \tag{9}$$

where the last term goes out because of Eq. (8). Again, we would like to take a look to the term $\partial_j(v_j^k v_i^0)$. We then approximate this term by a constant times v_i^k. Hence, due to this approximation the term reduces

$$\partial_j(v_j^k v_i^0) \approx U v_i^k \tag{10}$$

where U is a constant. So our equation of interest becomes

$$\rho^0(\partial_t v_i^k + U v_i^k + (v_j^0.\partial_j)v_i^k) - \mu^0 \partial_a \partial^a v_i^k = S_i. \tag{11}$$

Now, Eq. (11) looks like a diffusion equation with an advection part that could be solved by using the Green's function method. Dividing by ρ^0 at both sides of Eq. (11) and taking both of the Laplace Fourier transformation of this equation, we get

$$G = \frac{1}{-\omega + v_i^0 K_i - i\frac{\mu^0}{\rho^0}K^2}, \tag{12}$$

where, K_i is the component of the wave vector.

Now, taking the inverse Laplace transform and inverse Fourier transform of Eq. (12), we have the Green's function as

$$G = \frac{A}{\sqrt{4\pi\frac{\mu^0}{\rho^0}t}}\left(\exp\left\{\frac{-x^2 - y^2 - z^2 - |\mathbf{v^0}|^2t^2 - Ut^2}{4\frac{\mu^0}{\rho^0}t}\right\}\right) \tag{13}$$

where, A is a constant in time.

Now, in case of extremely high order perturbation, S_i (in Eq. (7)) contains higher order density, pressure etc. divided by the zeroth order density and pressure, they could be neglected. The reason can be given as, in the perturbation theory lower order terms dictates the dynamics. So, we can have a homogeneous form of Eq. (7), whose solution can be given as

$$v_i^k = \frac{A_i}{\sqrt{4\pi\frac{\mu^0}{\rho^0}t}}\left(\exp\left\{\frac{-x^2 - y^2 - z^2 - |\mathbf{v^0}|^2t^2 - Ut^2}{4\frac{\mu^0}{\rho^0}t}\right\}\right) \tag{14}$$

Now, if the flow has to be stable for any time, it's obvious that

$$|\mathbf{v^0}|^2 + U > 0$$

$$\implies |\mathbf{v^0}|^2 > -U \tag{15}$$

Also, the boundary conditions for accretion disk pose the constraint on the Green's function as

$$v_i^k = \frac{A}{\sqrt{4\pi \frac{\mu^0}{\rho^0} t}} \left(\exp\left\{ \frac{-r_{\min}^2 - z^2 - |\mathbf{v^0}|^2 t^2 - U^i t^2}{4\frac{\mu^0}{\rho^0} t} \right\} \right) = 0 \tag{16}$$

at the outer radius $r_{\max}$
and

$$v_i^k = \frac{A}{\sqrt{4\pi \frac{\mu^0}{\rho^0} t}} \left(\exp\left\{ \frac{-r_{\max}^2 - z^2 - |\mathbf{v^0}|^2 t^2 - U^i t^2}{4\frac{\mu^0}{\rho^0} t} \right\} \right) = 0 \tag{17}$$

at the inner radius $r_{\min}$.

4 Results

We got a solution for the kth order velocity perturbation for a turbulent accretion disk, Eq. (14). And from that solution, we can conclude that if Eq. (10) is made satisfied, the condition in Eq. (15) implies a stable configuration of the disk. If the value of the constant U is positive, then we can see that the flow stays stable always, but if the value of U gets negative, then the stability is depended on whether $|\mathbf{v^0}|^2 > |U|$ or not. If for a flow the constant U becomes zero, then also the solution stays stable.

Our study is mainly based on the assumption of Eq. (10), which we took to simplify the calculations. Though physical justification for this simplification is still under study, this simple approximation made it clear that the term $\partial_j(v_J^k v_i^0)$ really governs the stability for an accretion flow. If we can make it zero then no matter what the flow stays stable for the higher order perturbations. From Eqs. (16) and (17) we can get the instabilities which arise from the boundaries.

5 Discussion

The Green's function solution is performed for the velocity perturbation for an incompressible flow in the Cartesian grid which can also be applied to the local coordinate frame in the accretion disk. The boundary conditions ensure that the global stability must also get satisfied. We have got an approximate stability condition which can be stated for any order of perturbations, for the higher order, the source function must become smaller and smaller so that this stability condition must get satisfied for a

stable fluid. This condition can be stated on the primary flow and if this gets satisfied, one can infer that the flow stays stable for all higher order perturbations.

These initial results are calculated by very simplified assumptions, a more realistic stability condition can be obtained by solving the Green's function in a cylindrical polar coordinate system, along with more appropriate boundary conditions.

References

1. Abramowicz, M.A., Chen, X., Kato, S., Lasota, J.-P., Regev, O.: Thermal equilibria of accretion disks. ApJ **438**, L37 (1995)
2. Blumenthal, G.R., Lin, D.N.C., Yang, L.T.: On the overstability of axisymmetric oscillations in thin accretion disks. ApJ **287**, 774–784 (1984)
3. Chen, X.: Hot accretion discs with advection. Mon. Notices R. Astron. Soc. **275**(3), 641–648, 08 (1995)
4. Chen, X., Taam, R.E.: Variability of accretion disks surrounding black holes: the role of inertial-acoustic mode instabilities. ApJ **441**, 354 (1995)
5. Cowling, T.G.: The non-radial oscillations of polytropic stars. Mon. Notices R. Astron. Soc. **101**(8), 367–375, 12 (1941)
6. Giri, K.: Numerical Simulation of Viscous Shocked Accretion Flows Around Black Holes (2015)
7. Kato, S.: Pulsational instability of accretion disks to axially symmetric oscillations. Mon. Notices R. Astron. Soc. **185**(3), 629–642, 12 (1978)
8. Kato, S., Abramowicz, M.A., Chen, X.: Thermal instability of advection-dominated disks against local perturbations. PASJ **48**, 67–75 (1996)
9. Kato, S., Honma, F., Matsumoto, R.: Pulsational instability of transonic regions of accretion disks with conventional alpha-viscosity. PASJ **40**(6), 709–727 (1988)
10. Kato, S., Yamasaki, T., Abramowicz, M.A., Chen, X.: Thermal instability of advection-dominated disks against revised local perturbations. PASJ **49**, 221–225 (1997)
11. Kusunose, M., Takahara, F.: Two-temperature accretion disks in pair equilibrium : effects of unsaturated Comptonization of soft photons. PASJ **41**, 263–270 (1989)
12. Lightman, A.P., Eardley, D.M.: Black holes in binary systems: instability of disk accretion. ApJ **187**, L1 (1974)
13. Luo, C., Liang, E.P.: Stability and oscillations of thermal accretion discs around black holes. MNRAS **266**, 386–398 (1994)
14. Manickam, S.G.: Stability of accretion disc around a Black Hole: effects of Bremsstrahlung and Synchrotron Cooling (2004). http://arxiv.org/abs/astro-ph/0410745
15. Misra, R., Melia, F.: The crucial effects of advection on the structure of hot accretion disks. ApJ **465**, 869 (1996)
16. Mukhopadhyay, B.: Stability of accretion disks around rotating black holes: a pseudo–general-relativistic fluid dynamical study. Astrophys. J. **586**(2), 1268–1279 (2003)
17. Mukhopadhyay, B., Chakrabarti, S.K.: Stability of accretion disks in presence of nucleosynthesis. Astrophys. J. **555**(2), 816–821 (2001)
18. Nakamura, K.E., Matsumoto, R., Kusunose, M., Kato, S.: Global structures of advection-dominated two-temperature accretion disks. PASJ **48**, 761–769 (1996)
19. Narayan, R., Yi, I.: Advection-dominated accretion: a self-similar solution. ApJ **428**, L13 (1994)
20. Narayan, R., Yi, I.: Advection-dominated accretion: self-similarity and bipolar outflows. ApJ **444**, 231 (1995)
21. Narayan, R., Yi, I.: Advection-dominated Accretion: Underfed Black Holes and Neutron stars. ApJ **452**, 710 (1995)

22. Piran, T.: The role of viscosity and cooling mechanisms in the stability of accretion disks. ApJ **221**, 652–660 (1978)
23. Pringle, J.E.: Thermal instabilities in accretion discs. Mon. Notices R. Astron. Soc. **177**(1), 65–71, 10 (1976)
24. Shakura, N.I., Sunyaev, R.A.: A theory of the instability of disk accretion on to black holes and the variability of binary X-ray sources, galactic nuclei and quasars. MNRAS **175**, 613–632 (1976)
25. Shapiro, S.L., Lightman, A.P., Eardley, D.M.: A two-temperature accretion disk model for Cygnus X-1: structure and spectrum. ApJ **204**, 187–199 (1976)
26. Wandel, A., Liang, E.P.: Hybrid Accretion Disks in Active Galactic Nuclei. I. Struct.Spectra. ApJ **380**, 84 (1991)
27. White, T.R., Lightman, A.P.: Hot accretion disks with electron-positron pairs. ApJ **340**, 1024 (1989)
28. Wu, X.-B., Li, Q.-B.: the local stability of accretion disks with advection. ApJ **469**, 776 (1996)

Nanoelectronics

Nanosensor and Actuator Technologies for Wearable Mobile Patient Monitoring Systems: A Review

Gaurav Paliwal and Aaquil Bunglowala

Abstract Currently India's population is increasing at the rate of 1.2% and to provide good healthcare services to these people healthcare sector needs a transformation. Information and Communication Technology (ICT) along with nanotechnology revolution has opened up whole new opportunities for developing countries like India to improve the healthcare for the betterment of 1.34 billion lives. With the use of ICT and nano-electronics, we can provide our patients better and specialized healthcare services at a reduced cost. ICT-based healthcare initiatives like eHealth and mHealth includes healthcare centers, mobile telemedicine, electronic patient records, remote patient monitoring, mobile patient monitoring, health surveys, awareness raising, and decision support systems that can play a crucial role towards the accomplishment of development goals to enhance Healthcare services in India. Nanosensors and actuators will play a critical role in the success of these technologies. In this paper, we are going to present a comprehensive review of existing and future wearable healthcare sensor and actuator technologies along with their merits and demerits.

Keywords Wearable mobile patient monitoring · Nanosensors · Actuators · mHealth technology

Supported by SVKM's NMIMS, Indore.

G. Paliwal (✉)
Assistant Professor Department of Computer Engineering, R.C. Patel Institute of Technology, Shirpur, India
e-mail: gvpaliwal@gmail.com

A. Bunglowala
Professor School of Technology Management and Engineering, SVKM's NMIMS Deemed to be University, Mumbai, India
e-mail: aaquil.bunglowala@nmims.edu

S. Mukherjee et al. (eds.), *Computational Mathematics, Nanoelectronics, and Astrophysics*,
Springer Proceedings in Mathematics & Statistics 342,
https://doi.org/10.1007/978-981-15-9708-4_7

1 Introduction

The outburst in electronic technology and high speed wireless networks has opened a whole new door to improve the chronic healthcare. The wearable nanosensor technology has grown tremendously in the past decade. The mHealth and eHealth technologies has the power and proficiency to improve the patient monitoring and take the monitoring field to an entirely new level. The technology will not only provide assistance in the monitoring of chronic diseases, but it can also be used in many other fields like monitoring of on-field athletes and soldiers, disaster aid networks, and natural calamity conditions.

A Wearable Body Area Network (WBAN) comprises a large number and broad variety of wireless sensors and actuator nodes situated inside and on the human body. The all-new wearable sensors can also be deployed around the human body in daily wearables like jackets and shoes. The data acquired by the WBAN is further processed by the medical servers and used to draw some hypothetical deductions about the patient's condition. The healthcare servers continuously monitor the vitals of a particular person. These servers are capable of taking suitable countermeasures in case of any medical alert situation or trauma. The WBAN should also be capable of storing and communicating the data to other devices such as central node or the MBU. Adoption of certain standards from IEEE, ISO, and HL7 will be very beneficial in maintaining the compatibility between different devices and data.

The availability of high speed wireless networks [4] along with a decrease in size and cost of electronic devices has endorsed the growth of WBAN. A broad assemblage of sensors and actuators are present for selection according to the user comfort and safety. Using WBAN, the patients can actually experience better physical mobility and will no longer be forced to stay in hospitals for regular monitoring of chronic diseases. The system provides great possibilities and prospects for the development of mobile healthcare systems. The system presents good opportunities for mHealth, but along with opportunities, some challenges like security, accuracy, and safety should also need to be taken care of.

The rest of the paper is presented in the following sections. Sections 2 and 3 presents the system design of wearable body area networks that includes various sensors along with their data and energy requirements. Sections 4 and 5 focuses in the data fusion, data processing, and contextual information generation, respectively. In the subsequent sections, basic issues like usability, security, and privacy are covered and at the end conclusion and future directions are presented.

2 Wearable Body Area Network Design

The wearable body area network forms a physiological layer which will be deployed over the person's body for continuous biosignal processing. The main components of a WBAN typically consist of different biological sensors. The sensors or actuators

Table 1 Biosensors data generation and transfer rates

Biosensors	Sampling Frequency (Hz)	Sensitivity	Bits per sample	Data rate (bps)
Electroencephalography (EEG)	256 (x24 Ch.)	∼1 s	16	98,304
Electrocardiography (ECG)	200 (x3 Ch.)	∼1 s	12–16	7,200–9,600
Motion detection	50 (x9 Ch.)	NO	16	7,200
Glucose monitoring	40 200	NO	16	640–3,200
Blood oxygen (SpO_2)	60 (x2 Ch.)	NO	16	1,920
Blood pressure	120	NO	16	1,920
Cardiac output	40	NO	16	640
Respiration	50	NO	6	300
Body temperature	0.2	NO	12	2.4
Contextual and Activity Data [5, 22, 24]	–	–	–	20000

that are most frequently included in the WBAN are blood pressure monitor, respiration monitor, SpO_2, blood glucose, motion sensors, and ECG. Since these sensors are mounted on the human body it should follow the rules and regulations prescribed by ISO and IEEE along with that, it should be power efficient, easily wearable, easy to use, and should provide hassle-free connectivity [12]. Table 1 shows typical sensors included in the BAN for monitoring of physiological and contextual parameters with their sensitivity and data generation rates [5, 22]. Some of the advanced sensors like EEG and EMG can also be included in the system, but the data generated by these sensors is very hard to interpret and needs specialized systems to process.

2.1 Types of Devices

Wireless Sensor Node A device that acquires data on physical stimuli, processes the data if required and reports the information wirelessly. It contains several components: sensor hardware, microcontroller, a power unit, memory, and a transmitter [1].

Wireless Actuator Node The behavior of the actuator node changes in accordance with the data received through the node or from user interaction. The components of an actuator are similar to the sensors actuator hardware (e.g. hardware for medication monitoring or a pool to hold the medicine), a microcontroller, a power unit, memory, and a transceiver or receiver. These nodes are capable to perform certain actions when triggered by the control unit.

Wireless Central Node Central node is responsible to compile the entire sensor and actuator data. It processes the acquired data for information retrieval at the initial level. It informs the patient, doctor or caregiver via an external gateway or an actuator

about any irregularity in the biosignal. The components of the central node consists of a power unit, a microprocessor with huge processing power as compare to the sensors or actuators, a memory, and a transceiver.

These sensors are available with mainly two options to choose from invasive (sensors that are placed inside the skin) or noninvasive (sensors that are deployed on the body) sensors. Invasive sensors provide more accurate data as compared to noninvasive sensors but to achieve easy usability noninvasive sensors are preferred over invasive sensors. The WBAN based on noninvasive sensors can be easily used in the absence of any medical supervision. A trained person can easily connect and deploy these sensors on to the patient's body and since they are noninvasive in nature it will be safer as compared to the invasive sensors. These sensors will connect to a central micro control unit to provide access and control. The connectivity between the central node and the sensors can be provided by the Zigbee protocol [24]. Sensors used in the systems should follow the ISO/IEEE standard 11073-20601 [20] and HL7 standard [17] for biosignal acquisition and biosignal transfer. Data generated by these standards can be interpreted throughout the world on different platforms.

The wearable healthcare monitoring solutions are much beneficial as compared to the traditional healthcare systems in terms of operational cost, scalability, and restricted access to remote monitoring. Along with numerous advantages, the wearable sensor has some drawbacks like it is very uncomfortable to continuously wear multiple sensors for physiological data collection. If we use simple devices like bracelets or smart watches, the data collected is not of that accuracy. Besides all these, the user may have negative psychological effects of continuously wearing monitoring devices. The user might feel that he/she has some health problems which further causes stress and negative emotions. More seriously, the negative psychological effects may result in mental illness, especially when the patient feels lonely or depressed [6]. Hence, the BAN should be designed in such an innovative way that it will provide more comfortable, sustainable, and energy efficient structure to acquire the physiological data.

2.2 Innovative Sensor Designs Using Nanotechnology

To acquire complicated medical-level data, multifaceted devices with high accuracy are needed. As the complexity of these devices increases the system complexity, inconvenience also increases. So in order to be truly convenient for any wearable sensor network, it must be very comfortable and should not affect or disturb the normal life of that person. Here, we have mentioned some of the innovative wearable's that can really make the wearable network imperceptible to the user, and hence can improve the user experience to a great extent if incorporated into the BAN.

Smart Clothing With continuous improvement in wearable technology smart clothing proposes multiple connected devices to offer more meaningful information. These wearables are better than the traditional monitoring systems in terms of accuracy,

usability, comfort, washability, and real time monitoring. Smart clothing will improve the quality of experience (QoE) and quality of service (QoS) in the next generation because while wearing these wearables the user will not experience any different feeling than that of a jacket or pullover [6, 8].

Body Fluid Biomarkers and Sensors Body fluid sensors are one of the most established tools in traditional diagnostics. Blood and urine are the most frequently used body fluids for getting the different physiological parameters. Other body fluids that are readily available and do not require any invasive sampling are tears [9], sweat [27], and saliva [25]. These body fluids contain nearly 1500 types of proteins and some of them are present in sufficiently high concentration and can be used for medical monitoring purpose [32].

Implantable and edible biosensors In implantable and edible biosensors, all the components of the sensor including the circuitry and transmitters must be of the biocompatible or biodegradable material that does not cause inflammation or any adverse reaction into the host [28]. Also, to function over a long period, these biosensors need to have renewable and safe energy sources. These types of devices go beneath the skin via bloodstream or ingestion into the digestive tract to acquire the physiological biosignals. In this respect, MIT scientists have recently tested a device to monitor the heart rate and respiratory rate using sound waves in the gastrointestinal tract [31].

Intelligent tattoos, patches, and bio-stamps These biosensors are attached to the epidermis of the human body and are capable to sense the physiognomies on or under the skin physically, electrochemically or chemically. Electrochemical sensors, screen printing technologies, and flexible electrodes can provide high comfort to the patient without compromising any of the functionalities. The idea of intelligent patches, tattoos, innovative fabrication techniques, and electrodes has fledged in recent years, but still mostly limited to laboratories [10, 36].

Figure 1 shows some of these innovative wearables, implantable or edible physiological sensors.

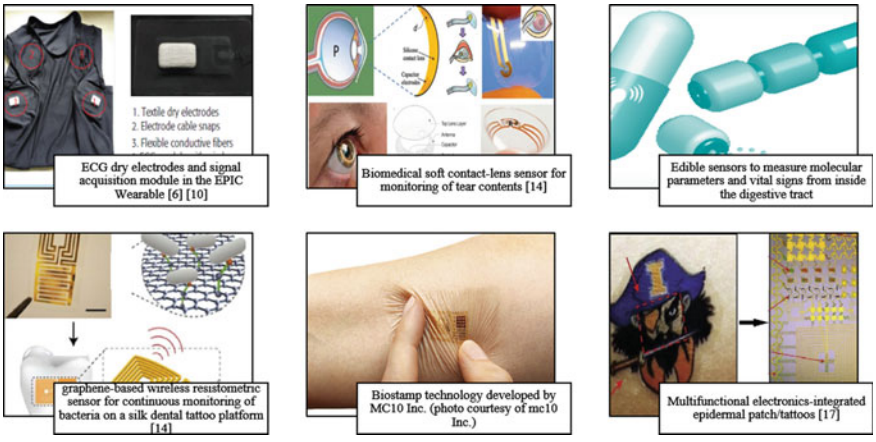

Fig. 1 Innovative wearables, implantable or edible physiological sensors

3 Energy or Power Requirements

The energy consumption for WBAN can be divided into three domains: biosignal sensing, data communication, and data processing [1]. The transfer of data is the most power consuming aspect among the three. The availability of power in the sensor or actuator nodes is often limited. In most cases, the energy requirement of sensing devices is fulfilled by batteries. The storage capacity of a battery mostly depends on both: dimension and weight. The size of the battery cannot be increased after a certain limit; as a consequence, the power consumption of the devices has to be reduced. In some applications, a WBAN's sensor or actuator node must operate while supporting a battery lifespan of months or even years without intervention. For example, a glucose monitor would need a lifespan lasting more than 5 years. Particularly for invasive embedded sensors and actuators, the lifespan is a critical constraint.

The necessity for battery recharging or replacement persuades inconvenience and cost penalty which is undesirable not only for invasive devices, but also for noninvasive ones. The life expectancy of a node for a specified battery capacity can be improved by scavenging energy throughout the system operation. If the scavenged energy is higher than the typical consumed energy, such systems could run everlastingly. However, energy scavenging can deliver only a small amount of energy [16, 26]. But a combination of reduced power consumption and energy scavenging is the optimal way out for realizing autonomous WBANs. For a Wireless Body Area Network, energy scavenging from on-body sources like body vibration and body heat appears to be very well suited. In the previous, a thermoelectric generator (TEG) is used to convert the temperature difference in-between the surroundings and the human body into electrical energy [15]. During communication, the heat produced by the devices is absorbed by the nearby tissue which increases the body temperature of the patient. To limit this temperature rise and to save energy, the power consumption should be regulated to a minimum. The quantity of power absorbed by the tissue is stated by the specific absorption rate (SAR). Since the device may be in close proximity to a human body, the localized SAR might be quite high. The localized SAR into the body tissues must be minimized and needs to conform to international and national SAR regulations. The guideline for transmitting close to the human body is analogous to the one for smartphones, with severe transmission power requirements [18, 19].

4 Biosignal Data Fusion and Processing

Characteristically, we consider the BAN as a single device that monitors the patient's physiological information, but in reality, it is a multi-device constellation of potentially heterogeneous sensors generating a vast amount of physiological data that cannot be interpreted independently. Moreover, WBAN's relying on a single node or

Table 2 Fusion parameters, applications and techniques at the different fusion levels [14]

Fusion level	Model	Parameter	Use	Technique
Data-level	Competitive	Number of sources, sampling rate, sensing synchronization, sensing periodicity, data buffering, aggregation strategy, sensor node platform	Spectral data mining, data adaptation, estimation of parameters, robustness and calibration, source recovery	Digital signal processing, coordinate transforms, Kalman filtering, weighted averaging, independent component analysis
Feature-level	Competitive, complementary, cooperative	Feature domain, feature extraction method, feature normalization, overlapping, processing model	Classification	Pattern recognition, clustering, neural networks
Decision-level	Competitive, complementary, cooperative	Decision fusion method, source diversity, classification periodicity, processing model	Decisional action	Expert systems, artificial intelligence

considering node data separately will have many limitations [11] like sensory deprivation, limited spatial coverage, uncertainty, and imprecision [23]. Alternatively, multiple sensor fusion data can provide many advantages such as improved signal to noise ratio, reduced ambiguity and uncertainty, increased confidence, enhanced robustness and reliability, robustness against interference, improved resolution, precision and hypothesis discrimination, integration of independent features, and prior knowledge [3, 30]. Therefore, it becomes a trivial task to create an effective fusion of data generated from these sensors to get the desirable perceptions.

The sensor fusion can be achieved through three different models that are competitive, complementary, and cooperative [34]. In competitive fusion, multiple equivalent sources of information are used to obtain the self-calibration and redundancy. It is very uncommon in practice even when we use multiple common sources of information because the sources are placed on different locations of the body so it provides complementary information instead of competitive information. Complementary fusion is used to improve the system's accuracy and reliability. In complementary fusion, each sensor captures a different aspect of the same phenomenon and the acquired data is compositely analyzed for high level information. And when it is not possible to get information from a signal source independently, cooperative fusion is used. In cooperative fusion, multiple signals are analyzed simultaneously to obtain the information. It is the most frequently used sensor fusion model.

In the same manner, the data abstraction or fusion for processing can be achieved on three different levels such as data-level fusion, feature-level fusion, and decision-level fusion. If the same physiological phenomenon is measured using multiple homogeneous sensors, the data-level fusion can be used because the sensor data can be directly fused. On the other hand, if data is generated from different heterogeneous sources, it cannot be combined at data-level, and feature-level or decision-level fusion techniques must be adopted. Table 2 shows different fusion levels and particular models that can be adopted with that level in conjunction with parameters, applications, and techniques.

After the fusion process, data must be further processed to extract the required information. The processing can be done using three different approaches given as centralized, distributed, and hybrid. The centralized approach processes the data in a fusion center, whereas in the distributed approach, each sensor performs independent processing of its own data and transfers the result to the fusion node for further processing. In hybrid data fusion, collection and pre-processing are performed with a distributed approach while a central node is responsible for performing decision-level computations.

5 WBAN Data Fusion for Contextual Information

The precision of any monitoring system depends on how well the acquired physiological data is correlated with the patient's current context. The context awareness for a system is defined as the state of knowledge of external and internal entities that cause the change in the user's condition, thus necessitating a different interpretation of the data in hand [29]. In the case of wearable healthcare, contextual information can be obtained from the vital signs, low level activities [33], environmental variables, occupancy, and object usage in the home environment. Figure 2 shows different parameters that can be used to draw contexts from the acquired data [35].

In addition to these, the data collected by kinematics sensors (accelerometer and gyroscope), GPS (location), gesture recognition units, fall detection units can improve the accuracy of the system to a great extent. The collected contextual data must be processed in close collaboration with the physiological data to generate correct contextual information. The contextual information generated from this analysis can be further used for the automated physiological diagnosis of the patient. For example, the heart rate variability of a cardiac patient can be correlated with contextual information such as a state of exertion, rest/on-move using physical activity recognition to get the perceptions of the patient's health condition. The system will need intensive machine learning-based algorithms and real time distributed sensing to draw such contexts from the obtained data.

The context aware systems provide relevant services and information to the patient where the relevancy of the information is totally dependent on the user's current action. The context awareness of the system can be active or passive in nature. In active context awareness, the system adapts in accordance with the changing contexts,

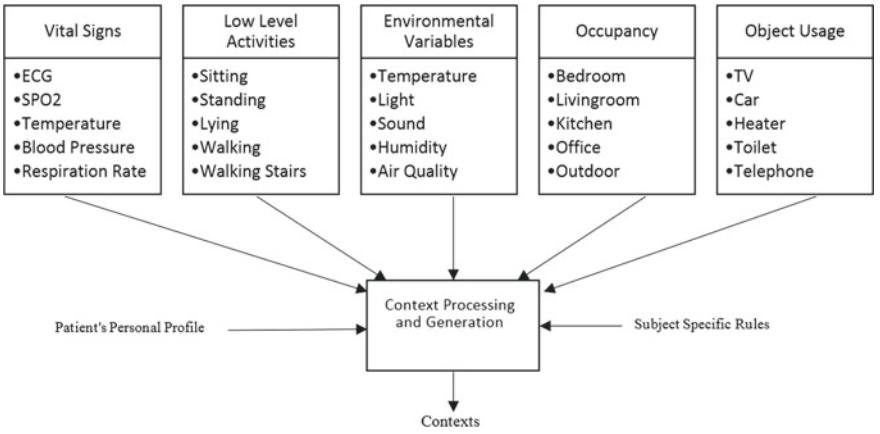

Fig. 2 Information used for generating or identifying the contexts

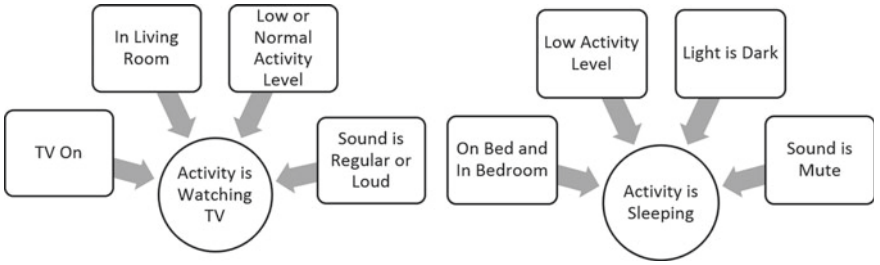

Fig. 3 High level context generation

whereas in the passive context awareness, the system becomes aware of the changes but does not adapt accordingly. In clinical decision-making systems, active awareness is considered better for achieving the anticipated healthcare goals. For the contexts generation from contextual data, a hierarchical structure can be used, i.e., we can first identify the low level activities and then these low level activities are further used to deduce the high level activities. The ambient sensing data like environmental variables, occupancy, and object usage can further improve the accuracy of activity prediction and contexts [5].

For example, we can consider sitting or walking as low level contexts since these are recognized through accelerometer and gyroscope sensor data. These contexts are then further processed to get high level activity interpretation like sleeping or exercising in collaboration with other related contexts. Figure 3 shows some high level context generating rules in WHMS. These interpretation rules should differ in accordance with the individual person or changing contexts.

In contextual information, we can also include the emotional state of a patient because it is a major driving force intended for medical conditions in many chronic diseases. The performance of emotional interface data is directly influenced by the

quality of the collected data. To achieve high accuracy in emotional analysis, we need more and more data. However, it is very difficult to meet the requirements of emotional data with limited resources of wearable devices. To solve the bottleneck created by limited resources and diversified data, we can use hybrid big emotion data analysis [7]. This technique is mainly based on physiology, video, and text data for sentiment or emotion analysis. The physiological data includes voice, pupil, posture, respiration, body temperature, heart rate, blood pressure, and body characterization. On the contrary, video-based analysis mainly focuses on multi-information fusion and visual features, mostly involving the video and image cognition and segmentation. In text-based analysis, we analyze and reason the subjective text with emotional words from social networks and messaging applications. The emotional analysis can offer a prodigious edge in terms of accuracy enhancement.

6 Usability

In most of the cases, a WBAN will be set up in a hospital, healthcare center, by a medical staff or by a trained person [13]. Subsequently, the network must be capable of configuring and sustaining itself automatically, that is self-organization and maintenance must be supported. Every time a node is placed on the body and turned on, it should be capable to connect the network and setup routes without any exterior intervention. The self-organizing and maintaining characteristic also embraces the problem of addressing the nodes. An address can be configured at the setup time by the network itself or at the manufacturing time (the MAC address). Additionally, the network should be rapidly reconfigurable, for adding or removing the services. A backup path should be set up when a route fails.

The devices might be scattered over and inside the whole body. The exact location of a device will be determined by the application, e.g., a temperature sensor could be placed almost anywhere, and however, a heart sensor (ECG) must obviously be placed near the heart. Researchers appear to disagree on the ideal location for certain sensor nodes like motion sensors, because the interpretation of the measured data keeps on changing almost every time [21]. The network should not be considered as a static one. The sensor nodes should have a minor form factor consistent by means of wearable and implanted applications. This will make WBAN unobtrusive and invisible.

7 Security and Privacy

The communication of health information over the Internet to servers and between sensors in a WBAN and is severely private and confidential [2, 13], and must be encrypted to defend the patient's privacy. The medical staff gathering the data needs to be assertive that the data is not tampered with and certainly originates from that

patient's body. Further, it cannot be expected that a normal person or the medical staff is proficient in setting up and managing authorization and authentication processes. Additionally, the network should be accessible when the user is not able to provide the password (e.g., to assurance of accessibility by paramedics or medical staff in trauma situations). Privacy and security protection mechanisms consume a significant amount of the available energy, so, consequently, they should be energy efficient and lightweight in nature.

8 Conclusion and Future Direction

WBAN is a very promising technology that can transform the next generation healthcare. WBAN carries out a new set of challenges in terms of energy efficiency, scalability, QoS, privacy, and security, which are highlighted in the paper. Along with these technical issues, there exist several non-technical issues like affordability, legal and ethical concerns, issues like user comfort, friendliness, and acceptance, which will also play a crucial role in the success of WBAN technology. WBAN technology requires extensive acceptance of key stakeholders in the healthcare domain, which includes the patients, caregivers, medical-electronics industry, policy makers, and patient advocacy groups for it to develop as a true pervasive technology. Although there are various advances in these areas, there are several challenges that still require to be addressed, particularly on energy efficient communication protocols, high bandwidth, and interoperability between WBAN and various wireless technologies.

References

1. Akyildiz, I.F., Su, W., Sankarasubramaniam, Y., Cayirci, E.: A survey on sensor networks. IEEE Commun. Mag. **40**(8), 102–114 (2002)
2. Bhargava, A., Zoltowski, M.: Sensors and wireless communication for medical care. In: Proceedings 14th International Workshop on Database and Expert Systems Applications, pp. 956–960 (2003)
3. Bosse, E., Roy, J., Grenier, D.: Data fusion concepts applied to a suite of dissimilar sensors. In: Canadian Conference on Electrical and Computer Engineering, 1996, vol. 2, pp. 692–695. IEEE (1996)
4. Bults, R., Wac, K., Van Halteren, A., Konstantas, D., Jones, V., Widya, I.: Body area networks for ambulant patient monitoring over next generation public wireless networks. In: 3rd IST Mobile and Wireless Communications Summit, pp. 27–30 (2004)
5. Cavallari, R., Martelli, F., Rosini, R., Buratti, C., Verdone, R.: A survey on wireless body area networks: technologies and design challenges. IEEE Commun. Surv. Tutorials **16**(3), 1635–1657 (2014)
6. Chen, M., Ma, Y., Li, Y., Wu, D., Zhang, Y., Youn, C.H.: Wearable 2.0: Enabling human-cloud integration in next generation healthcare systems. IEEE Commun. Mag. **55**(1), 54–61 (2017)
7. Chen, M., Zhang, Y., Li, Y., Hassan, M.M., Alamri, A.: AIWAC: Affective interaction through wearable computing and cloud technology. IEEE Wirel. Commun. **22**(1), 20–27 (2015)

8. Chen, M., Ma, Y., Song, J., Lai, C.F., Hu, B.: Smart clothing: connecting human with clouds and big data for sustainable health monitoring. Mobile Netw. Appl. **21**(5), 825–845 (2016)
9. Chu, M., Shirai, T., Takahashi, D., Arakawa, T., Kudo, H., Sano, K., Mochizuki, M.: Biomedical soft contact-lens sensor for in situ ocular biomonitoring of tear contents. Biomed. Micro Devices **13**(4), 603–611 (2011)
10. Coyle, S., Curto, V.F., Benito-Lopez, F., Florea, L., Diamond, D.: Wearable bio and chemical sensors. In: Wearable Sensors, pp. 65–83 (2015)
11. Elmenreich, W.: An Introduction to Sensor Fusion. Vienna University of Technology, Austria (2002)
12. Espina, J., Falck, T., Panousopoulou, A., Schmitt, L., Mlhens, O., Yang, G.Z.: Network topologies, communication protocols, and standards. In: Body sensor networks, pp. 189–236. Springer, London (2014)
13. Gauravpaliwal and Pankajkasar. Article: Wireless Body Area Network for Ubiquitous mhealth Mobile Patient Monitoring Systems: Architecture, Opportunities and Challenges. IJCA Proceedings on National Conference on Emerging Trends in Computer Technology NCETCT(3), 1–6 (2014)
14. Gravina, R., Alinia, P., Ghasemzadeh, H., Fortino, G.: Multi-sensor fusion in body sensor networks: State-of-the-art and research challenges. Inf. Fusion **35**, 68–80 (2017)
15. Gyselinckx, B., Penders, J., Vullers, R.: Potential and challenges of body area networks for cardiac monitoring, issue 6, supplement 1, , isce 32nd annual conference, november-december 2007, pages s165-s168. J. Electrocardiol. **40**(6), S165–S168. iSCE 32nd Annual Conference (2006)
16. Gyselinckx, B., Van Hoof, C., Ryckaert, J., Yazicioglu, R.F., Fiorini, P., Leonov, V.: Human++: autonomous wireless sensors for body area networks. In: Custom Integrated Circuits Conference, 2005. Proceedings of the IEEE 2005, pp. 13–19 (2005)
17. Health Level Seven International, Clinical and Administrative Domains, HL7 Messaging Standard Version 2.6
18. IEEE standard for safety levels with respect to human exposure to radio frequency electromagnetic fields, 3 khz to 300 ghz (1999)
19. International Commission on Non-ionizing Radiation Protection (ICNIRP), Guidelines for limiting exposure to time-varying electric, magnetic, and electromagnetic fields (up to 300 ghz). Health Phys. **74**(4), 494–522 (1998)
20. ISO/IEEE 11073-20601:2016, Health informatics—Personal health device communication - Part 20601: Application profile—Optimized exchange protocol, IT applications in health care technology, 2016-06, 2
21. Jovanov, E., Milenkovic, A., Otto, C., de Groen, P.C.: A wireless body area network of intelligent motion sensors for computer assisted physical rehabilitation. J. NeuroEng. Rehabil. **2**(1), 16–23 (2005)
22. Latr, B., Braem, B., Moerman, I., Blondia, C., Demeester, P.: A survey on wireless body area networks. Wirel. Netw. **17**(1), 1–18 (2011)
23. Murphy, R.R.: Biological and cognitive foundations of intelligent sensor fusion. IEEE Trans. Syst. Man Cybern.-Part A: Syst. Humans **26**(1), 42–51 (1996)
24. Negra, R., Jemili, I., Belghith, A.: Wireless body area networks: applications and technologies. Procedia Comput. Sci. **83**, 1274–1281 (2016)
25. Papacosta, E., Nassis, G.P.: Saliva as a tool for monitoring steroid, peptide and immune markers in sport and exercise science. J. Sci. Med. Sport **14**(5), 424–434 (2011)
26. Paradiso, J.A., Starner, T.: Energy scavenging for mobile and wireless electronics. IEEE Pervasive Comput. **04**(1), 18–27 (2005)
27. Schazmann, B., Morris, D., Slater, C., Beirne, S., Fay, C., Reuveny, R., Diamond, D.: A wearable electrochemical sensor for the real-time measurement of sweat sodium concentration. Anal. Methods **2**(4), 342–348 (2010)
28. Steinmetz, L. M., Jones, A.: Sensing a Revolution (2016)
29. Talaei-Khoei, A., Ray, P., Parameshwaran, N., Lewis, L.: A framework for awareness maintenance. J. Netw. Comput. Appl. **35**(1), 199–210 (2012)

30. Thomopoulos, S.C.: Sensor integration and data fusion. J. Field Robot. **7**(3), 337–372 (1990)
31. Traverso, G., Ciccarelli, G., Schwartz, S., Hughes, T., Boettcher, T., Barman, R., Swiston, A.: Physiologic status monitoring via the gastrointestinal tract. PloS one **10**(11), e0141666 (2015)
32. Tricoli, A., Nasiri, N., De, S.: Wearable and miniaturized sensor technologies for personalized and preventive medicine. Adv. Funct. Mater. **27**(15) (2017)
33. Viswanathan, H., Chen, B., Pompili, D.: Research challenges in computation, communication, and context awareness for ubiquitous healthcare. IEEE Commun. Mag. **50**(5) (2012)
34. Yang, G. Z., Andreu-Perez, J., Hu, X., Thiemjarus, S.: Multi-sensor fusion. In: Body Sensor Networks, pp. 301–354. Springer London (2014)
35. Yuan, B.: Context-Aware Real-time Assistant Architecture for Pervasive Healthcare (2014)
36. Zhu, X., Liu, W., Shuang, S., Nair, M., Li, C.Z.: Intelligent tattoos, patches, and other wearable biosensors. In: Medical Biosensors for Point of Care (POC) Applications, pp. 133–150 (2017)

Performance Analysis of MEMS Capacitive Pressure Sensor with Different Dielectrics

Sachin Kumar, Rashmi Ranjan Kumar, and Saurabh Kumar Pandey

Abstract In this manuscript, two Micro-Electro-Mechanical System (MEMS) capacitive pressure sensors with different dielectrics are designed and simulated with device simulation software. This paper describes the performance analysis of a capacitive pressure sensor working on the electromechanics interface. The sensors modeled have a square diaphragm membrane. Here we have used silicon carbide (SiC) as a diaphragm material. ZnO radical nanoclusters (R-ZnO) and $BaTiO_3$ (BT) nanoparticles are embedded into polyvinylidene fluoride (PVDF) (i.e., R-ZnO/BT/PVDF) and Ag@TiO_2 fillers into polytetrafluoroethylene (PTFE) (i.e., Ag@TiO_2/PTFE) as dielectric material. We have investigated the different performance parameters for the MEMS capacitive pressure sensor such as the total displacement, capacitance, sensitivity, etc., for the optimal design of pressure sensors. These pressure sensors will be used in a harsh environment involving high-temperature applications.

Keywords SiC · R-ZnO · BT · PVDF · Ag@TiO2 · PTFE · Sensitivity

1 Introduction

In this modern world, the demand for pressure sensors application in the latest gadgets such as automobile, bio-medical, industrial, and commercial applications has extremely increased [1–5]. Due to the latest research in the field of microscale and nanoscale fabrication technology, MEMS pressure sensors are being fabricated for the pressure range from ultra-low pressure to very high pressure [6]. This helps to reduce the product cost per unit. The importance of the MEMS pressure sensor

S. Kumar (✉)
Department of Electronics and Communications Engineering, National Institute of Technology Hamirpur, Hamirpur 177005, Himachal Pradesh, India
e-mail: sachin222sk@gmail.com

R. R. Kumar · S. K. Pandey
Sensors & Optoelectronics Research Group (SORG), Discipline of Electrical Engineering, Indian Institute of Technology Patna, Patna 801106, Bihar, India
e-mail: saurabh@iitp.ac.in

S. Mukherjee et al. (eds.), *Computational Mathematics, Nanoelectronics, and Astrophysics*,
Springer Proceedings in Mathematics & Statistics 342,
https://doi.org/10.1007/978-981-15-9708-4_8

is gaining interest due to lightweight, high reliability, high sensitivity, integrated to IC fabrication process, low power consumption, and small interface features [7–9]. Optical, capacitive, piezoresistive, resonance, acoustic transduction standard is utilized as a part of the ongoing work in the advancement of MEMS pressure sensor designing and manufacturing [10]. Among capacitive pressure, sensor rules were generally adopted in different works. As we know that most of the MEMS capacitive pressure sensors are based on silicon material which is not suited for the extremely high-temperature environment due to the limited operating of mechanical and electrical properties that can be degraded below the temperature of 300 °C [11]. So, we use silicon carbide material to improve the performance of a MEMS capacitive pressure sensor, which shows the emphasis on mechanical and thermal stability for its fabrication and makes it possible to operate in high-temperature applications.

The capacitive pressure sensor works on the principle of change in capacitance with the applied voltage or pressure [12]. These sensors have a sensing element of the constant area and give a response when pressure is applied to this area (e.g., gas pressure, fluid pressure, etc.). When we apply a force, the internal diaphragm of the pressure sensor gets deflected. The deflection of the diaphragm is quantified and converted into an electrical replication. This allows the pressure to be monitored by microprocessor, microcontroller, programmable logic controller (PLC), and computers along with the similar electrical instrument. So, the area of MEMS capacitive pressure sensor application is expanding, hence it is necessary to audit the way of innovative improvement and further imminent of MEMS pressure sensor.

The simulation and output study results of the designed pressure sensor are analysis using COMSOL 5.3 Multiphysics simulation software. COMSOL is a Multiphysics simulation software which provides conventional physics-based user interface IDE and unified workflow for electrical, mechanical, fluid, and chemical applications. The performance parameters used in this paper are the following.

Total Displacement—Total displacement is defined as the displacement of diaphragm membrane with a change in the applied pressure.

Total Capacitance—Total capacitance is defined as the capacitance of the model with change in the applied pressure.

Sensitivity—In this paper we analyze pressure sensitivity and temperature sensitivity of the model. Pressure sensitivity is defined as a change in capacitance with respect to change in the applied pressure [13], and temperature sensitivity is defined as a change in capacitance with respect to change in the operating temperature.

In this paper, we specially focused on the performance comparison of the MEMS capacitive pressure sensor using two different polymer composite materials like R-ZnO/BT/PVDF and Ag@TiO_2/PTFE, respectively, as a dielectric material. Silicon carbide has been used as diaphragm material. This paper is divided mainly into four sections. The second section describes the device structure and property of material used and the third section explains the different measurements and analyses carried out in the work. The fourth section presents the final conclusion.

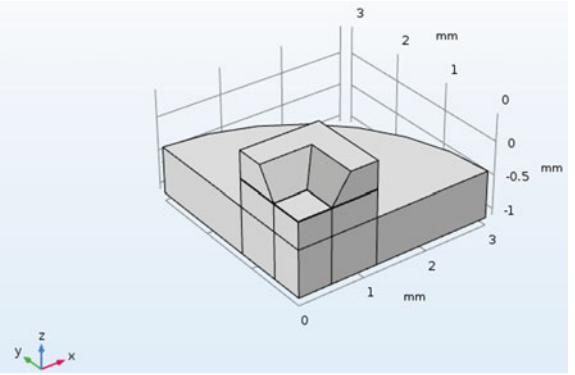

Fig. 1 3D COMSOL model of MEMS capacitive pressure sensor

2 Research Methodology

2.1 Device Structure

The 3D device structure of pressure sensor is shown in Fig. 1. Since the geometry of the model is symmetric so we have used only one by fourth of the geometry and symmetry boundary condition. The pressure sensor is part of a silicon carbide die that has been bonded to a metal plate at 70 °C. The design model is operating at room temperature.

It consists of silicon carbide, steel AISI 4340, and dielectric material. The polymer-matrix composition material that shows high-dielectric permittivity constant has received increasing interest recently for varied potential application in high charge storage electrical device [14]. Here, we have considered R-ZnO/BT/PVDF and Ag@TiO_2/PTFE as two different dielectric materials.

Property of SiC—SiC is a semiconductor material containing silicon (Si) and carbon (C). It is originally made by electrochemical reaction of silicon sand and carbon at extreme temperature. SiC consists of a tetrahedral of carbon and silicon atom with robust bounds within the space lattice. This produces very strong material. SiC isn't attacked by any acids or alkalis or liquefied salt up to 800 °C. It exhibits high thermal conductivity (20.7 W/m.K), low thermal expansion, and high strength, which make this material to have extraordinary thermal shock characteristics. It also has a low density and high elastic module. In air, SiC forms a protective SiO_2 coating at 1200 °C. Its melting point is about 1750 K. Properties of SiC that we have used for modeling are summarized in Table 1.

Ag@TiO_2&PTFE—Composition of core-shell Ag@TiO_2 nanoparticles and PTFE is used to get high-dielectric composites. This composite exhibits higher dielectric permittivity constant than of pure form of PTFE. Its dielectric loss for the composition containing 70% vol. of Ag@TiO_2 as a filler, at 10 MHz is about 0.005. Its dielectric loss is stable and remains small when the frequency reaches 1 MHz [15].

Table 1 Property of silicon carbide

Property	Value with unit
Young's modulus	137 GPa
Poisson's ratio	0.37
Density	3217 kg/M^3
Relative permittivity	9.66
Coefficient of thermal expansion	4.5e−6 K^{-1}

Table 2 Relative permittivity of used dielectric material

Dielectric	Value
Ag@TiO_2/PTFE	240
R-ZnO/BT/PVDF	175

R-ZnO/BT/PVDF—It is three-phase-percolative composition with ZnO radical nanocluster (R-ZnO) and $BaTiO_3$ (BT) nanoparticles implanted into polyvinylidene fluoride (PVDF). This composition exhibits small dielectric loss, large dielectric permittivity constant, and good thermal stability. These properties make the three-phase-percolative composition especially attractive for practical applications. The dielectric loss is about 0.45 [16] (Table 2).

3 Results and Discussion

The MEMS capacitive pressure sensor has been investigated with applied pressure from the range 0 Pa to 25 kPa. We have used different plots to show the variation of different analyzing performance parameters to identify the optimum one. We have also studied the effect of operating temperature from the range 290–1000 K to investigate the best response for high-temperature applications (Tables 3 and 4).

Capacitance of parallel plate capacitor is given by

$$C = \frac{\varepsilon KA}{d} \tag{1}$$

where ε = Permittivity of the free space.
d = Distance between two plates.
A = Area of the two plates.
K = Dielectric Constant.

From Eq. (1), we have concluded that capacitance is inversely proportional to distance between two plates of capacitor [17]. That means when the distance between the plates decreases it results in increase of capacitance value. Figures 2 and 3 shows the variation average and maximum displacements of the diaphragm membrane as

Table 3 Capacitance comparison for Ag@TiO_2/PTFE and R-ZnO/BT/PVDF dielectric material capacitor

Diaphragm material	Dielectric material	Pressure (Pa)	Capacitance (pF)
Silicon Carbide (SiC)	Ag@TiO_2/PTFE	0	176.8952
		5000	187.39
		10,000	200.8443
		15,000	219.1571
		20,000	247.219
		25,000	317.2877
	R-ZnO/BT/PVDF	0	128.9425
		5000	136.5702
		10,000	146.3304
		15,000	159.5579
		20,000	179.5823
		25,000	222.6961

Table 4 Pressure sensitivity comparison for Ag@TiO_2/PTFE and R-ZnO/BT/PVDF dielectric material capacitor

Diaphragm material	Dielectric material	Pressure (Pa)	Sensitivity (pf/Pa)	Mean sensitivity
Silicon Carbide (SiC)	Ag@TiO_2/PTFE	5000	2.1×10^{-3}	3.516×10^{-3} pf/Pa
		10,000	2.69×10^{-3}	
		15,000	3.664×10^{-3}	
		20,000	5.612×10^{-3}	
	R-ZnO/BT/PVDF	5000	1.526×10^{-3}	2.532×10^{-3} pf/Pa
		10,000	1.952×10^{-3}	
		15,000	2.646×10^{-3}	
		20,000	4.004×10^{-3}	

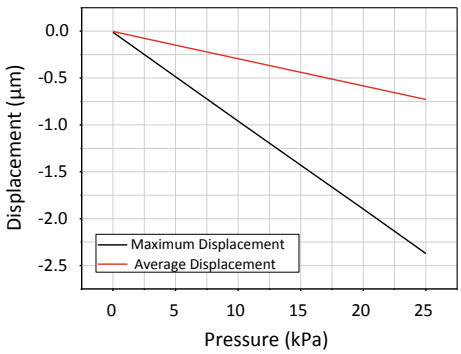

Fig. 2 Displacement and pressure graph for Ag@TiO_2/PTFE

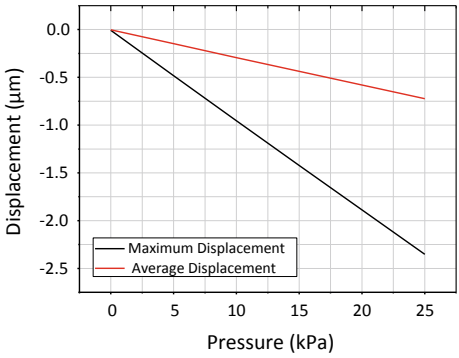

Fig. 3 Displacement and pressure graph for R-ZnO/BT/PVDF

a function of applied pressure for Ag@TiO_2/PTFE and R-ZnO/BT/PVDF dielectric material capacitor pressure sensor respectively. When we applied pressure of 10 kPa, the displacement of diaphragm membrane for Ag@TiO_2/PTFE and R-ZnO/BT/PVDF dielectric-based sensor from the center is 0.96008 μm and 0.9552 μm, respectively. The average displacement of the diaphragm membrane is 0.29471 μm and 0.29326 μm for Ag@TiO_2/PTFE and R-ZnO/BT/PVDF dielectric-based sensor, respectively. These results show that the displacement of diaphragm membrane is more dependent on pressure. So, with increase in pressure, the distance between two plates gets decreased which increases the capacitance.

The displacement of the diaphragm membrane due to applied pressure causes a change in capacitance due to a change in distance between plates of capacitor [17]. Figures 4 and 5 show the variation of capacitance with applied pressure for Ag@TiO_2/PTFE and R-ZnO/BT/PVDF dielectric-based sensor, respectively. From graphs, we have concluded that the capacitance of device will increases nonlinearly with increasing in applied pressure. The nonlinear response of graphs due to shear stress and strain distribution on the diaphragm causes complexity in designing the interface circuitry. At an applied pressure of 10 kPa, the capacitance becomes 200.8443 pF and 146.3304 pF for Ag@TiO_2/PTFE and R-ZnO/BT/PVDF dielectric-based, respectively. Similarly, when we increase the applied pressure to

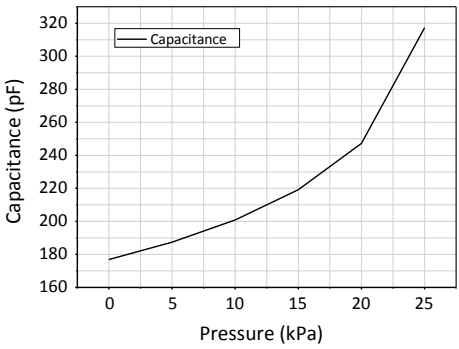

Fig. 4 Capacitance and pressure for Ag@TiO2/PTFE

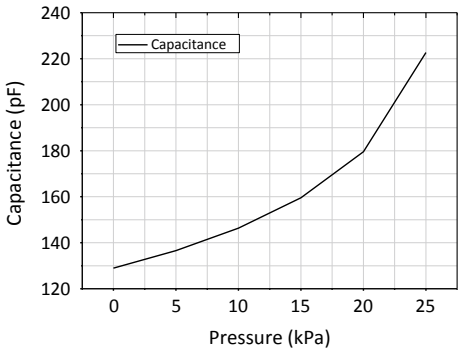

Fig. 5 Capacitance and pressure for R-ZnO/BT/PVDF

20 kPa, the value of capacitance becomes 247.219 pF and 179.5823 pF, respectively. So Ag@TiO_2/PTFE dielectric capacitor sensor gives better results for practical application.

The slope of the plotted curve has been used to measure the pressure sensitivity of the sensors. When we applied 5 kPa pressure, the sensitivity is 2.1×10^{-3} pf/Pa and 1.526×10^{-3} pf/Pa for Ag@TiO_2/PTFE and R-ZnO/BT/PVDF dielectric-based sensor, respectively. From the graphs, we have observed that the slope of capacitance changes for Ag@TiO_2/PTFE dielectric-based sensor is steeper as compared to R-ZnO/BT/PVDF dielectric-based sensor. Hence mean pressure sensitivity 3.516×10^{-3} pf/Pa and 2.532×10^{-3} pf/Pa have been obtained for Ag@TiO_2/PTFE and R-ZnO/BT/PVDF dielectric material capacitive pressure sensor, respectively.

Figures 6 and 7 show the variation of capacitance with operating temperature for Ag@TiO_2/PTFE and R-ZnO/BT/PVDF dielectric-based sensor, respectively. Graphs show that when we applied pressure 20 kPa, the capacitance of a device decreases with an increase in operating temperature. The Ag@TiO_2/PTFE dielectric-based material exhibits a large change in capacitance with increasing operating temperature. This evident that Ag@TiO_2/PTFE dielectric-based MEMS capacitive sensor is capable of functioning for high-temperature and high-power conditions enable producing high-performance enhancement to various varieties of systems and applications.

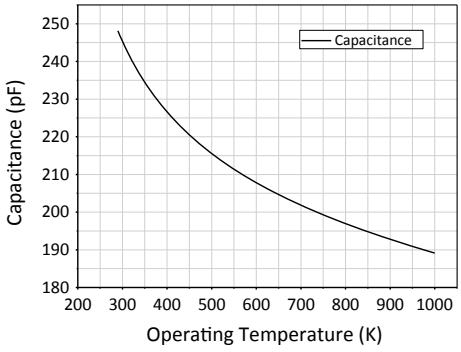

Fig. 6 Capacitance and operating temperature for Ag@TiO_2/PTFE

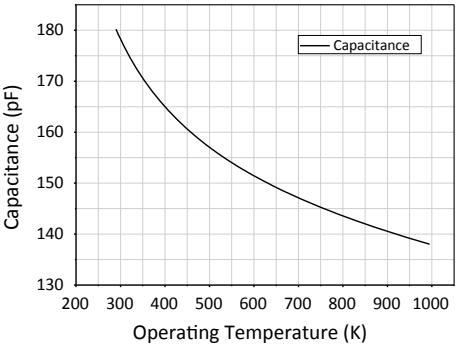

Fig. 7 Capacitance and operating temperature for R-ZnO/BT/PVDF

The temperature sensitivity of the model response is determined by the slope of the curve, which is close to 193.95 $\times$ 10^{-3} pF/K and 277.26 $\times$ 10^{-3} pF/K for Ag@TiO_2/PTFE and R-ZnO/BT/PVDF dielectric-based sensor, respectively. Hence, the temperature sensitivity of Ag@TiO_2/PTFE dielectric material capacitor is better than R-ZnO/BT/PVDF dielectric material capacitor.

4 Conclusion

In this paper, we have designed and analyzed performance parameters of MEMS Capacitive Pressure sensor using device simulation software. The measurement has been carried out for two different dielectric materials, namely, Ag@TiO_2/PTFE and R-ZnO/BT/PVDF. By using SiC and dielectric material performance of MEMS capacitive pressure increase with a maximum capacitance of 317.2877 pF. This is by introducing dielectric material and due to SiC thin film membrane because of its structural integrity of high thermal conductivity and Young's Modulus that can withstand a high operating temperature. Maximum output capacitance using Ag@TiO_2/PTFE dielectric material is given by 317.2877 pF and using R-ZnO/BT/PVDF dielectric material is given by 222.6961pF. The result of the simulation process shows that the capacitive pressure sensor using Ag@TiO_2/PTFE dielectric material shows better sensitivity and capacitance in comparison to others.

References

1. Abdelghani, L., Nasr-Eddine, M., Azouza, M., Abdellah, B., Moadh, K.: Modeling of silicon MEMS capacitive pressure sensor for biomédical applications. In: 2014 9th International Design and Test Symposium (IDT), pp. 263–266. IEEE (2014)
2. Ko, W.H., Wang, Q.: Touch mode capacitive pressure sensors for industrial applications. In: Proceedings IEEE The Tenth Annual International Workshop on Micro Electro Mechanical

Systems. An Investigation of Micro Structures, Sensors, Actuators, Machines and Robots, pp. 284–289. IEEE (1997)
3. Rey, P., Charvet, P., Delaye, M.T., Abou Hassan, S.: A high density capacitive pressure sensor array for fingerprint sensor application. In: Proceedings of International Solid State Sensors and Actuators Conference (Transducers' 97), vol. 2, pp. 1453–1456. IEEE (1997)
4. Hamanaka, M.E., Segundo, A.K.R., da Silva, S.A.L.: Portable non-invasive capacitive transducer for measuring fuel level. In: 2017 IEEE SENSORS, pp. 1–3 (IEEE)
5. Qiu, L.: Fingerprint sensor technology. In: 2014 9th IEEE Conference on Industrial Electronics and Applications, pp. 1433–1436. IEEE (2014)
6. Eaton, W.P., Smith, J.H.: Micromachined pressure sensors: review and recent developments. Smart Mater. Struct. **6**(5), 530 (1997)
7. Takahata, K., Gianchandani, Y.B.: A micromachined polyurethane/stainless-steel capacitive pressure sensor without cavity and diaphragm. In: The 13th International Conference on Solid-State Sensors, Actuators and Microsystems, 2005. Digest of Technical Papers. TRANSDUCERS'05, vol. 1, pp. 483–486. IEEE (2005)
8. Chavan, A.V., Wise, K.D.: Batch-processed vacuum-sealed capacitive pressure sensors. J. Microelectromech. Syst. **10**(4), 580–588 (2001)
9. Li, K., Chen, W., Zhang, W.: Design, modeling and analysis of highly reliable capacitive microaccelerometer based on circular stepped-plate and small-area touch mode. Microelectron. Reliab. **52**(7), 1373–1381 (2012)
10. Eaton, W.P., Smith, J.H., Monk, D.J., OBrien, G., Miller, T.F.: Comparison of bulk-and surface-micromachined pressure sensors. No. SAND-98–1779C; CONF-980918-. Sandia National Labs., Albuquerque, NM (United States) (1998)
11. Lee, S., Kim, J.-H., Ohba, T., Kim, Y.S., Kim, T-S.: A study on mechanical properties of thinned single crystal silicon wafer: Effect of size and direction. In: 2018 International Conference on Electronics Packaging and iMAPS All Asia Conference (ICEP-IAAC), pp. 339–340. IEEE (2018)
12. Huang, C.H., Lee, C.H., Hsieh, T.M., Tsao, L.C., Shaoyi, Wu., Liou, J.C., Wang, M.Y., Chen, L.C., Yip, M.C., Fang, W.: Implementation of the CMOS MEMS condenser microphone with corrugated metal diaphragm and silicon back-plate. Sensors **11**(6), 6257–6269 (2011)
13. Dwivedi, A., Khanna, G.: Performance evaluation of MEMS based capacitive pressure sensor for hearing aid application. Int. J. Adv. Eng. Res. Sci. (IJAERS) **2**(4) (2015). ISSN: 2349–6495
14. Lu, J., Wong, C.P.: Recent advances in high-k nanocomposite materials for embedded capacitor applications. IEEE Trans. Dielectr. Electr. Insul. **15**(5), 1322–1328 (2008)
15. Liang, F., Zhang, Lu., Wen-Zhong, Lu., Wan, Q.X., Fan, G.F.: Dielectric performance of polymer-based composites containing core-shell Ag@ TiO2 nanoparticle fillers. Appl. Phys. Lett. **108**(7), 072902 (2016)
16. Wang, G.: Enhanced dielectric properties of three-phase-percolative composites based on thermoplastic-ceramic matrix (BaTiO3+ PVDF) and ZnO radial nanostructures. ACS Appl. Mater. Interfaces. **2**(5), 1290–1293 (2010)
17. Shivaleela, G., Praveen, J., Mahendra, H.N., Nithya, G.: Comparative study on capacitive pressure sensor for structural health monitoring applications with coventorware. Int. Res. J. Eng. Technol. (IRJET) **04**(05) (2017). e-ISSN: 2395-0056

Modeling of Electrothermal Microactuator

Vikram Maharshi, Viphretuo Mere, and Ajay Agarwal

Abstract This paper presents the modeling of electrothermally actuated bimorph actuator for out-of-plane actuation application. Al-Si bimorph was optimized for higher displacement applications. Temperature distribution analysis of the Al-Si bimorph combination was chosen due to their larger displacement range. The modeling of Al-Si was performed with FEM and analytical analysis. Temperature distribution across the bimorph actuator with respect to length and applied voltage was optimized using FEM, lumped, and analytical analysis. The maximum temperature across Al-Si bimorph was achieved around 106 °C without convection and 85 °C with convection.

Keywords FEM · Lumped · COMSOL · Actuator · Bimorph

1 Introduction

The need for devices with a smaller size, high sensitivity, compact and low has led to the development of sensors and actuators at micro-scale. Micro-electro-mechanical-system (MEMS) technology is primarily used for such devices because of flexible of fabricating both the sensor [1–3] and actuator [4, 5] on a single chip. Thus, making it highly attractive for lab-on-chip applications. Micro-thermal actuator is one such device, which is used for actuating micromirror [6, 7]. Compared to the other methods such as electrostatic [8, 9] and piezo-electric [10, 11], thermal-based actuation [12–15] is preferable because of large actuation range at applied low voltage and

V. Maharshi (✉)
Department of Electrical Engineering, Indian Institute of Technology, Delhi, India
e-mail: vikrammaharshi007@gmail.com

V. Mere
Centre for Nano Science & Engineering, Indian Institute of Science, Bangalore, India
e-mail: viphretuomere@gmail.com

A. Agarwal
Smart Sensor Group, CSIR – CEERI, Pilani, India
e-mail: dr.ajay123@gmail.com

S. Mukherjee et al. (eds.), *Computational Mathematics, Nanoelectronics, and Astrophysics*,
Springer Proceedings in Mathematics & Statistics 342,
https://doi.org/10.1007/978-981-15-9708-4_9

makes it a viable platform for out-of-plane applications, such as biomedical imaging and laser beam steering [16]. Electrothermal actuators consist of two materials with different coefficients of thermal expansion (CTE). For a given temperature change, bimorph response by curling, the direction of curl depends on the stacking of material. Thus, it is possible to realize a robust actuator which contributes to its reliability. Other advantages of bimorph actuators are the actuation is more dependent on the modulus ratio than the total thickness, hence independent optimization of spring strength and force is also possible and the need for actuation voltage is very high in electrostatic actuation as compared to electrothermal actuation. In bimorph thermal actuator, the change in temperature across its length is achieved due to Joules heating, on the application on voltage. Thus, it is necessary to understand the heat distribution across the bimorph. In this paper, the modeling of electrothermal-based microactuator is presented. The thickness ratio of bimorph is optimized for different materials. The heat distribution along the length of the bimorph actuator is presented based on analytical calculation and lumped-based model. Finally, both the models are compared with finite element method (FEM) simulation performed using COMSOL. Heat distribution analysis was very important to get temperature and displacement distribution profile along the bimorph. The realization of the microactuator can be done using bulk as well as surface micromachining process [17].

2 Principle of Bimorph Actuation

A bimorph actuator consists of two layers with different coefficients of thermal expansion (CTE), as shown in Fig. 1. When the temperature of the bimorph is raised, the layers expand at different rates. This results in a mismatch in strain and the bimorph curls to minimize the total strain energy. The direction of curling is dependent on the stacking of the material and it is toward the material under tension.

On raising or lowering the temperature of the bimorph uniformly from '$T_{initial}$' to a new temperature 'T_{final}'. The CTE difference between the layers of the bimorph

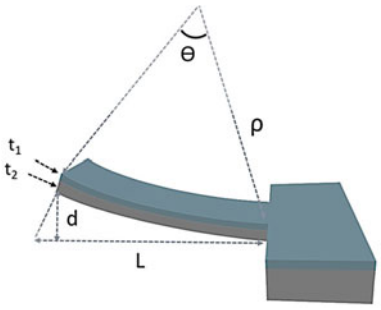

Fig. 1 Schematic of bimorph cantilever

will cause strain to develop in each layer. The difference in the strain that develops is given by Eq. (1).

$$\Delta\varepsilon_T = (\alpha_2 - \alpha_1) \cdot (T_b - T_o) = \Delta\alpha \cdot \Delta T \tag{1}$$

where 'α' represents the CTE of the specific material. The tip displacement (d) of a thermal bimorph actuator with length L, total thickness, $t_b = (t_1+t_2)$ and at a temperature difference of ΔT is given in Eq. 1 [15],

$$d = \frac{L^2}{2\rho} = \beta \frac{\Delta\alpha \Delta T L^2}{t_b} \tag{2}$$

$$\beta = 6 \frac{(1+m)^2}{\left(\frac{1}{nm} + nm^3 + 2(2m^2 + 3m + 2)\right)}$$

$$m = \frac{t_1}{t_2}, n = \frac{E_1}{E_2}$$

where L, $t_{1,2}$ ΔT, Δα, β, are length, thickness, temperature difference, CTE difference of the material stack, respectively (Fig. 2).

3 Simulations

Geometry optimization of bimorph actuator was done using COMSOL Multiphysics tool. A combination of different materials was simulated. Figure 3 shows the optimization of thickness ratio for different materials in bimorph actuator. Top layer as well as bottom layer material varied with one fixed material. It was observed that Al-Si bimorph achieved maximum displacement.

4 Electrothermal Models of Bimorph

In this section, the heat transfer in thermal microactuator is studied using a one-dimensional (1D) heat equation and lumped element model. Joules heating is used as a heat source. In bimorph, heat is dissipated via conduction, convection, and radiation as shown in Fig. 4. Below 300 °C, the Joule heat generated within the device is largely conducted to the ground via the device anchors [16]. An analytical model for the static temperature distribution in a cantilever has been developed [18]. The basic model considers a uniform internal heat source and considers the conduction in the cantilever and convection to the surrounding gas (air). heat loss from radiation is neglected for simplification since the maximum temperature of the cantilever is

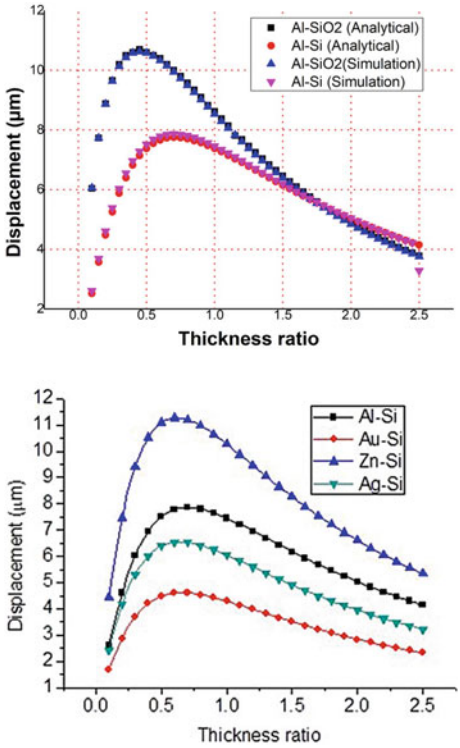

Fig. 2 Displacement versus thickness ratio: **a** upper layer material fixed and the bottom layer is varied; **b** bottom layer fixed is fixed as Si and the upper layer is varied

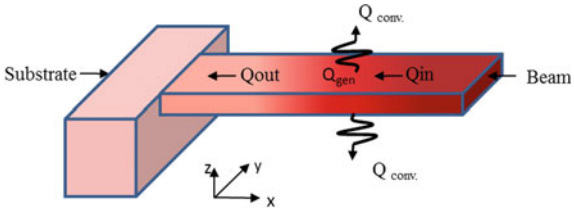

Fig. 3 Temperature distribution across a cantilever beam

assumed to be less than 200 °C as discussed earlier. Above this temperature range, aluminum which is used as the heater element will reach its softening point.

In cantilevers, heat distribution is uniform across the thickness because of the small thickness. Thus, the heat transfer in the z-direction is reduced convection through the surface. Furthermore, the temperature throughout the cantilever width is uniform (y-direction). Thus, the problem can be simplified to a one-dimensional case, where the temperature is only a function of the position x along the cantilever length as

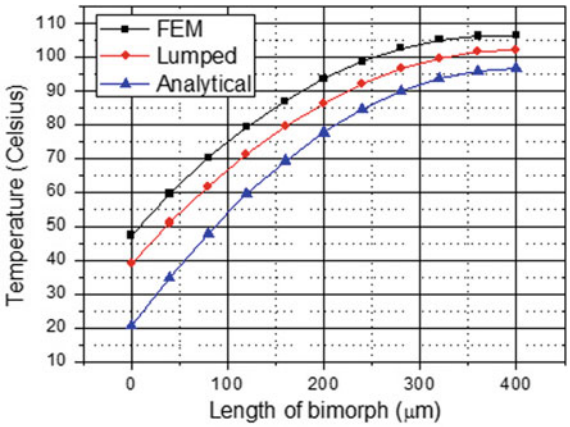

Fig. 4 Temperature distribution across the (Al-Si) bimorph actuator for different voltages

shown in Fig. 3. Considering the unit cell of the cantilever in the steady state, the energy conservation law implies that the amount of heat generated inside the cell plus the heat flowing into the cell is equal to the heat that flows out plus the heat lost by convection on both surfaces:

$$Q_{\text{gen}} + Q_{\text{in}} = Q_{\text{out}} + 2Q_{\text{conv.}} \tag{3}$$

$$Q_{\text{gen}} = q_{\text{gen}} \cdot \mathrm{d}x \cdot \mathrm{d}y \tag{4}$$

$$Q_{\text{in}} = -k \cdot \left.\frac{\mathrm{d}T(x)}{\mathrm{d}x}\right|_{x+\mathrm{d}x} \cdot t \cdot \mathrm{d}y \tag{5}$$

$$Q_{\text{out}} = -k \cdot \left.\frac{\mathrm{d}T(x)}{\mathrm{d}x}\right|_{x-\mathrm{d}x} \cdot t \cdot \mathrm{d}y \tag{6}$$

$$Q_{\text{conv}} = -h[T(x) - T_{\text{air}}] \cdot \mathrm{d}x \cdot \mathrm{d}y \tag{7}$$

Where $q_{\text{gen}} or\ P_{\text{el,}}$ is the electric power dissipated by Joule effect per unit surface, t is the cantilever thickness, k is the thermal conductivity, and h is the convection heat transfer coefficient of the cantilever. Using above Eq. (7),

$$T^{n}(x) - \frac{2h}{k \cdot t}T(x) = \frac{q_{\text{gen}} + 2hT_{\text{air}}}{k \cdot t} \tag{8}$$

The solution form of the differential Eq. (7) is [18]:

$$T(x) = C_1 e^{\sqrt{\frac{2h}{kt}}x} + C_2 e^{-\sqrt{\frac{2h}{kt}}x} + C_3 \tag{9}$$

This is the static temperature distribution equation of the cantilever, where C_1, C_2, and C_3 are constants and can be determined by applying the following boundary conditions:

By inserting Eq. (8) into (9):

$$C_3 = T_{\text{air}} + \frac{q_{\text{gen}}}{2h} \tag{10}$$

At $x = 0$, the temperature in the cantilever is the same as in the substrate:

$$T(0) = C_1 + C_2 + C_3 = T_{\text{sub}} \tag{11}$$

At $x = L$, i.e., at the end of the cantilever heat transfer by conduction is zero,

$$\frac{\mathrm{d}}{\mathrm{d}x} T(x)_{x=L} = 0 \tag{12}$$

Assuming the substrate temperature the same as that of the environment (air), C_1, and C_2 can be derived as

$$C_1 = -\frac{\frac{q_{\text{gen}}}{2h} e^{-\sqrt{\frac{2h}{kt}}L}}{e^{\sqrt{\frac{2h}{kt}}L} + e^{-\sqrt{\frac{2h}{kt}}L}} \tag{13}$$

$$C_2 = \frac{\frac{q_{\text{gen}}}{2h} e^{\sqrt{\frac{2h}{kt}}L}}{e^{\sqrt{\frac{2h}{kt}}L} + e^{-\sqrt{\frac{2h}{kt}}L}} \tag{14}$$

Equation (9) can be written as

$$T(x) = \frac{q_{\text{gen}}}{2h}\left(1 - \frac{\cosh\left(\sqrt{\frac{2h}{kt}} \cdot (L - x)\right)}{\cosh\left(\sqrt{\frac{2h}{kt}} \cdot L\right)}\right) + T_{\text{air}} \tag{15}$$

If the convection is neglected ($h = 0$) the one-dimensional heat Eq. (18) is further simplified as

$$T^n(x) = \frac{q_{\text{gen}}}{k \cdot t} \tag{16}$$

And applying the same boundary conditions, the solution of the equation is given as

$$T(x) = -\frac{q_{\text{gen}}}{2k \cdot t} x^2 + \frac{q_{\text{gen}} \cdot L}{k \cdot t} \cdot x + T_{\text{air}}$$

The temperature distribution of the actuator from FEM simulations was compared with the 1D heat equation and 1D lumped element model (without convection). The lumped model and the analytical solution were implemented using MATLAB. The equations used for predicting the temperature across are as follows:

- 1D heat transfer equation with heat generation without convection (equation).

$$T(x) = -\frac{q_{gen}}{2k \cdot t}x^2 + \frac{q_{gen} \cdot L}{k \cdot t} \cdot x + T_{air} \tag{17}$$

- 1D lumped element model without convection.

$$T(x) = P[R_{TA}(-\frac{x^2}{2L_A^2} + f\frac{x}{L_A}) + fR_{TL}] + T_{air} \tag{18}$$

Figures 4 and 5 show the temperature distribution across the bimorph length and with a different voltage by using FEM, analytical, and lumped analysis which are in good agreement. The temperature across the bimorph length increases with the longer length beam. Maximum temperature distribution across bimorph was observed below 300 °C at 0.35 V. Conduction losses were considered for heat loss mechanism since the device will be operated below 250 °C.

Figure 6 shows the steady state, the temperature profile of the bimorph. The graphs for h = 0 and h = 25 [W/m^2. K] (i.e. without convection and natural convection) are almost coinciding with each other, thus we can conclude that the device performance is not affected much and remains stable. However convective heat transfer becomes significant for (h = 250 [W/m^2. K] (forced convection), thus the overall temperature distribution is reduced on account of this phenomenon.

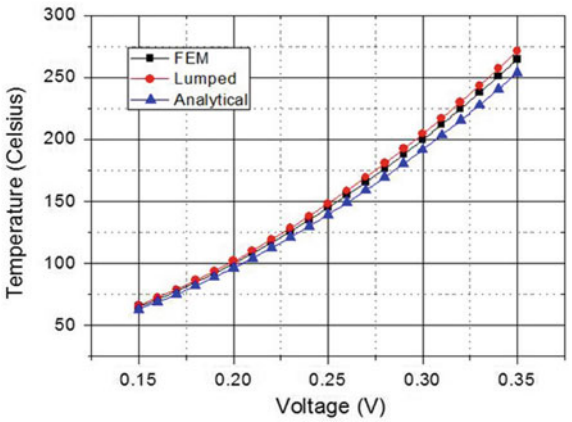

Fig. 5 Temperature distribution across the bimorph actuator for 0.2 V applied voltage

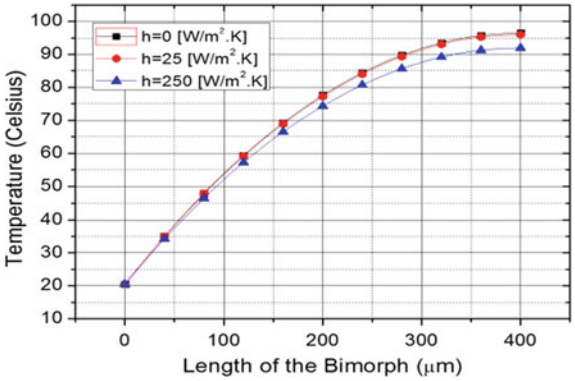

Fig. 6 Temperature distribution across the bimorph actuator with or without convection for 0.2 V applied voltage

5 Conclusion

In the paper, we present the modeling of electrothermal-based microactuator, which works on the principle of coefficient of thermal expansion. Geometry and the material combination for the bimorph actuator were optimized. Temperature distribution across the bimorph actuator length with respect to applied voltage was optimized using FEM, lumped, and analytical analysis. All three analyses are in good agreement. The maximum temperature across Al-Si bimorph was achieved around 106 °C without convection and 85 °C with convection. Radiation losses were not considered for heat loss mechanism since the device will perform under 250 °C.

Acknowledgements The authors acknowledge the support of Smart Sensor Labs at CSIR- CEERI Pilani.

References

1. Xie, H., Fedder, G.: CMOS z-axis capacitive accelerometer with comb-finger sensing. In: Proceedings IEEE Micro Electro Mechanical Systems (MEMS), pp. 496–501 (2000)
2. Yazdi, N., Ayazi, F., Najafi, K.: Micromachined inertial sensors. Proc. IEEE **86**(8), 1640–1659 (1998)
3. Albarbar, A., Mekid, S., Starr, A., Pietruszkiewicz, R.: Suitability of MEMS accelerometers for condition monitoring: an experimental study. Sensors **8**, 784–799 (2008)
4. Mere, V., Vikram Maharshi, A., Agarwal, A.: Thermally actuated MEMS micromirror: design aspects. Asian J. Phys. **23**(4), 00–001 (2014a)
5. Milanovic, V., Matus, G.A., Mccormick, D.T.: Gimbal-Less monolithic silicon actuators for tip-tilt-piston micromirror applications. selected topics in quantum electronics. IEEE J. **10**(3), 462–471 (2004)

6. Maharshi, V., Mere, V., Agarwal, A.: Deaign and fabrication of electro thermal 1-D micro mirror. In: IEEE Electron Devices Kolkata Conference (EDKCON), pp. 419–422. kolkata. India (2018)
7. Mere, V., Vikram Maharshi, A., Agarwal, A.: Thermally actuated MEMS micromirror: design aspects. Asian J. Phys. **23**, 631–640 (2014b)
8. Abdel-Rahman, E.M., Younis, M.I., Nayfeh, A.H.: Characterization of the mechanical behavior of an electrostatically actuated microbeam. J. Micromech. Microeng. **12**(6), 759–766 (2002)
9. Hassanzadeh, A.: Design Considerations for Basic MEMS Electrostatic Actuators. 978–1–4244–3325–4/09/©2009 IEEE
10. Harris, N.R., Hill, M., Torah, R., Townsend, R., Beeby, S., White, N.M., Ding, J.: A multilayer thick-film PZT actuator for MEMs applications. Sens. Actuators A **132**, 311–316 (2006)
11. Kanno, I.: Piezoelectric MEMS for energy harvesting. J. Phys.: Conf. Ser. **660**, 012001 (2015)
12. Ogando, K., La Forgia1, N., Zárate, J.J., Pastoriza, H.: Design and characterization of a fully compliant out-of-plane thermal actuator. Sens. Actuators A **188**, 349–358 (2012)
13. Jia, K., Pal, S., Xie, H.: An electrothermal tip–tilt–piston micromirror based on folded dual s-shaped bimorphs. J. Microelectromech. Syst. **18**(5) (2009)
14. Moulton, T., Anantha Suresh, G.K.: Micromechanical Devices with embedded electro-thermal-compliant actuation. Sens. Actuators A **90**, 38±48 (2001)
15. Nilesh, D., Mankameandg, K., Suresh, A.: Comprehensive thermal modelling and characterization of an electro-thermal-compliant micro actuator. J. Micromech. Microeng. **11**, 452–462 (2001)
16. Xie, H., Pan, Y., Fedder, G.K.: A SCS CMOS micromirror for optical coherence tomographic imaging. In: The Fifteenth IEEE International Conference on Micro Electro Mechanical Systems, 2002, pp. 495–498. IEEE (2002)
17. Maharshi, V., Mere, V., Agarwal, A.: Multi-layered [Au/Si3N4/SiO2] thermal actuator realization using metal passivated TMAH micro-machining. Eng. Res. Express, IOP **1**, 015006 (2019)
18. Todd, S.T.: Electrothermomechanical Modelling Of a 1-D Electro thermal MEMS Micromirror

Influence of High-K and Low-K Dielectrics on Drain Current of GaN HEMTs

Shivanshu Mishra, Sandeep Dhakad, Niketa Sharma, Kuldip Singh, Ashok Chauhan, Priyavart Prajapat, and Nidhi Chaturvedi

Abstract This paper reports on the influence of high-k and low-k dielectric passivation on the drain current performance of GaN HEMTs. Four different dielectric materials, namely, SiN_x, Al_2O_3, HfO_2, and SiO_2 were deposited and their effect on drain current was compared. Among all the dielectric materials used, the high-k Al_2O_3 passivation showed the best performance. In this case, the drain current increased by 84%. Even after having the highest k value, the HfO_2 did not deliver better results than Al_2O_3 and SiN_x. A comparison of PECVD deposited SiO_2 (low-k) and SiN_x (high-k) showed strong thickness-dependent performance.

Keywords High-k and low-k dielectrics · High electron mobility transistor (HEMT) · III-V material · Al_2O_3 and HfO_2

1 Introduction

AlGaN/GaN HEMTs have shown great performance capabilities in the areas of high power, high voltage, microwave, and biosensors due to its properties of large bandgap, high electron mobility, high carrier concentration, high saturation velocity with high electric field value [1–6]. However, the performance of these devices is limited by the trapping effects on the surface [7]. Si_3N_4 and SiO_2 had shown to be able to reduce the effects of surface trapping of charges [8, 9]. The traps capture electrons and then act as a virtual gate on the surface, which deplete channel electrons and decrease the output current of the device [10]. People are working intensively to reduce this effect on the surface of the device because it is responsible for degrading the output power and overall performance of the device [11]. The surface traps can be suppressed significantly with the help of the passivation of dielectric materials [12].

S. Mishra (✉) · S. Dhakad · N. Sharma · K. Singh · A. Chauhan · P. Prajapat · N. Chaturvedi
Smart Sensor Area, CSIR- Central Electronics Engineering Research Institute, Pilani 333031, India
e-mail: shivanshuceeri@gmail.com

S. Mishra · N. Chaturvedi
Academy of Scientific and Innovative Research, New Delhi 110020, India

S. Mukherjee et al. (eds.), *Computational Mathematics, Nanoelectronics, and Astrophysics*,
Springer Proceedings in Mathematics & Statistics 342,
https://doi.org/10.1007/978-981-15-9708-4_10

Low-k dielectric materials are used to passivate the HEMTs but nowadays people are moving toward high-k dielectric materials because of its superior properties such as better insulating and capacitive property, high thermal stability, and sound interface qualities [13].

In this paper, we are reporting on the thickness-dependent effect of high-k and low-k dielectrics passivation on drain current performance of GaN HEMTs.

2 Experimental Details

The AlGaN/GaN-based HEMTs were fabricated on sapphire and silicon carbide (SiC) substrates for several experiments. The epitaxial stack consists of 2 nm AlN nucleation layer, followed by a 2.3 μm thick unintentionally doped GaN buffer layer, and finally followed by a 25 nm-thick *n*-type $Al_{0.25}Ga_{0.75}$ N layer. These epilayers were grown on the Sapphire and SiC substrate by MOCVD as shown in Fig. 1. The device fabrication process consists of five lithography levels as ohmic contact formation, mesa isolation, Schottky contact formation, interconnects, and passivstion.

Source and drain ohmic contacts were e-beam evaporated of Ti/Al/Ni/Au and then annealed at 830 °C in the nitrogen environment [14]. Devices were ion implanted using Ar^+ and N^+ for isolation [15]. Then nickel-based Schottky contacts (gate) were formed. Two different unit gate widths of 2 × 50 μm and 2 × 125 μm were designed and fabricated along with a gate length of 2 μm. Gates and source pads were interconnected using Au metal pads for biasing. These devices were characterized and then passivated using SiO_2 as low-k dielectric and SiN_x, Al_2O_3, and HfO_2 as high-k dielectric materials. SiO_2 and SiN_x were deposited using PECVD and Al_2O_3 and HfO_2 were deposited using ALD (Atomic Layer Deposition). Deposited film thicknesses of SiO_2 and SiN_x were 100, 150, and 240 nm. The drain current was measured in each case before and after passivation and the effect of thickness variation

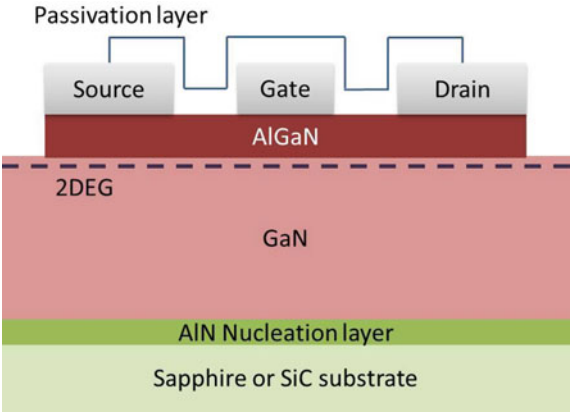

Fig. 1 Schematic cross section of AlGaN/GaN HEMT

was checked for comparison. All the measurements were carried out at zero-volt gate bias.

3 Result and Discussion

Figure 2 is showing an effect of thickness variation of SiO_2 on the percentage change in current. The saturated drain current of the device without passivation was 520 mA/mm and increased to 610 mA/mm after passivation of 100 nm-thick SiO_2. Therefore, for the thickness of 100 nm, the improvement in the current was measured to be 17%. The drain current increased because of an increment in charge concentration of 2DEG [16]. SiO_2 passivation layer employed for AlGaN/GaN HEMT seems to suppress the negative virtual gate effect due to increment in drain current [17]. However, as the thickness of SiO_2 layer increased from 100 to 150 nm, the betterment in the current reduced. A minor improvement of 1% was recorded for a thickness of 150 nm. Furthermore, for even thicker layers of 200–240 nm, the output current starts decreasing. The reason behind was probably quality and strain issues related to thicker layers of SiO_2. This thickness variation was tested on Sapphire as well as on SiC. Hence for better performance of the device, a thin layer of SiO_2 (100–150 nm) is recommended.

In another test of passivation, the high-k dielectric materials namely SiN_x, Al_2O_3 and HfO_2 were deposited. Figure 3 shows the effect of the thickness of SiN_x on the current change. In this case, as the thickness increased from 100 to 150 nm, the current improved. For the thickness of 150 nm, the saturated drain current increased from 500 mA/mm to 670 mA/mm indicating a higher sheet carrier concentration in the channel. The reason behind was probably the increase in positive charge at the interface of SiN_x/AlGaN which neutralized the AlGaN polarization charge thereby

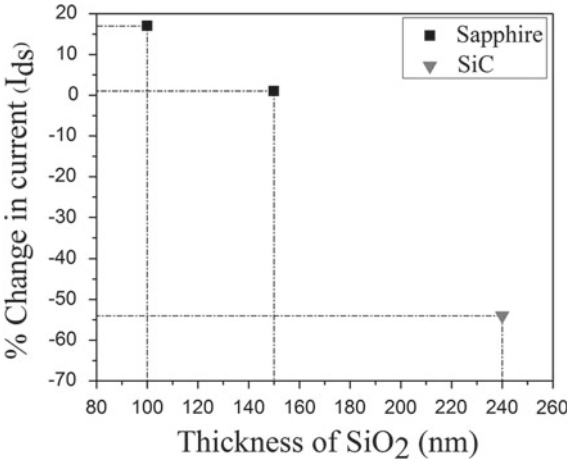

Fig. 2 % change in I_{ds} for various thicknesses of SiO_2

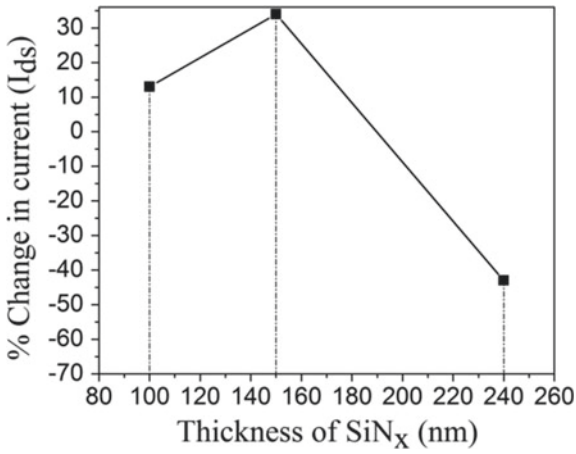

Fig. 3 % change in I_{ds} for various thicknesses of SiN_x

mitigating the surface-related problems from the channel [18]. However again a threshold value of around 180 nm of SiN_x thickness was recorded beyond which the performance of the device started degrading probably due to the strain generation at the interface of SiN_x/AlGaN for a thicker layer of SiN_x. Therefore, 150 nm thickness of SiNx is recommended for the best performance of the device.

In Fig. 4, both traditional high-k (SiN_x) and low-k (SiO_2) dielectric materials are compared for 100 and 240 nm thickness. For a thin layer of 100 nm, the SiO_2 proved better due to improvement in the current, whereas for a thick layer of 240 nm SiN_x proved to be more promising. Therefore for the proper operation of device, the thickness of the passivation layer must be optimized.

The possible reason behind could be the change in the traps concentrations and strain level with thicknesses in combination with the dielectric constant of material.

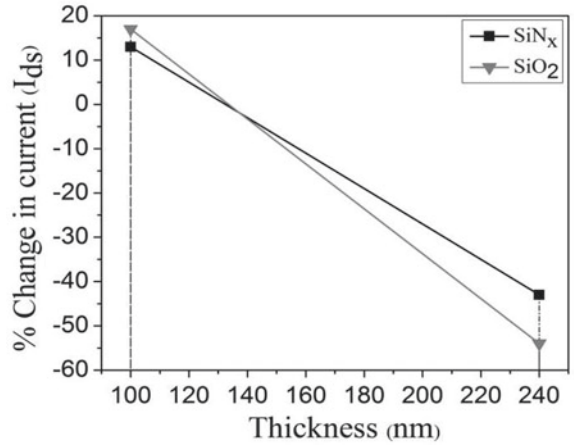

Fig. 4 Thickness-dependent comparison of SiO_2 and SiN_x

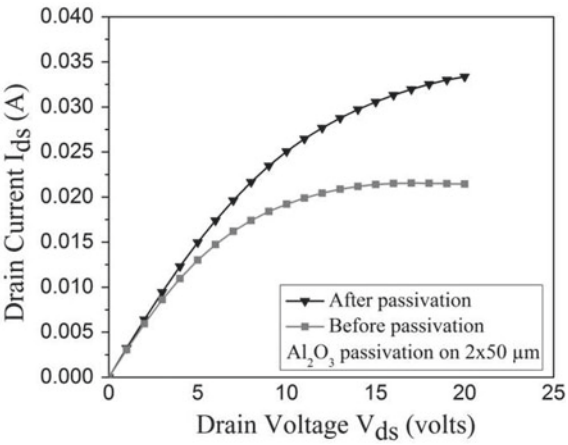

Fig. 5 High-k Al_2O_3 effect on drain current

Hence, the performance of high-k and low-k dielectric materials deposited using PECVD is strongly thickness dependent.

After studying the effect of traditionally used high-k and low-k dielectric materials, we deposited high-k Al_2O_3 and HfO_2 using atomic layer deposition (ALD) for betterment in the drain current. Figure 5 compares the current before and after the passivation of Al_2O_3. This figure also shows the negative conductance at a large drain to source voltage. This decrease in current at the large drain to source voltage is due to the self-heating and especially results in the decrease in mobility. In addition to self-heating, deep traps are also present in the AlGaN/GaN heterostructure and can reduce the performance of the device [19].

A drastic improvement in the output drain current was observed after the deposition of Al_2O_3. The improvement with increasing thickness saturates at about 30 nm [20]. The percentage improvement in current from its unpassivated value was about +84%. This indicated an effective suppression of surface traps in gate-to-drain/source regions using Al_2O_3 passivation layer. In addition, due to the large difference in the bandgap, the chances of traps charging might have reduced due to a possible reduction in the leakage current.

Similarly, the passivation of HfO_2 also showed an increment in the current from its unpassivated value as shown in Fig. 6. However, an increment in current value was only 18% which was less as compared to the case of Al_2O_3. The possible reason behind this could be related to the strain development in very high-k dielectric films. The HfO_2 has a higher dielectric constant as compared to Al_2O_3 due to which the film could not get relaxed properly on the deposited surface and leads to defects at the interface and in the bulk of materials [13].

Next, we made a comparison of all the four dielectric materials used for the device passivation. Optimized values of thicknesses were used to show the best performance of an individual. Figure 7 clearly shows the best performance of Al_2O_3. When compared to the low-k dielectric material, all the high-k dielectric materials showed better performance in comparison. Passivation by SiN_x proved much more

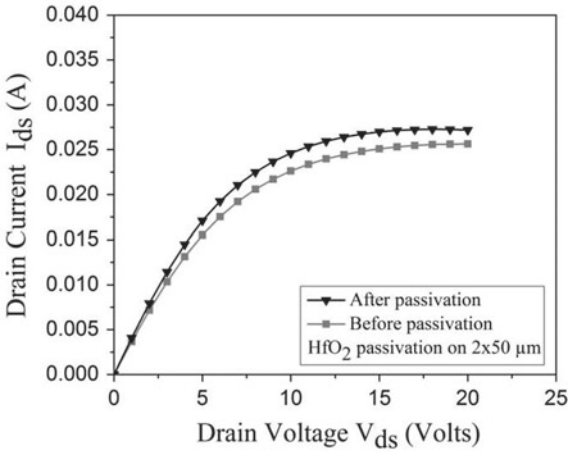

Fig. 6 High-k HfO_2 effect on drain current

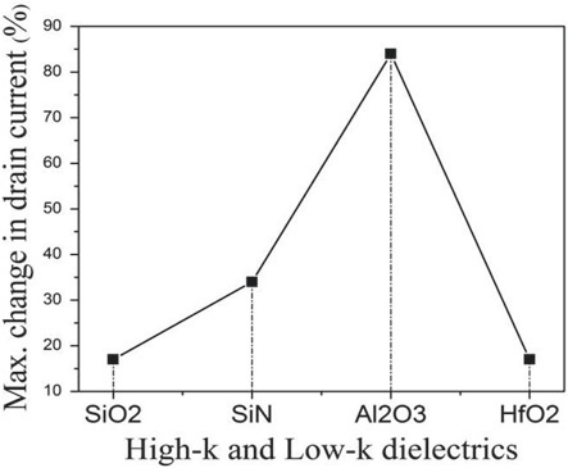

Fig. 7 Comparison of high-k and low-k passivation

useful as compared to the HfO_2 even though the dielectric constant of nitride is low. One of the possible reasons behind was related to the interface defects of HfO_2 because of its very high dielectric constant and hence the low band gap difference.

4 Conclusion

To passivate GaN HEMTs, four different high-k and low-k dielectric materials were deposited using Atomic Layer Deposition (ALD) method and Plasma Enhanced Chemical Vapor Deposition (PECVD) method. When compared to the low-k dielectric material, all the high-k dielectric materials showed better performance of drain current. The SiNx (high-k) and SiO2 (low-k) were compared for 100 and 240 nm

thickness. Both of them showed strong thickness-dependent performance. For a thin passivation layer of 100 nm, the SiO_2 proved better due to much improvement in the drain current whereas, for a thick passivation layer of 240 nm SiN_x proved to be more promising. A drastic increase in the drain current was observed after the deposition of Al_2O_3. The recorded percentage improvement in current from its unpassivated value was about +84%. Deposition of HfO_2as the highest k dielectric material could not show the best improvement in the drain current as compared to SiNx and Al_2O_3.The reason behind was possibly related to the low bandgap difference with AlGaN and hence the charging of traps in large volume.

Acknowledgements The authors acknowledge the support of Director, CSIR-CEERI and Budget Head PSC-201 Microsensys. The authors gratefully acknowledge Dr. Vandana from CSIR-NPL for the ALD deposition facility. The authors are also thankful to Mr. B.C Pathak, Mr. Arvind, Mr. Ashok Gupta, Mr. Pawan Kumar, Mr. Bhupendra Kushwaha, Mr. Prem, Mr. Anand Upadhyay, and Mr. Prateek Kothari for their help in device fabrication and characterization.

References

1. Ueda, T., Uemoto, Y., Tanaka, T., Ueda, D.: GaN transistors for power switching and millimeter-wave applications. Int. J. High Speed Electron. Syst. **19**(1), 145–152 (2009)
2. Herbecq, N., Jeune, I.R., Linge, A., Zegaoui, M., Jeannin, P.O., Rouger, N., Medjdoub, F.: Above 2000V breakdown voltage at 600 K GaN-on-silicon high electron mobility transistors. Phys. Status Solidi A **213**(4), 873–877 (2016)
3. Sun, H., Alt, A.R., Tirelli, S., Marti, D., Benedickter, H., Piner, E., Bolognesi, C.R.: Nanometric AlGaN/GaN HEMT Performance with Implant or Mesa Isolation. IEEE Electron Device Lett. **32**(8), 1056–1058 (2011)
4. Li, B., Tang, X., Wang, J., Chen, K.J.: Optoelectronic devices on AlGaN/GaN HEMT platform. Phys. Status Solidi A **213**(5), 1213–1221 (2016)
5. Mishra, U.K., Shen, L., Kazior, T.E., Wu, Y.F.: GaN-based RF power devices and amplifiers. Proc. IEEE **96**(2), 287–305 (2008)
6. Ren, F., Pearton, S.J.: Recent Advances in Wide-Bandgap Semiconductor Biological and Gas Sensors. In: Semiconductor Device-Based Sensors for Gas, Chemical, and Bio Applications, pp. 43–96. CRC Press, Boca Raton London New York (2011)
7. Arulkumaran, S., Egawa, T., Ishikawa, H., Jimbo, T.: Appl. Phys. Lett. **81**, 3073 (2002)
8. Arulkumaran, S., Egawa, T., Ishikawa, H., Jimbo, T., Umeno, M.: Appl. Phys. Lett. **73**, 809 (1998)
9. Vertiachikh, A.V., Eastman, L.F., Schaff, W.J., Prunty, T.: Electron. Lett. **38**, 388 (2002)
10. Liao, W.C., Chen, Y.L., Chen, Z.X., Chyi, J.I., Hsin, Y.M.: Gate leakage current induced trapping in AlGaN/GaN Schottky-gate HFETs and MISHFETs. Nanoscale Res. Lett. **9**(1), 474 (2014)
11. Meneghesso, G., Verzellesi, G., Pierobon, R., Rampazzo, F., Chini, A., Mishra, U.K., Zanoni, E.: Surface related drain current dispersion effects in AlGaN-GaN HEMTs. IEEE Electron Device Lett. **51**, 1554–1561 (2004)
12. Green, B.M., Chu, K.K., Chumbes, E.M., Smart, J.A., Shealy, J.R., Eastman, L.F.: The effect of surface passivation on the microwave characteristics of undoped AlGaN/GaN HEMTs. IEEE Electron Device Lett. **21**, 268–270 (2000)
13. Huang, P., Yang, Z.C., Chu, P.K.: Hafnium-based High-k gate dielectrics, advances in solid state circuit technologies, Paul K Chu (Ed.), InTech (2010). https://doi.org/10.5772/8631.

14. Chaturvedi, N., Zeimer, U., Würfl, J., Tränkle, G.: Mechanism of ohmic contact formation in AlGaN/GaN high electron mobility transistors. Semicond. Sci. Technology. **21**, 175–179 (2006)
15. Sharma, N., Bhardwaj, S., Dhakad, S., Periasamy, C., Chaturvedi, N.: Ar based Ion implantation and Ar RIE of thin and thick AlGaN/GaN HEMTs, WOCSDICE-EXMATEC, Portugal (2016)
16. Ha, M.W., Chul, S., Lee, J.H., Her, J.C. et al.: Silicon dioxide passivation of AlGaN/GaN HEMTs or high breakdown voltage. IEEE Naples, Italy (2006)
17. Vetury, R., Zhang, N.Q., Keller, S., Mishra, U.K.: The impact of surface states on the DC and RF characteristics of AlGaN/GaN HFETs. IEEE Trans. Electron Devices **48**, 560–566 (2001)
18. Prunty, T.R., Smart, J.A., Chumbes, E.M., Ridley, B.K., Eastman, L.F., Shealy, J.R.: Passivation of GaN/GaN heterostructures with silicon nitride for insulated gate transistors. In: Proceedings of 2000 IEEE/Cornell Conference on High Performance Devices, pp. 208–214. Itheca, NY (2000)
19. Gassoumi, M., Grimbert, B., Gaquiere, C., et al.: Semiconductors **46**, 382 (2012). https://doi.org/10.1134/S1063782612030104https://doi.org/10.1134/S1063782612030104
20. Lee, D.S., Laboutin, O., Cao, Y., Johnson, W., Beam, E., Ketterson, A., Schuette, M., Saunier, P., Palacios, T.: Impact of Al2O3 passivation thickness in highly scaled GaN HEMTs. IEEE Electron Device Lett. **33**, 976–968 (2012)

Comparative Study and Analysis of Different Perovskite Solar Cells with Inverted Architecture

Himanshu Dixit, Deepak Punetha, and Saurabh Kumar Pandey

Abstract An intensive numerical estimation and optimization for perovskite solar cell with inverted design has been performed by employing a simulation tool. Multiple elements affecting the execution of photovoltaic devices have been precisely interpreted, particularly physical parameters of buffer and perovskite absorber layer. By parameter optimization, we have obtained a simulated power conversion efficiency (PCE) of 12.90% with open-circuit voltage (Voc) 1.14 V, short circuit current density (Jsc) 29.27 mA/cm^2, and a fill factor (FF) 84.75%. The function of defect density has also been studied for exploring the performance of cell module and comparative analysis with alternative absorber material ($CH_3NH_3SnI_3$ and $FASnI_3$) has also been discussed.

Keywords Simulation · Absorber layer · Perovskite · SCAPS-1D · Photovoltaic · Inverted architecture

1 Introduction

Organic–inorganic halide perovskites have attained considerable attention as an active layer in solar cells since the existence of methylammonium lead halide (CH3NH3SnI3) perovskites. The features showed by these materials like strong light absorption coefficient, bandgap tuning, low-temperature solution-based processing, excellent solubility in polar solvents, high diffusion length, high carrier mobility, etc., make perovskite materials convenient for low-cost solar cell applications. Within a very short span power conversion efficiency of perovskite solar cells (PSC) has climbed from 3.8% to 22.7% [1, 2]. In spite of various advantages of perovskites, the

H. Dixit (✉)
Department of Electronics Engineering, Rajasthan Technical University, Kota 324009, Rajasthan, India
e-mail: himanshudixit270@gmail.com

D. Punetha · S. K. Pandey
Sensors and Optoelectronics Research Group (SORG), Department of Electrical Engineering, Indian Institute of Technology Patna, Bihar 801103, India

S. Mukherjee et al. (eds.), *Computational Mathematics, Nanoelectronics, and Astrophysics*, Springer Proceedings in Mathematics & Statistics 342,
https://doi.org/10.1007/978-981-15-9708-4_11

utility of these materials in commercial applications is restricted by their stability in the environment. In this simulation work, we have modeled three perovskite solar cells with different absorber layers, namely, methylammonium tin iodide (MASnI3), formamidinium tin iodide (FASnI3), and cesium tin iodide (CsSnI3).

Three different tin-based perovskite solar cells were designed and simulated by device simulation software. Simulated models were investigated by comparing with photovoltaic parameters depicted in literature. Influence of perovskite thickness, bandgap, defect density, and working temperature was calculated and it revealed that what optimized parameters should be used to prepare perovskite solar cells with excellent efficiency [3]. Miscellaneous candidates for the absorber layer were employed to discuss various photovoltaic parameters. Results clarify that perovskite solar cell with CH3NH3SnI3 as an absorber layer can attain comparatively higher PCE which is because of its wide bandgap, excellent stability in air, and good charge carrier mobility as compared to FASnI3 and CsSnI3. Additionally, it is feasible to deposit by solution-based low-temperature processing technique which makes it appropriate with various wafers.

2 Simulation Procedure

2.1 Device Methodology

The solar cell structure is analyzed with SCAPS-1D (a Solar Cell Capacitance Simulator) simulation tool. Up to 7 semiconducting layers can be investigated in this simulation program. Almost all photovoltaic parameters like bandgap (Eg), relative permittivity (ε), working temperature (T), electron and hole mobility (μn and μp), electron affinity (χ), conduction and valance band density of states (Nc and Nv), donor and acceptor doping concentration (ND and NA), all defects (trapping sites) can be easily graded in this simulation work. There are three types of recombination models utilized in SCAPS, namely, band-to-band (direct) recombination, auger carrier recombination, and Shockley–Read–Hall (SRH) recombination. We can also permit tunneling here, it can be either intra-band (within bands) or through interfaces of semiconducting layers. The photovoltaic device can be illuminated either from p-side (hole transporting material) or from n-side (electron transporting material). Different working points like temperature (K), voltage (V), and frequency (Hz) should be given by the user. The simulated program calculates J-V (current density––voltage) curve, quantum efficiency (QE), different energy bands, carrier density, and generation-recombination profile.

2.2 *Device Structure*

We have simulated three different models based on tin halide perovskites and calibrated the impact of thickness, bandgap, defect density, and operating temperature on device performance. Planar heterojunction structure with FTO/C60/1st Interface layer/Perovskite absorber layer/2nd Interface layer/NiO/Au has been taken for the simulation study. Methylammonium tin iodide ($CH_3NH_3SnI_3$), formamidinium tin iodide ($FASnI_3$), and cesium tin iodide ($CsSnI_3$) are utilized as various absorber layers for this simulation work [4]. Parameters for various layers are picked on the basis of experimental information and available literature. For both electrons and holes thermal velocities are 10^7 cm/s. Tin-based perovskite shows p-type semiconducting behavior attributed to self-doping of Sn^{2+} into stable state Sn^{4+} so the active layer is a p-type material with doping density of 10^{19} cm^{-3}. Defects in the active layer are basically in the Gaussian distribution with having 0.1 eV characteristics energy and 10^{17} cm^{-3} defect density. The work functions for both metal contacts and FTO are 5.1 eV and 4.4 eV, respectively. Tunneling through traps of interfaces is strictly prohibited in this simulation work [5]. A heterojunction PSC structure is shown in Fig. 1 (Table 1).

3 Results and Discussion

In this section, three multilayer structures, $MASnI_3$, $FASnI_3$, and $CsSnI_3$ absorber layers have been simulated. All configurations have reforming characteristics without any source of light. As the buffer layer is illuminated with light, it exhibits a shift

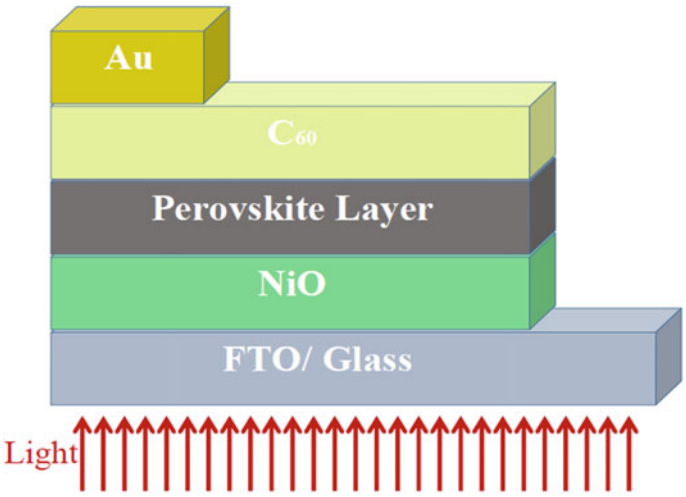

Fig. 1 Schematic architecture of simulated PSC model

Table 1 Simulation parameters for FASnI3 based PSC

Parameters	FTO	NiO	$MASnI_3$	$FASnI_3$	$CsSnI_3$	C60
Thickness (nm)	500	350	350	350	350	30
Bandgap Eg (eV)	3.50	3.80	1.30	1.41	1.27	1.9
Electron Affinity (eV)	4.00	1.46	4.17	4.47	4.47	2.65
Dielectric Permittivity	9.00	11.75	8.2	8	18	4.5
CB Effective Density of States cm^{-3}	2.2E + 18	2.2E + 20	1.0 + E18	6.76E + 17	5.76E + 16	1.44E + 21
VB Effective Density of States cm^{-3}	1.8E + 19	1.8E + 19	1.0 + E18	6.76E + 17	5.76E16	1.44E + 21
Mobility (ue) cm^2/vs	20	2.8	1.6	1.6	4.37	1.0E-2
Mobility (uh) cm^2/vs	10	2.8	1.6	1.6	4.37	1.0E-5
Shallow Uniform Acceptor Density cm^{-3}	–	1.0E + 18	3.2E15	1.0E + 19	1.0E + 19	2E14
ShallowUniformDonor Density cm^{-3}	2.0E + 19	–	–	–	–	–
Total Defect Density cm^{-3}	$_{10}15$	$_{10}15$	$_{10}15$	$_{10}13$	$_{10}15$	$_{10}15$
Electron Thermal Velocity cm/s	1E7	1E7	1E7	1E7	1E7	1E7
Hole Thermal Velocity	1E7	1E7	1E7	1E7	1E7	1E7

in Jsc attributed to more generation of charge carriers through light photons thus it can be estimated that NiO/Perovskite/C60 hetero-structure precisely works as a solar cell.

3.1 Effect of Defect Density

There are too many defects always present in ETM, HTM, or absorber layer such as dislocations, pin-holes, vacancies, etc. These defects affect the charge carrier recombination and reduce the carrier lifetime [6]. In this simulation, we varied defect density from 10^{10} to 10^{18} cm^{-3}. Up to $10^{15}/cm^3$ device performance keeps constant then it decreases with an increase in defect density (Fig. 2 and Table 2).

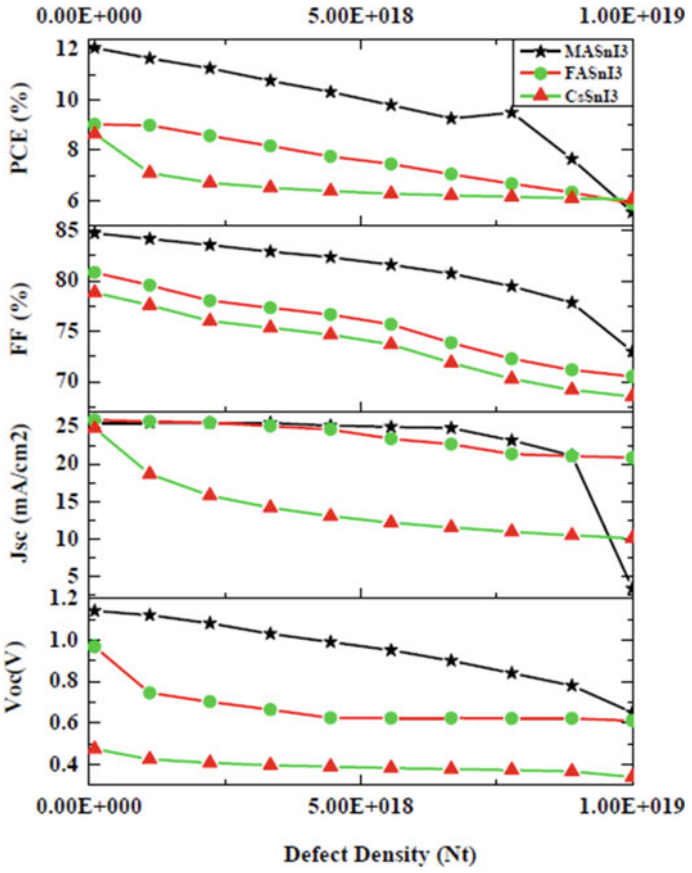

Fig. 2 Variation in solar parameters with defect density of photovoltaic device

Table 2 Optimized parameters attained while varying defect density

Perovskite Layer	Voc (V)	Jsc (mA/cm^2)	FF (%)	PCE (%)
$MASnI_3$	1.14	25.56	84.75	12.06
$FASnI_3$	0.97	25.95	80.85	9.01
$CsSnI_3$	0.47	24.81	78.85	8.64

3.2 Effect of Band Gap

Perovskites have a tunable bandgap which can be varied from 1.3 eV to 2.15 eV. Photovoltaic device performance can be improved by a suitable band gap matching of ETM, HTM, and absorber layer. As we go from 1.3 eV to 2.15 eV all photovoltaic parameters decreases except Voc [6, 7]. Current density reduces because of a decrease

in the absorption of light photons. Open-circuit voltage increases since the separation of excitons occurs after the generation of charge carriers, which boosts the Voc. Due to the mismatching of HTM and absorber layers fill factor decreases. So overall with an increase in bandgap device performance and efficiency decreases (Fig. 3 and Table 3).

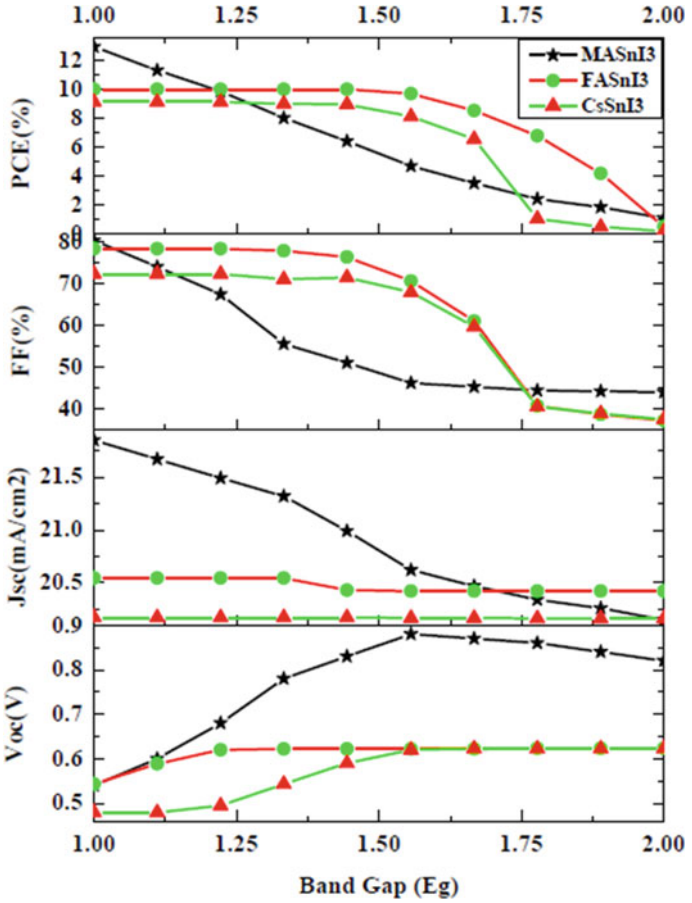

Fig. 3 Variation in solar parameters with band gap of photovoltaic device

Table 3 Optimized parameters attained while varying bandgap

Perovskite Layer	Voc (V)	Jsc (mA/cm^2)	FF (%)	PCE (%)
$MASnI_3$	0.88	21.85	80.44	12.90
$FASnI_3$	0.62	20.55	78.45	9.99
$CsSnI_3$	0.62	20.17	72.41	9.10

3.3 *Effect of Operating Temperature*

The working temperature for solar cell device varies from 300 to 450 K [8]. As the temperature goes up, deformation happens which leads to more defects. These defects behave as recombination sites and ultimately carrier diffusion length reduces. So power conversion efficiency (PCE) of the device decreases [9]. Best solar cell performance is obtained at 300 K (Fig. 4 and Table 4).

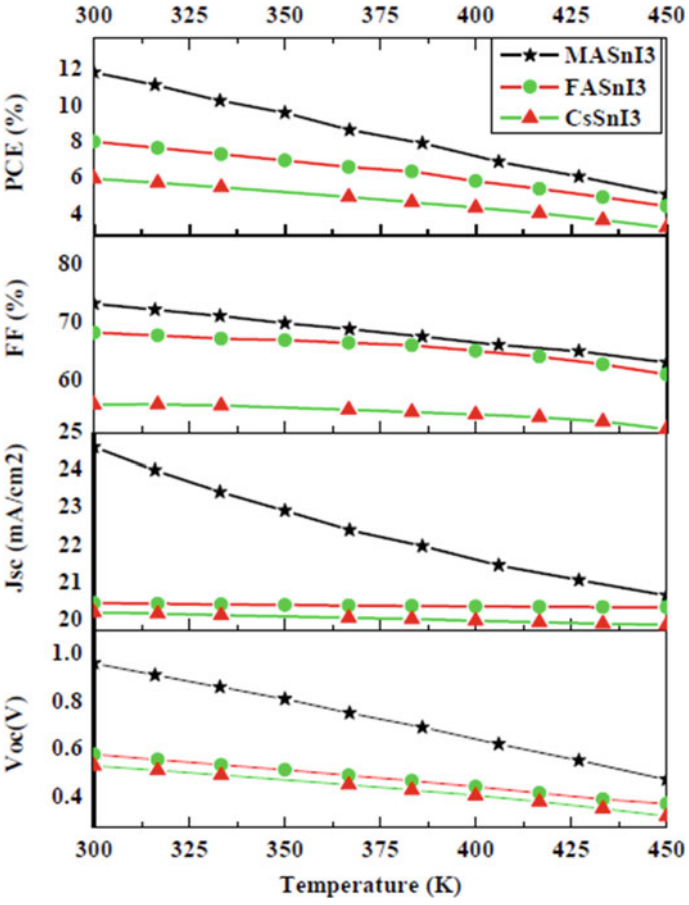

Fig. 4 Variation in solar parameters with operating temperature of photovoltaic device

Table 4 Optimized parameters attained while varying operating temperature

Perovskite layer	Voc (V)	Jsc (mA/cm^2)	FF (%)	PCE (%)
$MASnI_3$	0.96	24.61	73.19	11.86
$FASnI_3$	0.58	20.42	68.18	8.01
$CsSnI_3$	0.53	20.18	55.82	5.94

3.4 Effect of Thickness

If absorber layer thickness is low then there will be less light absorption and low power conversion efficiency. As thickness increases the number of charge carriers also increases and so does the efficiency of the device. Here we varied the thickness of the perovskite layer from 01 to 1um [9, 10]. As thickness increases current density also increases because of more electron–hole pairs but undesirable recombination sites also come into the picture so after some time efficiency reduces (Fig. 5 and Table 5).

4 J-V and Quantum Efficiency

Current density–voltage (J-V) and quantum efficiency curves are the most essential part of solar cell performance analysis. For each absorber layer, J-V and QE plots are shown in Fig. 6 which are almost identical to each other. Tin-based perovskites have a very narrow bandgap so absorption shifts toward near-infrared region (NIR) [11–13]. Here quantum efficiency curves are covering the whole visible spectrum (400–750 nm) of solar radiation. By analyzing the QE curve, broad absorption maximum up to 98.63% for MASnI3, 89.90% for FASnI3, and 82.71% for CsSnI3 achieved in this simulation work [14, 15] (Table 6).

5 Conclusion

Three different tin-based perovskite solar cells were designed and simulated by SCAPS-1D. Simulated models were investigated by comparing with photovoltaic parameters depicted in the literature. Influence of perovskite thickness, bandgap, defect density, and working temperature was calculated and it revealed that what optimized parameters should be used to prepare perovskite solar cells with excellent efficiency. Miscellaneous candidates for the absorber layer were employed to discuss various photovoltaic parameters. Results clarify that perovskite solar cell with $CH_3NH_3SnI_3$ as an absorber layer can attain comparatively higher PCE which is because of its wide bandgap, excellent stability in air, and good charge carrier mobility as compared to $FASnI_3$ and $CsSnI_3$. Additionally, it is feasible to deposit

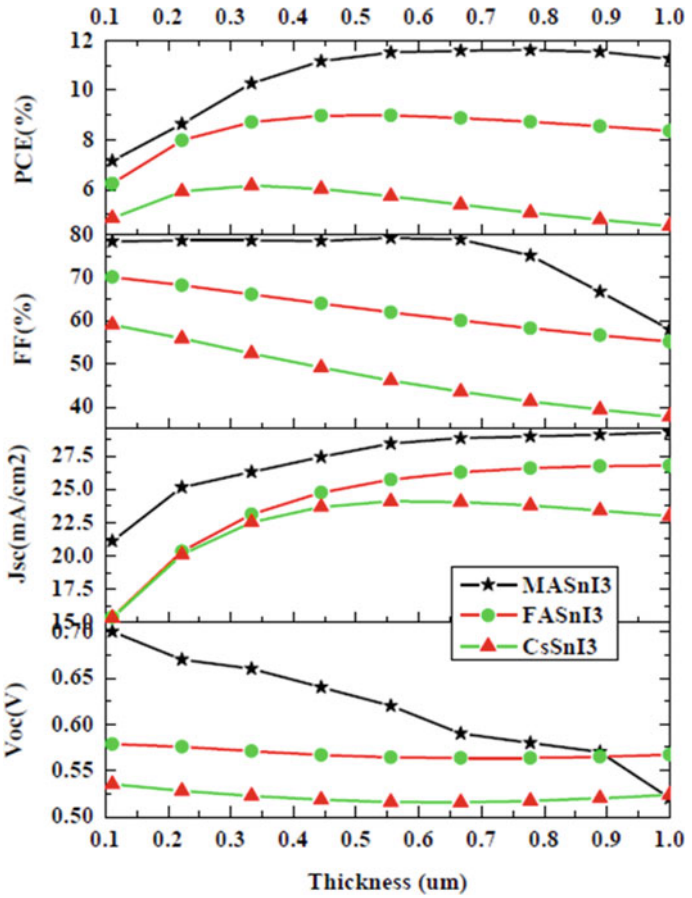

Fig. 5 Variation in solar parameters with thickness of photovoltaic device

Table 5 Optimized parameters attained while varying perovskite thickness

Perovskite layer	Voc (V)	Jsc (mA/cm^2)	FF (%)	PCE (%)
$MASnI_3$	0.7	29.27	79.18	11.61
$FASnI_3$	0.58	26.77	70.11	8.99
$CsSnI_3$	0.53	22.95	59.06	6.16

by solution-based low-temperature processing technique which makes it appropriate with various wafers.

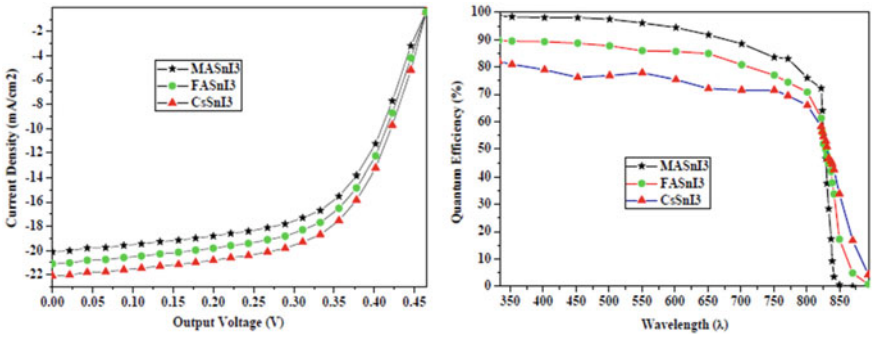

Fig. 6 J-V and QE-Wavelength curves obtained for each absorber layer which are almost identical to each other

Table 6 Comparative optimization for each absorber layer taking all parameters into consideration

Perovskite layer	Voc (V)	Jsc (mA/cm^2)	FF (%)	PCE (%)
$MASnI_3$	1.14	29.27	84.75	12.90
$FASnI_3$	0.97	26.77	80.85	9.99
$CsSnI_3$	0.62	24.81	78.85	9.10

Acknowledgements The authors are thankful to Marc Burgelman, University of Gent, Belgium for endowing SCAPS-1D employed in the simulation study.

References

1. Baktash, A., Amiri, O., Sasani, A.: Improve efficiency of perovskite solar cells by using magnesium doped ZnO and TiO2 compact layers. Superlattices Microstruct. **93**, 128–137 (2016)
2. Hossain, M.I., Alharbi, F.H., Tabet, N.: Copper oxide as inorganic hole transport material for lead halide perovskite based solar cells. Sol. Energy **120**, 370–380 (2015)
3. Lin, L., Jiang, L., Yu, Q., Yu, Y.: Modeling and analysis of HTM-free perovskite solar cells based on ZnO electron transport layer. Superlattices Microstruct. **104**, 167–177 (2017)
4. Minemoto, T., Murata, M.: Theoretical analysis on effect of band offsets in perovskite solar cells. Sol. Energy Mater. Sol. Cells **133**, 8–14 (2015)
5. Sun, X., Asadpour, R., Nie, W., Mohite, A.D., Alam, M.A.: A physics-based analytical model for perovskite solar cells. IEEE J. Photovoltaics **5**(5), 1389–1394 (2015)
6. Minemoto, T., Murata, M.: Impact of work function of back contact of perovskite solar cells without hole transport material analyzed by device simulation. Curr. Appl. Phys. **14**(11), 1428–1433 (2014)
7. Konstantakou, M., Stergiopoulos, T.: A critical review on tin halide perovskite solar cells. J. Mater. Chem. A **5**(23), 11518–11549 (2017)
8. Zhang, A., Chen, Y., Yan, J.: Optimal design and simulation of high-performance organicmetal halide perovskite solar cells. IEEE J. Quantum Electron. **52**(6), 1–6 (2016)

9. Du, H.J., Wang, W.-C., Zhu, J.-Z.: Device simulation of lead-free CH3NH3SnI3 perovskite solar cells with high efficiency. Chin. Phys. B **25**(10), 108802 (2016)
10. Lipovšek, B., Krč, J., Topič, M.: Microtextured light-management foils and their optimization for planar organic and perovskite solar cells. IEEE J. Photovoltaics (2018)
11. Teimouri, R., Mohammadpour, R.: Potential application of CuSbS2 as the hole transport material in perovskite solar cell: a simulation study. Superlattices Microstruct. (2018)
12. Lin, J., Lai, M., Dou, L., Kley, C.S., Chen, H., Peng, F., Sun, J. et al.: Thermochromic halide perovskite solar cells. Nat. Mater. 1 (2018)
13. Bishnoi, S., Pandey, S.K.: Device performance analysis for lead-free perovskite solar cell optimisation. IET Optoelectron. (2018)
14. Olyaeefar, B., Ahmadi-Kandjani, S., Asgari, A.: Classical modelling of grain size and boundary effects in polycrystalline perovskite solar cells. Sol. Energy Mater. Sol. Cells **180**, 76–82 (2018)
15. Tan, K., Lin, P., Wang, G., Liu, Y., Xu, Z., Lin, Y.: Controllable design of solid-state perovskite solar cellsby SCAPSdevicesimulation. Solid-State Electron. **126**, 75–80 (2016)

Growth and Characterization of ZnO Nanostructures: Materials for CO and Ethanol Sensing

Sumita Choudhary, Ajay Agarwal, Vikas Saini, Arnab Hazra, and Subhashis Gangopadhyay

Abstract Controlled growth of ZnO-based nanostructures, starting from a vertical nanowall surface morphology to laterally grown highly anisotropic nanorods/wires formation has successfully been achieved by controlled thermal oxidation of thin Zn films for a temperature range of 100–700 °C. The as-grown ZnO nanorods were further used for carbon monoxide gas sensing at low temperatures (down to 150 °C) as well as ethanol vapour sensing at room temperatures. Thin films of Zn were deposited on glass and silicon substrate at room temperature, using a vacuum-assisted thermal evaporation technique. Structure, morphology and chemical property of ZnO layers were investigated using various surface characterization techniques such as X-ray diffraction (XRD), scanning electron microscopy (SEM), X-ray photoemission spectroscopy (XPS) and Raman spectroscopy. The XRD and SEM results are in very good correlation and showed vertical growth morphology of ZnO nanowall/sheet structures at a relatively lower oxidation temperature up to 400 °C. However, at higher oxidation temperature, lateral growths started to dominate over the vertical growth. Oxidation at 700 °C appeared with laterally grown one-dimensional (1D) ZnO nanowires/rods of high density. Raman spectroscopy and XPS results suggested that the vertical growth is mainly initiated by the metallic Zn film morphology, whereas the lateral growth is strongly dominated by the oxide (ZnO) formation. Finally, laterally grown ZnO nanorods could successfully sense CO gas and ethanol vapour. A drastic enhancement in CO gas sensitivity for a concentration of 230 ppm was clearly observed in dynamic gas flow mode even for a wide range of operating temperature.

S. Choudhary · S. Gangopadhyay (✉)
Department of Physics, Birla Institute of Technology and Science, (BITS) Pilani, Rajasthan 333031, India
e-mail: subhagan@yahoo.com; subha@pilani.bits-pilani.ac.in

A. Agarwal · V. Saini
CSIR-Central Electronics Engineering Research Institute (CEERI) Pilani, Rajasthan 333031, India

A. Hazra
Department of Electronic and Electrical Engineering, Birla Institute of Technology and Science, (BITS) Pilani, Rajasthan 333031, India

S. Mukherjee et al. (eds.), *Computational Mathematics, Nanoelectronics, and Astrophysics*,
Springer Proceedings in Mathematics & Statistics 342,
https://doi.org/10.1007/978-981-15-9708-4_12

Keywords Metal oxides · Semiconductor nanostructure · ZnO nanorods · Gas sensor · CO · Thermal oxidation · Thin films

1 Introduction

Monitoring and early detection of harmful and toxic gases are of very high practical importance for both domestic and industrial environments. Over the past few decades, enormous research efforts have been directed toward the development of suitable gas sensing devices for a number of important fields, including industrial process control, safety measurements, disease diagnoses, and environmental monitoring. Among various dangerous and poisonous gases, carbon monoxide (CO) is one of the most dangerous for human health. CO gas can be produced from an incomplete combustion of fossil fuels which are mostly used in automobiles [1], electricity generation [2] and domestic burning of fuels. Hence, to increase the combustion efficiency and to reduce the pollutant emission, highly sensitive CO gas sensors will be of great technological needs. Similarly, sensing and monitoring of ethanol vapour are also very important to test the alcohol levels of a driver, as well as in the field of chemical synthesis.

Currently, three types of solid-state gas sensors are in large-scale use based on: (a) resistance modulation of semiconducting surface, (b) solid electrolytes (electrochemical) and (c) catalytic combustion (pellistors). However, metal-oxide (MO_x)-based semiconductor gas sensors are the most popular as they offer low cost, high sensitivity and operational simplicity, along with the compatibility of combining with other electronic devices. The active part of a semiconductor gas sensor consists of a metal-oxide surface with a high surface to volume ratio which is exposed to the gas molecules to be detected. The adsorbed gas species can significantly alter the electrical properties of the semiconducting surface by changing the free charge carrier density, which finally leads to the detection/monitoring process. Among various semiconducting (MO_x) gas sensors, post-transition metal oxides with d^{10} electronic configuration such as SnO_2 and ZnO are the most widely used n-type semiconductors for gas sensor applications. Recently, various CO gas sensors have successfully been developed using various metal oxides such as SnO_2, ZnO, CuO, TiO_2, MoO_3 and Fe_2O_3 [3–7]. Among them, ZnO is found to be a very versatile and important material as it offers various types of nanostructures formation. It is an n-type semiconductor of direct band gap of ~3.5 eV [8] and exhibits a wurtzite crystal structure [9]. In general, ZnO nanostructures suffer from an unintentional oxygen vacancy and stoichiometry issues, which finally limits/controls its electronic performances. Moreover, ZnO thin films appear to be transparent to visible light and also having excellent mechanical and thermal stability at room temperature [10]. However, p-type doping is found to be a very difficult for ZnO and only a few acceptors elements are available [11]. All these properties make ZnO-based nanostructures a most widely used material with numerous applications in blue light LEDs [12], UV laser [13], UV detector [14,

15], piezoelectric devices [16], transparent electrodes [17], as well as in gas sensors [18–20].

In order to improve the gas sensing ability of ZnO-based sensors, several approaches have been explored. Various metal ions were doped in ZnO thin films. Au can successfully detect NO_2 [21], while Sn-doped ZnO shows good sensitivity to ethanol vapour [22]. However, in order to improve the sensitivity, a controlled formation of metal-oxide nanostructures required more attention to achieve a higher surface to volume ratio. In this aspect ZnO might be a very good candidate as it may occur in 1D (nanorods [23], needles [24], and wires [25]), 2D (nanosheet [26], pellets) and 3D (nanoflower [27]) nanostructures. Among those, one-dimensional (1D) ZnO nanostructures have a high surface to volume ratio which regarded as a promising material for gas sensing performance [28, 29]. Recently, gas sensors based on ZnO 1D nanostructures have been fabricated with enhanced gas sensing properties [30]. These ZnO gas sensors are based on ZnO nanowires film without any alignment symmetry [29–31]. Various growth techniques have been employed by different groups such as spin pyrolysis [32], sol–gel [33], chemical vapour deposition (CVD) [34], pulsed laser deposition (PLD) [35–37], magnetron sputtering [38], molecular beam epitaxy (MBE) [39] and e-beam evaporation [40]. In this paper, we report a controlled growth of ZnO-based nanostructures by systematically varying the oxidation temperatures, their various analytical characterizations and finally leading towards successful usage in CO gas and ethanol vapour sensing applications.

2 Experimental Details

2.1 Preparation of Nanostructured ZnO Thin Films

Thin Zn films were deposited on glass and Si substrates at room temperature using a vacuum-assisted thermal evaporation technique. Prior to any deposition, substrates were ultrasonically cleaned using ethanol, acetone and iso-propanol in *ex situ* and then dried under dry N_2 gas. During the deposition, the chamber pressure remained ~10^{-5} mbar and the evaporation rate was maintained about ~3 Å/sec to have a uniform and homogeneous Zn film. Afterwards, the as-grown Zn films were thermally oxidized within a furnace in air ambient for different oxidation temperatures (100–700 °C) and durations (3–10 h). A slow cooling rate (10 °C/min) was preferred to minimize the possible thermal stress and improve the crystalline quality of the oxide films.

2.2 Characterization of Thin ZnO Films

Powder X-ray diffractometer (XRD) from Rigaku Mini Flux II was utilized to investigate the crystallographic structures of ZnO thin films. For XRD analysis, Cu-K_α radiation ($\lambda = 0.154$ nm) was used as an X-ray source (30 kV, 15 mA) and θ–2θ scan was performed in a 2θ range of 30–60° with a step size of 0.01° and an acquisition time of 1.00 s. The surface morphology of the ZnO films was analysed with a commercial field emission scanning electron microscopy (FESEM) from Nova NanoSem 450 operated from 0.5 to 30 kV. Raman spectroscopy measurements were also performed to distinguish the oxide phases of the films, using a commercial Raman unit from Horiba Scientific. Finally, X-ray photoemission spectroscopy (XPS) measurement was performed to find the oxidation states of Zn and the purity of the oxides layer. During XPS measurements, the base pressure of the chamber was maintained below $<10^{-9}$ mBar and monochromatic Al K_α (1486.6 eV) line was used as X-ray sources. All binding energies of the emitted photoelectrons are calibrated to the C1s line at 284.5 eV.

2.3 ZnO-Based Gas Sensor System

The CO gas sensing experiments (resistive) of ZnO nanostructures were performed in a dynamic gas flow mode for different temperatures (150–280 °C) and CO gas concentrations (100–320 ppm), However, for ethanol vapour static mode of resistive sensing was used at room temperatures. For gas/vapour sensing measurements, thin layer of gold (~100 nm) was deposited on ZnO nanostructures as top electrodes, using vacuum-assisted thermal evaporation through a Cu figure mask. A schematic side and top views of the ZnO nanostructure-based gas sensor are depicted in Fig. 1a. Figure 1b shows the actual photograph of the ZnO film with top Au electrodes placed over the base heater in gas sensor setup.

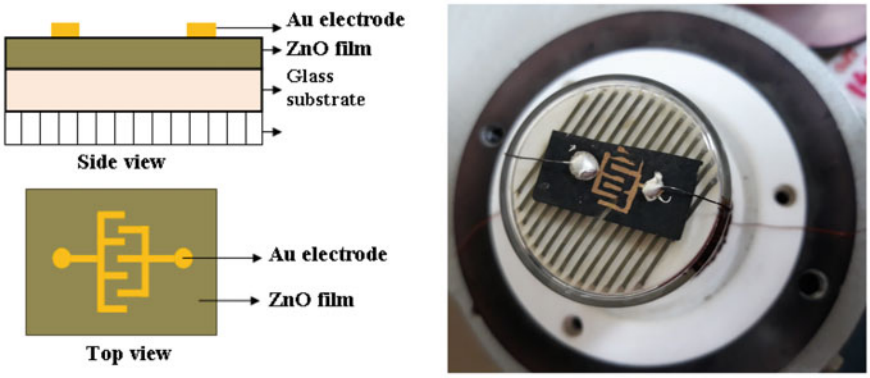

Fig. 1 Schematic side and top views(left) and digital image (right) of the Au/CuO gas sensors on glass substrate

In the case of dynamic gas flow mode, ZnO nanostructure-based sensors were kept over a heater, inside an airtight glass chamber, equipped with a controlled gas flow setup. Dry air (300 CCM) was continuously flown into the airtight glass chamber during the measurement. The CO gas concentrations were controlled by changing the mixing ratio of dry air to CO gas, using a mass flow controller (series 2000, computerized multicomponent gas mixer). The operating temperature for ZnO-based gas sensors was controlled and monitored using a PID temperature microcontroller. CO sensing was carried out on a commercial gas sensing measurement system, where ZnO films were preheated for overnight to improve the thermal stability of the contact junction. The whole device was set up in such a way that data recording and monitoring were automatically performed. In the case of static mode of ethanol vapour sensing, device impedance was measured at room temperatures for two different concentrations of ethanol vapour using GWInstek 6300 LCR meter. Initial vacuum pressure of ~50 mmHg was created in a closed glass chamber and increased qualitatively with time (maximum 90 min).

3 Results and Discussion

3.1 Structural Characterizations

In order to understand the formation of ZnO thin film during thermal annealing of Zn films in air, XRD technique has been extensively utilized, as shown here in Fig. 2. As-deposited Zn thin film shows a strong diffraction peak (2θ value) centred at 43.45°, which can be attributed to the (101) reflection plane of cubic Zn structure (Fig. 2I(a)).

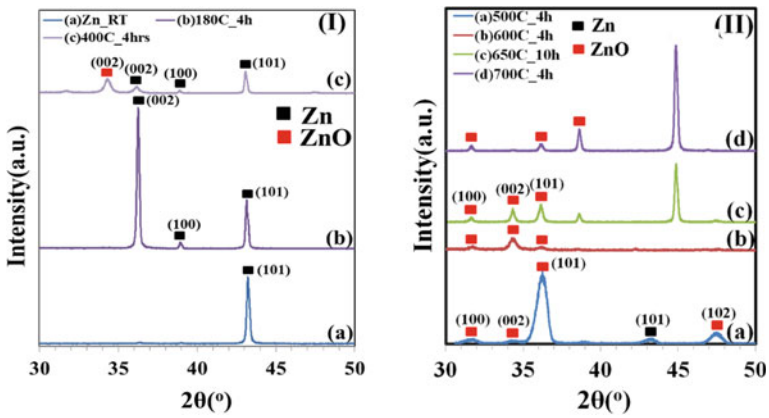

Fig. 2 XRD patterns of thin zinc film I(a) as-grown and thermally oxidized at 180 °C for 4hrs. (I(b)), 400 °C for 4hrs. (I(c)) and (II(a)) 500 °C for 4hrs., 600 °C(II(b)), 650 °C for 10hrs. (II(c)) and 700 °C for 4hrs (II(d))

However, after annealing at 180 °C for 4hrs a drastic change in the XRD pattern has been observed. Two additional diffraction peaks appeared at 36.05 and 39.8°, which are originated from (002) and (100) reflection planes, respectively, of hexagonal Zn structure (Fig. 2I(b)). Surprisingly, no trace of oxide formation is found in XRD at this temperature. Further increase in oxidation temperature of about 400 °C for 4hrs results in ZnO formation and two strong oxide peaks appeared at 34.33 and 36.15°, which represent the (002) and (101) reflection planes of zinc oxide, respectively (Fig. 2I(c)). However, the metallic Zn (101) diffraction peak is also clearly visible here. This finding suggests that oxide formation starts on top of the Zn film surface, when the oxidation temperature is increased to 400 °C. Further increase in oxidation temperature to 500 °C for 4h results in a very different diffraction pattern with a strong and dominating (101) diffraction line of ZnO (Fig. 2II(a)). However, after annealing at 600 °C for 4 h, (002) plane of ZnO starts to dominate over the (100) and (101) planes (Fig. 2II(b)). In case of annealing at 650 °C for 10 h, diffraction pattern drastically changes and the ZnO peaks are getting sharpened (Fig. 2II(c)). In future, increase in oxidation temperature to 700 °C for 4 h results in a very strong (101) peak and (002) peak is almost disappeared (Fig. 2II(d)). However, a sharp and strong diffraction line at 45.62° is also observed for high oxidation temperature, which is not related to any ZnO phase (Fig. 2II(d)). All these results are in good agreement with earlier reported values of ZnO diffraction peak positions [41, 42], JCPDS card No. 79–2205].

3.2 Surface Morphology

To investigate the surface morphologies of the zinc films oxidized at different oxidation temperatures (180–700 °C) and correlated them with above-mentioned XRD patterns, scanning electron microscopy (SEM) was used as a characterization technique. The surface morphology of as-grown thin Zn film shows faceted sidewall morphology of irregular grains (Fig. 3(a)).

Figure 3(b) represents the SEM image of thin Zn films annealed at 240 °C for 4hrs where 2D vertical growth of nanowall structures was clearly observed [30]. It can be concluded from both SEM and XRD results of 240 °C annealing for 4hrs that (002) plane of metallic Zn was mostly responsible for the vertical nanowall structures (perpendicular to the substrate surface). The surface morphology of ZnO film at 400 °C for 4hrs [Fig. 3(c)] was almost similar to nanowall structures observed at 240 °C. After annealing at 400 °C, the sidewall surfaces of the nanowalls became rougher and this might be an indication of oxide formation at this temperature, which is also complementary with earlier XRD result [43, 44]. Oxidation at 500 °C for 4hrs drastically changed the surface morphology of ZnO film from a vertical (nanowall) towards a lateral (nanosheet) growth front (Fig. 3(d)). Nanowalls were further deformed into nanosheets at about 600 °C temperature [45]. Almost all nanowalls were converted into porous nanosheets (Fig. 3(e)). At around 650 °C, another transition of 2D lateral growth to 1D nanorod growth of ZnO thin films have

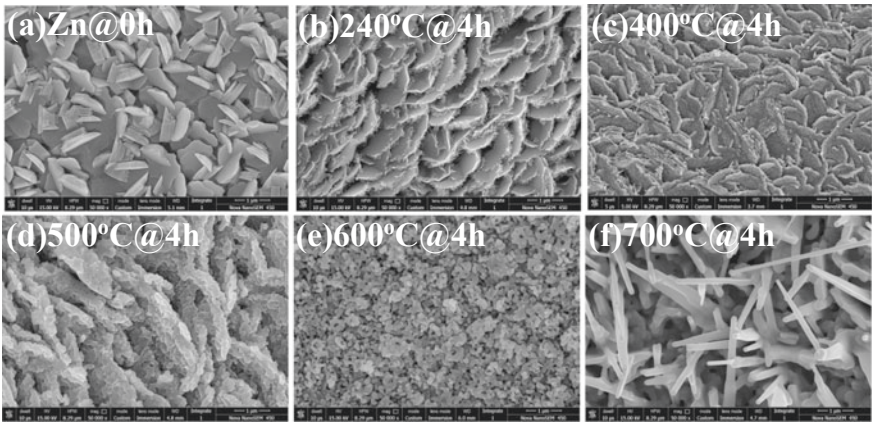

Fig. 3 FESEM results of (**a**) as-grown Zn film and thermally oxidized at (**b**) 240 °C, (**c**) 400 °C, (**d**) 500 °C, (**e**) 600 °C and (**f**) 700 °C for 4 h

been observed (not shown here). Future increased in oxidation temperature to around 700 °C for 4hrs significantly altered the ZnO nanosheet surface morphology to 1D nanorod structure (Fig. 3(f)) [41]. From all XRD and SEM results, it is quite obvious that (002) plane of metallic Zn might be the building block of initial ZnO nanowalls formation and about 500 °C morphological transition of ZnO films from vertical to lateral growth occurred. The strong peak of (002) diffraction line was responsible for the laterally grown porous nanosheet growth at a higher oxidation temperature of 600 °C. Overall, both XRD and SEM results are very much complementary with each other for oxidation temperature ranges from room temperature to 700 °C. A very similar type of ZnO nanostructures morphology was also obtained for the silicon substrate.

3.3 Chemical Properties and Oxidation States

3.3.1 Raman Spectroscopy

To identify the oxide phases of thin zinc films annealed at different oxidation temperatures, Raman spectroscopy has been used as a characterizing tool as shown in Fig. 4. All Raman spectroscopy measurements were performed within a spectral region of 280–700 cm^{-1}. A strong peak appeared at 563.6 cm^{-1} from the as-deposited Zn films which is mainly contributed by the metallic phase of Zn, which can be explained in the following manner. The peak at 563.6 cm^{-1} could be the contribution from the E1 (LO) mode of ZnO associated with oxygen deficiency [46]. Such a strong intensity at 563.6 cm^{-1} indicates that the as-grown Zn film is severely oxygen deficient (*i.e.*, metallic Zn). The intensity of the Raman peak at 563.6 cm^{-1} became lower during

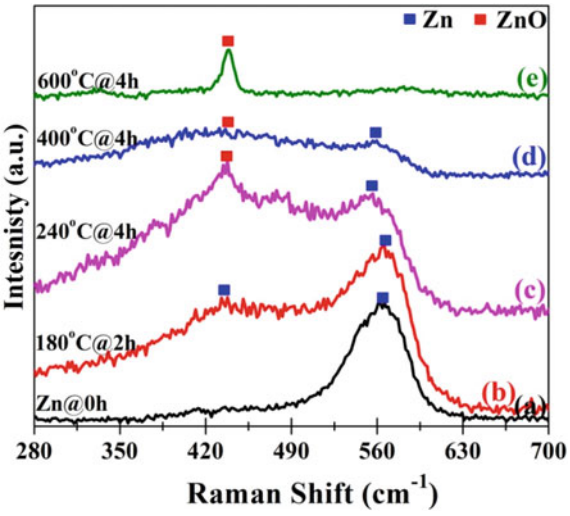

Fig. 4 Raman spectra of as-grown Zn film and thermal oxidation of Zn films at 180, 240, 400 and 600 °C for 4 h in air

the increase of annealing temperature from 180 °C to 400 °C. In addition, the peak at 563.6 cm^{-1} is also shifted towards a lower value at 554.7 cm^{-1}. Both these findings indicate a lower oxygen vacancy within the ZnO film by the formation of an initial oxide layer on top of Zn films which appeared with a mixed phase of metallic Zn and ZnO. Further annealing at 600 °C shows a single phase of ZnO formation. The broad peaks associated with the oxygen vacancies of ZnO films almost disappeared. Moreover, Raman peak at 438.7 cm^{-1} originated from the ZnO E2 mode became significantly stronger, suggesting a very low oxygen vacancy (pure oxide phase, *i.e.* ZnO).

3.3.2 X-ray Photoelectron Spectrometry (XPS)

In order to analyse the chemical compositions and the defect states of the ZnO thin films, XPS measurements of ZnO (nanorods) thin film were performed, as shown in Fig. 5. All binding energy positions of the XPS spectra have been calibrated using the carbon C1s peak (284.5 eV) as a reference. The survey spectrum of ZnO thin film appeared with different binding energy lines of O1s (530.7 eV), Zn 3 s (137.8), Zn 3p (86.9), Zn 3d (8.9 eV), Zn $2p_{3/2}$ (1021.7 eV) Zn $2p_{1/2}$ (1045.2 eV) along with Auger lines of Zn (LMM), Zn (KLL), Zn (LMM_3) [47]. All these binding energy positions are similar to the matrix elements of ZnO wurtzite structure [48, 49]. Figure 5(insets) represent the typical high-resolution scans of O1s (inset (a)) and Zn2p (inset (b)) binding energy spectra. High-resolution scan of the O1s XPS spectrum of the nanorods ZnO thin films shows a strong asymmetry. The main peak centred towards the lower BE (530.9 eV) can be attributed to oxygen atoms within the ZnO lattice whereas a weak shoulder at higher energy side can be due to the O-ions, vacancies, and contaminants. The binding energy positions of $Zn2p_{3/2}$ and

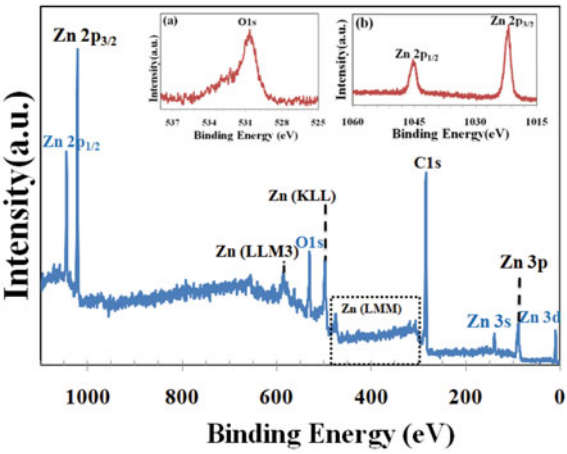

Fig. 5 XPS survey scan of ZnO nanorods formed after air annealing of Zn films at 700 °C for 4 h. Insets show the high-resolution spectra of O1s and Zn2p binding energy peaks

Zn $2p_{1/2}$ appeared at 1021.7 and 1045.2 eV, respectively, which are in agreement with the reported values ZnO [50]. Hence, from the XPS results, it can be concluded that the nanorods are made of pure ZnO with only a few oxygen vacancies.

3.4 Gas Sensing Properties of ZnO Nanostructure

It is quite well known that the gas sensing mechanism of ZnO nanostructures belongs to the surface controlled reaction (surface–volume ratios) in which the adsorption of oxygen plays an important role. Therefore, within this work, ZnO nanorods of high surface-volume ratio were preferred for the creation of high-efficiency ZnO gas sensors. As mentioned earlier, a dynamic gas flow mode was used for the CO gas sensing at lower operating temperatures (230 °C) and a static mode was used for the ethanol vapour sensing at room temperature. Typical resistance curves of ZnO nanorods in the presence of dry air and target gas (CO) concentration from 140 to 320 ppm is depicted in Fig. 6 whereas Fig. 7 represents the ethanol sensing at room temperature.

The common sensing mechanism of n-type semiconductor (ZnO) involves in the formation of a charge depletion layer on the oxide film surface, due to the electron trapping by adsorbed oxygen species [51, 52]. ZnO is an intrinsic n-type semiconductor due to the oxygen vacancies and interstitial zinc defects. In presence of dry airflow, oxygen molecules are generally chemisorbed onto the ZnO surface in the forms of oxygen ions (O^{-2}, O^{-} and $O_2{}^{-}$). Reducing gas (CO) adsorption/desorption reactions lead to the release/trapping of carriers (electrons for n-type) and thus an increase/decrease in electrical conductivity. Therefore, when the reducing gases (CO) are injected into the chamber, it reacts with the oxygen ions and releases electron

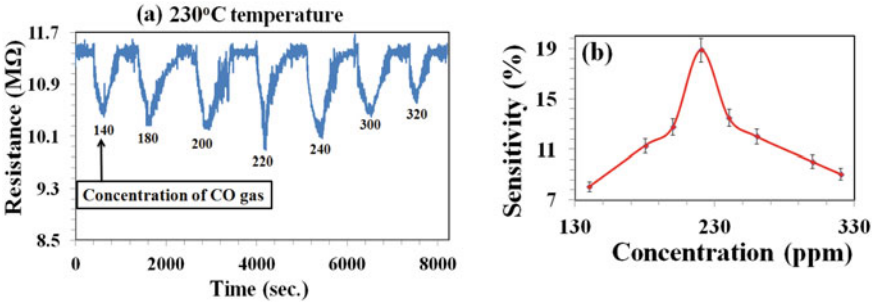

Fig. 6 CO gas sensing for different concentrations of CO at 230 °C temperature using ZnO nanorods: (**a**) resistance curves and (**b**) response curve

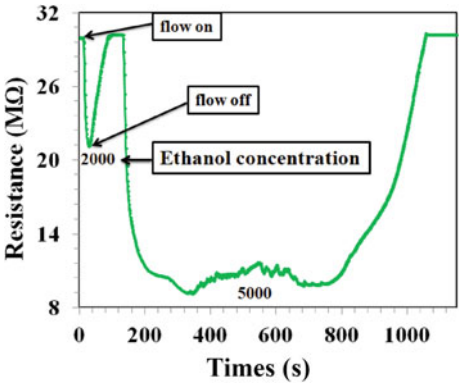

Fig. 7 Ethanol vapour sensing of ZnO nanorods sensor at room temperature

to the conduction band. As a result, an increase in conductivity or decrease in resistance is observed. However, the appropriate reaction mechanisms on ZnO surface for different temperature regimes have been reported by Takata et al. [53] as given below.

$$2CO + O_2^- \rightarrow 2CO_2 + e^- \quad \text{(below 100 °C)}$$

$$CO + O^- \rightarrow CO_2 + e^- \quad \text{(below 100 °C to 300 °C)}$$

$$CO + O^{2-} \rightarrow CO_2 + 2e^- \quad \text{(above 300 °C)}$$

At lower temperature, CO molecules do not have enough thermal energy to react with the surface adsorbed oxygen species. As a result, a significantly high resistance has been observed below 100 °C [53]. Figure 6(a) shows a drastic decrease in surface resistance in presence of CO gas of different concentrations at an operating temperature of 230 °C. The sensitivity '*S*' of the sensor is defined here in the form

of

$$S = \Delta R / R_a,$$

where $\Delta R = |R_a - R_g|$, R_a and R_g are the sensor resistances in air ambient and in target gas (CO) ambient, respectively [55]. The sensitivity of ZnO thin film sensor strongly depends on the concentration of the CO gas. Figure 6(b) shows the sensor response of the ZnO nanorods at 230 °C as a function of CO gas concentration (100–320 ppm). A gradual increase in CO sensitivity from 140 to 220 ppm, and afterwards a decrease in gas sensitivity for further CO gas concentration have been observed. An enhanced CO gas sensitivity has been found for a CO concentration of 220 ppm. Initially, an increase in CO concentration enhances the chemisorption process of CO, which in turn improves the gas sensitivity of the ZnO samples. However, the reduction in sensitivity at higher CO gas concentration (above 220 ppm) might be attributed to the difficulties in the exothermic CO gas adsorption process [56]. Finally, an enhanced CO gas sensitivity has been found for a CO concentration of 220 ppm. Static mode ethanol vapour sensing of ZnO nanorods at room temperatures is shown in Fig. 7 for two different ethanol concentrations. A similar kind of sensing mechanism can be used to explain the ethanol vapour sensing of the ZnO nanorods at room temperature, as explained here [57, 58]:

$$C_2H_5OH + 6O^- \rightarrow 2CO_2 + 3H_2O + 6e^-$$

where the resistance of ZnO nanorods decreases with the concentration of ethanol vapour due to the adsorbed oxygen ions on the surface.

4 Conclusion

Controlled growth and characterization of ZnO-based nanostructures and their successful implementation towards the sensor fabrication for CO gas and ethanol vapour have systematically been studied. A vertical growth morphology of ZnO nanowall/sheet structures at relatively lower oxidation temperature, (below 500 °C), followed by a transition from vertical to lateral growth morphology of layered structure around 550 °C and finally 1D ZnO nanorods/wires growth at 700 °C have been observed. Controlled growth of these nanostructures is found to be very much sensitive to the crystalline plane of ZnO lattice as well as oxidation temperature of the Zn films. Sensing properties of the ZnO nanorods for CO gas and ethanol vapour with various concentrations were investigated. A significantly enhanced CO gas sensitivity (19%) was obtained at a relatively lower temperature of 230 °C for 220 ppm of CO concentration. Moreover, these ZnO nanorods were able to sense ethanol vapour, even at room temperature.

Acknowledgements We gratefully acknowledge the DST-FIST sponsored powder XRD support of the Department of Physics and the vacuum deposition system of the Department of Mechanical Engineering of BITS Pilani for the Cu film deposition. We also acknowledge the instrumental support (gas sensing measurements) from the CEERI, Pilani. We are also thankful for the financial support from the 'BITS Research Initiation Grant' from BITS, Pilani.

References

1. Balan, K.N., Valarmathi, T.N., Reddy, M.S.H., Reddy, G.A., Sai Srinivas, J.K.M.K., Vasan.: IOP Conf. Series: Mater. Sci. Eng. **197**, 012012 (2017a)
2. Kim, D., Chang, I.S.: Bioresour. Technol. **100**, 4527–4530 (2009)
3. Li, C., Lv, M., Zuo, J., Huang, X.: Sensors **15**, 3789–3800 (2015)
4. Leonardi, S.G.: Chemosensors **5**, 17 (2017b)
5. Hubner, M., Simion, C.E., Tomescu-Stanoiu, A., Pokhrel, S., Barsana, N., Weimar, U.: Sens. Actuators B **153**, 347–353 (2011)
6. Maziarz, W., Kusior, A., Zajac, A.T.: Beilstein J. Nanotechnol. **7**, 1718–1726 (2016)
7. Tang, H., Yan, M., Zhang, H., Li, S., Ma, X., Wang, M., Yang, D.: Sens. Actuators B **114**, 910–915 (2006)
8. Meyer, B.K., Alves, H., Hofmann, D.M., Kriegseis, W., Forster, D., Bertram, F., Christen, J., Hoffmann, A., Strabburg, M., Dworzak, M., Haboeck, U., Rodina, A.V.: Phys. Status Solidi B **241**, 231 (2004)
9. Oxide, Z.: Bulk, Thin Films and Nanostructures, Processing, Properties and Application, editted by C. Elsevier, Jagadish and S. J. Pearton (2006)
10. Bacaksiz, E., Parlak, M., Tomakin, M., Ozcelik, A., Karakiz, M., Altunbas, J.: Alloy. Compd. **466**, 447–450 (2008)
11. Janotti, A., Van de Walle, C.G.: Rep. Prog. Phys. **72**(1–29), 126501 (2009)
12. Tsukazaki, A., Kubota, M., Ohtomo, A., Onuma, T., Ohtani, K.: J. Appl. Phys. **44**, 20 (2005)
13. Tang, Z.K., Wong, G.K.L., Yu, P., Kawasaki, M., Ohtomo, A., Koinuma, H., Segawa, Y.: Appl. Phys. Lett. **72**, 3237 (1998)
14. Alaie, Z., Nejad, S.M., Yousefi, M.H.: Mater. Sci. Semicond. Proce. **29**, 16–55 (2015)
15. Basak, D., Amin, G., Mallik, B., Paul, G.K., Sen, S.K.: J. Cryst. Growth **256**, 73–77 (2003)
16. Wang, X., Zhou, J., Song, J., Liu, J., Xu, N., Wang, Z.L.: Nano Lett. **6**, 2768–2772 (2006)
17. Girtan, M.: Sol. Energy Mater. Sol. Cells **100**, 153–161 (2012)
18. Leonardi, S.G.: Chemosensors **5**, 1–28 (2017b)
19. Le Hung, N., Ahn, E., Park, S., Jung, H., Kim, H., Hong, S.K.: and D. Kim J. Vac. Sci. Technol. A **27**, 1347–1351 (2009)
20. Krishnakumara, T., Jayaprakashb, R., Pinnac, N., Donatod, N., Bonavitae, A., Micalie, G., Neri, G.: Sens. Actuators B **143**, 198–204 (2009)
21. Dilonardo, E., Penza, M., Alvisi, M., Di Franco, C., Palmisano, F., Torsi, L., Cioffi Beilstein, L.: J. Nanotechnol. **7**, 22–31 (2016)
22. Zhang, P., Pan, G., Zhang, B., Zhen, J., Sun, Y.: Mater. Res. **17**, 817–822 (2014)
23. Wahab, H.A., Salama, A.A., El-Saeid, A.A., Nur, O., Willander, M., Battisha, I.K.: Results in Phys. **3**, 46–51 (2013)
24. Cao, B., Cai, W., Zeng, H.: Appl. Phy. Lett. **88**, 161101–1–161101–3 (2006)
25. Wang, X., Ding, Y., Li, Z., Song, J., Wang, Z.L.: J. Phys. Chem. C**113**, 1791–1794 (2009)
26. Umar, A., Hahn, Y.B.: Nanotechnology **17**, 2174–2180 (2006)
27. Zhang, H., Yang, D., Ji, Y., Ma, X., Xu, J., Que, D.: J. Phys. Chem. B **108**, 3955–3958 (2004)
28. Zhang, D.H., Li, C., Liu, X.L., Tang, T.: and C. W. Zhou Appl. Phys. Lett. **83**, 1845 (2003)
29. Wan, Q., Wang, T.H.: Chem. Commun. **30**, 3841 (2005)
30. Li, Q.H., Liang, Y.X., Wan, Q., Wang, T.H.: Appl. Phys. Lett. **85**, 6389 (2004)

31. Chen, Y.J., Nie, L., Xue, X.Y., Wang, Y.G., Wang, T.H.: Appl. Phys. Lett. **88**, 083105 (2006)
32. Ramesh kumar, C., Subalakshmi, R.: J. Chem. Pharma. Res. **7**, 459 (2015)
33. Zegadi, C., Abdelkebir, K., Chaumont, D., Adnane, M., Hamzaoui, S.: Adv. Mat. Phys. Chem. **4**, 93 (2014)
34. Li, B.H., Zhang, J.Y., Zhao, D.X., Fan, X.W., Tang, Z.K.: J. Cryst. Growth **373**, 301–302 (2007)
35. Tsoutsouva, M.G., Panagopoulos, C.N., Papadimitriou, D., Fasaki, I., Kompitsas, M.: Mater. Sci. Eng. B **176**, 480–483 (2011)
36. Sun, X.W., Kwok, H.S.: J. Appl. Phys. **86**, 408 (1999)
37. Jin, B.J., Im, S., Lee, S.Y.: Thin Solid Films **366**, 107–110 (2000)
38. Hosseinnejad, M.T., Shirazi, M., Ghoranneviss, M., Hantehzadeh, M.R., Darabi, E.: Inorg. Organomet. Polym. **26**, 405 (2016)
39. Lu, Y.M., Wang, X., Zhang, Z.Z., Shen, D.Z., Yao, B., Li, B.H., Zhang, J.Y., Zhao, D.X., Fan, X.M., Tang, Z.K.: J. Cryst. Growth **301–302**, 373–377 (2007)
40. Mahmood, A., Ahmed, N., Raza, Q., Khan, T.M., Mehmood, M., Hassan, M.M., Mahmood, N.: Phys. Scr. **82**(1–8), 065801 (2010)
41. Khanlary, M.R., Vahedi, V., Reyhani, A.: Molecules **17**, 5021–5029 (2012)
42. Lim, K., Hamid, M.A.A., Shamsudin, R., Al Hardan, N.H., Mansor, I., Chiu, W.: Materials **9**(4), 300 (2016)
43. Isah, K.U., Ramalan, A.M., Ahmadu, U., Ibrahim, S.O., Yabagi, J.A., Jolayemi, B.J.: Asian J. Appl. Sci. **9**, 159–169 (2016)
44. A. Umar and Y. B. Hahn Nanotechnology **17,** 2174–2180(2006)
45. Exarhos, G.J., Sharma, S.K.: Thin Solid Films **270**, 27 (1995)
46. Ryu, H.W., Park, B.S., Akbar, S.A., Lee, W.S., Hong, K.J., Seo, Y.J., Shin, D.C., Park, J.S., Choi, G.P.: Sens. Actuators B **96**, 717–722 (2003)
47. Kumar, N., Srivastava, A.K., Patel, H.S., Gupta, B.K., Varma. G.D.: Eur. J. Inorg. Chem. **2015**, 1912–1923 (2015)
48. Ievtushenko, A., Khyzhun, O., Shtepliuk, I., Tkach, V., Lazorenko, V., Lashkarev, G.: Acta Phys. Pol. A **124**, 858–861 (2013)
49. Zulkifli, Z., Subramanian, M., Tsuchiya, T., Rosmi, M.S., Ghosh, P., Kalita, G., Tanemura, M.: RSC Adv. **4**, 64763 (2014)
50. Wen, Z., Zhu, L., Zhang, Z., Ye, Z.: Sens. Actuators B **208**, 112–121 (2015)
51. Williams, D.E.: Sens. Actuators B **57**, 1 (1999)
52. Kolmakov, A., Zhang, Y., Cheng, G., Moskovits, M.: Adv. Mater. **15**, 997 (2003)
53. Takata, M., Tsubone, D., Yanagida, H.: J. Am. Ceram. Soc. **59**, 4–8 (1976)
54. Aroutiounian, V.M., Aghababian, G.S.: Sens. Actuators B **50**, 80–84 (1998)
55. Hsiao, C.C., Luo, L.S.: Sensors **14**, 12219–12232 (2014)
56. Chang, S.J., Hsueh, T.J., Chen, I.C., Huang, B.R.: Nanotechnology **19**(1–5), 175502 (2008)
57. Shewale, P.S., Yu, Y.S., Kim, J.H., Bobade, C.R., Uplane, M.D.: J. Anal. Appl. Pyrolysis **112**, 348–356 (2015)
58. Wang, J., Yang, J., Han, N., Zhou, X., Gong, S., Yang, J., Hu, P., Chen, Y.: Mater. Des. **121**, 69–76 (2017)

First-Principle Study of Cl Functionalized Armchair AlN Nanoribbons

Rachana Yogi and Neeraj K. Jaiswal

Abstract Density functional theory-based first-principle calculations have been performed to study the structural and electronic properties of Cl functionalized armchair AlN nanoribbons (AAlNNRs). Functionalization was modeled in five different configurations. It is revealed that all structures prefer non-magnetic ground state. Moreover, functionalization of Al (N) by Cl (H), i.e., Cl -AlNNR-H results in energetically most favorable configuration over others. Further, the electronic bandgap depends strongly upon the Cl functionalization of the ribbon. Semiconductor to metallic transition is also noticed for selective structures which may find potential applications in upcoming nanoelectronic devices.

Keywords AlN · Nanoribbon · Fermi energy · Band structure

1 Introduction

The successful synthesis of single and multi-layer aluminum nitride (AlN) nanosheets promotes its applications in advanced electronic devices. The geometry of 2D AlN is very much similar to graphene [1–3]. AlN nanoribbons (NRs) exhibit electronic properties completely dependent on edge shape of NRs. Three different types of edges known as zigzag, armchair, and chiral have been obtained in NRs [4]. AlN is a large bandgap semiconductor. Pristine zigzag AlNNRs (ZAlNNRs) are stable with in-direct bandgap (3.4 eV) [5], whereas armchair AlNNRs (AAlNNRs) exhibit direct bandgap (3.9 eV). The availability of large bandgap and large ionic nature of Al-N bonds makes AlNNR a potential candidate for optical and nanoscale electronic devices [4]. Du et al. [6] investigated the structural and electronic properties of armchair AlNNR with different edge terminated by F and Pd. The results indicate

R. Yogi · N. K. Jaiswal (✉)
Discipline of Physics, Indian Institute of Information Technology Design & Manufacturing, Jabalpur 482005, India
e-mail: neeraj@iiitdmj.ac.in

S. Mukherjee et al. (eds.), *Computational Mathematics, Nanoelectronics, and Astrophysics*, Springer Proceedings in Mathematics & Statistics 342,
https://doi.org/10.1007/978-981-15-9708-4_13

that the bandgap increased after adsorption of F and H on the edges on NR. The bandgap remains direct after adsorption of F and H atom and adsorption of Pd makes the NR metallic in nature. The effect of Mn doping on zigzag AlNNR is also explored by Aghili et al. [4], and they observed half-metallic behavior which extends the application of AlNNR for spin filtering in nano-electronics. A systematic study of sensing of Cl on ZBNNR is also carried out by Srivastava et al. [7], which indicates that bare ZBNNR posses half-metallic nature, whereas adsorption of Cl turns them semiconductor. The negative differential resistance (NDR) behavior is also observed in ZBNNR. The electronic and transport properties of ZGaNNR with edge fluorination were also investigated revealing NDR behavior [8]. Cl is yellow-green gas with sharp odor [9]. The atomic mass of Cl is larger than oxygen, therefore, the presence of Cl gas near the ground level is probably high. Nowadays, Cl is highly used chemical in various industries. Major applications of Cl are in disinfectants, bleaching industry, purification of drinking and swimming pool water, etc. [10, 11]. In cold storage to control the growth of bacteria a large amount of Cl gas is used. The high concentration of Cl gas exposer is very much harmful to human health [12]. Therefore, it would be interesting to investigate the interaction of Cl with AlN nanoribbons.

2 Computational Details

The structural and electronic properties of AAlNNR with Cl functionalization have been investigated using first principles calculations within density functional theory (DFT) as accomplished in Atomistix Toolkit Virtual NanoLab (ATK-VNL) package [13]. The generalized gradient approximation (GGA) of Perdew, Burke, and Ernzerhof was used to account the exchange correlation [14]. Further, we have considered double ζ polarized basis set for all constituent atoms. The Monkhorst Pack Grid [15] for k-point sampling was selected $1 \times 1 \times 50$ for the sampling of the Brillouin zone centered at Γ. 70 Ry mesh cutoff energy was used. During the geometry optimization, we used Puley mixer algorithm with 1×10^{-5}Ry tolerance for self-consistent iteration loop, and all the atoms are free to change their initial position toward minimum energy state. The optimization was carried until the force and stress between each atom is less than 0.05 eV/Angstrom and 0.05eV/Å^3, respectively. In Fig. 1, the geometry of bare (Fig. 1a) AlNNR and pristine Fig. 1b AlNNR are presented. Figure 2 shows the optimized considered configurations of AAlNNR. Five different configurations are considered for Cl functionalization. In Fig. 2, the configuration (a) Bare AlNNR, (b) Pristine AlNNR, (c) both edges are functionalized by Cl (Cl-AlNNR-Cl), (d) Cl adsorbed on edge Al while edge N having H atom (Cl-AlNNR-H), (e) Cl attached on edge N and edge Al having H atom (H-AlNNR-Cl), (f) and (g) Cl adsorbed on edge Al (N) and another edge is bare (Cl-AlNNR and AlNNR-Cl).

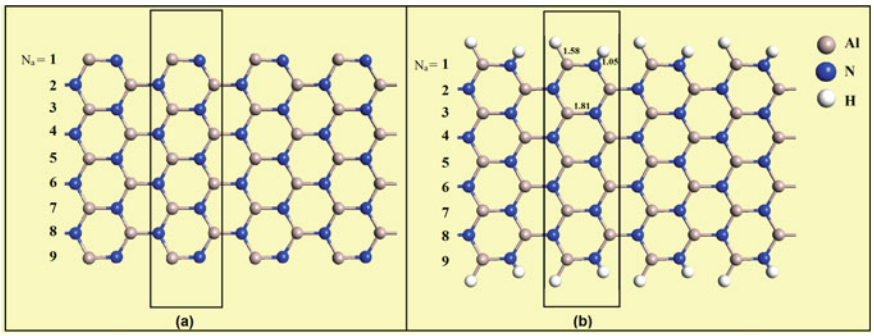

Fig. 1 Schematic diagrams of armchair **(a)** bare and **(b)** pristine nanoribbon at width 9

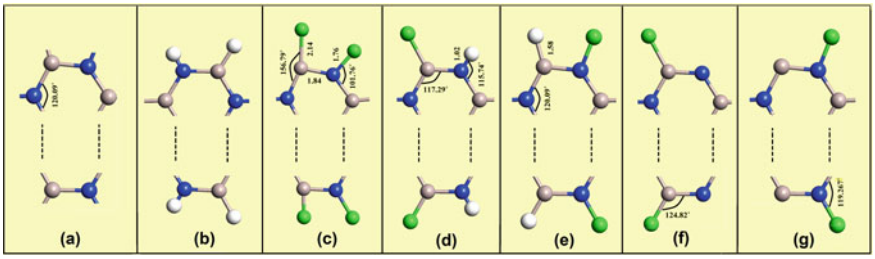

Fig. 2 The optimized structures of AAlNNR **a** Bare, **b** Pristine **c** Cl-AlNNR-Cl, **d** Cl-AlNNR-H, **e** H-AlNNR-Cl, **f** Cl-AlNNR, and **g** AlNNR-Cl. The blue, grey, white, and green spheres represent N, Al, H, and Cl atoms, respectively

3 Result and Discussion

3.1 Structural Stability

Initially, the supercell model of armchair AlNNR is optimized and the obtained lattice constant is 5.43 Å. The structures under investigations are depicted in Fig. 2. The optimized bond length of AAlNNR for Al-N, Al-Cl, and N-Cl are 1.84 Å, 2.14 Å, and 1.76 Å respectively. The optimized bond lengths and lattice constant show good agreement with previously reported data [16, 17]. The optimized geometry shows that there are insignificant changes in the structure parameters (like bond length, bond angle) for all the considered configurations. To comment on the structural stability of considered configurations, we have calculated the adsorption energy (E_{ad}) for pristine and Cl adsorbed using the following relation:

E_{ad}= 1/n [E_t-E_b-n($E_{Cl/H}$)] [18].

where E_t, E_b, $E_{Cl/H}$ are the total energies of considered configurations, bare NR, isolated Cl or H atom used for functionalization and n is the number of Cl/H atoms.

Table 1 The calculated adsorption energy (E_{ad}), Fermi energy (E_F), and bandgap (Eg) in eV as a function of ribbon width for considered configurations of AAlNNR

Configurations	Width (N_a)	E_{ad}	E_F	Eg
Pristine	5	–4.97	–2.55	4.0
	7	–4.79	–2.71	3.9
	9	–4.97	–3.10	3.8
Cl-AlNNR-Cl	5	–4.13	–3.17	2.9
	7	–4.14	–3.30	3.0
	9	–4.15	–3.29	3.0
Cl-AlNNR-H	5	–5.55	–3.01	3.9
	7	–5.55	–33.15	3.9
	9	–5.55	–3.11	3.8
H-AlNNR-Cl	5	–3.64	–3.38	2.9
	7	–3.64	-3.44	2.7
	9	–3.64	–3.34	2.8
Cl-AlNNR	5	–4.30	–6.00	M
	7	–4.21	–5.97	M
	9	–4.20	–5.93	M
AlNNR-Cl	5	–2.53	–3.53	M
	7	–2.54	–3.74	M
	9	–2.54	–3.74	M

The calculation of E_{ad} for pristine and considered configurations for Cl adsorption are tabulated in Table 1. It is evident from Table 1 that the E_{ad} for all the cases are negative which indicates that all the considered configurations are exothermic in nature as well as thermodynamically stable. It is also observed that irrespective of ribbon width, the adsorption energy of Cl-AlNNR-H is energetically more favorable than other considered configurations. Similarly, we also observed that the configuration AlNNR-Cl is least stable. One can also conclude that ribbon widths do not affect the qualitative behavior of NRs.

3.2 Electronic Properties

To analyze the electronic properties of AAlNNR functionalized with Cl, we modeled five different configurations. We consider edges as adsorption site as in NRs the edges are more reactive as compare to central region because of dangling bonds. The guest atom (chlorine in our case) when adsorbed on the edges changes electronic properties as observed from the band structure and density of states (DOS) profiles.

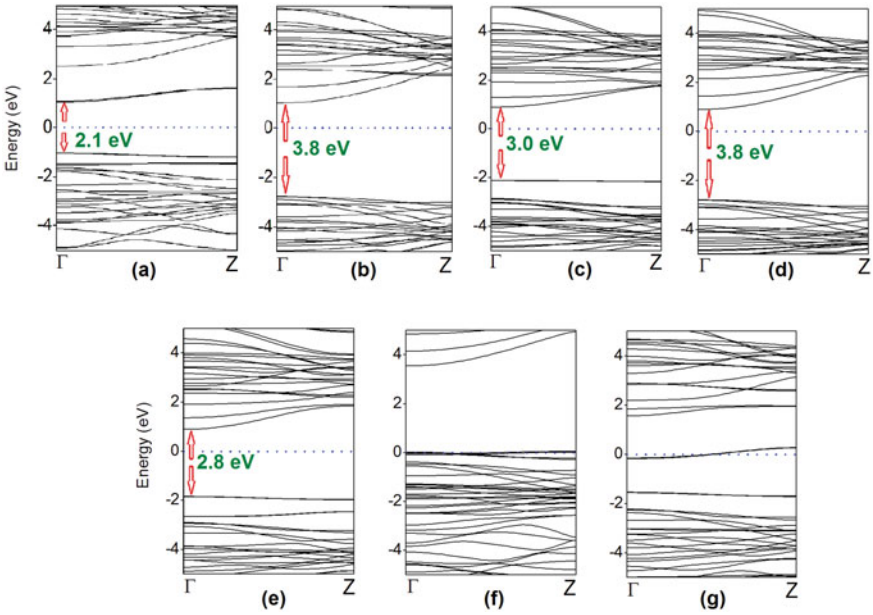

Fig. 3 The electronic band structures of considered AAlNNR in different configurations **a** Bare, **b** Pristine **c** Cl-AlNNR-Cl, **d** Cl-AlNNR-H, **e** H-AlNNR-Cl, **f** Cl-AlNNR, and **g** AlNNR-Cl. The dotted line at 0 eV represents the Fermi level

In the present work, we explored the electronic properties of AAlNNRs at various ribbon widths ($N_a = 5, 7$ and 9). However, since the findings are qualitatively similar, here we present results for $N_a = 9$ NRs. First, we calculated the band structure of armchair NR with bare and pristine configurations as shown in Fig. 3a, b and compared the findings with obtained results. It is observed that bare and pristine AAlNNR exhibits semiconductor behavior with direct bandgap. It is noticed (Table 1) that the Fermi energy (E_F) shifts as the ribbon width N_a changes. The Fermi energy of Cl functionalized AlNNR is observed to be shifting downward as compared to the pristine one which indicates toward introduction of p-type character. Moreover, Cl-AlNNR is found to exhibit the most negative Fermi energy value which supports strong p-type behavior of this structure among all.

The obtained electronic band structures of all considered structures are compared in Fig. 3. It is noticed that functionalization of both the edges of ribbons results in semiconducting behavior with the bandgap greater than the bare NRs. However, the bandgap remains direct similar to that of bare one. The reduction in E_g as compared to pristine NR is noticed upon adsorption of Cl atoms. Cl-AlNNR and AlNNR-Cl configurations (Fig. 3f, g) show metallic nature which is due to the generation of additional energy states near the Fermi level. The observed behavior is further confirmed by corresponding DOS profiles (Fig. 4).

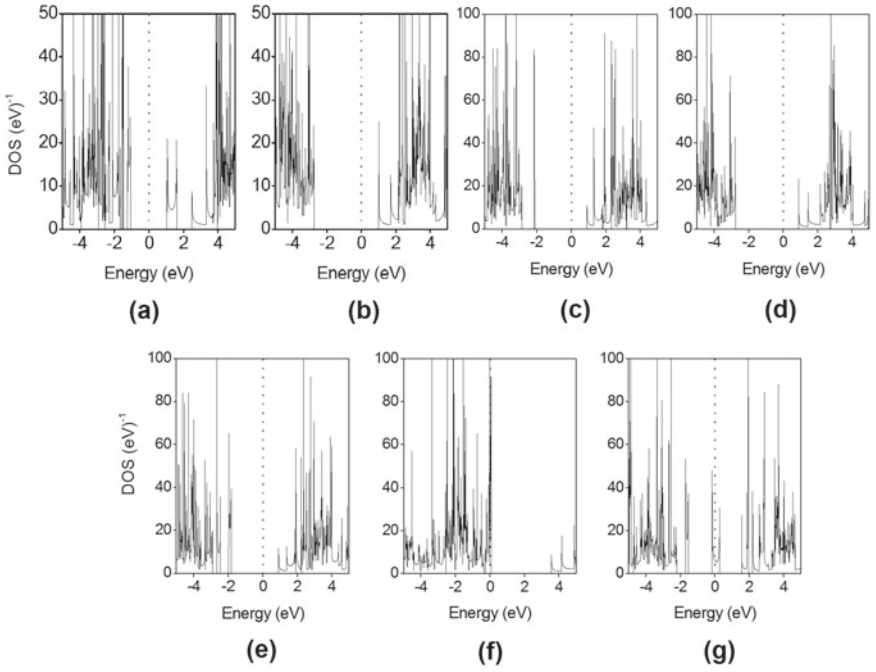

Fig. 4 The DOS profiles for considered AAlNNR in different configurations **a** Bare, **b** Pristine **c** Cl-AlNNR-Cl, **d** Cl-AlNNR-H, **e** H-AlNNR-Cl, **f** Cl-AlNNR, and **g** AlNNR-Cl with Cl functionalization. The dotted line at 0 eV represents the Fermi level

It is noticed that DOS profiles further support the corresponding band structures. The absence of electronic states around the Fermi level for bare and both edges functionalized AlNNR ensures typical semiconducting behavior. On the other hand, the presence of electronic peaks across the Fermi level in one edge functionalized NRs further confirms their metallic character. Thus, a semiconducting to metallic transition could be possible in AAlNNR via Cl functionalization.

4 Conclusion

In Summary, we have performed first-principle calculations to study the functionalization of Cl atom on the edges of AAlNNR. We find that Cl atom significantly influences the electronic properties of AlNNRs. All the NRs are stable in NM ground state after adsorption of Cl atom. The Cl-AAlNNR-H configuration is the most preferred among all. The variation in bandgap can also be observed in all the cases. Present findings indicate the possibility to tailor the electronic properties of AAlNNR via selective Cl functionalization.

References

1. Tsipas, P., Kassavetis, S., Tsoutsou, D., Xenogiannopoulou, E., Golias, E., Giamini, S., Grazianetti, C., Chiappe, D., Molle, A., Fanciulli, M., Dimoulas, A.: Evidence for graphite-like hexagonal AlN nanosheets epitaxially grown on single crystal Ag (111). Appl. Phys. Lett. **103**, 251605-1-251605-4 (2013)
2. Bacaksiz, C., Sahin, H., Ozaydin, H., Horzum, S., Senger, R.T., Peeters, F.M.: Hexagonal AlN: Dimensional-crossover-driven band-gap transition. Phys. Rev. B **91**, 085430-085430–7 (2015)
3. Jiao, Y., Du, A., Zhu, Z., Rudolph, V., Smith, S.C.: Adsorption of carbon dioxide and nitrogen on single-layer aluminum nitride nanostructures studied by density functional theory. J. Phys. Chem. C **114**, 7846–7849 (2010)
4. Aghili, S., Beiranvand, R., Elahi, S., Abolhasani, M.: Half-metallic ferromagnetism in Mn-doped zigzag Al N nanoribbon from first-principles. J. Magn. Magn. Mater. **420**, 122–128 (2016)
5. Du, A., Smith, S.C., Lu, G.: First-principle studies of electronic structure and C-doping effect in boron nitride nanoribbon. Chem. Phys. Lett. **447**, 181–186 (2007)
6. Du, X.-J., Chen, Z., Zhang, J., Ning, Z.-R., Fan, X.-L.: First-principles study on armchair Al N nanoribbons with different edge terminations. Superlattices Microstruct. **67**, 40–46 (2014)
7. Srivastava, P., Jaiswal, N.K., Tripathi, G.K.: Chlorine sensing properties of zigzag boron nitride nanoribbons. Solid State Commun. **185**, 41–46 (2014)
8. Inge, S.V., Jaiswal, N.K., Kondekar, P.N.: Realizing negative differential resistance/switching phenomena in zigzag Ga N nanoribbons by edge fluorination: A DFT Investigation. Adv. Mater. Interf. **4**, 1700400-1–1700400-9 (2017)
9. Cotton, A.F., Wilkinson, G., Bochmann, M., Murillo, C.A.: Advanced Inorganic Chemistry. Wiley, New YorK (1999)
10. Martinez, T.T., Long, C.: Explosion risk from swimming pool chlorinators and review of chlorine toxicity. J. Toxicol. Clin. Toxicol. **33**, 349–354 (1995)
11. Babu, R.V., Cardenas Jr., V., Sharma, G.: Acute respiratory distress syndrome from chlorine inhalation during a swimming pool accident: a case report and review of the literature. J. Intensive Care Med. **23**, 275–280 (2008)
12. White, C.W., Martin, J.G.: Chlorine gas inhalation: human clinical evidence of toxicity and experience in animal models. Proc. Am. Thorac. Soc. **7**, 257–263 (2010)
13. Brandbyge, M., Mozos, J.-L., Ordejón, P., Taylor, J., Stokbro, K.: Density-functional method for nonequilibrium electron transport. Phys. Rev. B **65**, 165401-1–165401-17 (2002)
14. Perdew, J.P., Burke, K., Ernzerhof, M.: Generalized gradient approximation made simple. Phys. Rev. Lett. **77**, 3865–3868 (1996)
15. Monkhorst, H.J., Pack, J.D.: Special points for Brillouin-zone integrations. Phys. Rev. B **13**, 5188–5192 (1976)
16. Qi, Y.-Y., Zhang, Y., Zhang, J.-M., Ji, V., Xu, K.-W.: Structural and electronic properties of a single c chain doped zigzag aln nanoribbon. Comput. Theor. Chem. **974**, 151–158 (2011)
17. Rao, Q.-L., Wang, Y.-X., Chen, Z., Du, X.-J., Sun, T.-T.: A first-principles study of a single C-chain doped Al N nanoribbons. Superlattices Microstruct. **84**, 36–44 (2015)
18. Sun, G., Zhao, P., Zhang, W., Li, H., He, C.: Adsorption of gas molecules on armchair Al N nanoribbons with a dangling bond defect by using density functional theory. Mater. Chem. Phys. **186**, 305–311 (2017)

Studies on Resistive Switching of $Cu/Ta_2O_5/Pt$ Devices for Non-volatile Memory Application

T. Nivedya, V. K. Sahu, R. S. Ajimsha, A. K. Das, and P. Misra

Abstract In recent times, memory devices based on resistive switching (RS) phenomena in dielectric materials have become a strong contender for the futuristic universal memory. Among other materials being explored for RS application, tantalum pentaoxide (Ta_2O_5) has emerged as potential candidate due to its large dielectric constant and compatibility with the existing complementary metal-oxide semiconductor process. In view of this, we have studied the resistive switching memory characteristics of Ta_2O_5 thin film in $Cu/Ta_2O_5/Pt$ device configuration. About 200 nm thick films of Ta_2O_5 were deposited on platinum-coated silicon (Pt/Si) substrate by Pulsed Laser Deposition (PLD) method. On the top of Ta_2O_5 thin film, Cu electrodes of radius ~100 μm and thickness ~ 100nm were grown by RF magnetron sputtering using shadow masking. The RS behaviour of $Cu/Ta_2O_5/Pt$ devices was studied by current–voltage (I-V) measurements at room temperature. The as-fabricated $Cu/Ta_2O_5/Pt$ devices showed repeatable and reliable, non-volatile bipolar resistance switching for 100 cycles, indicating good endurance. Due to virgin low resistance state of the device, the initial electroforming step was not required for bipolar RS. The mean resistance of high resistance state (HRS) and low resistance state (LRS) was ~300 MΩ and 500 Ω respectively with very high resistance ratio of $\sim 10^6$. The $Cu/Ta_2O_5/Pt$ devices showed good data retention up to 10^3 s. The resistive switching mechanism in $Cu/Ta_2O_5/Pt$ devices was understood in terms of redox reaction based formation and rupturing of conducting filaments constituting copper ions. The conduction mechanism in LRS was explained on the basis of Ohmic

T. Nivedya (✉)
Department of Physics, National Institute of Technology Karnataka, Surathkal, Mangalore 575 025, India
e-mail: tnivedya@gmail.com

V. K. Sahu · R. S. Ajimsha · A. K. Das · P. Misra (✉)
Oxide Nano Electronics Lab, Laser Material Processing Division, Raja Ramanna Centre for Advanced Technology, Indore 452 013, India
e-mail: pmisra@rrcat.gov.in

V. K. Sahu · P. Misra
Homi Bhabha National Institute, BARC Training School Complex, Anushaktinagar, Mumbai 400 094, India

S. Mukherjee et al. (eds.), *Computational Mathematics, Nanoelectronics, and Astrophysics*, Springer Proceedings in Mathematics & Statistics 342,
https://doi.org/10.1007/978-981-15-9708-4_14

conduction, whereas Schottky emission and space charge limited conduction (SCLC) were found as possible conduction mechanisms in HRS. Our studies clearly show that Ta_2O_5-based resistive switching devices may have applications in futuristic universal non-volatile memory technology.

Keywords Resistive switching · Ta_2O_5 thin film · Pulsed Laser Deposition

1 Introduction

Non-volatile Memories (NVM) have been playing a significant role in today's advance electronic devices. Complementary metal-oxide semiconductor (CMOS) based flash memory, one among the well-developed and widely used NVM devices due to its low cost, high integration density and reliability, is facing technological limitations in terms of scaling potential and speed limitations like high operational voltage (~12 V), difficulty in scaling below 20 nm technology nodes, a limited number of write/erase cycles ($<10^6$), low write/erase speed (~μs/ms), etc. [1]. Therefore, research on next generation NVMs is being pursued widely both in academia and industry. Even though ferroelectric random access memory (FeRAM) [2] phase-change memory (PCM) [3], etc. have been proposed as candidates for future memory technology, Resistive Random Access Memory (RRAM or ReRAM) is being considered as the most competitive as well as promising one to replace the existing CMOS based memory technology, mainly because of the simple device structure, ease of fabrication, fast switching, high endurance and low power consumption [4–10]. In addition, most of the popular materials being researched for the RRAM application can be grown easily by the existing fabrication technologies.

Resistive Random Access Memory (RRAM) or Resistive Switching (RS) memory is an NVM, which works on the principle of resistance change, i.e. resistance of the device can be toggled between two resistance states; high resistance state (HRS) and low resistance state (LRS) under an applied voltage. The process of transition from HRS to LRS is called the SET process and LRS to HRS is called the RESET process. During the set process, to prevent the permanent breakdown the current is limited and this current is called compliance current (I_C). In the reset process, compliance current is not needed, as it is a current-controlled phenomenon. The threshold voltage corresponding to set processes is called set voltage (V_{SET}) and the reset process is called reset voltage (V_{RESET}). If both set and reset voltages are of the same polarity, then it is called unipolar RRAM and if they are of opposite polarity then it is called bipolar RRAM. Usually, the resistance states of the pristine devices are HRS. For a pristine device, to initiate the resistive switching behaviour, voltage more than the set voltage is applied. This phenomenon is called electroforming process and the corresponding voltage is called forming voltage. Further in order to read the resistance state of the device, a small read voltage, less than threshold voltages, is applied, and the process is called the read process [11]. The mechanism of switching for the resistive memory switching devices is generally understood in terms of rupture

and reformation of conductive filaments (CF) formed in the dielectric metal-oxide. The CFs are narrow conducting channel having diameter ~ few nanometers, formed within the dielectric and connects the top and bottom electrodes. When the filament has connected the top and bottom electrode the device will be in LRS and whereas when the CF is broken, the device will be in HRS.

As a challenger to flash memory, the development of good RRAM materials which are also compatible with existing memory technology is a major task. Currently TiO_2 [12], Ta_2O_5 [13], HfO_2 [14], NiO [15], and complex oxides such as $LaGdO_3$ and $SmGdO_3$ etc. [6]. have been studied extensively for resistive switching memory applications. Ta_2O_5 is found to be one of the promising materials for resistive switching application due to its high dielectric constant (~25), large bandgap (~4.6 eV), and easy compatibility with existing memory technologies. The aim of this work was to fabricate Cu/Ta_2O_5/Pt-Si RRAM device structures using Pulsed Laser Deposition (PLD) and Radio-Frequency (RF) magnetron sputtering and study the resistive switching characteristics of the devices using current–voltage (I-V) measurements for non-volatile memory application. Various other characterizations such as transmission spectroscopy using UV–Visible spectrophotometer, X-Ray Diffraction (XRD), and Scanning Electron Microscope (SEM) were performed to study the structural and optical properties of PLD grown Ta_2O_5 thin film before device fabrication to ascertain the quality of the grown film.

2 Experimental

As discussed above, we have studied resistive switching behaviour in Cu/Ta_2O_5/Pt-Si device, in which Ta_2O_5 forms the resistive switching oxide layer and Copper (Cu) and platinum (Pt) are top and bottom electrodes, respectively. High-quality Ta_2O_5 has been deposited on Pt/Si by Pulsed Laser Deposition technique.

Properly cleaned Ta_2O_5 target (99.95% pure) in the form of pellet is fixed on the target carousel and Pt-Si substrate is fixed on the substrate holder using silver paste. The chamber is pumped to get a vacuum of ~10^{-3} mbar using a rotary pump and using a turbo molecular pump (TMP) a base vacuum of ~10^{-7} mbar was achieved. The substrate temperature was kept at ~300 °C and Ta_2O_5 thin films were deposited on Pt-Si in an ambiance of oxygen gas (99.95% pure) having a partial pressure 5×10^{-2} mbar. For ablating the Ta_2O_5 target, KrF excimer laser of wavelength 248 nm having energy 150 mJ, repetition rate 10 Hz, and pulse width 30 ns was used. The distance between target and substrate was ~5.5 cm. The numbers of laser pulses were kept at 4500 during deposition to grow the required thickness of ~200 nm.

The top electrode of Cu is deposited on Ta_2O_5/Pt-Si by Radio-Frequency (RF) magnetron sputtering using a shadow mask of diameter 200 μm. The Cu target is cleaned and fixed on a sputter gun. The substrate, Ta_2O_5/Pt-Si is loaded on the substrate holder. Using a rotary pump and TMP a vacuum of ~10^{-7} mbar was achieved inside the sputtering chamber. Argon gas having partial pressure ~1.5×10^{-2} mbar is introduced into the chamber. The deposition was continued for ~15 min using RF

power of ~25 W at room temperature. During deposition, the substrate is continuously rotated to ensure uniform deposition. Thus Cu/Ta_2O_5/Pt-Si devices having Metal–Insulator–Metal structure with Ta_2O_5 thin film of thickness ~200 nm sandwiched between top Cu and bottom Pt electrodes was fabricated.

3 Results and Discussion

To study the optical properties ofTa_2O_5 thin films, optical transmittance spectroscopy of as-fabricated Ta_2O_5 film was performed using UV–Visible spectrophotometer. The obtained spectrum is shown in Fig. 1a. The Ta_2O_5 thin film showed a high transmission of ~80% in the UV–visible spectral range. The bandgap of Ta_2O_5 is estimated by Tauc's plot as shown in Fig. 1b and found to be ~ 4.67 eV. To study the structural characteristics of Ta_2O_5 thin film, X-ray diffraction studies were performed on as-grown Ta_2O_5 thin film. XRD patterns of Ta_2O_5 thin film grown on Pt-Si is shown in Fig. 2a in which plot of intensity versus 2θ (θ; angle of diffraction) is shown. The absence of diffraction peaks for Ta_2O_5 shows that it is amorphous in nature. The observed peak in the graph corresponds to (220) plane of platinum originating from

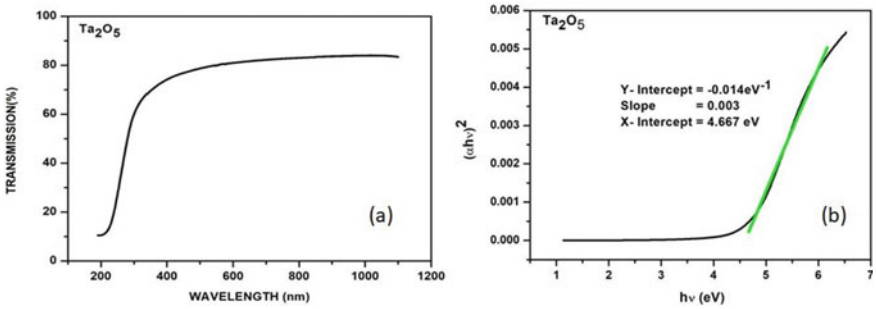

Fig. 1 **a** Transmission spectra of Ta_2O_5 thin film **b** corresponding Tauc plot

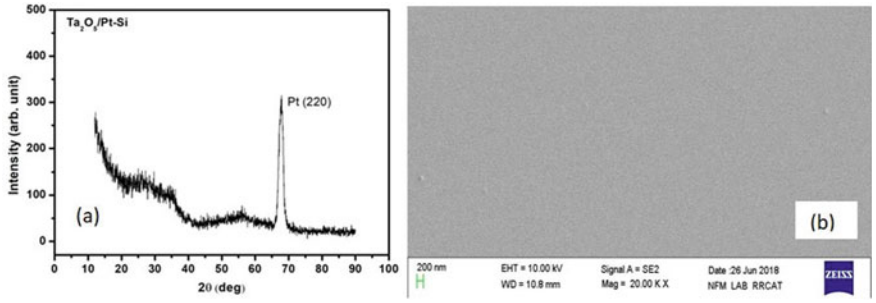

Fig. 2 **a** XRD pattern **b** SEM image of Ta_2O_5 thin film on Pt-Si substrate

the substrate. Figure 2b shows the SEM image of Ta_2O_5 thin film. A smooth surface without grains and grain boundaries can be observed in the SEM image which is a clear indication of the amorphous nature of the grown film. Also, it can be seen from the micrograph that the Ta_2O_5 thin film is free from pinholes and particulates.

To study the resistive switching characteristics of Cu/Ta_2O_5/Pt devices such as set and reset voltages, reset current, endurance, retention, etc. the I-V measurements at room temperature were carried out using an electrical microprobe station (Make: Ecopia; Model: EPS300) with source and measure unit (SMU; Keithley 2611A). A compliance current of 10 μA has been prefixed. The I-V measurements on the as-fabricated Cu/Ta_2O_5/Pt devices showed repeatable and reliable non-volatile bipolar resistance switching. The different processes associated with the bipolar resistive switching of Cu/Ta_2O_5/Pt devices are shown in Fig. 3. The most important behaviour observed in the Cu/Ta_2O_5/Pt devices was that the electroforming process was not required to initiate the RS behaviour due to the initial low resistance state of the virgin device.

When the negative voltage applied to the Cu electrode increased, the current also increased as shown in process 1 in Fig. 3. However, for a particular voltage, the current dropped drastically which indicates that the device has changed its resistance state from LRS to HRS. This sudden decrease in current is shown as the reset process in the Fig. 3. The device retained its state when the applied voltage and hence current reduced to zero as shown in process 2. After reset process, the device again switched to LRS from HRS when a voltage with opposite polarity was applied at the Pt electrode. The current was very low initially indicating the HRS state of the device but increased

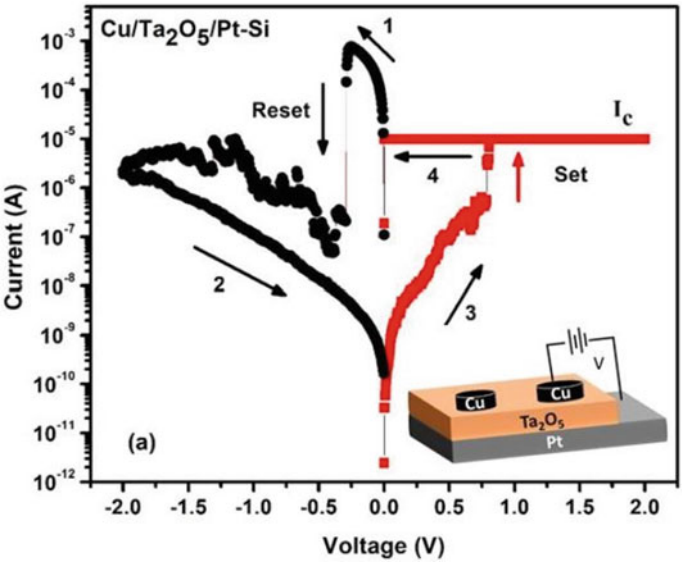

Fig. 3 Typical I-V Curve for Cu/Ta_2O_5/Pt devices showing bipolar resistive switching

with voltage as shown as process 3. For a particular voltage, the current increased abruptly which indicates that the device has changed its state from HRS to LRS. This process is shown as set in the figure. Because of the prefixed compliance current, the current flowing through device remained constant with increasing voltage. After the set process when the voltage was decreased the current also decreased but the device retained its HRS which is shown as process 4. This one set and reset process constitute one resistive switching cycle for the device.

To study the endurance property of the device, we have repeated the switching cycle for the device for 100 times. The $Cu/Ta_2O_5/Pt$ devices showed repeatable and reliable bipolar resistive switching behaviour for 100 test cycles. The device which was initially in LRS changed its state to HRS on the application of a suitable voltage of positive polarity at the Pt bottom electrode. When the polarity is reversed the devices undergone set process and resistance state changed from HRS to LRS. The operating voltages of the device were less than 1 V, where the mean set voltage was ~0.80 V and mean reset voltage was ~ −0.31 V. Figure 4a depicts set and reset voltage distribution for 100 cycles of operation which indicates the good endurance and reliability of the device. A small sense voltage of ~0.1 V was used to read the resistance of the device after switching events. The device resistance was found to change from ~100 s of MΩ (HRS) to ~100 s of Ω (LRS). The distribution of resistance in HRS and LRS is as shown in Fig. 4b. Even though there is statistical variation in resistances of both HRS and LRS, there exists a clear resistance window (R_{HRS}/R_{LRS}) to distinguish between the two states. The mean R_{HRS} and R_{LRS} are estimated to be ~ 300 MΩ and ~ 500 Ω with a relative standard deviation of ~84 and 103% respectively.

In order to find how long the device will remain in the particular state, the resistance state of both HRS and LRS was read for ~10^3 s by applying 0.1 V. The retention data showed that $Cu/Ta_2O_5/Pt$ devices can remain in a resistance state over 10^3 s without any degradation. The stable resistance values of both states with time are shown in Fig. 5. This ensures good data retention capability of the device. The behaviour

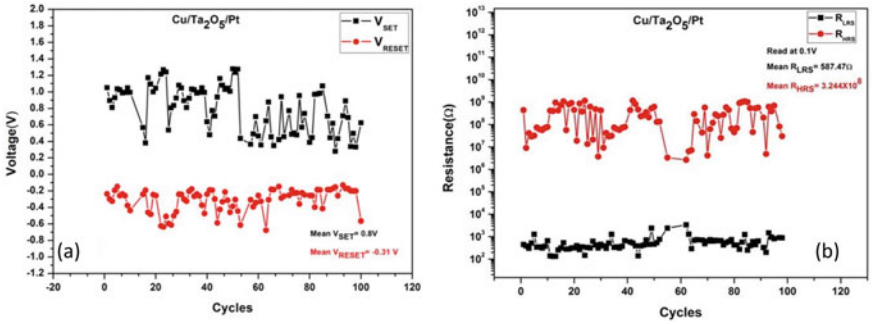

Fig. 4 Distribution of **a** SET and RESET voltages and **b** resistances in HRS and LRS read at 0.1 V for 100 switching cycles

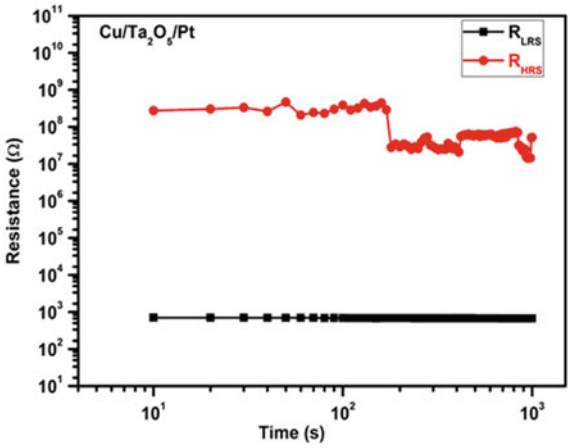

Fig. 5 Time retention characteristics of the resistance states of Cu/Ta_2O_5/Pt devices

shown by the device to remain in the same resistance in the absence of any external voltage reflects the non-volatility Cu/Ta_2O_5/Pt devices.

Even though the complete mechanism of resistive switching is still not clearly understood, generally formation and rupture of conduction filament under applied voltage is well accepted to explain bipolar resistive switching behaviour. Possible resistance switching mechanism in Cu/Ta_2O_5/Pt devices is the electrochemical formation of Cu metal filament in the active layer during the set process and dissolution of the filament during the reset process. Since the Cu/Ta_2O_5/Pt devices were initially in a low resistance state electroforming process was not required. A conduction filament of Cu atoms may have formed between top and bottom electrodes due to the diffusion/penetration of Cu atoms in Ta_2O_5 matrix during the sputtering deposition of Cu top electrodes. In this condition, on the application of positive polarity voltage to platinum electrode and negative polarity to Cu electrode, these Cu atoms in the conduction filament undergo oxidation such that Cu ions are formed. These ions move to the cathode (Cu electrode), there they undergo reduction to Cu atoms. The conductive filament is then ruptured and the device switches to high resistance state. When the voltage polarity is changed i.e. positive voltage to top electrode (Cu) and negative voltage to bottom electrode (Pt), the Cu atoms in the top electrode undergo oxidation to form Cu ions and these ions will move down to the cathode where they undergo reduction to Cu atoms. Thus initiating from the bottom electrode a conducting filament of Cu atoms will start growing through the insulating layer and connects the two electrodes. Thus current will increase abruptly indicating that the device switched back to a low resistance state. The schematic of the described mechanism is shown in Fig. 6.

In order to study the conduction mechanism, the linear fit of *ln* I Vs *ln* V has been done for both LRS and HRS. In the case of LRS, it can be seen that the current and voltage are in linear relation with a slope of ~0.98 as shown in Fig. 7a. This is due to the fact that the conduction is taking place through the conducting filament made up of Cu atoms, hence the conduction is considered Ohmic in nature. In case of

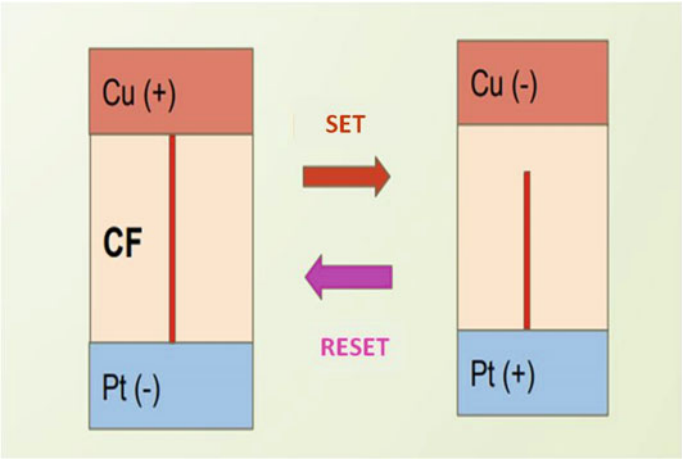

Fig. 6 Schematic of conducting filament-based resistive switching mechanism

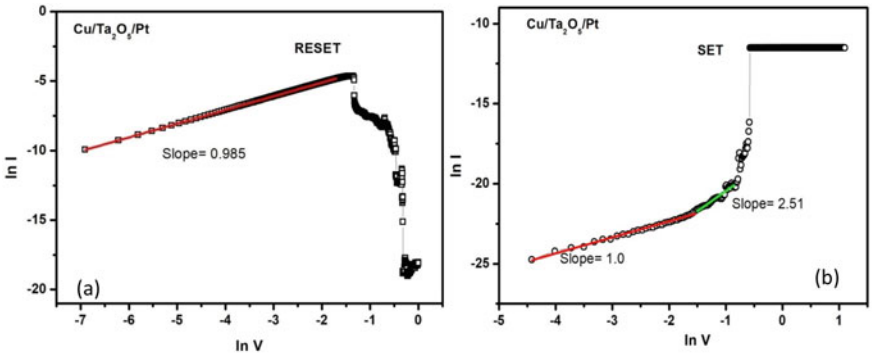

Fig. 7 Linear fit of ln I versus ln V curve for **a** LRS **b** HRS

HRS, the current varied linearly with voltage in the low voltage regime, whereas for high voltage region the current is no longer linear with voltage as shown in Fig. 7b. From the plot for HRS, it can be seen that the slope ~1 for low voltage which can be attributed to the thermally ejected electrons from the conduction band of Pt to the conduction band of Ta_2O_5. This kind of conduction mechanism is called Schottky emission in which electrons in the metal will acquire energy to overcome the metal–dielectric interface barrier (Schottky barrier) to go to the dielectric and participate in the conduction through the dielectric. In case of a high voltage regime in HRS, the current–voltage relationship is not linear and the slope is ~2. This type of conduction is generally termed as space charge limited conduction. When the voltage is low thermally ejected carriers will be more than injected carriers. The injected carriers will fill the traps in the dielectric. As the voltage increases strong injection will

occur such that traps are get filled up and space charges will be formed. So at higher voltages, the injected carrier density will be more than thermally ejected carriers. When all traps get saturated, then the current will be controlled by space charges and current and voltage will be having a square law relation ($J \propto V^2$). This kind of conduction in dielectrics is called Space Charge Limited Conduction (SCLC). Thus, conduction mechanism in Cu/Ta_2O_5/Pt devices was dominated by Ohmic behaviour in LRS and Schottky emission and space charge limited conduction in HRS.

4 Conclusions

In conclusion, we have fabricated Cu/Ta_2O_5/Pt-Si RRAM devices to study the resistive memory switching. For this, we have deposited tantalum pentaoxide (Ta_2O_5) thin films having thickness ~200 nm on commercially procured Pt-Si substrate by pulsed laser deposition technique and top Cu electrodes were deposited by RF sputtering. The as-fabricated Cu/Ta_2O_5/Pt-Si devices showed repeatable and reliable bipolar, non-volatile resistive memory switching behaviour. The thin films were found to be highly transparent (~80%) in visible spectral region with band gap of ~4.67 eV. XRD studies indicated amorphous nature of the thin films and SEM studies of Ta_2O_5 thin films revealed smooth and pinhole-free surface. Resistive switching behaviour of the Cu/Ta_2O_5/Pt-Si RRAM devices was studied using I-V characterization at room temperature. The Cu/Ta_2O_5/Pt-Si devices showed repeatable and reliable bipolar resistive switching with good endurance property when switched for over 100 times. The mean voltages for the set and reset processes of the device were ~ $+0.80$ and -0.31 V respectively with a mean reset current ~400 μA clearly indicating low power operation of the memory devices. There exists a clear resistance contrast of ~10^6 between HRS and LRS along with good retention behaviour of ~10^3 s. The resistive switching mechanism of the Cu/Ta_2O_5/Pt-Si devices was understood in terms of electrochemical rupture of Cu metal filament in the active layer during the reset process and reformation during set process. The conduction mechanism was explained in terms of Ohmic conduction in LRS whereas Schottky emission and space charge limited conduction (SCLC) in HRS. Our studies clearly indicate that Ta_2O_5thin-film-based resistive switching devices may have important implications in the development of futuristic non-volatile data storage solutions.

Acknowledgements The work reported in this paper was carried out in Raja Ramanna Centre for Advanced Technology (RRCAT) under the Indian Science Academies' Summer Research Fellowship Program 2018. The authors acknowledge Dr. S. K. Rai of Synchrotrons Utilization Section and Ms. Rashmi Singh of Laser and Functional Material Division, RRCAT for their help in XRD and SEM measurements, respectively. One of the authors, Ms. Nivedya T, would like to thank Prof. P. A. Naik, Director, RRCAT for mentoring and Shri R. Kaul, Head, Laser Material Processing Division, RRCAT for encouragement during the course of project work.

References

1. Pavan, P., Bez, R., Olivo, P.: Flash memory cells-an overview. Proc. IEEE **85**, 8 (1997)
2. Liu, X., Liu, Y., Chen, W., Li, J., Liao, L.: Ferroelectric memory based on nanostructures. Nanoscale Res. Lett. **7**(1), 285 (2012)
3. Chang Chang, T., Chang Chang, K., Ming Tsai, T., Jian, T., Sze, M.: Resistance random access memory. Mater. Today **19**, 5 (2016)
4. Lacaita, A.L.: Phase change memories: State-of-the-art, challenges and perspectives. Solid-State Electron. **50**, 1 (2006)
5. Tao, L.Y., Bing, L.S., Bing, L.H., Su, L., Ming, L.: An overview of resistive random access memory devices. Chinese Sci. Bull. **56** (2011)
6. Misra, P., Sharma, Y., Khurana, G., Katiyar, R.S.: Resistive switching characteristics of mixed oxides. Emerging Mater. Res. **4**(1), 18–31 (2017)
7. Waser, R., Aono, M.: Nanoionics-based resistive switching memories. Nat. Mater. **6** (2007)
8. Kukreja, L.M., Das, A.K., Misra, P.: Studies on nonvolatile resistance memory switching in ZnO thin films. Bull. Mater. Sci. **32** (2009)
9. Sahu, V.K., Misra, P., Ajimsha, R.S., Das, A.K., Joshi, M.P., Kukreja, L.M.: Resistive memory switching in ultrathin TiO_2 films grown by atomic layer deposition. In: AIP Conference Proceedings, p. 1731 (2016)
10. Pan, F., Chen, C., Shun Wang, Z., Chao Yang, Y., Yang, J., Zeng, F.: Nonvolatile resistive switching memories-characteristics, mechanisms and challenges. Progress Nat. Sci. Mater. Int. **20** (2010)
11. Kumar, D., Aluguri, R., Chand, U., Tseng, T.Y.: Metal oxide resistive switching memory: Materials, properties and switching mechanisms. Ceramics Int. **43** (2017)
12. Sahu, V.K., Das, A.K., Ajimsha, R.S., Misra, P.: Studies on transient characteristics of unipolar resistive switching processes in TiO_2 thin film grown by atomic layer deposition. J. Phys. D Appl. Phys. **51**(21), 215101 (2018)
13. Sahu, V.K., Misra, P., Das, A.K., Ajimsha, R.S., Singh, B.: Quantized conductance in Ta_2O_5 based resistive random access memory devices. AIP Conf. Proc. **1832**(1), 120026 (2017)
14. Lian, X., Miranda, E., Long, S., Perniola, L., Liu, M., Sune, J.: Three-state resistive switching in HfO_2-based RRAM. Solid-State Electron. **98**, 38–44 (2014)
15. Misra, P., Sahu, V.K., Ajimsha, R.S., Das, A.K., Singh, B.: Studies on resistive switching times in NiO thin films grown by pulsed laser deposition. J. Phys. D Appl. Phys. **50**(41), 415106 (2017)

Development of HF-VHF-UHF Flicker Noise Source Head Using Miniature Gas Discharge Tube

Narendra Y. Pawar, S. A. Gangal, and A. D. Shaligram

Abstract This paper describes the design, circuit, packaging of HF, VHF, UHF flicker noise source head. A miniature capsule-type gas discharge tube containing inert gases like Argon, Neon, or a mixture of inert gases with pressure in excess of 50 to 100 Torr is used to develop a flicker noise head. Applied with adjustable dc bias arrangement using fabricated adjustable dc power supply gas discharge tube generates flicker (1/f) in the range 0.1–800MHz. The generated flicker is responsible for the flicker noise in the same range of frequencies. With 50 Ω coupling network to gas discharge tube generated noise power is measured by a spectrum analyzer. Measured noise power is mathematically converted into noise temperature and then into ENR (excess noise ratio). ENR of 35 dB for 1 MHz to ENR of 3.5 dB for 800 MHz was observed and follows general theoretical (1/f) flicker noise pattern.

Keywords Noise source head · Gas discharge tube · Flicker noise · ENR (Excess Noise Ratio)

1 Introduction

Any conductor subjected to a temperature above absolute zero will generate noise due to molecular agitation and random fluctuations of electric current. Similarly, any gas discharge which is an electrical current flow across an interstitial gap of gas turning insulated gas into conductor will produce thermal noise. Thermal noise [1] is called white noise. White noise generators having a flat noise spectrum from 0.1 to 40 GHz using avalanche diode [2] and low-pressure gas discharge argon tubes [3] coupled to microwave waveguides. These are commercially available by various manufacturers [4]. ENR from 5 to 15 dB is achievable using avalanche diode and low-pressure gas discharge tubes using argon or neon gases (5 to 20 Torrs) [5]. Generated noise using avalanche diode and low-pressure gas discharge tube have flat amplitude over the mentioned operating frequency spectrum [6]. Pseudorandom noise sources

N. Y. Pawar (✉) · S. A. Gangal · A. D. Shaligram
Department of Electronic Science, Savitribai Phule Pune University, Pune, India
e-mail: narendrapawar19722003@yahoo.com

S. Mukherjee et al. (eds.), *Computational Mathematics, Nanoelectronics, and Astrophysics*,
Springer Proceedings in Mathematics & Statistics 342,
https://doi.org/10.1007/978-981-15-9708-4_15

that use digital m-sequencing techniques have limited bandwidths. Commercially available white noise sources are substantially expensive. Flicker (1/f) noise has a different characteristic than white noise or arbitrary digital noise. The noise output of flicker noise source decreases by 3 dB or more per octave of frequency. An electrical circuit or device that generates continuous flicker can be used as flicker noise source. Using a 50 Ω coaxial mount a very cost-effective flicker noise source head can be fabricated using a miniature gas discharge tube for large bandwidths and sufficient noise powers. Miniature gas discharge tubes when subjected to avalanche voltage produce continuous arc due to high-pressure gas contained in it. These tubes are used for protection from high voltage spikes and protection from lightening. Miniature gas discharge tubes have similar characteristics like tunnel diode. When used with current limiting avalanche mode it will produce continuous flicker. This paper describes noise generated due to flickering in the miniature gas discharge tube. Flicker will be generated due to AC or DC breakdown ionizing voltage applied across the gas discharge tube with a current limiting mechanism. When properly coupled to a 50 Ω impedance network this gas discharge mechanism can be used as a wideband flicker noise source for measuring various noise parameters of communication circuits like LNA, IF Amplifiers, mixers in HF, VHF, UHF ranges.

2 Design and Development of Flicker Noise Head

Developed noise head is to be used with 50Ω impedance systems. It could be part of a noise figure measurement system having 50 Ω i/p and o/p impedances. This is the prime reason the whole noise head is fabricated around two 50 Ω type N connectors.

Fabricated flicker noise source head consists of a miniature gas discharge tube of 5 mm dia. and 15 mm length is used which is commercially available for protecting the telephone subscriber circuit from spikes and overvoltages. This tube contains inert gas like argon, neon, or a mixture of both at 50 to 100 Torr.

A 50 Ω impedance matching network is fabricated and coupled to gas discharge tube. Figure 1 shows the block and circuit diagram of the fabricated noise head. Figure 2 shows a photograph of a fabricated noise source.

Power supply needed to power up the noise head is designed and fabricated. This Zener regulated power supply can supply 300–400 V with a current of 100 mA. Figure 3 shows a circuit diagram of the fabricated noise source. This power supply uses a series of Zener diodes in a series current limiting resistor as a primary regulator with two high voltage transistors (Q1 and Q2) in Darlington fashion to amplify the current.

Circuit Description of Flicker Noise Head. As shown in Fig. 1 noise head circuit has a DC biasing network which consists of bypass capacitor 1 kpf/1 kv rating connected between +Ve dc line and ground, furthermore, DC line is connected to 390 μH molded RF choke. RF choke is connected to 220 kΩ current limiting resistor which is connected to discharge anode of gas discharge tube. The cathode of discharge tube is grounded. 220 kΩ resistor and anode junction of the discharge tube

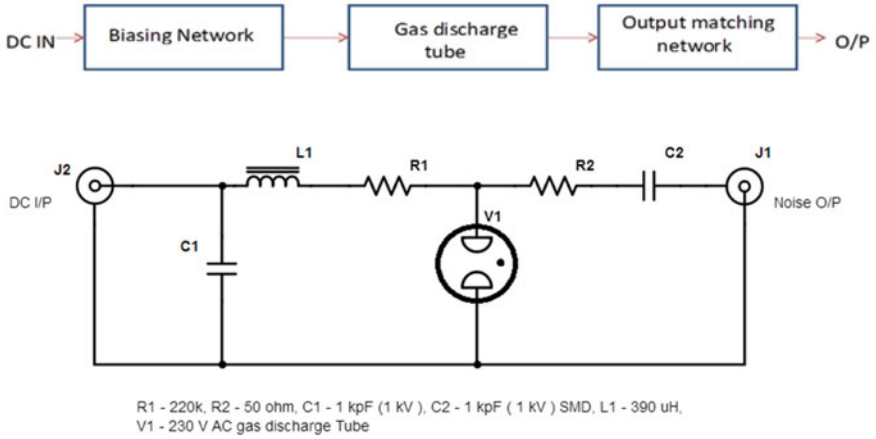

Fig. 1 Block diagram and circuit for flicker noise head

Fig. 2 Photograph of developed flicker noise head

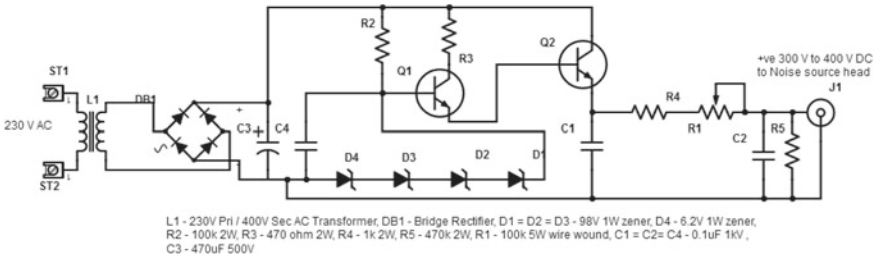

Fig. 3 Power supply circuit for noise source head

is connected to 50 Ω noninductive carbon composition resistor, the other end of this resistor is coupled to 50 Ω type N female connector through 1kpf/1kv ceramic SMD capacitor. All the components are mounted in air by soldering them to each other in 1.25 inch by 3-inch brass chassis fabricated around two 50 Ω N-type connectors to give support to the chassis.

3 Working of the Noise Source Head

Discharge in miniature gas tube occurs due to ionization of Argon or Neon gas contained in the tube at 230 v AC or 300 v DC. Regulated DC power supply of 300–400 v is applied to noise head. Adjusting 100 kΩ potentiometer, in turn, adjusting the current through gas discharge tube the flicker generated by gas discharge is stabilized. Too low current through the tube will generate irregular flicker or will stop gas discharge abruptly. Too high of current will saturate the discharge and will quench the flicker and a continuous arc will be produced which will not generate the necessary flicker noise. To get continuous stable flicker noise the current through the discharge tube should be adjusted to an optimum value by observing the generated noise output on the spectrum analyzer. The current between 1 and 2 mA produces a steady flicker in the gas discharge tube.

4 RF Measurements and Performance Measurements

RF measurement and performance and measurement of generated flicker noise power is accomplished by using a sensitive spectrum analyzer with a preamplifier. Rhode and Schwarz FHS3 spectrum analyzer with preamplifier is used for this measurement. Fabricated noise head is connected to spectrum analyzer input then DC power supply is connected to the DC input of noise head. Power supply is switched on and output flicker noise generated is observed on spectrum analyzer. Potentiometer in dc power supply is adjusted to get stable flicker in gas discharge tube so that continuous and stable flicker noise spectrum is observed on the spectrum analyzer. Once stable noise output is observed, noise amplitude and frequency response of generated flicker noise is measured by choosing appropriate ranges on spectrum analyzer. The graph of measured noise amplitudes at various frequencies and calculated ENRs are shown in Fig. 4. For calculating ENR following formulae used [7].

$$\text{Measured Noise Output (dBm)} = 10 * \log\left(\text{k} * \text{Tn} * \left(\Delta\text{f}/0.001\right)\right) \tag{1}$$

$$\text{ENR (dB)} = 10 * \log\left((\text{Tn} - \text{Tamb})/\text{Tamb}\right) \tag{2}$$

Where

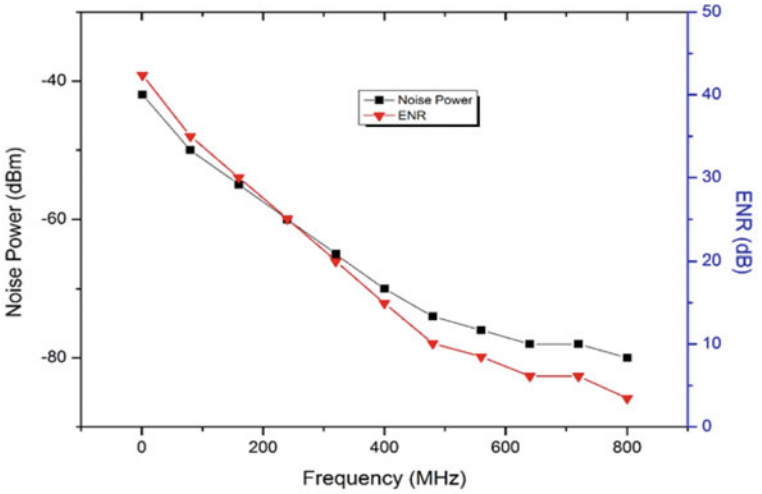

Fig. 4 Graph of Noise Power and ENR versus Frequency

$k = 1.3806 * 10^{-23}$ Nm/K Boltzmann constant,
Δf = Video Bandwidth of spectrum analyzer (1 MHz),
Tn = Noise temperature of gas discharge in Kelvin,
Tamb = 273 + room temperature (25 °C) = 298 °Kelvin.

Photographs of measured noise floor and flicker noise output powers using spectrum analyzer are shown in Fig. 5.

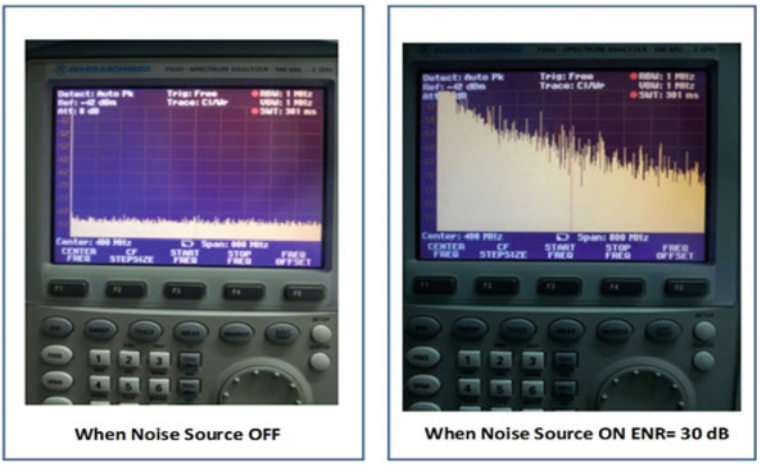

Fig. 5 Photographs of measured noise floor and flicker noise output powers using Spectrum Analyzer

5 Conclusions

A 50 Ω output impedance HF, VHF, UHF (0.1 to 800 MHz) flicker noise head is developed using readily available miniature gas discharge tube used for protection of telephone subscriber circuit. Adjustable Zener regulated DC power is developed and used to power up the noise head. Optimally dc biased gas discharge tube produces steady flicker noise. With 50 Ω impedance matched network flicker noise output is measured and calibrated with a spectrum analyzer. With calibration of ENR printed on noise head, it can be used for various noise-related measurements in communications circuits. The measured output of fabricated flicker noise head follows the general flicker (1/f) noise pattern theoretically expected.

References

1. Mumford, W.W.: Broad-band, microwavenoise source. Bell. Tech. J. **28**, 608–618 (1949)
2. Noisecom application notes -112 Noisecom.
3. Denson, H.: Plasma Noise Sources of Improved Accuracy. IEEE (1968)
4. Hewlett Packard Noise Notes 57–1,57–2 H.P.
5. Randa, J., Dunleavy, L.P., Terrel, L.A.: Stability measurement on noise sources. IEEE Trans. Inst. Meas. **2m**, 368–372 (2001)
6. Achkar, J.: Set of waveguide primary thermal noise standard and related calibration stem. IEEE Trans. Inst. Meas. **48**(2), 638–641 (1999)
7. Miller, D., Arthur, N.S.: Measurements, and Receiver Noise Definitions. Proc. IEEE **55**, 865–877 (1967)

Profiling and Imaging of RBC Using Coherent Gradient Sensing and Fourier Fringe Analysis

Jitendra Dhanotia, Shivangi Bande, Vimal Bhatia, and Shashi Prakash

Abstract In the present communication, profiling and imaging of red blood cell (RBC) using coherent gradient sensing (CGS) technique coupled with Fourier fringe analysis has been proposed. The RBC of a healthy person has a definite structure; it has been identified using double grating shearing interferometry and the direct phase determined using the Fourier transform method. Good accuracy and resolution in profiling have been achieved.

Keywords Optical metrology · Fringe analysis · Interferometry · Image processing · RBC imaging

1 Introduction

Testing and analysis of the biological specimen is an important process in medical sciences. Light plays a vital role in the analysis of such samples due to easy generation, detection, and analysis [1]. Light also has ability to penetrate living tissue harmlessly and deeply, thereby providing means for getting valuable information on the health and function of cells. It plays a dominant role in microscopic imaging, in biosensors, and in laser therapy and surgery. Optical techniques such as microscopy [2], interferometry [3], holography [4], and optical coherence tomography (OCT) [5] have been used for testing biological specimen. The microscopic analysis of cells requires the use of chemical reagents, special equipment, and qualified personnel; thereby restricting its use. Other techniques have relatively high sensitivity to the environmental perturbations, use expensive and elaborate equipment. On the contrary, grating shearing interferometric methods have probably been the most used optical

J. Dhanotia · V. Bhatia
Signals and Software Group, Discipline of Electrical Engineering, Indian Institute of Technology Indore, Indore 453552, India

S. Bande · S. Prakash (✉)
Photonics Laboratory, Department of Electronics & Instrumentation Engineering, Institute of Engineering & Technology, Devi Ahilya University, Khandwa Road, Indore 452017, India
e-mail: sprakash_davv@rediffmail.com

S. Mukherjee et al. (eds.), *Computational Mathematics, Nanoelectronics, and Astrophysics*, Springer Proceedings in Mathematics & Statistics 342,
https://doi.org/10.1007/978-981-15-9708-4_16

methods outside the laboratory surroundings [6]. The highlight of these methods has been its extreme simplicity, low cost, and ability to be transferred to locations outside the laboratory.

Agrawal et al. used the Talbot effect and computationally complex Hilbert transform to obtain the three-dimensional phase information of RBCs [7]. In this communication, we proposed a CGS interferometer for achieving a 3D profile of the healthy RBCs. Since CGS produced the sinusoidal profile of the recorded fringe pattern and hence, it is capable to remove noise before recording the interferograms. FTM is much easier and computationally efficient to interpret. The proposed technique has been used to determine the structural property of the RBC. To increase the sensitivity and reliability in the detection and identification process, advanced signal processing techniques, i.e., FTM has been incorporated into the testing procedure to obtain the 3D profile of the specimen under study. The 3D phase profile shall lead to the determination of the morphology of the structure under study. The requirement of self-imaging distance between the gratings has been alleviated.

2 Basic Theory

Figure 1 shows the experimental arrangement for testing and analysis of RBC using CGS and FTM. The basic principle of CGS is described below as shown in Fig. 2. The plane wavefront is incident on a pair of Ronchi gratings G_1 and G_2 having the same pitch 'p' and separation 'd'. The diffracted light emerging from the grating G_1 makes a diffraction angle $\theta = \sin^{-1}(\lambda/p)$. Finally, the diffracted light emerging

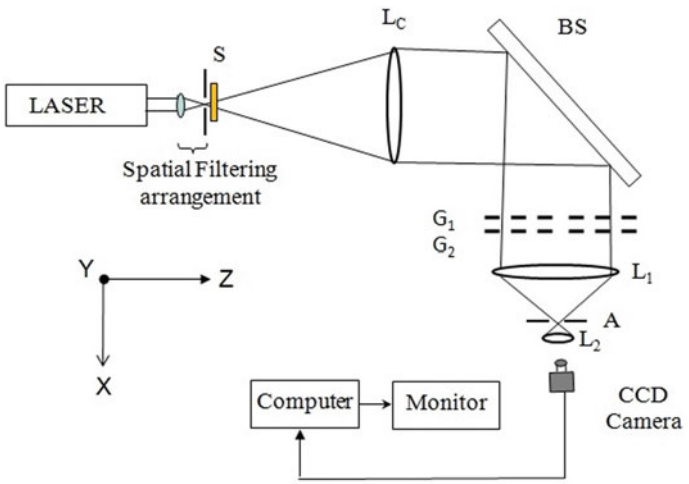

Fig. 1 Schematic of the experimental arrangement for profiling of RBC of a healthy person using CGS

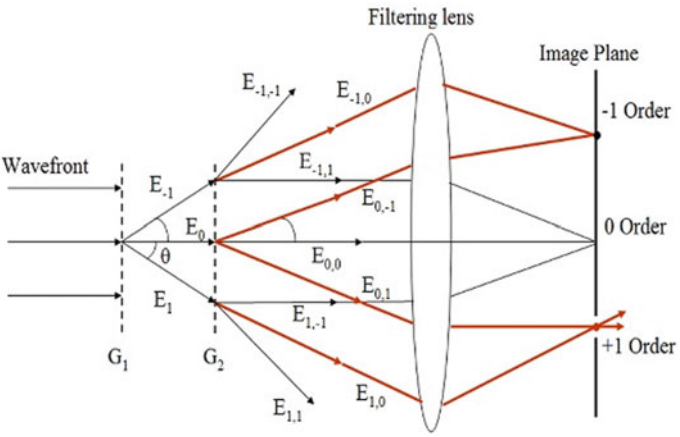

Fig. 2 Basic principle of Coherent Gradient Sensing system

from the set of gratings consists of zero and several other diffraction orders. The first order is selected and allowed to propagate, while the remaining orders are blocked as shown in Fig. 2. On allowing the first order, shearing interferometric fringes appear onto the CCD chip. This first-order fringe pattern is used to determine the gradient phase of the object under study. Digital image processing is used in the experiment to find the structural properties of the sample.

In the experimental arrangement, the glass slide of blood smear is placed close to the pinhole. The interferograms has been recorded using CCD camera. The recorded fringe pattern can be described by

$$g(x, y) = a(x, y) + b(x, y)\cos[2\pi f_{ox}x + 2\pi f_{oy}y + \psi(x, y)] \tag{1}$$

where $a(x, y)$ is the background noise, $b(x, y)$ is the variation in fringe visibility and $\psi(x, y)$ is the phase information of interest; f_{ox} and f_{oy} are the spatial carrier frequency in the x and y direction, respectively. On applying FT, the desired phase, $\psi(x, y)$, may be obtained as [8]

$$\psi(x, y) = \tan^{-1}\left[\frac{\mathrm{Im}(C(x, y))}{\mathrm{Re}(C(x, y))}\right] \tag{2}$$

By applying the phase unwrapping algorithm over $\psi(x, y)$, we obtain a continuous phase map.

3 Experimental Setup and Results

Figure 1 shows the experimental setup for testing and analysis of the biological sample using CGS. Light from 15 mW (632 nm) He–Ne laser is spatially filtered using a combination of the pinhole of 5 μm diameter and microscopic objective of magnification 45X. The diverging beam so obtained is collimated using a collimating lens (L_c) of focal length 250 mm and is diverted using beam splitter BS towards the CGS setup comprising of gratings G_1 and G_2. Gratings G_1 and G_2 have the same period and are placed at an arbitrary distance. The gratings G_1 and G_2 are also placed on the precision rotational stage. The gratings are kept in such a manner that grating lines make equal but opposite angle with the horizontal. Since a Ronchi grating produces several diffraction orders, several sheared wavefronts are produced. The two first orders, produced by the two gratings, are isolated and made to interfere as shown in Fig. 2. Initially, the biological sample (blood smear on glass slide) is not used in the setup. The interferometric fringe pattern has been obtained in the field of view as anticipated and shown in Fig. 3a.

Now, the test specimen, i.e., blood smear of the healthy individual on glass slide is introduced near the pinhole. By introducing the specimen, the vertical fringe patterns deteriorated as predicted and shown in Fig. 3b. The zoomed portion (an RBC structure of healthy person) corresponding to Fig. 3b is shown in Fig. 3c. Spatial filtering arrangement comprising lens L_1, aperture A, and lens L_2 has been used to directly record the image on the CCD chip. For the automatic recording, CCD has been used.

Towards the accurate measurement of phase, the FT algorithm has been used to analyze the recorded fringe pattern. The phase map so obtained shows the structural property, shape of the RBC under study.

The CGS interferometer has been used for testing and analysis of RBC of the healthy person. Several interferograms were recorded corresponding to the RBC sample of different people. In the recorded interferogram, the fringes are vertical in the absence of the glass plate (without blood smear). The presence of blood smear causes deviation in the vertical fringe patterns. For undertaking phase/measurement of the recorded images, FTM has been used. Toward this, necessary codes have been developed. The FTM involves finding the FFT of the recorded interferogram to obtain its Fourier spectra. In the next step, the first-order Fourier spectra are selected and

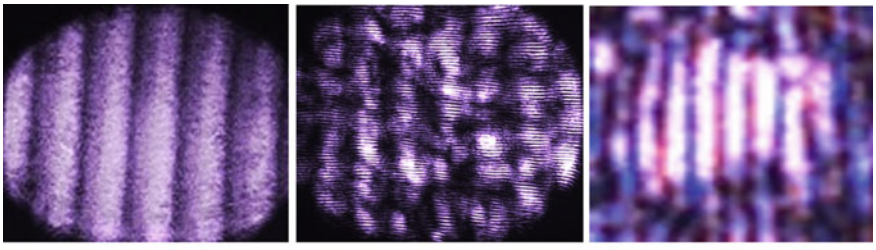

Fig. 3 Recorded image of using CGS technique **a** without sample, **b** with sample, and **c** a zoomed (one RBC structure) portion corresponding to interferogram as shown in Fig. 3b

shifted to the center position. Finally, the inverse FT of the centrally shifted spectra provides the necessary phase information of the recorded interferogram. To obtain a reliable phase map, the field corresponding to the wrapped phase map is scanned and 2π is added or subtracted every time an edge is detected. Figure 4 corresponds to the phase map obtained for the recorded image (Fig. 3b) with a blood sample of a healthy person. Figure 5a represents the reconstructed phase map of a single RBC. Figure 5b shows the 2D profile corresponding to Fig. 5a. It has a circular disc type structure. The structure of RBC varies based on the type of disease. Thus, the diseases can be identified using optical techniques based on the structure of the RBC

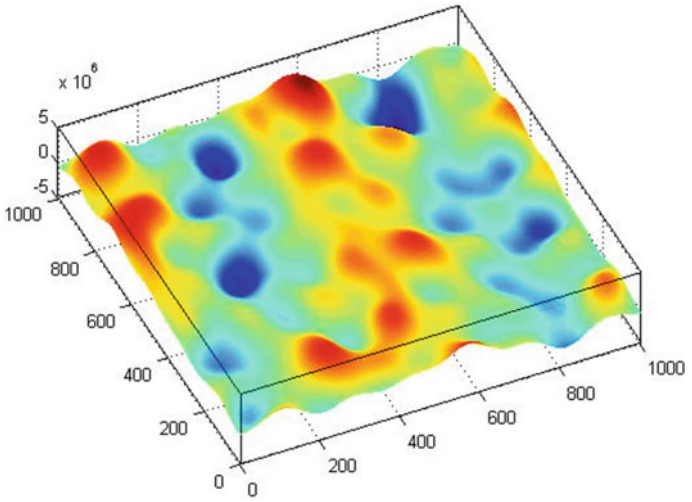

Fig. 4 3D phase map obtained using FTM

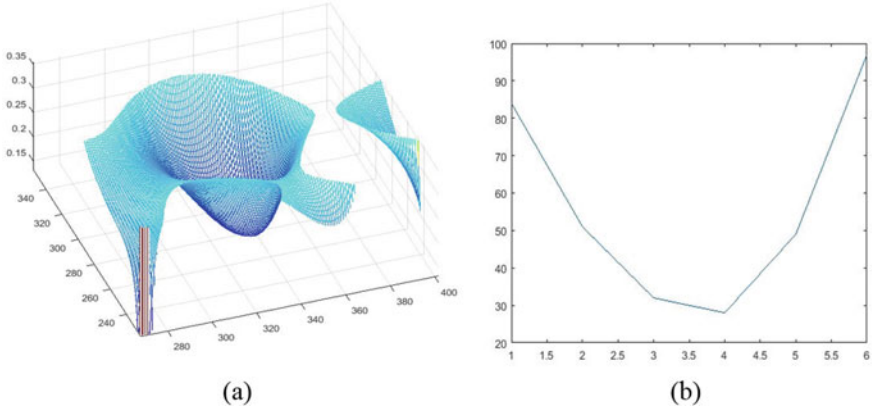

Fig. 5 **a** 3D phase map of single RBC, and **b** 2D map corresponding to Fig. 5a

of the infected or healthy person. Good agreement has been found between current work and previously reported literature [9–11]. The research has been further carried out for the determination of size, shape, and other properties of RBC for healthy as well as diseased infected individuals.

4 Conclusion

In conclusion, we have successfully demonstrated the applicability of the CGS technique for profiling of RBC of a healthy person. Automated fringe analysis using Fast FTM has been used to obtain qualitative results. The results of the investigations match well with standard results. The setup demonstrated is simple, noncontact, and effective for testing biological specimen. The technique is based on CGS; hence the requirement of self-imaging distance between the gratings as in other techniques has been alleviated.

Acknowledgements This work is supported by the Visvesvaraya PhD scheme of Ministry of Electronics and Information Technology, and Science and Engineering Research Board (EMR/2016/003115).

References

1. https://en.wikipedia.org/wiki/Light.
2. Anna, T., Srivastava, V., Mehta, D.S., Shakher, C.: High-resolution full-field optical coherence microscopy using a Mirau interferometer for the quantitative imaging of biological cells. Appl. Opt. **50**, 6343 (2011)
3. Nolte, D.D.: Optical Interferometry for Biology and Medicine. Springer New York Dordrecht Heidelberg London (2012)
4. Javidi, B., Moon, I., Yeom, S., Carapezza, E.: Three-dimensional imaging and recognition of microorganism using single-exposure online digital holography. Opt. Exp. **13**, 4492–4506 (2005)
5. Srivastava, V., Anna, T., Sudan, M., Mehta, D.S.: Tomographic and volumetric reconstruction of composite materials using full-field swept-source optical coherence tomography. Meas. Sci. Tech. **23**, 055203–055212 (2012)
6. Dhanotia, J., Prakash, S., Rana, S., Sasaki, O.: Slope measurement of bent plates using double grating shearing interferometry. App. Opt. **50**, 2958–2963 (2011)
7. Agarwal, S., Kumar, V., Shakher, C.: Analysis of red blood cell parameters by Talbot-projected fringes. J. Biomed. Opt. **22**, 106009 (2017)
8. Dhanotia, J., Prakash, S.: Automated collimation testing by incorporating the Fourier transform method in Talbot interferometry. Appl. Opt. **50**, 1446–1452 (2011)
9. Moon, I., Daneshpanah, M., Anand, A., Javidi, B.: Cell Identification with Computational 3D Holographic Microscopy. Opt. Photonics News **22**, 18–23 (2011)
10. Moon, I., Anand, A., Cruz, M., Javidi, B.: Identification of Malaria Infected Red Blood Cells via Digital Shearing Interferometry and Statistical Inference. IEEE Photonics J. **5**, 1–8 (2013)
11. Liu, R., Anand, A., Dey, D.K., Javidi, B.: Entropy-based clustering of embryonic stem cells using digital holographic microscopy. J. Opt. Soc. Am. A **31**, 677–684 (2014)

Mean Square Error-Based Approach for the Detection of Focal Position of a Lens

Shivangi Bande, Jitendra Dhanotia, Vimal Bhatia, and Shashi Prakash

Abstract Determination of focal length of a lens is a common problem encountered in optical instrumentation; however, there exist very few solutions which are simple, inexpensive and yield automated output. In this paper, we present the results of investigation undertaken towards determining the focal length a test lens with high accuracy and precision by undertaking digital processing of self-images obtained at two Talbot planes using single linear grating. Light from a collimating lens is incident onto a test lens and mirror combination; the back-reflected light is incident onto a beam splitter to draw the beam for interferometric evaluation. Single CCD camera is used to capture self-images at the first and highest feasible Talbot plane for different positions of a given test lens. Self-images have been processed digitally to find mean square error (MSE) corresponding to each position of the lens. MSE is lowest when the lens is positioned at its focal length, for all other positions of lens MSE remains higher. Hence, focal position can be exactly differentiated from all other positions of lens. Also, it has been observed that MSE increases as the distance between Talbot planes increases. Hence, if the MSE is calculated for the first and the farthest Talbot plane, sensitivity is improved. To achieve high sensitivity, Talbot self-images at the first and till the eight Talbot planes (due to practical limitations) are analysed.

Keywords Optical metrology · Self-images · Image processing · Mean square error

S. Bande · S. Prakash (✉)
Photonics Laboratory Department of Electronics and Instrumentation Engineering, Institute of Engineering and Technology Devi Ahilya University, Khandwa Road, Indore 452017, India
e-mail: sprakash_davv@rediffmail.com

J. Dhanotia · V. Bhatia
Signals and Software Group Discipline of Electrical Engineering, Indian Institute of Technology Indore, Indore 453552, India

S. Mukherjee et al. (eds.), *Computational Mathematics, Nanoelectronics, and Astrophysics*, Springer Proceedings in Mathematics & Statistics 342,
https://doi.org/10.1007/978-981-15-9708-4_17

1 Introduction

Laser-based optical techniques are preferred by industries and laboratories for the analysis of product qualities. Optical instrumentation provides non-invasive way of estimating parameters with high accuracy and in less computation time. Focal length is one of the important parameters to estimate and evaluate the optical properties of any lens system. Numerous optical techniques have been proposed for the measurement of focal length of a lens. Initially, classical methods such as nodal slide, image magnification and focometer were reported [1]. They were based on geometrical optics. Subsequently, measurements techniques based on interferometric methods such as Talbot interferometry [2, 3], Lau interferometry [4], moiré deflectometry [4, 6], etc., have been widely used. These techniques mostly employ the principle of interference/diffraction. Based on the above principles, focal length measurement techniques are broadly categorised as manual and automated. Most of the manual techniques have used the concept of fringe spacing and fringe rotation. The process involved is time consuming and tedious [3]. Automated techniques have used the principle of phase measurement to estimate focal length of an optical component [7]. However, automated interferogram analysis techniques suffer from the issues such as phase ambiguity, noise and phase unwrapping [7].

To circumvent the above issues, we propose a simple MSE-based automated measurement for the detection of focal position of a lens with improved sensitivity and high accuracy. The experimental setup uses single linear grating and a CCD camera. Test lens is translated along optic axis. For each position of the test lens, images at two different self-imaging planes have been captured and analysed using MSE-based algorithm developed in Matlab. The lowest value of MSE is indicative of exact focal position of the test lens. High accuracy and resolution in the measurement have been achieved. The technique neither requires the complex phase measurement procedure nor the dual camera assembly.

2 Basic Theory

Self-imaging phenomenon (Talbot effect) occurs when a grating is placed in the path of a collimated beam. Exact self-images of the grating are formed at certain well-defined planes (Talbot planes) perpendicular to the direction of propagation of the beam [3].

$$Z_T = 2kp^2/\lambda \tag{1}$$

where k is an integer, p is pitch of the grating, λ is wavelength of light used and Z_T is Talbot plane/self-imaging plane.

MSE is frequently used in signal processing. It is one of the most widely used, full-field image quality metric. It is defined as follows [8]

$$MSE = \frac{1}{MN} \sum_{i=1}^{M} \sum_{j=i}^{N} [x(i,j) - y(i,j)]^2 \tag{2}$$

where x(i, j) represents the original (reference) image, y(i, j) represents the distorted (modified) image and (i, j) represents the pixel position in image of size $M \times N$. MSE is computed as mean of the sum of the square of the differences between two corresponding pixel positions of the two images. If both the images are identical, then difference value is zero for each corresponding pixel position, and hence, MSE is computed to zero. MSE measures the difference between predicted values and the observed values from the environment. MSE finds application in different areas as signal processing, climatology, forecasting and regression analysis to verify the experimental results [8–11].

3 Experimental Setup

Figure 1 shows the experimental setup for determining focal position of test lens using self-imaging phenomena. The beam from He-Ne laser is spatially filtered and collimated using microscopic objective and collimating lens Lc. The collimated light falls on test lens L_T and back propagates by reflecting plane mirror. A beam splitter BS diverts the beam towards grating G. A CCD camera is positioned at first Talbot plane Z_1, and then moved to second Talbot plane Z_2 to capture the self-images for a given position of test lens L_T. Test lens is translated on precision translation stage of resolution 1μm.

Initially lens L_T is kept relatively close to the mirror ('in-focus' position). For this position, self-images of the grating G at both the Talbot planes (Z_1 and Z_2) have been recorded and stored in a computer memory. MSE algorithm is used for the comparison and similarity analysis of recorded images.

Next, test lens is gradually translated away from the mirror and for each position of the test lens self-image pair has been recorded (at Z_1 and Z_2) and analysed. There has been gradual decrease in the MSE value as the lens is moved away from the mirror. Finally, when the lens reaches a position such that mirror is at its focal plane, the minimum value of MSE approaching zero, is achieved. This position is known as 'at-focus', or 'focal position' of the test lens. For achieving higher accuracy in the determination of focal position, a series of interferograms have been recorded near this 'at-focus' position and analysed using MSE. The lowest value of MSE is indicative of effective focal position of the test lens. Test lens has been translated along the optic axis and the corresponding self-images have been analysed. MSE computed for 'out-focus' position of the test lens L_T shows an increase compared to the 'at-focus' position.

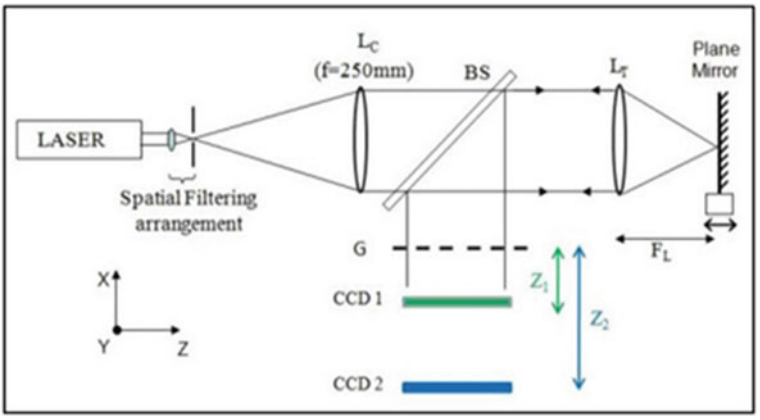

Fig. 1 Experimental setup for the detection of focal position of test lens

4 Results and Discussion

The self-imaging phenomenon coupled with MSE algorithm has been successfully applied for the determination of focal position of the test lens. For different positions of the test lens, a pair of self-images (at Z_1 and Z_2) have been recorded and processed digitally in MATLAB environment using MSE algorithm.

Figure 2a, b shows the recorded interferograms for 'at-focus' position of the test lens at first and second Talbot plane, respectively. Corresponding intensity profile along the centre row of the interferogram is shown in Fig. 3a, b, respectively.

Intensity profile has a square wave shape since Ronchi grating has been used in experimentation. Intensity profile alone is not sufficient to distinguish between

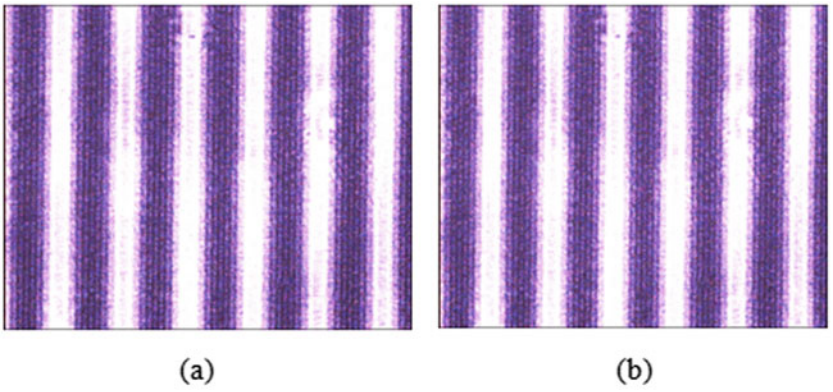

Fig. 2 Recorded interferograms for 'at-focus' position of the test lens **a** first Talbot plane, and **b** second Talbot plane

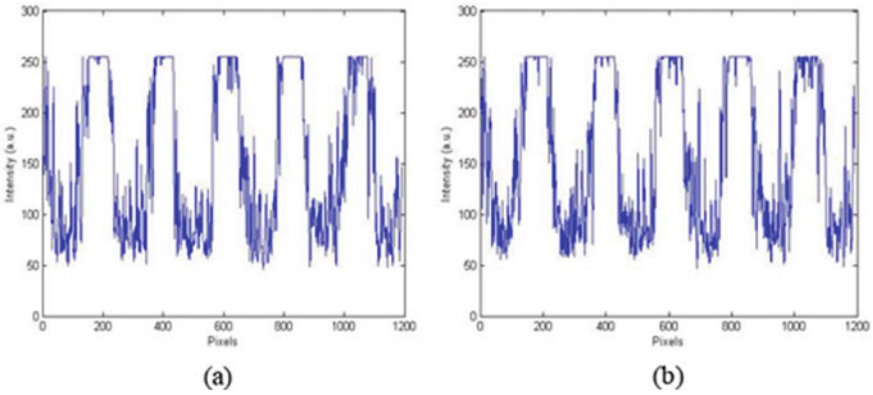

Fig. 3 Intensity profile along the centre row of the interferograms for 'at-focus' position of the test lens **a** first Talbot plane, and **b** second Talbot plane

Table 1 Comparison of measured values of focal length with the standard values

S. No.	Standard f (mm)	Measured f (mm)	Δ f (mm)	(Δf / f) × 100
1	120	119.20	0.8	0.66
2	180	178.5	1.5	0.8333
3	250	247	3.0	1.2
4	300	296.1	3.9	1.3

the self-images due to small differences, and hence, MSE-based algorithm has been needed to detect the linear period variation in the self-images with high accuracy. It has been observed that MSE has the lowest value when test lens is positioned at 'at-focus' position else for any other positions the MSE has a higher value. At the 'at-focus' position the two self-images are identical, and hence have high similarity, so the MSE is minimum. There has been mismatch in period of the grating images at 'in-focus' and 'out-focus' position of the lens leading to relatively higher values of MSE. Above experiment has been carried out with four lenses of different focal lengths to verify the algorithm.

Table 1 compares the mean value of focal length determined by the above experiment with the standard focal length. The experiment has been repeated five times with each lens and the mean values are reported.

It has been reported in literature that as the measurements are taken at higher Talbot plane the sensitivity in measurement increases [12]. In order to verify this for the present experiment, we recorded self-images of the grating at higher Talbot planes and computed the MSE for the first and the higher Talbot plane keeping the test lens position fixed. We recorded images till eighth Talbot plane for the lens under measurement.

Figure 4 shows the variation of MSE computed between the self-images of first Talbot plane and each higher Talbot planes corresponding to 'in-focus' position of

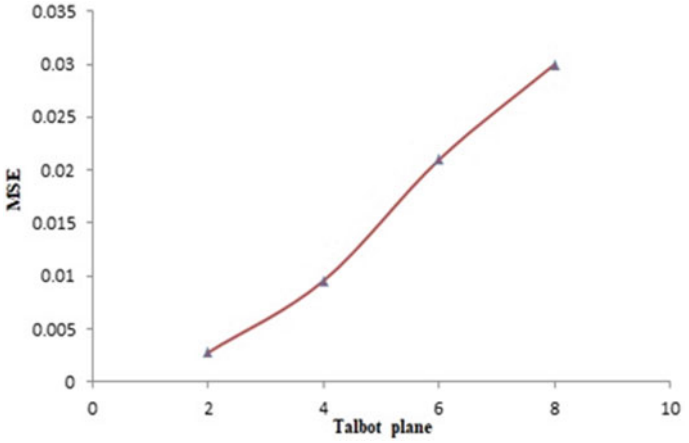

Fig. 4 Computed MSE between the self-images of first and each higher Talbot plane corresponding to 'in-focus' position ($\Delta f = -2$ μm) for the test lens of focal length 250 mm

test lens of focal length 250 mm. It has been observed that larger MSE value is obtained when self-images compared are captured by mounting cameras at higher Talbot plane. MSE computed for captured images at 1st and 8th Talbot plane is highest while it is lowest for the captured images at 1st and 2nd Talbot plane.

5 Conclusion

Focal position has been detected and evaluated with increased accuracy and resolution. Self-images of Ronchi grating are captured at two Talbot planes. Similarity between the self-image pair has been used as a measure to determine focal length of a lens. MSE-based approach has been undertaken for ascertaining the similarity with high accuracy. Lowest value of MSE corresponds to matching between self-images and the focal position of the lens. Further, sensitivity in measurement can be improved by capturing self-images at the first and the farthest Talbot plane.

Acknowledgements This work is supported by Visvesvaraya Ph.D. scheme of Ministry of Electronics and Information Technology, and Science and Engineering Research Board (EMR/2016/003115).

References

1. Kingslake, R., ed.: Applied Optics and Optical Engineering, vol. 1, Chap. IV, p. 208. New York (1965)
2. Sriram, K.V., Kothiyal, M.P., Sirohi, R.S.: Direct determination of focal length by using Talbot Interferometry. Appl. Opt. **31**, 5984–5988 (1992)
3. Bernardo, L.M., Soares, O.D.D.: Evaluation of the focal distance of a lens by Talbot interferometry. Appl. Opt. **27**, 296–301 (1988)
4. Thakur, M., Shakher, C.: Evaluation of the focal distance of lenses by white-light Lau phase interferometry. Appl. Opt. **41**, 1841–1845 (2002)
5. Geatt, I., Kafri, O.: Determination of the focal length of nonparaxial lenses by Moiré deflectometry. Appl. Opt. **26**, 2507–2508 (1987)
6. Keren, E., Bar-Ziv, E., Glatt, I., Kafri, O.: Measurements of temperature distribution of flames by moiré deflectometry. Appl. Opt. **20**, 4263–4266 (1981)
7. Singh, P., Faridi, M.S., Shakher, C., Sirohi, R.S.: Measurement of focal length with phase-shifting Talbot interferometry. Appl. Opt. **44**, 1572–1576 (2005)
8. Gupta, H.V., Kling, H., Yilmaz, K.K., Martinez, G.F.: Decomposition of the mean squared error and NSE performance criteria: implications for improving hydrological modelling. J. Hydrol. **377**, 80–91 (2009)
9. Basseville, M.: Distance measures for signal processing and pattern recognition. Signal Process **18**, 349–369 (1989)
10. Franti, P.: Blockwise distortion measure for statistical and structural errors in digital images. Signal Process. Image Commun. **13**, 89–98 (1998)
11. Willmott, C.J., Matsuura, K.: Advantages of the mean absolute error (MAE) over the root mean square error (RMSE) in assessing average model performance. Clim. Res. **30**, 79–82 (2005)
12. Shakher, C., Prakash, S., Nand, D., Kumar, R.: Collimation testing with circular gratings. Appl. Opt. **40**, 1175–1179 (2001)

Viability Assessment of Kidney Bean Seed (*Phaseolus Vulgaris sp.*) Using Robust Biospeckle Indexing Technique

Puneet Singh, Amit Chatterjee, Vimal Bhatia, and Shashi Prakash

Abstract In this work, we have used biospeckle analysis to assess the viability of kidney bean seeds. Biospeckle analysis is a noncontact and nondestructive technique for the detection and evaluation of different biological and nonbiological samples when illuminated by a highly coherent laser source. Groups of kidney seeds (viable and nonviable) were provided similar germination conditions for the same time. Activity images for each group were recorded through a CCD camera and processed using highly efficient robust indexing based inertia moment (IM) and absolute value of difference (AVD) techniques. To consider the inhomogeneity of the sample, the random time history of speckle pattern (RTHSP) was used. Obtained results conclusively establish biospeckle analysis as an efficient tool for evaluating the viability of kidney beans.

Keywords Biospeckle · Instrumentation · Laser · Seed viability · Speckle

1 Introduction

Seed viability [1] is referred to as the capability of the seed to germinate properly under suitable conditions. This is a major factor that directly affects the yield of agricultural crop; hence it can result in severe distress to the people associated with agricultural industry, particularly the farmers. Therefore, analyzing the viability of the seeds before sowing is a necessary step to ensure the optimum quality of the crops. There are different test that have been used to characterize the seed sample

P. Singh · A. Chatterjee · V. Bhatia
Signals and Software Group Discipline of Electrical Engineering, Indian Institute of Technology, Indore 453446, India

S. Prakash (✉)
Photonics Laboratory Department of Electronics and Instrumentation Engineering, Institute of Engineering and Technology Devi Ahilya University, Khandwa Road, Indore 452001, India
e-mail: sprakash_davv@rediffmail.com

S. Mukherjee et al. (eds.), *Computational Mathematics, Nanoelectronics, and Astrophysics*, Springer Proceedings in Mathematics & Statistics 342,
https://doi.org/10.1007/978-981-15-9708-4_18

in terms of their germination characteristic. But the reproductivity of these methods has always been the concern.

In this paper, we have evaluated the viability of kidney bean (*Phaseolus Vulgaris sp.*) seeds using biospeckle analysis. For viable seeds, higher germination percentage results in magnified chemical and physical activities, which in turn, enhance its dynamicity. Image analysis is performed in MATLAB interface by combining robust indexing strategies and RTHSP. The proposed strategy possesses high accuracy and lowest standard deviation as compared to conventional techniques.

2 Theory

The biological activity of the sample changes as time varies, this activity variation results in intensity fluctuation of the biospeckle image recorded by the camera. To analyze the change in the activity of the sample, time-series images were recorded and analyzed by using different numerical and visual methods. The common method to analyze the successive speckle images is to calculate the inertia moment (IM) [2] and absolute value of difference (AVD) [3] from the generated time history. The time history is generated by selecting a particular row/column (preferably the middle one) from the biospeckle data and placed side by side to generate the new image called time history of the speckle pattern (THSP) [2]. However, all the biological object and even nonbiological object do not possess microlevel homogeneity. Hence, the conventional THSP method does not consider the variation generated due to the inhomogeneity of the sample and results in higher standard deviation. An alternative way to generate the temporal history of the biospeckle images is to select random points from the image stack. In this method, THSP is generated by selecting an n-random point from the first speckle frame and making those point locations fixed for the remaining images. The multiple points selected from each biospeckle image are converted into the column and placed side by side; the generated final image is termed as random time history of speckle pattern (RTHSP) [4]. Still the RTHSP based indexing method using standard Inertia moment (IM) and absolute value of differences (AVD) has its own limitation and produces erroneous results. As it possesses considerably high standard deviation, this needs to be minimized further using mathematical operations. The use of these methods also results in a huge variation in the activity values even when the sample does not have high activity. Hence, to address this issue we have combined RTHSP based temporal history with the robust indexing [5] to consider the inhomogeneity of the sample, as well as reducing the standard deviation. Once the RTHSP is generated, the co-occurrence matrix (COM) [2] is formulated by considering number of successive occurrences of pixel values in each row of the RTHSP, and is given by

$$M_{\mathrm{COM}} = \left[N_{i,j}\right] \tag{1}$$

In order to quantify the dynamicity of the specimen, normalization of the COM is performed. Conventional IM and AVD methods consider single image parameter (j) based COM normalization, and result in higher standard deviation. To circumvent this drawback, robust indexing was proposed that considers both the image parameters (i, j). This is mathematically expressed as [5]

$$M_{ij} = \frac{N_{ij}}{\sum_{i,j} N_{ij}} \tag{2}$$

Finally, the overall activity of the biospeckle data is given by the spread of the COM values around the principal diagonal by using IM and AVD methods. These methods are given below

1. Inertia moment (IM): The spreading of COM values around the principal diagonal can be given as the sum of matrix value times its squared row distance from the principal diagonal. This is mathematically expressed as

$$IM = \sum_{i,j} M_{i,j}(i-j)^2 \tag{3}$$

2. Absolute value of difference (AVD): An alternative way to characterize the COM is its first order moment and is given by

$$AVD = \sum_{i,j} M_{i,j}\,|i-j| \tag{4}$$

3 Experimental Arrangement

3.1 Sample Preparation

Viable and nonviable bean seeds were procured and 20 seeds were selected from both the seed lot. These seeds were washed with sterilized distilled water and soaked in germination paper for 24 h to initiate the germination process. The seed samples were finally used under the biospeckle setup for experimentation.

3.2 Experimental Setup

The schematic of the experimental arrangement used for viability assessment of seed is shown in Fig. 1. We used a He-Ne laser source (15 mW, 632.8 nm) to illuminate the seed sample. The intensity of the light beam is adjusted using a beam attenuator to attain the proper intensity level. The quality test protocol [6] is followed to get

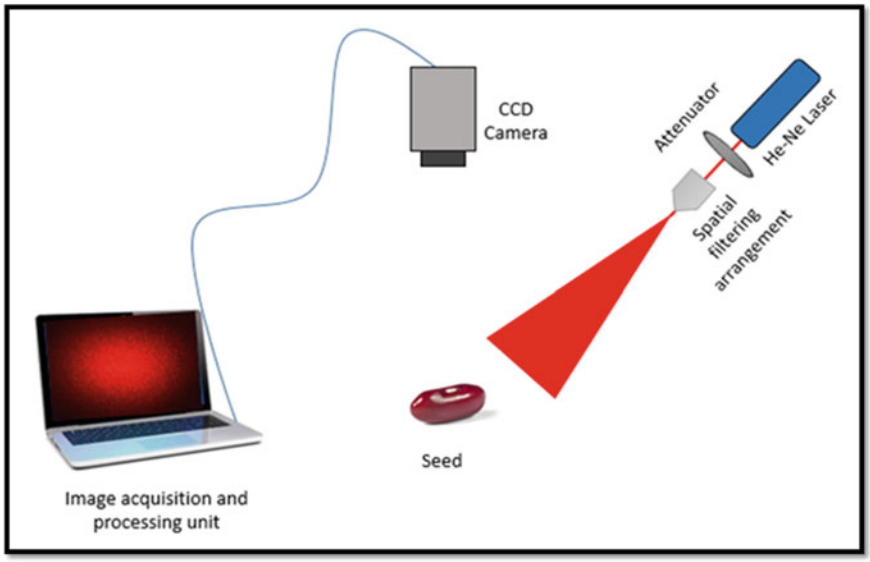

Fig. 1 Experimental set for biospeckle analysis

the actual activity parameter, and thereby removing the possibility of any erroneous result. A high frame rate camera (Basler Corp., 32 fps) records the successive sample biospeckle images. These images were digitized to 8-bit using a frame grabber card and stored in the computer for analysis purpose. The MATLAB based image analysis is developed to extract the activity information to distinguish between viable and nonviable seeds. Figure 2 shows the kidney bean seed and its speckle image. Figure 3 shows RTHSP for (a) nonviable and (b) viable seed. Figures 4 and 5 depict the COM for viable and nonviable samples, respectively.

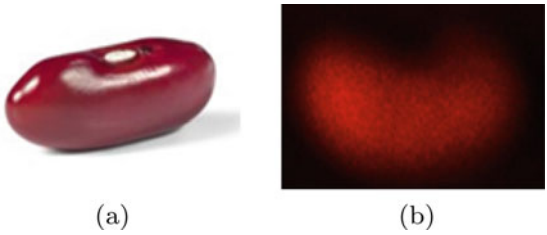

Fig. 2 **a** Kidney bean seed, and **b** speckle image of the seed

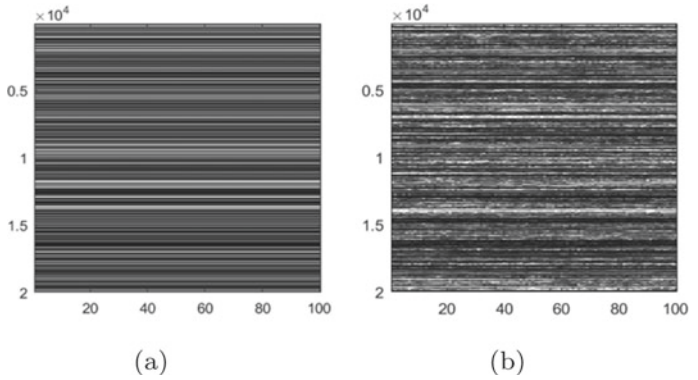

Fig. 3 RTHSP for **a** nonviable seed, and **b** viable seed

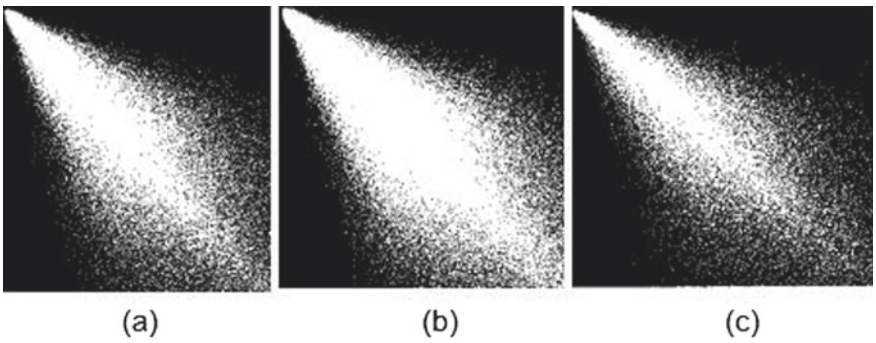

Fig. 4 COM for viable kidney bean seeds, **a** sample 1, **b** sample 2, and **c** sample 3

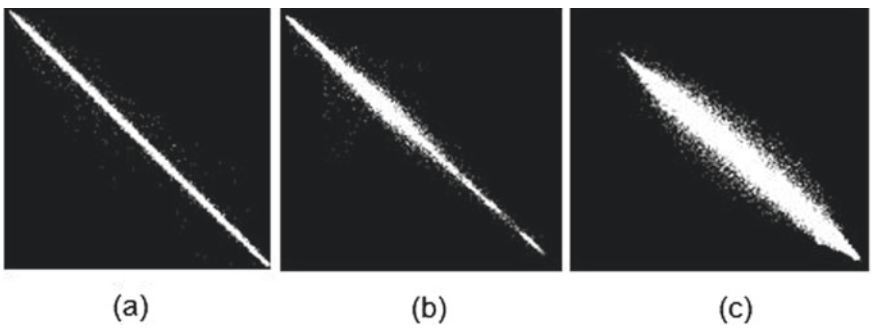

Fig. 5 COM for nonviable kidney bean seeds, **a** sample 1, **b** sample 2, and **c** sample 3

Table 1 IM and AVD index for viable and nonviable

Sample	IM (a.u.)	AVD (a.u.)	Viability assessment (Y/N)
1	831.78	332.48	Y
2	883.53	325.03	Y
3	846.37	341.25	Y
4	385.14	69.26	N
5	396.19	64.56	N
6	389.52	67.25	N

4 Results and Discussion

To quantify the activity of the seed sample, first and second order moment of the co-occurrence matrix is calculated. To distinguish between viable and nonviable seed groups numerically, the values of robust IM and AVD are calculated. The comparison of the different IM and AVD values for different seed samples is given in Table 1. By comparing the numerical values of the samples, the viability can be easily determined.

5 Conclusion

Biospeckle analysis was applied to study the viability of kidney bean seeds by considering the inhomogeneity of the samples. Two dynamic speckle techniques namely RTHSP and robust indexing are employed in conjunction with IM and AVD techniques. The robust normalization presented better accuracy if compared to the traditional normalization in the outputs of the IM and AVD methods, whereas random temporal history efficiently assesses the dynamicity of homogeneous, as well as heterogeneous samples. The experimental results show a significant dependence of the IM and AVD values on seed viability of kidney bean seeds. Hence, it is possible to distinguish between viable and nonviable tissue by quantitative measure means or through a qualitative display, using the COM. More extensive validation of the technique is required with greater populations, so that statistical analysis can be employed for comparison with standard germination tests. Nevertheless, the proposed technique is fast, easy to implement, and requires only laser and standard digital image processing components. It could be a useful tool to assess other diverse agricultural specimens.

Funding This publication is an outcome of the R & D work undertaken project under the Visvesvaraya PhD Scheme of Ministry of Electronics & Information Technology, Government of India, being implemented by Digital India Corporation & Department of Science & Technology project grant (EMR/2016/003115/EEC).

References

1. Hampton, J.G., Kahre, L., Van Gastel, A.J.G.: Quality seed from production to evaluation. Seed Sci. Technol. **24**, 393–407 (1996)
2. Arizaga, R., Trivi, M., Rabal, H.: Speckle time evolution characterization by the co-occurrence matrix analysis. Opt. Laser Technol. **31**, 163–169 (1999)
3. Braga, R.A., Nogre, C.M.B., Costa, A.G., Safadi, T., Costa, F.M.: Evaluation of activity through dynamic laser speckle using absolute value of the differences. Opt. Commun. **284**, 646–650 (2011)
4. Braga, R.A., González-Peña, R.G., Viana, D.C., Rivera, F.P.: Dynamic laser speckle analyzed considering inhomogeneities in the biological sample. J. Biomed. Opt. **22**, 04501001–0450110 (2017)
5. Cardoso, R.R., Braga, R.A.: Enhancement of the robustness on dynamic speckle laser numerical analysis. Opt. Lasers Eng. **63**, 19–24 (2014)
6. Moreira, J., Cardoso, R.R., Braga, R.A.: Quality test protocol to dynamic laser speckle analysis. Opt. Laser Eng. **61**, 8–13 (2014)

Automated Fast Anti-Spoof Biometry Using Random Temporal History and Numerical Indexing Based Biospeckle Analysis

Amit Chatterjee, Puneet Singh, Vimal Bhatia, and Shashi Prakash

Abstract In recent years, we have witnessed the adoption and evolution of biometric technology in various versatile applications such as access control, surveillance, and forensic investigations. However, one of the constraints in conventional biometric systems is the high possibility of the system being tricked or spoofed by forged biometrics, such as by artificial samples, photographs, video clips, etc. To identify such a spoof attack for fingerprint biometry, in this paper we propose an automated biospeckle based fast, simple, low-cost, and full-field technique. The specimen is illuminated by collimated light from a coherent laser source. The back-reflected light from the specimen is captured by a CCD camera, resulting in the formation of a dynamic granular shaped speckle pattern on the detector screen. To avoid the false results generated due to noise and vibrations, a spatial support is used. For automated processing of the recorded time-series images to estimate the dynamicity, an efficient and fast numerical biospeckle analysis strategy is introduced by combining statistical temporal history, numerical indexing, and region of interest selection strategy. Simulation studies confirm accuracy, high speed, and memory compactness of the proposed technique. It has been established that the proposed strategy is proficient in testing genuineness of the biometric traits.

Keywords Speckle · Biospeckle · Simulation · Biometrics · Spoof detection

A. Chatterjee (✉) · P. Singh · V. Bhatia
Signals and Software Group Discipline of Electrical Engineering, Indian Institute of Technology Indore, Indore 453446, India
e-mail: phd1601102005@iiti.ac.in

S. Prakash
Photonics Laboratory Department of Electronics and Instrumentation Engineering, Institute of Engineering and Technology Devi Ahilya University, Khandwa Road, Indore 452001, India

S. Mukherjee et al. (eds.), *Computational Mathematics, Nanoelectronics, and Astrophysics*, Springer Proceedings in Mathematics & Statistics 342,
https://doi.org/10.1007/978-981-15-9708-4_19

1 Introduction

In today's world, authentication of an individual is considered as a cornerstone of many security applications. There are several physiological traits (like a fingerprint, DNA, iris, retina, face, etc.) and behavioral traits (like a signature, typing rhythm, voice, etc.), that are unique to an individual and can be used as a biometric signature [1]. The present technological evolution has allowed the use of biometrics in many diverse environments, such as in research laboratory, national security, defense bases, security printing and minting corporations, surveillance, e-commerce, etc. Nowadays, even devices such as laptops, mobile phones, tablets use fingerprint biometric sensors for individual's authentication, as these devices contain sensitive information regarding bank account, personal identification number, etc. Also, biometric sensors have enormous potential to be installed in houses, vehicles, lockers as a substitute for today's lock and key system. This will eventually eliminate the requirement of carrying keys, remembering complicated passwords, and make life easier, as well as highly secure. However, one of the most predominant challenges in the majority of biometric identification frameworks is the possibility to recognize a spoofing attack. In such an attack, the stolen biometrics records can be easily exploited and mimicked by impostors to get unauthorized access to the biometric system, without the consent of the genuine user. Spoof attacks are gaining popularity because other forms of unauthorized data access require in-depth knowledge regarding the network and extensive hacking skills. Artificial dummies with embedded fingerprints can be prepared from household supplies for less than $10. Therefore, there is a need to strengthen the biometric device and prevent different types of fraudulent attacks.

Over the past few years, extensive research efforts have been introduced for spoof detection and prevention based on various techniques [2–9]. Towards this, Reddy et al. [2] proposed a biometric liveliness detection method based on the principle of pulse oximetry. However, the use of microcontroller based electronic circuit makes the overall experimental arrangement complex. Cheng et al. [3] introduced time domain optical coherence tomography (OCT) based technique to distinguish between artificial agents commonly used to spoof a commercial fingerprint reader. Autocorrelation analysis of the speckles generated in different skin layers of biological samples due to OCT imaging was analyzed for liveliness detection. The mechanical scanning in the reference arm of the OCT system of experimental arrangement reduces measurement accuracy and is time-consuming. Bossen et al. [4] have analyzed internal fingerprints using frequency domain OCT. The experimental arrangement can extract internal fingerprint, i.e., fingerprint of papillary layer, causing immunity from fake or dead finger spoofing with a high success rate. The drawback of the system is its long acquisition time for commercial applications. Liu and Buma [5] proposed a spoof-proof biometric technology using spectral domain OCT technique. Using this arrangement, mapping of the eccrine glands which lie underneath the fingertip skin was performed. Presence or absence of these glands provides information regarding spoof attacks successfully. However, this technique possesses similar drawbacks as [4]. Liu and Chen [6] used swept source Doppler OCT to capture vital vascular

fingerprints for highly sensitive and reliable personal identification. Auksorius and Boccara [7] devised a new imaging technique called oblique full-field OCT for fingerprint imaging from inside of the finger. With this proposed strategy, two major drawbacks of conventional OCT system, i.e., large memory requirement and slow speed of operation are alleviated. Darlow and Connan [8] presented a technique for the acquisition of high quality anti-spoof fingerprint image by performing internal and surface fingerprint blending using OCT. Darlow et al. [7] extended the concept of [8] by making an automated anti-spoof device. However, OCT based systems are difficult to align at locations outside the laboratory and have relatively high sensitivity to environmental noise. Additionally, the relatively high cost of the tunable laser source and detector increases the overall system cost.

In recent decades, a nondestructive and noninvasive optical imaging technique, called biospeckle analysis has attracted research attention. Biospeckle is a dynamic statistical interference pattern, which is created when a biological sample is irradiated by a coherent source. Several studies have been reported using biospeckle technique which include assessment of fruit drying [10], measurement of static scatterer concentration in phantom body fluids [11], imaging of seed and root tissues [12], fruit bruising monitoring [13], drying of adhesives [14, 15], quality testing of agricultural crops [16], and many more. To assess the overall dynamicity from dynamic speckle images, two types of techniques namely numerical and visual are widely used in the past. Numerical techniques (i.e., inertia moment, absolute value difference, wavelet entropy, etc.) assign a quantitative value to each dynamic level by taking a single column from each speckle image. Hence, poor accuracy and erroneous results are obtained (mainly for objects having anisotropic activity). Visual techniques (i.e., Fujii's method, generalized difference, subtraction average, structural function, modified structural function, etc.) provide accurate qualitative visualization of object activity (isotropic and anisotropic). However, due to performing pixel-by-pixel operation, these techniques require very high processing time. This drawback restricts the use of visual techniques in real-life instrument development applications. Also, both types of techniques require manual selection of speckle region, hence these techniques were unfit for real-time industrial applications. In our previous work, we proposed a technique to detect fingerprint spoofing using a combination of modified structural function and non-normalized histogram based biospeckle analysis [17]. The system is capable of detecting different types of spoof attacks efficiently. However, three step biospeckle operations (2D visual, statistical, and numerical) and 3D fingerprinting (acquisition and matching) make the overall system response slow. Moreover, the use of visual technique for biospeckle processing leads to unwanted memory wastage by storing the entire stack of image frames.

In the present manuscript, we report our investigations towards the development of a fast, memory compact biospeckle analysis based simple, efficient, and low-cost system capable of biometric spoof detection. The most common biometric trait, i.e., fingerprint is tested using the proposed system. The laser wavefront emerging from a collimating lens, when imposed on a physical biometric surface generates a dynamic pattern. To analyze this pattern and circumvent all the drawbacks arising in conventional biospeckle analysis technique, a combination of modified temporal history,

region of interest (ROI) selection, and numerical indexing based biospeckle analysis is introduced. The strategy is tested and compared with modified structural function based numerical indexing [17] using a simulation study; the results so obtained are also verified using experimental investigation. Based on the results, it can be inferred that the combination of the techniques is capable of detecting biometric spoofing in a fast, efficient, and automated way. Using the proposed strategy, an automated biometric spoof detection system is also realized.

2 Theory

When an object having intermolecular activity is illuminated by a coherent light source, a dynamic interference pattern of granular shape is observed. This phenomenon is known as biospeckle [16]. Analysis of spatio-temporal variation of biospeckles includes the following approaches:

1. Modified temporal history of speckle patterns (MTHSP): A convenient way of presenting the evolution of speckle pattern with time is to analyze its time history. A certain column (preferably middle) from each successive speckle pattern is selected and placed next to each other. The resulting image is called "time history of speckle pattern" (THSP). Being an 8-bit gray level matrix, the THSP can contain 256 possible pixel values from 0 (black) to 255 (white). However, no real-life dynamic activities possess homogeneity (not even homogeneous objects); hence accuracy of conventional THSP based numerical indices is poor. Hence, Braga et al. [18] proposed to calculate the temporal history by taking random number of points from the first speckle pattern in the sequence and making those point locations fixed in time. To eliminate the requirement of manual operation and reduce memory wastage before the creation of THSP, an automated region of interest (ROI) selection [19] is employed. As the pixel positions of the object in the captured frame are known, n-random points from ROI of the first frame are selected and placed in the first column of THSP matrix. These point locations are made fixed during all consecutive time frames. Next, the points from each frame of the speckle sequence are collected and placed side-by-side in the constructed THSP image. To distinguish this approach from conventional THSP, we termed this as modified THSP (MTHSP). Due to a random selection of n-number of points (where the value of n is not fixed and can be chosen by the programmer independently), the accuracy of numerical indices increases and the heterogeneity associated with the object is taken care of.
2. Co-occurrence matrix (COM): For quantitative evaluation of biospeckle activity, it is a common convention to calculate the second and first order moment of COM. For a highly dynamic object, COM resembles a diverging shape from the main diagonal. With the decrease in bio-activity (blood flow, respiration, muscular tremor, etc.), the coefficient of COM concentrate towards the main diagonal.

It can be defined as a number of successive occurrences of pixel values in each row of THSP. This is mathematically expressed as

$$M_{\mathrm{COM}} = \left[N_{i,j}\right] \tag{1}$$

where, elements of matrix M_{COM} are the number of occurrence of an intensity value i, that is immediately followed by value j. For a highly dynamic object, COM resembles a diverging shape from the main diagonal. With the decrease in bio-activity (blood flow, respiration, muscular tremor, etc.), the coefficient of COM concentrate towards the main diagonal.

3. Inertia Moment (IM): It is a texture descriptor which provides a numerical value of biospeckle activity map. Normalization in COM is essential in order to compute its IM value. Mathematically, this can be expressed as

$$M_{ij} = \frac{N_{ij}}{\sum_{i,j} N_{ij}} \tag{2}$$

Here, each row of the matrix is divided by the number of times the first gray level appears, resulting in the summation of each row of normalized COM (M_{ij}) equals to 1.

The spread of M values around the main diagonal can be measured as the sum of matrix value times its squared distance from the main diagonal. This is second order moment of Mij and called "moment of inertia". This is mathematically given by

$$IM = \sum_{i,j} M_{i,j}(i-j)^2 \tag{3}$$

4. Absolute value of difference (AVD): An alternative measurement of IM method for biospeckle analysis is AVD. It is the first order moment and mathematically given as [20]

$$AVD = \sum_{i,j} M_{i,j}\,|i-j| \tag{4}$$

This method originated from the basic idea that the main information to be searched from COM is the summation of difference. The square term of IM can amplify the variation of time history which is reduced through AVD method.

5. Modified structural function (MSF): For the generation of 2D visual activity map, MSF method is used. The analysis is based on the summation of the absolute difference between pixels of two images I_k and I_{k+l} separated by a window m. This can be mathematically expressed as

$$MSF = \sum_{k=1}^{m-1} |I_k(x,y) - I_{k+1}(x,y)| \tag{5}$$

where k is sequence index, x and y are coordinates of intensity matrix I_k, m is the total number of speckle images, and MSF (x, y) is the resulting 2D visual activity map. Next, to extract the numerical index from the visual map, same process as [17] is used.

3 Experimental Arrangement

3.1 Sample Preparation

There are few common ways in which a spoof attack can arise in a biometric recognition system, including layered fake samples, dummy samples, photographs, dead samples, etc. Therefore, the following types of samples were used to test the performance of the spoof detection system:

1. Real human finger for training the system.
2. Photograph and video of the trait.
3. Human finger with a layer of cello tape: This sample is used to simulate spoofing by a fake layer (made by gelatine, wax, agar, etc.) containing the fingerprint.
4. Artificial samples made of household cement: This is used to replicate the rightful owner's finger and present it to the detection system in place of a real one. Plasticene, liquid silicon rubber, gelatine can also be used for this purpose.

3.2 Setup

A schematic of an experimental arrangement for biometric spoof detection using biospeckle analysis is shown in Fig. 1. Light from the He-Ne laser of power 15mW and wavelength of 632.8 nm is spatially filtered using an aperture of 5 micron and a microscopic objective (MO) of magnification of 60x. The expanded laser beam is then directly incident upon the specimen and due to surface roughness, speckle patterns are formed. To avoid the influence of unwanted tremor (e.g., postural tremor, kinetic tremor, psychogenic tremor, etc.) that can generate false results, the biometric trait is presented in front of the detection system with a special support (not shown in the schematic diagram) [21]. Different types of samples, as described in the previous section are tested in the detection system and the corresponding dynamic speckle patterns recorded using a CCD camera having a resolution of 1295 $\times$ 975 pixels, and a frame rate of 32 fps (Basler Corp., Germany). For processing the time series data, various algorithms written in MATLAB environment are used for the analysis.

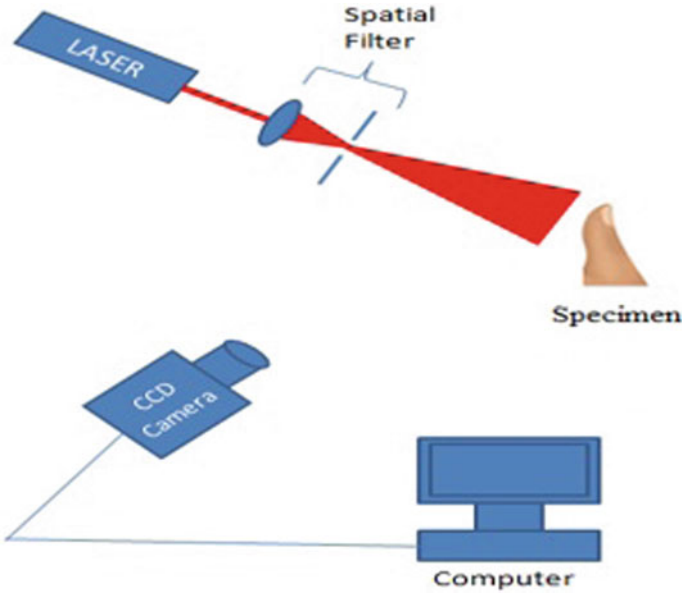

Fig. 1 Schematics of experimental setup

4 Results and Discussion

4.1 Numerical Simulation

A numerical simulation model for the generation of the synthetic speckle pattern is employed. This is shown in Fig. 2a. Two sets of 100 speckle patterns (static and dynamic) having a dimension of 400 × 400 pixels each are simulated to test the proposed technique against existing numerical and visual analysis. Rotational speckle sequences are generated by using "imrotate" MATLAB function [22]. For the dynamic rotating pattern, the rotation angle is adjusted to be 10; whereas for the static pattern, no rotation is applied in the sequence. Both the patterns are processed using the techniques stated in Sect. 2. Figure 2b, c shows the COM corresponding to the rotating and static diffuser model. Since the rotating model contains high dynamicity, the shape of COM resembles a cloud. For the static model, the values of COM are concentrated around the principal diagonal. Figure 2d, e show the corresponding 2D full-field dynamicity visualization using MSF technique. To assess the activity using IM and AVD technique, at first, MTHSPs are constructed (for both dynamic and static model) by collecting n-random data points (for demonstration, the values of n are chosen to be 10000, 20000, and 40000, respectively) from the first speckle frame of the speckle field and making those point locations fixed for all consecutive frames. Collected data points from each frame are placed side-by-side, and MTHSPs (with dimensions of 10000 × 100, 20000 × 100, and 40000×100, respectively) are

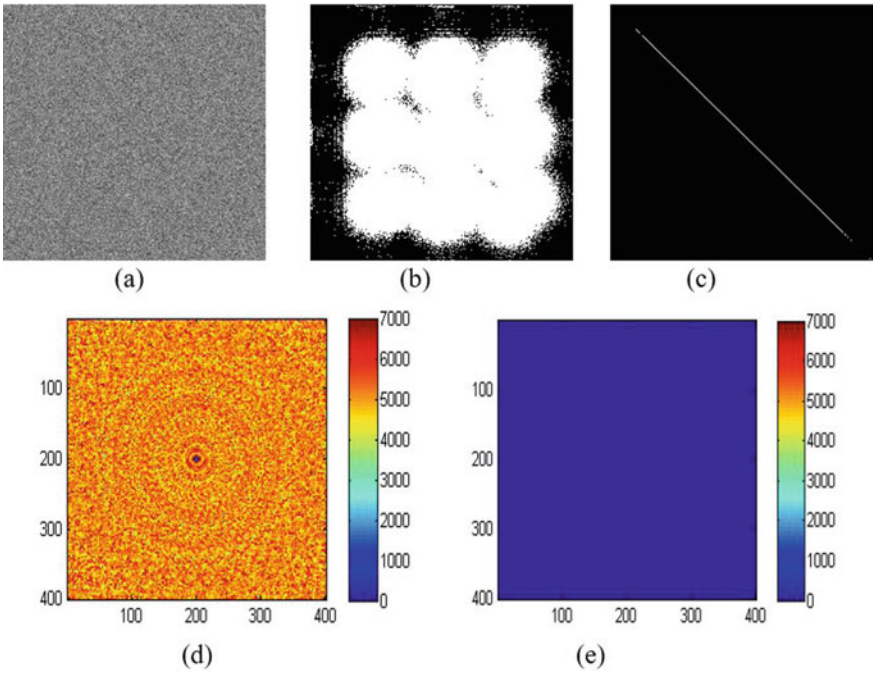

Fig. 2 Simulation results, **a** Simulated speckle pattern, **b** COM for rotating diffuser, **c** COM for static diffuser, **d** MSF activity map for rotating diffuser, and **e** MSF activity map for static diffuse

generated. The results retrieved from each sequence are tabulated in Table 1. For the static pattern, the value of all the indices becomes zero. Comparison between different numerical indices reveals that, with the increase of data points, the standard deviation of IM and AVD technique reduces. Although histogram based index for MSF technique have no standard deviation at all, this method have high computational complexity. For n = 40000, the value of standard deviation for IM and AVD is negligible as compared to other values. Hence, for practical experimentation, we have chosen the same value of n.

4.2 Automated Analysis and Quality Test Protocol

The genuineness of a physical biometric trait is tested by using the phenomena of internal blood flow and muscular reflexes. For real trait, due to these factors, generated speckle patterns become dynamic when laser light interacts with it. With an added layer (cello tape), this effect is reduced and for fake samples (or dead organs), this phenomenon is almost absent. To analyze the genuineness of incoming fingerprint, 100 successive images of 950 × 1250 pixels each with a sampling rate of 0.05s for

Table 1 Numeric parameters corresponding to aimulation based rotating diffuser model

No. coefficient (n)	IM value# (a.u.)		AVD value# (a.u.)		Histogram based index for MSF (a.u.)	
	Mean	SD	Mean	SD	Mean	SD
n = 10000	1.7898×10^{6}	7.0465×10^{4}	1.7192×10^{4}	402.7	–	–
n = 20000	1.8220×10^{6}	5.1099×10^{4}	1.7708×10^{4}	234.5	–	–
n = 40000	1.9133×10^{6}	2.8545×10^{6}	1.8156×10^{4}	70.95	–	–
n = (400 × 400) (Full-field anaysis)	–	–	–	–	5.13021×10^{5}	0

(# Mean and Standard are calculated consecutive simulated.)

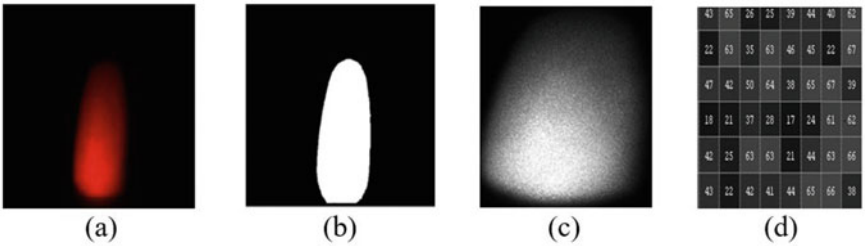

Fig. 3 **a** Speckle pattern of a human finger, **b** ROI mask, **c** Cropped region of speckle activity, and **d** Saturation map of a small portion of (**c**)

each sample are grabbed (Fig. 3a). Next, ROI mask is generated (Fig. 3b) and the region of finger speckle activity is cropped (Fig. 3c). The angle of the laser beam was so adjusted to minimize specular reflection and obtain high contrast "Quality test protocols" are followed to avoid the generation of false activity map [14]. A window of 8 × 6 pixels from the cropped region is selected to show the saturation map for the same (Fig. 3d). Saturation parameter indicates under-illumination or over-illumination (of the laser beam) by inferring pixel level of speckle frames. If the pixel values are 255 (over-illumination) or towards 0 (under- illumination), biospeckle activity cannot be obtained accurately. Hence, the laser beam intensity should be properly adjusted to avoid such erroneous conditions. Average saturation of speckle frames should not exceed 50% of the highest saturation level (in this case, the gray level of 255) in order to ensure accurate estimation of dynamicity.

4.3 Robustness Against Low Level Spoof Attacks (Photo and Video Attack)

For protecting the sensor against image and video attack, both the incident angle of the laser beam and reflectance angle to the camera is adjusted to 45°. As a result,

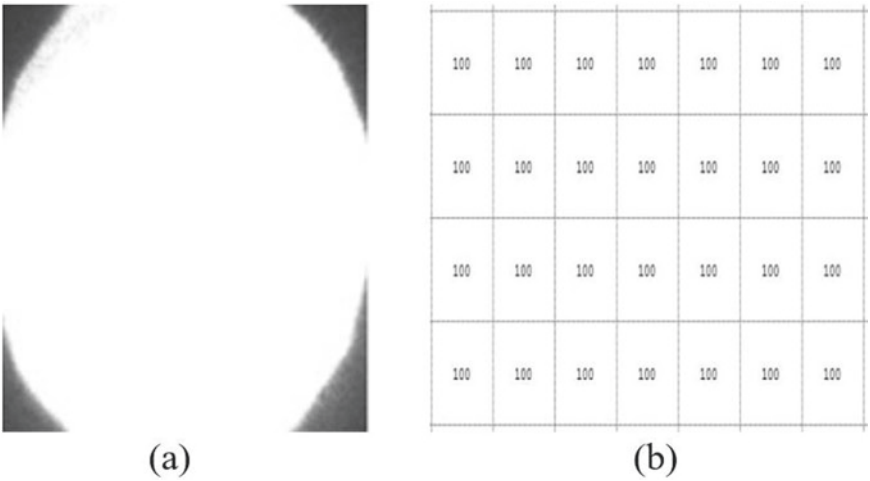

Fig. 4 **a** Speckle pattern for video attack, and **b** Corresponding saturation map

whenever an intruder attempts to access the secured system using a photograph or a video of the respective biometric trait, in place of scattering (due to interaction of the laser light with biospecimen, scattering takes place), reflection occurs. This will fail the saturation parameter of QTP and the system will not process further. The recorded speckle pattern and corresponding saturation map for a video is shown in Fig. 4a, b. Hence the technique is robust against photo and video attack.

4.4 Robustness Against High Level Spoof Attacks

For visual inspection of spoofing, non-normalized MSF method is utilized. Non-normalized MSF indicates that the MSF results are calculated in non-normalized scale (i.e., between 0 and infinity), and no prior normalization (i.e., scaling the map between 0 and 255) is performed over it. Pseudo-color results by application of MSF method are shown in Fig. 5a–c. Here, according to the color bars, red represent high activity, whereas blue represents low activity. In Fig. 5a, red and yellow colors are dominant which depicts a real finger. On the other hand, in Fig. 5b, c, the blue color is prominent that represents a dummy. In this way, the technique is capable of discriminating between the real and fake fingers depending on their activity map. For numerical analysis of finger spoofing, MTHSPs were constructed by selecting a certain column for each successive speckle patterns and placing them side-by-side. The dimension of the resultant image was of 40000×100 pixels. For high activity (real finger), MTHSP shows its resemblance with an ordinary speckle pattern. The corresponding COM shows a spread around the main diagonal. Low activity (cement

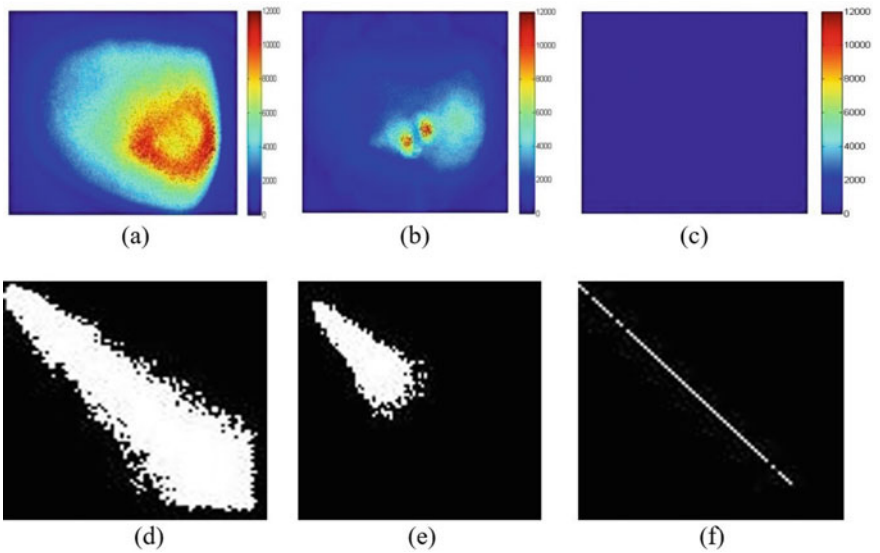

Fig. 5 **a** MSF activity map for a live finger, **b** MSF activity map for a cello taped finger, **c** MSF activity map for a cement finger, **d** COM for a live finger, **e** COM for a cello taped finger, and **f** COM for a cement finger

Table 2 Numeric parameters for different real and fake biometric sample

Type of sample	IM value (a.u.)	AVD value (a.u.)	Histogram based index for MSF (a.u.)
Live specimen	3.568×10^5	3.798×10^3	976
Cello taped specimen	1.6251×10^5	2.1625×10^3	402
Cement made specimen	11.125×10^3	538	23.52

finger) of sample results in a horizontal parallel bar-shaped pattern of THSP, its COM have points in the main diagonal only (Fig. 5d–f). The values of IM and AVD index corresponding to real and fake samples are calculated and tabulated in Table 2.

5 Conclusion

This study has demonstrated the construction of a biometric spoof detection system using an automated fast biospeckle analysis. Following points can be retrieved from this investigation:

1. An efficient biospeckle analysis strategy by combining MTHSP, ROI selection, and numerical indexing techniques (IM and AVD) is proposed. Highlights of the

strategy include its simplicity, automated operation, fast operating speed, memory compactness, high accuracy (95% confidence interval), the capability of handling object inhomogeneities, etc.
2. Spoof detection of the prominent biometric trait, namely fingerprint, was successfully undertaken using different numerical and visual biospeckle analysis techniques. The proposed analysis technique is robust against photo attacks, video attacks, artificial specimen, etc.
3. Overall the proposed system is fast, simple, low-cost, and full-field. A biometric recognition system, when combined with biospeckle module can provide high security and a unique way for detection and personal verification.

Funding Visvesvaraya Ph.D. scheme of Ministry of Electronics and Information Technology (MeitY) and Department of Science and Technology project grant (EMR/2016/003115/EEC).

References

1. Hawthorne, M.: Fingerprints: Analysis and Understanding. CRC Press, Taylor and Francis group (2009)
2. Reddy, P.V., Kumar, A., Rahman, S.M.K., Mundra, T.S.: A new antispoofing approach for bi-ometric devices. IEEE Trans. Biomed. Cir. Syst. **2**, 328–37 (2008)
3. Cheng, Y., Larin, K.V.: Artificial fingerprint recognition by using optical coherence tomography with autocorrelation analysis. Appl. Opt. **45**, 9238–45 (2006)
4. Bossen, A., Lehmann, R., Meier, C.: Internal fingerprint identification with optical coher-ence tomography. IEEE Phot. Technol. Lett. **22**, 507–509 (2010)
5. Liu, M., Buma, T.: Biometric mapping of fingertip eccrine glands with optical coherence tomography. IEEE Phot. Technol. Lett. **22**, 1677–1679 (2010)
6. Liu, G., Chen, Z.: Capturing the vital vascular fingerprint with optical coherence tomog-raphy. Appl. Opt. **52**, 5473–54777 (2013)
7. Auksorius, E., Boccara, A.C.: Fingerprint imaging from the inside of a finger with full-field optical coherence tomography. Biomed. Opt. Exp. **6**, 4465–4471 (2015)
8. Darlow, N.L., Connan, J.: Efficient internal and surface fingerprint extraction and blend-ing using optical coherence tomography. Appl. Opt. **54**, 9258–9268 (2015)
9. Darlow, N.L., Webb, L., Connan, J.: Automated spoof-detection for fingerprints using opti-cal coherence tomography. Appl. Opt. **55**, 3387–3396 (2016)
10. Cardoso, R.R., Braga, R.A.: Enhancement of the robustness on dynamic speckle laser numerical analysis. Opt. Las. Eng. **63**, 19–24 (2014)
11. Jayanthy, A.K., Sujatha, N., Reddy, M.R.: Non-invasive assessment of static scatterer concentration in phantom body fluids using laser speckle contrast analysis technique. Opt. Las. Eng. **49**, 553–556 (2011)
12. Godinho, R.P., Silva, M.M., Nozela, J.R., Braga, R.A.: Online biospeckle assessment without loss of definition and resolution by motion history image. Opt. Las. Eng. **50**, 366–72 (2012)
13. Pajuelo, M., Baldwin, G., Rabal, H.J., Cap, N., Arizaga, R., Trivi, M.: Bio-speckle assessment on bruising in fruits. Opt. Las. Eng. **40**, 13–24 (2003)
14. Moreira, J., Cardoso, R.R., Braga, R.A.: Quality test protocol to dynamic laser speckle analysis. Opt. Las. Eng. **61**, 8–13 (2014)
15. Balamurugan, R., Rajarajan, G.: Study of drying process of paint by dynamic speckle with B/D pixel counting technique. Opt. Las. Eng. **98**, 62–68 (2017)
16. Zdunek, A., Adamiak, A., Piecywek, P.M., Kurenda, A.: The biospeckle method for the investigation of agricultural crops: A review. Opt. Las. Eng. **52**, 276–285 (2014)

17. Chatterjee, A., Bhatia, V., Prakash, S.: Anti-spoof touchless 3D fingerprint recognition sys-tem using single shot fringe projection and biospeckled analysis. Opt. Las. Eng. **95**, 1–7 (2017)
18. Braga, R.A., González-Peña, R.G., Viana, D.C., Rivera, F.P.: Dynamic laser speckle analyzed considering inhomogeneities in the biological sample. J. Biomed. Opt. **2017**(22), 04501001–0450110 (2017)
19. Si, J., Lin, H., Abousleman, G.: Detecting region of interest in images. SPIE Newsroom **1–3** (2006)
20. Braga, R.A., Nogre, C.M.B., Costa, A.G., Safadi, T., Costa, F.M.: Evaluation of activity through dynamic laser speckle using absolute value of the differences. Opt. Commun. **284**, 646–650 (2011)
21. Rocon, E., Pons, J.L.: Exoskeletons In Rehabilitation Robotics: Tremor Suppression. Springer, Berlin (2001). https://doi.org/10.1007/978-3-642-17659-3
22. Guzmán, M.N., Sendra, G.H., Rabal, H.J., Trivi, M.: Island analysis of low-activity dynamic speckles. Appl. Opt. **53**, 14–21 (2014)